

# **Analysis of Ultrasonic Vibration Combined with Sustainable Cooling Strategies for Machining Difficult-to-cut Materials**

## **Doctoral Thesis**

by

**“Jay Airao”**

**(2018mez0018)**



**DEPARTMENT OF MECHANICAL ENGINEERING  
INDIAN INSTITUTE OF TECHNOLOGY ROPAR**

**March, 2023**

# **Analysis of Ultrasonic Vibration Combined with Sustainable Cooling Strategies for Machining Difficult-to-cut Materials**

A Thesis Submitted  
In Partial Fulfillment of the Requirements  
for the Degree of

**DOCTOR OF PHILOSOPHY**

by

**“Jay Airao”**

**(2018mez0018)**



**DEPARTMENT OF MECHANICAL ENGINEERING  
INDIAN INSTITUTE OF TECHNOLOGY ROPAR**

**March, 2023**

Your Full Name: *Analysis of ultrasonic vibration combined with sustainable cooling strategies for machining difficult-to-cut materials*

Copyright © 2022, Indian Institute of Technology Ropar

All Rights Reserved

## Declaration of Originality

I hereby declare that the work which is being presented in the thesis entitled **Analysis of ultrasonic vibration combined with sustainable cooling strategies for machining difficult-to-cut materials** has been solely authored by me. It presents the result of my own independent investigation/research conducted during the time period from **January 2019** to **November 2022** under the supervision of **Dr. Chandrakant K. Nirala**, Assistant Professor, Mechanical Department, Indian Institute of Technology Ropar. To the best of my knowledge, it is an original work, both in terms of research content and narrative, and has not been submitted or accepted elsewhere, in part or in full, for the award of any degree, diploma, fellowship, associateship, or similar title of any university or institution. Further, due credit has been attributed to the relevant state-of-the-art and collaborations with appropriate citations and acknowledgments, in line with established ethical norms and practices. I also declare that any idea/data/fact/source stated in my thesis has not been fabricated/ falsified/ misrepresented. All the principles of academic honesty and integrity have been followed. I fully understand that if the thesis is found to be unoriginal, fabricated, or plagiarized, the Institute reserves the right to withdraw the thesis from its archive and revoke the associated Degree conferred. Additionally, the Institute also reserves the right to appraise all concerned sections of society of the matter for their information and necessary action. If accepted, I hereby consent for my thesis to be available online in the Institute's Open Access repository, inter-library loan, and the title & abstract to be made available to outside organizations.

Signature



Name: Jay Airao

Entry Number: 2018mez0018

Program: Ph.D.

Department: Mechanical

Indian Institute of Technology Ropar

Rupnagar, Punjab 140001

Date: 05/04/23



## Acknowledgments

The work presented in this dissertation would have not been possible without my close association with many people. I take this opportunity to extend my sincere gratitude and appreciation to all those who made this dissertation work possible.

First and foremost, I wish to thank my supervisor **Dr. Chandrakant K. Nirala**, Assistant Professor, Department of Mechanical Engineering, IIT Ropar, for introducing me to this exciting field of research. Dr. Nirala is not only a scholarly instructor but also a portrait of inspiration and encouragement, without whom it would have not been possible for me to complete my work. I appreciate all his contributions of time, ideas, and funding to make my Ph.D. experience productive and stimulating.

I am very much thankful to **Dr. Anshu Dhar Jayal** and **Dr. Rakesh Kumar Maurya**, for motivating and inspiring me to do the research.

I express my sincere gratitude to **Dr. Navneet Khanna**, Assistant Professor, Department of Mechanical & Aero-Space Engineering, IITRAM, Ahmedabad for permitting me to use the cryogenic machining setup for performing experiments. His continuous support, guidance, cooperation, encouragement, facilitating all the requirements for the experiment, and going out of his way to help has been paramount.

I would further like to express my appreciation to the members of my Doctoral Committee members: **Dr. Ekta Singla** (Chairperson, Associate professor, Mechanical Department, IIT Ropar), **Dr. Anupam Agrawal** (Associate professor, Mechanical Department, IIT Ropar), **Dr. Sachin Kumar** (Associate professor, Mechanical Department, IIT Ropar), **Dr. Saifullah Payami** (Assistant professor, Electrical Department, IIT Ropar), for reviewing my experimental work and providing me the technical guidance from time to time to improve the quality of my work. I also thanks **Prof. Karali Patra**, Indian Institute of Technology Patna, for providing important insights in my synopsis seminar.

I thank all the workshop staff members **Jaswinder Singh, Jaskaran Singh, Randheer Singh, Bhupendrajee, Ramveerjee, Yograjee** and **Girdharjee** for helping me in conducting the experiments. Moreover, I thank to **Mr. Amit Kaushal** for helping me in characterization processes.

My special regards to my seniors, juniors and friends, **Hreetabh Kishore, Sohaib Raza, Mohit Raj Saxena, Rahul Nadda, Abhishek Gupta, Mainak Pal, Raushan Kumar, Gopal Chandra Pal, Neeraj Kumar Yadav, Neha Vishnoi, Vivek K, Sudhendu Tiwari** for always standing by my side in every difficulty and sharing a great relationship as compassionate friends.

**Jay Airao**

## Certificate

This is to certify that the thesis entitled **Analysis of ultrasonic vibration combined with sustainable cooling strategies for machining difficult-to-cut materials**, submitted by **Jay Airao (2018mez0018)** for the award of the degree of **Doctor of Philosophy** of the Indian Institute of Technology Ropar, is a record of bonafide research work carried out under my (our) guidance and supervision. To the best of my knowledge and belief, the work presented in this thesis is original and has not been submitted, either in part or full, for the award of any other degree, diploma, fellowship, associateship or similar title of any university or institution. In my (our) opinion, the thesis has reached the standard of fulfilling the requirements of the regulations relating to the Degree.

*Chandrakant K. Nirala*

Signature of the Supervisor

Dr. Chandrakant K. Nirala

Department of Mechanical Engineering

Indian Institute of Technology Ropar

Rupnagar, Punjab 140001

Date: 05.04.03

## Lay Summary

Conventional machining is the most general process in material removal trades. The metal cutting process involves a permanent distortion induced due to force applied by a cutting tool. A severe distortion of the workpiece material generates heat, mainly in the distortion areas. The heat generated depends upon the workpiece materials and machining parameters such as cutting speed, feed and depth of cut. The workpiece materials, such as mild steel, brass, aluminum, copper, etc., are easy to cut and may not produce a large amount of heat. On the other hand, some hard materials, such as stainless steel, titanium, and nickel produce a large amount of heat during the cutting process. It results in rapid tool wear, high cutting forces, poor surface quality, etc. Therefore, it is necessary to remove the heat generated during machining processes using coolants. Traditional synthetic oil-based coolants are not considered environmental friendly. To reduce the consumption of traditional coolants, alternative cooling approaches such as MQL (minimum quantity lubrication) and LCO<sub>2</sub> have been used to remove the heat. The present work uses the MQL and LCO<sub>2</sub>, along with ultrasonic vibration, to reduce the tool wear, machining forces, and surface roughness during the machining of hard materials. The ultrasonic vibration is provided using the in-house developed setup. The machining responses, such as machining forces, tool wear, and surface quality, are analyzed under the combined effect of ultrasonic vibration and coolants such as MQL and LCO<sub>2</sub>. The results show that the combined effect of ultrasonic vibration and coolants is advantageous in improving metal cutting performances during the machining of hard materials. Moreover, the machining responses are estimated using the analytical formulation. This method uses a well-organized formulation of mathematical relationships for predicting the desired output. The formulation predicts the machining forces and friction behavior, considering the ultrasonic vibration. Moreover, the prediction of the tool wear is attempted using the software. This method is called finite element modeling (FEM). The results show that the above-mentioned methods predict machining responses with less error. In the extension of the thesis work, micro level of cutting of different metallic materials is executed. The responses such as tool wear, surface properties and chips formed are analysed.

## Abstract

The metal-cutting process induces a severe plastic deformation of the workpiece material at the deformation zones, generating heat. Machining difficult-to-cut materials further enhance heat generation, reducing tool life and degrading surface quality. Using cutting fluids to remove the heat from the deformation zone is a common approach used by metal-cutting industries. It is observed that the conventional synthetic oil-based cutting fluids are not biodegradable and require expensive treatment for disposal. In this regard, applying ultrasonic vibration combined with a sustainable cooling/lubrication strategy is proposed to enhance the machinability of difficult-to-cut materials and to reduce the consumption of conventional cutting fluids. An indigenously developed setup is used for implementing ultrasonic vibration to the cutting tool. MQL (minimum quantity lubrication) and LCO<sub>2</sub> (liquid carbon dioxide) are employed for cooling and lubrication purposes. The machinability of Ti6Al4V and Inconel 718 is examined under the combined effect of ultrasonic vibration and cooling/lubrication strategies. The responses, such as tool wear, surface quality, power consumption, and cutting forces, are analyzed. The combination of ultrasonic vibration and LCO<sub>2</sub> offers a significant reduction in tool wear and hence power consumption and specific cutting energy for both the workpiece materials, Inconel 718 and Ti6Al4V. Quantitatively, the UAT combined with LCO<sub>2</sub> approximately reduced the flank wear by 35-70% and 32-60% for Ti6Al4V and Inconel 718, respectively.

In the other phase of the thesis work, analytical and finite element models are developed to estimate the machining responses, considering the ultrasonic vibration. The analytical model is developed to predict machining forces and tribological characteristics under the effect of ultrasonic vibration. The developed analytical model is validated by conducting experiments on the SS 304 stainless steel. The analytical model showed a very good agreement at a lower value of cutting speed and feed rate. The tool wear and machining forces are estimated using finite element modeling and validated with experimental observations. The FEM and experimental results were in close agreement with an approximate error of 2-25%.

In the extension of the thesis work, the downscaling of conventional machining is explored using different workpiece materials such as wrought Ti6Al4V, SLM Ti6Al4V, and Nimonic 90. Comparing the micro machinability of wrought and SLM Ti6Al4V, higher hardness and instability of the  $\beta$  phase at a higher temperature in the LPBF Ti6Al4V are mainly responsible for enhanced tool wear. On the other hand, equiaxed grains and balanced yield strength and hardness of wrought Ti6Al4V are primarily accountable for reduced tool wear.

**Keywords:** Ultrasonic-assisted machining; Sustainable machining; Modelling; Cryogenic; Tool wear; Micromachining;

## List of Publications from Thesis

### Journal

- (1) **Airao J**, Nirala CK. Analytical Modelling of Machining Forces and Friction Characteristics in Ultrasonic Assisted Turning Process. *ASME Journal of Manufacturing Science and Engineering*, 2021;144(2):021014. <https://doi.org/10.1115/1.4052129>
- (2) **Airao J**, Nirala CK, Bertolini R, Krolczyk GM, Khanna N. Sustainable cooling strategies to reduce tool wear, power consumption and surface roughness during ultrasonic assisted turning of Ti6Al4V. *Tribology International*, 2022;169:107494. <https://doi.org/10.1016/j.triboint.2022.107494>
- (3) **Airao J**, Nirala CK, Khanna N. Novel use of ultrasonic-assisted turning in conjunction with cryogenic and lubrication techniques to analyse the machinability of Inconel 718. *Journal of Manufacturing Processes*, 2022;81:962-975. <https://doi.org/10.1016/j.jmapro.2022.07.052>
- (4) **Airao J**, Nirala CK, Finite Element Modeling and Experimental Validation of Tool Wear in Hot-Ultrasonic Assisted Turning of Nimonic 90, *Journal of Vibration Engineering & Technologies*, 2022, <https://doi.org/10.1007/s42417-022-00776-6>.
- (5) **Airao J**, Nirala CK. Machinability analysis of Titanium 64 using ultrasonic vibration and vegetable oil. *Materials and Manufacturing Processes*, 2022;37(16):1893-1901. <https://doi.org/10.1080/10426914.2022.2065015>
- (6) **Airao J**, Kishore H, Nirala CK, Tool wear behaviour in micro turning of Nimonic 90 under vegetable oil-based cutting fluid. *ASME Journal of Micro Nano Manufacturing*. 2021;9(4):041003. <https://doi.org/10.1115/1.4053315>
- (7) **Airao J**, Nirala CK, Effect of microstructure on tool wear in micro turning of wrought and selective laser melted Ti6Al4V. *Materials Letters*. 2022;327:133078. <https://doi.org/10.1016/j.matlet.2022.133078>.
- (8) **Airao J**, Kishore H, Nirala CK, Measurement and Analysis of tool wear and surface characteristics in micro turning of wrought Ti6Al4V and SLM Ti6Al4V. *Measurement*. 2022;206:112281

### Conference Proceeding

- (1) **Airao J**, Nirala CK. Finite element modeling of ultrasonic assisted turning with external heating. *Procedia CIRP.*, 2021;102:61-66. <https://doi.org/10.1016/j.procir.2021.09.011>
- (2) **Airao J**, Nirala CK, Outeiro J, Khanna N. Surface integrity in ultrasonic-assisted turning of Ti6Al4V using sustainable cutting fluid. *Procedia CIRP.*, 2022;108:55-60. <https://doi.org/10.1016/j.procir.2022.04.068>
- (3) **Airao J**, Nirala CK. Machinability of Ti-6Al-4V and Nimonic-90 in ultrasonic-assisted turning under sustainable cutting fluid. *Materials Today: Proceedings.*, 2022;62:7396-7400. <https://doi.org/10.1016/j.matpr.2022.02.312>

# Table of Contents

Declaration	iv
Acknowledgement	v
Certificate	vi
Lay Summary	vii
Abstract	viii
List of Publication	ix
List of Figures	xii
List of Tables	xvi
Notations and Abbreviations	xvii
1. Introduction	1
1.1 Turning as a conventional machining process	1
1.2 Assisted Machining	3
1.3 Summary	7
2. Literature Review	9
2.1 Ultrasonic- assisted machining processes	9
2.2 Cooling/lubrication strategies	13
2.3 Modelling of ultrasonic-assisted turning process	22
2.4 Research gaps	30
2.5 Objectives	31
3. Experimental procedure	31
3.1 Horn design	31
3.2 Components for the UAT setup	41
3.3 Materials and methods	43
3.4 Process parameters	46
3.5 Cooling strategies	46
3.6 Measurement and characterization	50
4. Modelling of ultrasonic assisted turning process	56
4.1 Analytical modelling	56
4.2 Finite element modelling	74
5. Experimental Analysis on the combined effect of ultrasonic vibration and cutting fluids	91
5.1 Experimental Analysis for Inconel 718	91

5.2	Experimental Analysis for Ti6Al4V	110
5.3	Surface integrity analysis for Ti6Al4V	124
6.	Experimental investigation on the downscale of machining	130
6.1	Experimental Analysis for Nimonic 90 in micro-turning	131
6.2	Experimental Analysis for selective laser melted and wrought Ti6Al4V in micro-turning	142
7.	Conclusions	158
	References	160

## List of Figures

<b>Figure 1.1</b>	Schematic of turning process	1
<b>Figure 1.2(a)</b>	Schematic of single point cutting process	2
<b>Figure 1.2(b)</b>	Heat generated in different machining zones	2
<b>Figure 1.3(a)</b>	Schematic of Induction-assisted machining	3
<b>Figure 1.3(b)</b>	A schematic of Plasma-assisted machining	3
<b>Figure 1.3(c)</b>	A schematic of Gas-assisted machining	3
<b>Figure 1.3(d)</b>	A schematic of Electrical current-assisted machining	3
<b>Figure 1.3(e)</b>	A schematic of Laser-assisted machining	3
<b>Figure 1.4(a)</b>	A schematic of ultrasonic-assisted turning setup	5
<b>Figure 1.4(b)</b>	Tool engagement with workpiece	5
<b>Figure 1.4(c)</b>	Tool disengagement with workpiece	5
<b>Figure 1.5</b>	Tool vibration cycle in 1D UAM	6
<b>Figure 2.1</b>	Definition of minimum quantity cooling and lubrication (MQCL)	15
<b>Figure 2.2</b>	MQL supply system	16
<b>Figure 2.3</b>	Schematic of EMQL	17
<b>Figure 3.1</b>	Complex exponential representation of $f(t) = A \cos(\omega t + \phi)$	31
<b>Figure 3.2</b>	Displacement from equilibrium and stresses in a pure longitudinal wave	32
<b>Figure 3.3</b>	A horn showing pressure force on a small elemental strip	35
<b>Figure 3.4</b>	Different types of horn	36
<b>Figure 3.5</b>	Schematic of stepped horn	36
<b>Figure 3.6</b>	Effect of terminal diameter ratio and shape function on the magnification factor	39
<b>Figure 3.7</b>	Amplitude distribution of stepped acoustic horn	39
<b>Figure 3.8</b>	Design of horn by FEM	40
<b>Figure 3.9</b>	Horn used for conducting UAT experiments	40
<b>Figure 3.10</b>	Components used for UAT setup	42
<b>Figure 3.11</b>	UAT setup mounted on conventional lathe for performing experiments	42
<b>Figure 3.12</b>	Cutting insert used to perform the experiments	44
<b>Figure 3.13</b>	Machine tool used to perform the experiments	45
<b>Figure 3.14</b>	Schematic of conventional wet cooling approach used during machining	47
<b>Figure 3.15</b>	Setup used for MQL in machining	49
<b>Figure 3.16</b>	Liquid carbon dioxide (LCO <sub>2</sub> ) cylinder	49
<b>Figure 3.17</b>	Force measurement using dynamometer	51
<b>Figure 3.18</b>	Taylor Hobson Surtronic S128 surface roughness tester	51
<b>Figure 3.19</b>	Fluke 435 power quality and energy analyser	53
<b>Figure 3.20</b>	Optical and scanning electron microscopes	54



<b>Figure 4.1</b>	Schematic of UAT process	57
<b>Figure 4.2</b>	Tool displacement and velocity in UAT process	57
<b>Figure 4.3</b>	Relation between thermal number and heat conducted back to workpiece	61
<b>Figure 4.4</b>	Stresses induced on rake face of the tool during machining	62
<b>Figure 4.5</b>	Flow chart for analytical modelling of machining forces and friction characteristics	64
<b>Figure 4.6(a)</b>	Variation in TWCR maximum shear angle with frequencies ( $A=10\mu\text{m}$ )	65
<b>Figure 4.6(b)</b>	Variation in maximum shear angle with frequencies ( $A=10\mu\text{m}$ )	65
<b>Figure 4.7(a)</b>	Variation in TWCR with amplitudes ( $F=20\text{ kHz}$ )	66
<b>Figure 4.7(b)</b>	Variation in maximum shear angle with amplitudes ( $F=20\text{ kHz}$ )	66
<b>Figure 4.8(a)</b>	Variation in cutting force with cutting speed at a feed rate of 0.1 mm/rev	69
<b>Figure 4.8(b)</b>	Variation in cutting force with feed rate at a cutting speed of 50 m/min	69
<b>Figure 4.9(a)</b>	Variation in thrust force with cutting speed at a feed rate of 0.1 mm/rev	70
<b>Figure 4.9(b)</b>	Variation in thrust force with feed rate at a cutting speed of 50 m/min	70
<b>Figure 4.10(a)</b>	Variation in coefficient of friction with cutting speed at a feed rate of 0.1 mm/rev	71
<b>Figure 4.10(b)</b>	Variation in coefficient of friction feed rate at a cutting speed of 50 m/min	71
<b>Figure 4.11(a)</b>	Variation in tool-chip contact length with cutting speed at a feed rate of 0.1 mm/rev	72
<b>Figure 4.11(b)</b>	Variation in tool-chip contact length with feed rate at a cutting speed of 50 m/min	72
<b>Figure 4.12</b>	Finite element model of the tool and workpiece	74
<b>Figure 4.13</b>	Boundary conditions used for tool and workpiece	78
<b>Figure 4.14(a)</b>	Inhouse developed UAT setup	78
<b>Figure 4.14(b)</b>	Workpiece preheated at $200^{\circ}\text{C}$ just before HUAT	78
<b>Figure 4.15</b>	Results of tool crater wear obtained from FEM and experiments at set 1 (30 m/min, 0.2 mm/rev, 0.4 mm)	79
<b>Figure 4.16</b>	Results of tool crater wear obtained from FEM and experiments at set 2 (70 m/min, 0.1 mm/rev, 0.2 mm)	81
<b>Figure 4.17</b>	Width of the flank wear obtained for both the sets Experimentally	83
<b>Figure 4.18</b>	Results of tool flank wear obtained from FEM and experiments at set 1 (30 m/min, 0.2 mm/rev, 0.4 mm)	83
<b>Figure 4.19</b>	Results of tool flank wear obtained from FEM and experiments at set 2 (70 m/min, 0.1 mm/rev, 0.2 mm)	86
<b>Figure 4.20(a)</b>	Average value of tool-chip contact length measured for set 1 (30 m/min, 0.2 mm/rev, 0.4 mm)	87
<b>Figure 4.20(b)</b>	Average value of tool-chip contact length measured set 2 (70 m/min, 0.1 mm/rev, 0.2 mm)	87
<b>Figure 4.21(a)</b>	Average cutting forces generated for set 1 (30 m/min, 0.2 mm/rev, 0.4 mm)	88
<b>Figure 4.21(a)</b>	Average cutting forces generated for set 2 (70 m/min, 0.1 mm/rev, 0.2 mm)	88
<b>Figure 4.22(a)</b>	Average feed forces generated for set 1 (30 m/min, 0.2 mm/rev, 0.4 mm)	89
<b>Figure 4.22(b)</b>	Average feed forces generated for set 2 (70 m/min, 0.1 mm/rev, 0.2 mm)	89

<b>Figure 5.1</b>	Morphology of tool crater wear observed in CT and UAT, under different conditions	93
<b>Figure 5.2</b>	Penetration of the cutting fluid in conventional and ultrasonic assisted turning	96
<b>Figure 5.3</b>	Average width of flank wear measured under different cutting environments	97
<b>Figure 5.4</b>	Morphology of tool flank wear observed in CT and UAT, under different conditions	98
<b>Figure 5.5</b>	Average power consumption measured in CT and UAT under different conditions	102
<b>Figure 5.6</b>	Average surface roughness measured in CT and UAT under different conditions	103
<b>Figure 5.7(a)</b>	Variation in specific cutting energy with tool wear during CT and UAT under different cooling strategies	105
<b>Figure 5.7(b)</b>	Variation in average surface roughness with tool wear during CT and UAT under different cooling strategies	105
<b>Figure 5.8</b>	Chips geometry and morphology observed in CT and UAT under different cooling strategies	106
<b>Figure 5.9</b>	Average width of flank wear measured under different cooling strategies	111
<b>Figure 5.10</b>	Morphology of tool flank wear observed in CT and UAT, under different conditions	112
<b>Figure 5.11</b>	Morphology of rake face wear observed in CT and UAT, under different conditions	115
<b>Figure 5.12</b>	Power consumption measured in CT and UAT under different cooling strategies	117
<b>Figure 5.13</b>	Average surface roughness measured in CT and UAT under different cooling strategies	119
<b>Figure 5.14</b>	Variation in specific cutting energy and average surface roughness with tool wear during CT and UAT under different cooling strategies	120
<b>Figure 5.15</b>	Chips geometry and morphology observed in CT and UAT under different cooling strategies	121
<b>Figure 5.16</b>	Average surface roughness measured in CT and UAT and dry and VCF conditions	125
<b>Figure 5.17</b>	Surface topography measured in CT and UAT, under dry and VCF conditions	126
<b>Figure 5.18</b>	Cross section of deformed layer in CT and UAT, under dry and VCF conditions	127
<b>Figure 5.19</b>	Average variation in microhardness for different machining conditions	129
<b>Figure 6.1</b>	Size effect in micro-scale machining process	130
<b>Figure 6.2</b>	Experimental setup used for $\mu$ -turning	132
<b>Figure 6.3</b>	Arrangement of molecule in vegetable oil and lubrication film of vegetable oil formed on a surface of workpiece	132
<b>Figure 6.4(a)</b>	A typical flank wear	133
<b>Figure 6.4(b)</b>	Average width of flank wear for each set under different conditions	133
<b>Figure 6.5</b>	Characteristics of flank wear for set 1 ( $V$ : 10 m/min, $F$ : 0.03 mm/rev, $a_p$ : 0.06 mm)	134
<b>Figure 6.6</b>	Characteristics of flank wear for set 2 ( $V$ : 25 m/min, $F$ : 0.02 mm/rev, $a_p$ : 0.05 mm)	134
<b>Figure 6.7</b>	Characteristics of flank wear for set 3 ( $V$ : 40 m/min, $F$ : 0.01 mm/rev, $a_p$ : 0.04 mm)	134
<b>Figure 6.8</b>	Characteristics of crater wear for set 1 ( $V$ : 10 m/min, $F$ : 0.03 mm/rev, $a_p$ : 0.06 mm)	138
<b>Figure 6.9</b>	Characteristics of crater wear for set 2 ( $V$ : 25 m/min, $F$ : 0.02 mm/rev, $a_p$ : 0.05 mm)	138
<b>Figure 6.10</b>	Characteristics of crater wear for set 3 ( $V$ : 40 m/min, $F$ : 0.01 mm/rev, $a_p$ : 0.04 mm)	138

<b>Figure 6.11</b>	Chips morphology observed for different cutting conditions	139
<b>Figure 6.12</b>	Microstructure of (a) wrought and (b) selective laser melted Ti6Al4V	142
<b>Figure 6.13</b>	Average flank wear width in wrought and SLM Ti6Al4V in different sets of process parameters	144
<b>Figure 6.14</b>	Morphology of tool wear for wrought Ti6Al4V at $V$ : 28 m/min and $f$ : 20 $\mu\text{m}/\text{rev}$	146
<b>Figure 6.15</b>	Morphology of tool wear for SLM Ti6Al4V at $V$ : 28 m/min and $f$ : 20 $\mu\text{m}/\text{rev}$	147
<b>Figure 6.16</b>	Morphology of tool wear for wrought Ti6Al4V at $V$ : 56 m/min and $f$ : 20 $\mu\text{m}/\text{rev}$	148
<b>Figure 6.17</b>	Morphology of tool wear for SLM Ti6Al4V at $V$ : 56 m/min and $f$ : 20 $\mu\text{m}/\text{rev}$	149
<b>Figure 6.18</b>	Morphology of tool wear for wrought Ti6Al4V at $V$ : 28 m/min and $f$ : 30 $\mu\text{m}/\text{rev}$	150
<b>Figure 6.19</b>	Morphology of tool wear for SLM Ti6Al4V at $V$ : 28 m/min and $f$ : 30 $\mu\text{m}/\text{rev}$	151
<b>Figure 6.20</b>	Average surface roughness measured in wrought and SLM Ti6Al4V under different cutting speeds and feed rates	154
<b>Figure 6.21</b>	Surface topography observed in wrought and SLM Ti6Al4V under different cutting speeds and feed rates	154
<b>Figure 6.22</b>	Chip geometry and morphology observed in wrought and SLM Ti6Al4V under different cutting speed and feed rate	156

## List of Tables

<b>Table 1.1</b>	Different types of UAM cutting types and mechanisms	7
<b>Table 2.1</b>	Summary of UAT processes and its consequences	12
<b>Table 2.2</b>	Types of fluids used in machining operations	14
<b>Table 2.3</b>	Summary of the recent work being performed using MQL and cryogenic cooling	20
<b>Table 2.4</b>	Summary of the recent work being performed in modeling of ultrasonic assisted machining processes	27
<b>Table 3.1</b>	Different types of materials used for acoustic horn	33
<b>Table 3.2</b>	Mechanical properties of Ti6Al4V	43
<b>Table 3.3</b>	Chemical structure of Ti6Al4V	43
<b>Table 3.4</b>	Mechanical properties of Nimonic 90	44
<b>Table 3.5</b>	Chemical structure of Nimonic 90	44
<b>Table 3.6</b>	Chemical structure of Inconel 718	44
<b>Table 3.7</b>	Cutting inserts designation	45
<b>Table 3.8</b>	Specifications of the machine tool used for experiments	46
<b>Table 3.9</b>	Process parameters used for experiments	46
<b>Table 3.10</b>	Properties of canola oil	48
<b>Table 3.11</b>	Details of cooling strategies employed	49
<b>Table 3.12</b>	Details of surface roughness tester	52
<b>Table 3.13</b>	Details of power analyzer	53
<b>Table 3.14</b>	Details optical and scanning electron microscopes	54
<b>Table 4.1</b>	Input process parameters for experimentation	68
<b>Table 4.2</b>	Johnson-cook and thermo-mechanical constant of SS304 steel	68
<b>Table 4.3</b>	Input process parameters used for FEM	75
<b>Table 4.4</b>	Johnson-cook parameters for Nimonic 90	76
<b>Table 4.5</b>	Properties considered for FEM	76
<b>Table 4.6</b>	Properties of coating material	76
<b>Table 5.1</b>	Conditions used to perform the experiment	92
<b>Table 5.2</b>	Details of cooling strategies employed	92
<b>Table 5.3</b>	Comparison of LCO <sub>2</sub> with other cooling strategies for CT and UAT of Inconel 718	107
<b>Table 5.4</b>	Comparison of LCO <sub>2</sub> with other cooling strategies for CT and UAT of TI-6Al-4V	122
<b>Table 5.5</b>	Components and process parameters used for experiments	124
<b>Table 6.1</b>	Experimental conditions used in micro-turning of Nimonic 90	130
<b>Table 6.2</b>	Chemical composition of Nimonic 90	131
<b>Table 6.3</b>	Elemental structure of Ti6Al4V (wt%)	143
<b>Table 6.4</b>	Conditions used for experiments	143

## Notations and Abbreviations

$\alpha$	Rake angle ( $^{\circ}$ )	$E$	Modulus of elasticity (MPa)
$\beta$	Friction angle ( $^{\circ}$ )	$F$	Frequency (Hz)
$\gamma_p$	Shear strain at primary zone	$F_c$	Cutting force (N)
$\dot{\gamma}_p$	Shear strain rate at primary zone (1/S)	$F_{ce}$	Cutting force obtained from the experiment (N)
$\gamma_s$	Shear strain at secondary zone	$F_{csp}$	Cutting force obtain from SCE (N)
$\dot{\gamma}_s$	Shear strain rate at secondary zone (1/S)	$F_f$	Feed force (N)
$\epsilon$	Plastic strain	$F_{sf}$	Friction force at secondary zone (N)
$\epsilon_f$	Effective strain	$F_{sh}$	Shear force (N)
$\dot{\epsilon}$	Strain rate ( $s^{-1}$ )	$F_{sn}$	Normal force at secondary zone (N)
$\epsilon_0$	Reference strain rate ( $s^{-1}$ )	$F_t$	Thrust force (N)
$\eta$	Speed of sound through solid (m/s)	$F_{te}$	Thrust force obtained from the experiment (N)
$\rho$	Density ( $Kg/m^3$ )	$K_t$	Thermal conductivity ( $m^2/s$ )
$\tau$	Frictional shear stress (MPa)	$K_p$	Flow stress at primary zone (MPa)
$\tau_p$	Shear stress at primary zone (Mpa)	$K_s$	Flow stress at secondary zone (Mpa)
$\tau_s$	Shear stress at secondary zone (Mpa)	$L_c$	Tool-chip contact length (mm)
$\mu$	Coefficient of friction	$N_p$	The thermal number used to find the temperature at the primary zone
$\mu_e$	Coefficient of friction from experiment	$P_l$	power required when the machining tool is running without contact between tool and workpiece (Watt)
$\omega$	Angular frequency (rad/s)	$P_M$	Power consumed during actual machining (Watt)
$\omega_n$	Natural frequency of horn (rad/s)	$P_T$	Power require during cutting operation (Watt)
$\lambda$	Frequency of the wave (rad/s)	$R_a$	Average surface roughness ( $\mu m$ )
$\xi$	Characteristic of stress distribution at secondary zone	$T$	Period of a vibration cycle (s)
$\sigma$	Flow stress of workpiece material (MPa)	$T_w$	Workpiece temperature ( $^{\circ}C$ )
$\sigma_1$	Maximum principal stress (MPa)	$T_0$	Room temperature ( $^{\circ}C$ )

$\sigma_f$	Flow stress (MPa)	$T_i$	Temperature at tool chip interface ( $^{\circ}\text{C}$ )
$\sigma_n$	Contact pressure at tool chip interface (MPa)	$T_m$	Melting temperature of workpiece material ( $^{\circ}\text{C}$ )
$\sigma_{nn}$	Normal stress (MPa)	$T_t$	Tool temperature ( $^{\circ}\text{C}$ )
$\sigma_{uts}$	Ultimate tensile strength (Mpa)	$T_w$	Workpiece temperature ( $^{\circ}\text{C}$ )
$\phi$	Shear angle ( $^{\circ}$ )	$V$	Cutting speed (m/min)
$\phi_{EF}$	Effective shear angle ( $^{\circ}$ )	$V_s$	Sliding velocity at tool chip interface (m/min)
$\theta_p$	The temperature at the primary zone ( $^{\circ}\text{C}$ )	$V_t$	Velocity given to the cutting tool (m/min)
$\theta_s$	The temperature at the secondary zone ( $^{\circ}\text{C}$ )	$V_R$	Relative cutting velocity (m/min)
$a$	Amplitude ( $\mu\text{m}$ )	$V_{cr}$	Critical cutting velocity (m/min)
$a_p$	Depth of cut (mm)	$V_{ch}$	Chip velocity (m/min)
$c$	Speed of the sound wave in the solid material	$V_{EF}$	Effective cutting velocity (m/min)
$f$	Feed rate (mm/rev)	$V_{sh}$	Shear velocity (m/min)
$h$	Heat convection coefficient ( $\text{W}/\text{m}^2$ $^{\circ}\text{C}$ )	$VB$	Width of flank wear (mm)
$h_p$	Heat transfer coefficient at processing zone	CM	Conventional machining
$l$	Length of horn (mm)	CT	Conventional turning
$m$	Thermal softening coefficient	JC	Johnson-cook
$m_f$	Constant of shear friction	LCO <sub>2</sub>	Liquid carbon dioxide
$n$	Hardening coefficient	LN <sub>2</sub>	Liquid nitrogen
$q_t$	Heat flux at tool-environment interface	WC	Tungsten carbide
$q_w$	Heat flux at workpiece-environment interface	ALE	Arbitrary Lagrangian-Eulerian
$r$	chip thickness ratio	BUE	Built-up edge
$s$	Velocity of pressure wave (m/s)	CVD	Chemical vapor deposition
$t$	Time (s)	FEM	Finite element modeling
$t_c$	Engagement time (s)	MQL	Minimum quantity lubrication
$t_0$	Uncut chip thickness (mm)	PVD	Physical vapor deposition
$t_{ss}$	The thickness of the secondary shear zone (mm)	RPM	Revolution per minute

$t_1$	Chip thickness (mm)	SCE	Specific cutting energy (J/mm <sup>3</sup> )
$w$	Crater wear (mm)	SEM	Scanning electron microscopy
$A$	Amplitude (μm)	UAD	Ultrasonic assisted drilling
$A_h$	Cross-section of the solid bar (mm <sup>2</sup> )	UAM	Ultrasonic-assisted machining
$A_{sh}$	Area of the shear plane (mm <sup>2</sup> )	UAT	Ultrasonic-assisted turning
$B$	Hardening modulus (MPa)	UTS	Ultimate tensile strength
$C$	Strain rate sensitivity coefficient	HUAT	Hot ultrasonic-assisted turning
$D$	Material constant for damage	MQCL	Minimum quantity cooling and lubrication
$D_0$	Input diameter of horn (mm)	TWCR	Tool-workpiece contact ratio
$D_1$	Output diameter of horn (mm)		

Conventional machining processes such as turning, milling, drilling, etc., have been used for material removal for the last few decades. Machining is the most widespread process in material removal industries. The investment in machining is increasing year by year continuously. The global machining market is estimated to be worth \$341.91 billion, reaching \$414.17 Billion by 2023 [1]. Machining technologies develop from innovative improvements in machine tools, fixtures, clamping systems, cutting tool materials, etc. All the machining processes currently satisfy production requirements such as surface quality, flexibility, energy consumption, ecological standards, etc. The machining process is mainly influenced by workpiece material, tool materials, machine tool rigidity, cutting environment, part complexity, etc. Machining responses such as cutting force, surface integrity, power consumption, tool wear, chip formation, etc., depending upon the machining process performance.

### 1.1 Turning as a Conventional Machining Process

Turning is a metal cutting process in which a single-point cutting tool removes the material from the workpiece, as presented in Figure 1.1. The turning process is almost exclusively performed on a center lathe. The tool is fed linearly in a longitudinal axis to generate a cylindrical geometry. A relative motion is needed between the tool and workpiece to execute a turning operation. The primary motion is achieved by a cutting speed. In addition to that, the tool must be fed laterally to the workpiece (feed direction). The depth to be cut is given in a radial direction of the workpiece. Typically, the cutting speed, feed rate, and depth of cut are measured in m/min, mm/rev, and mm, respectively.

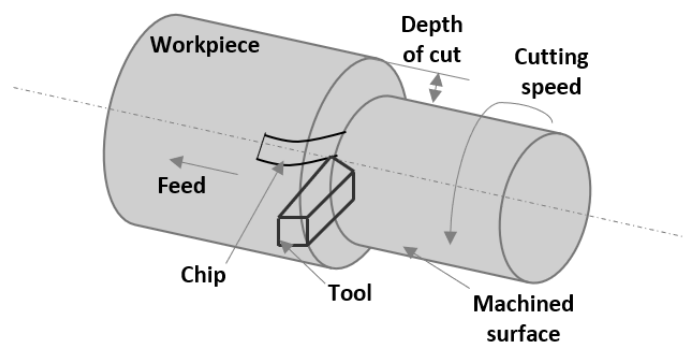


**Figure 1.1** Schematic of turning process

The geometrical description of practical machining operation is complex. Figure 1.2(a) presents a simplified machining model in two dimensions. As the tool penetrates into the workpiece, the chip is produced by shear deformation along a shear plane, which is oriented at



an angle of  $\phi$  with a surface of a workpiece. The mechanical energy is consumed along a shear plane to deform the material plastically. The tool makes an angle with a direction perpendicular to the surface of the workpiece called rake angle,  $\alpha$ , which determines the direction of chip flow. During machining, the cutting edge of the tool is situated a certain distance below the surface of the workpiece. This corresponding chip thickness before cutting is called uncut chip thickness  $t_0$ . As the chip is formed, the thickness increases to  $t_1$ . The chip thickness ratio ( $r$ ) is defined using equation (1.1).

$$r = \frac{t_0}{t_1} \quad (1.1)$$

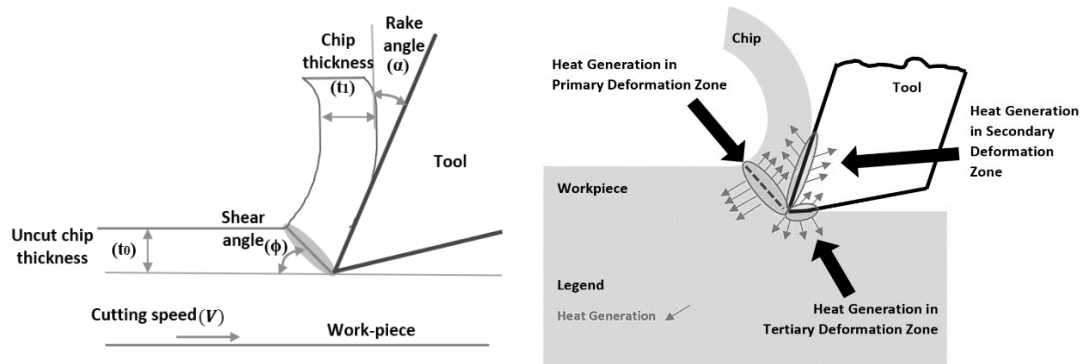


**Figure 1.2** (a) Schematic of single point cutting process and (b) heat generated in different machining zones

The machining processes are conducted at a very high strain rate, and thus it produces very high heat in the deformation zones. Figure 1.2(b) shows heat generation at primary, secondary, and tertiary deformation zones. It is clear from the figure that the tool face receives a very high heat from the chip and workpiece. The heat to be transferred to the tool is considerably affected by the workpiece materials, cutting speed, feed, depth of cut, tool geometry, and cutting fluids. Thus, minimizing the heat generation during the machining process is needed to increase the machinability of workpiece materials.

The machining of soft metals such as brass, mild steel, and aluminum responds well under dry conditions. On the other hand, hard materials such as stainless steel, Titanium alloys, Nickel-based superalloy, etc., are considered as difficult-to-cut materials. The conventional machining processes used to machine those advanced materials have become challenging attributed to their low thermal conductivity, high shear modulus, high hardness, etc. [2]. It could be seen that the performance of machining of advanced materials could be further enhanced by implying some external energy to the existing process or by changing workpiece material properties. The external energies are used in different ways at the processing zone in the hybrid or assisted machining process. The external energy could be in the form of heating, cooling, and ultrasonic vibration. Those external energies “assist” the existing process to enhance the machining responses. Industrial demands drive the need for a hybrid machining process to

achieve higher tolerances, better surface quality, fatigue properties, etc. The output responses such as surface quality, cutting forces, energy consumption, microstructures, tool wear, etc., could be achieved in the desirable ranges.

## 1.2 Assisted Machining

### 1.2.1 Heat-assisted machining

The demand for advanced high-strength materials increases in high-temperature applications such as aerospace, automotive, marine, etc. The properties such as high hardness, low thermal conductivity, higher shear modulus, etc., induce high cutting force, poor surface quality, and higher tool temperature and lead to reduce the performance of components [3]. If those materials are machined at a higher temperature, it will lead to better machining performances. It is attributed to a reduction in flow stress and strain hardening rate at a higher temperature, reducing the hardness of the materials softer due to thermal softening. Heat-assisted machining uses the external heat source to heat the workpiece, improving the machining performance by reducing hardness, yield strength, and strain hardening of materials. In order to apply the heat effectively during machining, the heat source should be controllable and local. External heat sources, such as induction, plasma, gas, electrical current, and laser, have been used during machining processes, as shown in Figure 1.3. It is noted that an inappropriate application of heat sources may produce undesirable microstructural changes in the workpiece materials during machining.

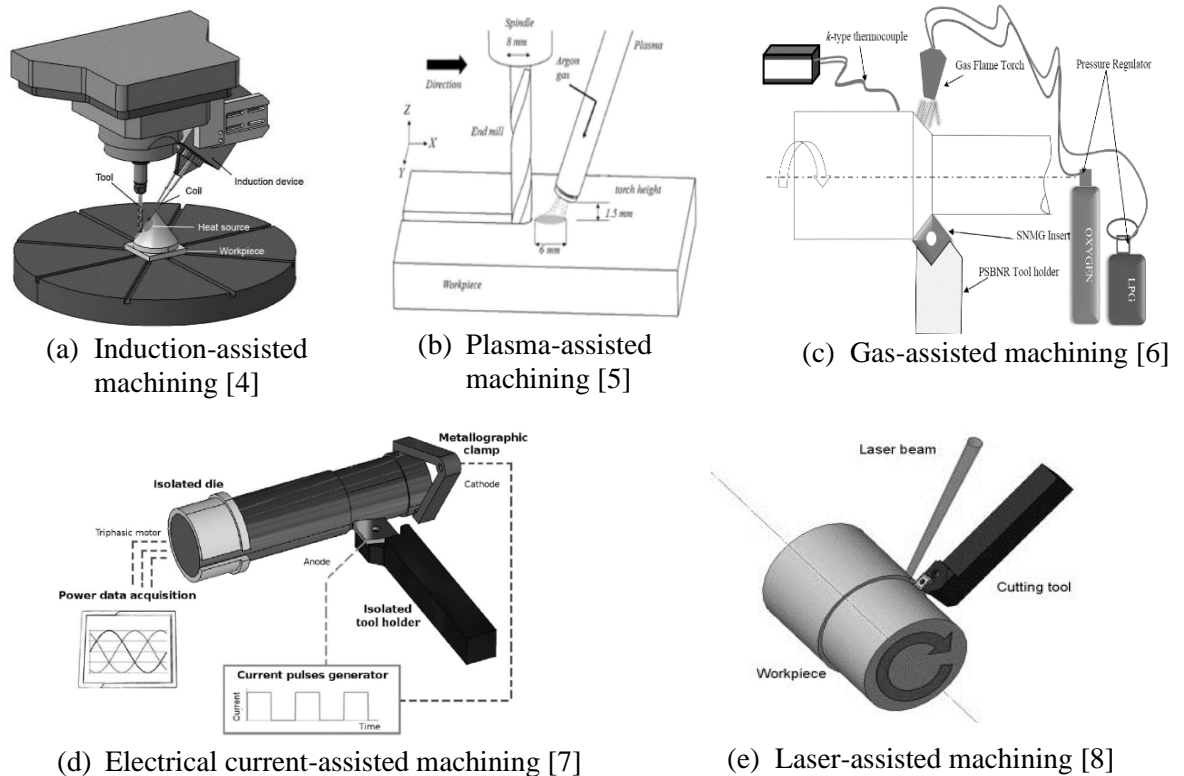


**Figure 1.3** Schematic of heat-assisted machining processes

### 1.2.2 Cooling/lubrication-assisted machining

External assistance is also provided using metal cutting fluids to the processing zone. The metal cutting fluids provide efficient cooling/lubrication and remove heat from the primary, secondary, and tertiary deformation zone in machining. [9]. Proper selection of cutting fluids along with its delivery system is important as it affects surface quality, temperature, cutting forces, tool life, surface integrity, etc., induced during machining processes. The most popular cooling strategy is flood cooling, in which a cutting fluid is delivered to the machining zone. Flood cooling is a conventional technique often used for turning, milling, drilling, etc. It has been observed that the maintenance, disposal, and storage cost of conventional metal cutting fluids are two times higher than the total machining cost. Moreover, according to the reported data, 80% of skin diseases are caused by cutting fluids [10]. National Institute of Occupational Safety and Health (NIOSH) informed that over 1 million workers are under the stimulus of toxicology effects caused by cutting fluids. Therefore, it is necessary to get rid of or minimize the use of metal cutting fluids. In this regard, recent studies are being performed using alternative cooling and lubrication techniques such as solid lubrication, high-pressure jet, minimum quantity lubrication (MQL), vegetable oils, and cryogenic coolants such as liquid carbon dioxide ( $\text{LCO}_2$ ) and liquid nitrogen ( $\text{LN}_2$ ), etc., [11-13]. It is found that the MQL, vegetable oils, and cryogenic coolants are sustainable and do no harm to human beings and thus are very useful in metal-cutting sectors.

MQL is the substitute for the conventional flood cooling strategy. A very small amount of the oil particles is mixed with compressed air to form mist, which is supplied at the cutting zone using a nozzle. When the mist particles are supplied to the cutting zone, it produces a cooling and lubricating effect [13]. Like MQL, vegetable oils are environment-friendly, less toxic, and biodegradable. The majority of vegetable oils comprise of triglycerides, having a molecular structure with a long chain of fatty acids. The triglyceride structure provides sufficient qualities of lubricants. Moreover, the fatty acid produces a high-strength lubricating film, interacting with the metallic surface and dropping friction and wear [10]. Similarly, cryogenic coolants such as  $\text{LN}_2$  and  $\text{LCO}_2$  are being used to eliminate the heat from the machining zone during machining processes. The cryogenic coolant easily evaporates into the atmosphere, leaving the chips dried and reducing the disposal cost. The  $\text{LN}_2$  is considered recyclable and environmentally friendly. The  $\text{LCO}_2$  is not harmful if the waste  $\text{LCO}_2$  obtained from the processes is used for machining before releasing it into the atmosphere [14]. The cryogenic coolants efficiently remove the heat and improve machinability.

### 1.2.3 Ultrasonic-assisted machining

It has been observed from previous sections that the machinability of the materials can be improved either by heating or cooling/lubrication. Other than heating and cooling, external energy in the form of ultrasonic vibrations could also be used to improve the machinability of materials. It has been seen that ultrasonic-assisted machining (UAM) as a hybrid technique combined with conventional machining processes has been broadly investigated for more than 50 years. Ultrasonic vibration is generated due to the interaction between ultrasonic waves and guiding media. The UAM uses ultrasonic vibration to be superimposed on the cutting process of the cutting tool. The vibrating cutting tool comes in contact with the workpiece directly and cuts the material. Kinetically, the system is different from a conventional machining process, as the cutting tool translates as in conventional machining but with superimposed vibro-impacts, leading to improved cutting conditions. The advantages of this method are not priory obvious because machine-tool vibration (chatter) has to be vigorously suppressed in most cases. Interestingly, when an externally controlled vibration is imposed on a cutting tool, significant improvements in surface finish, noise, and tool-wear reduction are observed. Prior studies of vibration machining have shown that the vibration system needs to be tuned to resonance to achieve the maximum possible benefit from the vibratory cutting process.

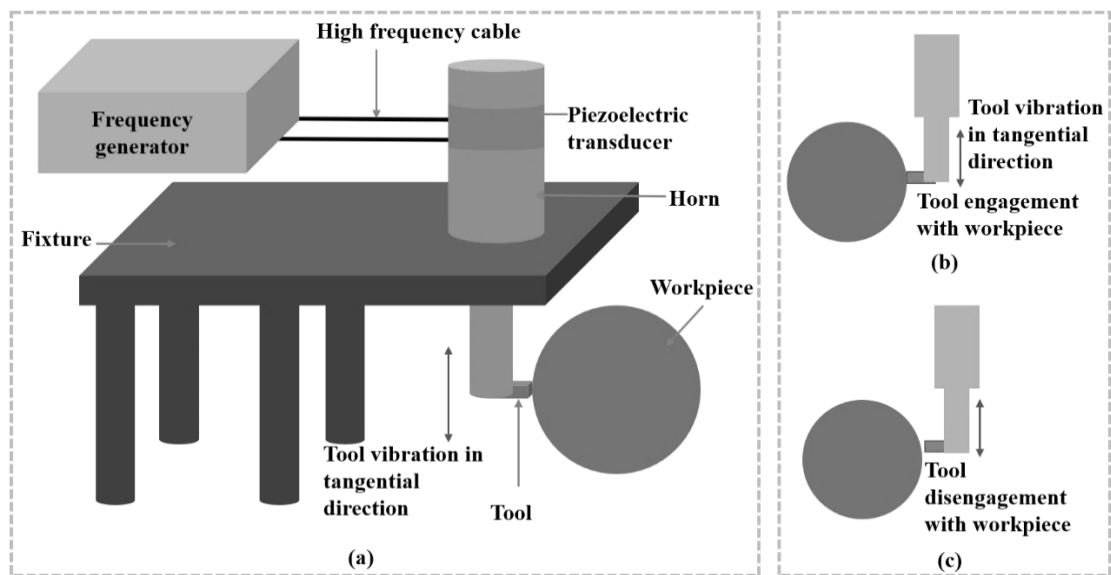


**Figure 1.4** (a) A schematic of ultrasonic-assisted turning setup, (b) tool engagement and (c) disengagement with workpiece

The schematic of ultrasonic-assisted turning (UAT) is shown in Figure 1.4. It consists frequency generator, high-frequency cable, piezoelectric transducer, and an ultrasonic horn. The frequency generator converts the low-frequency signal (50-60 Hz) to the high-frequency signal (20 kHz). The transducer converts the high-frequency electrical signal into mechanical displacement (amplitude). The horn attached to the transducer vibrates at the resonant frequency

and transmits the vibrations to the tool attached at the end. The horn should be stayed at a node point to obtain efficient output. The resonant frequency and amplitude control are critical factors to consider for designing an ultrasonic horn. If the design of the horn is inappropriate, then the power supplied to it converts into heat, leading to reduced vibration amplitudes. In the absence of a feedback device, the design should be optimized to use the vibration at a desired frequency and amplitude [15].

The UAT is different from conventional turning (CT) in the cyclic cutting characteristics of the cutting tool. The periodic cutting action for a cycle of vibration is schematically presented in Figures 1.4(b) and 1.4(c). During the engagement period, the tool interacts with the workpiece, and cutting action occurs, as shown in Figure 1.4(b). The tool leaves contact with the workpiece during the disengagement period, as shown in Figure 1.4(c). This action repeats in the subsequent vibration cycles, and cutting takes place due to ultrasonic vibration.

It can be seen from Figure 1.5 that the sinusoidal cutting action of the tool takes place in UAT. The insert comes in contact with the workpiece at 'y' and remains engaged with the workpiece for ' $t_c$ ' time and disengage at 'z'. The insert remains ideal or disengages with the workpiece until the next cycle start. The cycle repeats from 'y1' where an insert again comes in contact with the workpiece [16]. A term  $R$  (tool-workpiece contact ratio) to relate the cutting time and the ideal time is given by equation (1.2).

$$R = \frac{t_z - t_y}{T} \quad (1.2)$$

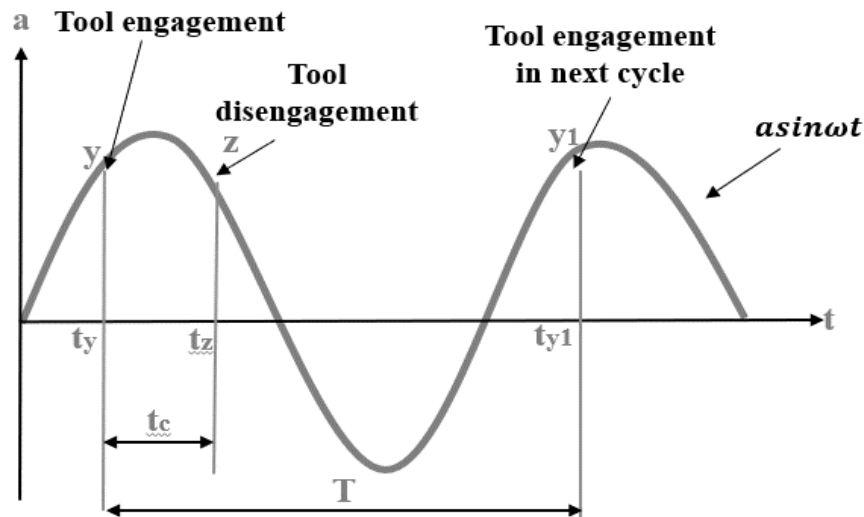


**Figure 1.5** Tool vibration cycle in 1D UAM [17]

It can be seen that TWCR is mainly dependent on frequency, amplitude, and cutting speed. As the amplitude and frequency increase, TWCR decreases, and hence average cutting force per unit of time decreases.

Considering the separation criteria between tool and workpiece, the UAM process is further divided into four categories which are 1D, 2D, and 3D UAM processes. The cutting mechanism of different types of UAM is given in Table 1.1.

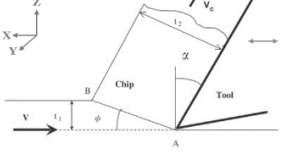
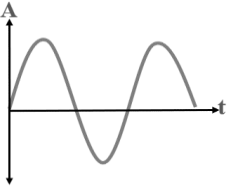
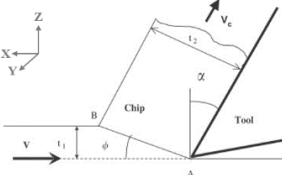
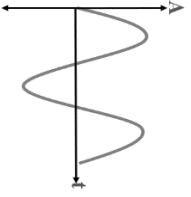
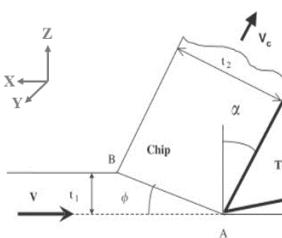

In the 1D UAM, the tool vibrates in the cutting velocity direction or in the feed direction [18]. The typical cutting type in 1D UAM is shown in Table 3. It generally operates at frequencies of 20-40 kHz and amplitudes of 3-20  $\mu\text{m}$  [19]. The interrupted and nonlinear cutting in 1D UAM alters the amplitude while machining and results in poor surface quality. The critical cutting velocity used to define the separation criteria is given by equation (1.3).

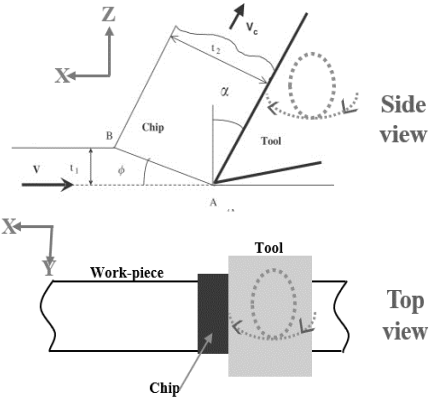
$$V_{cr} = 2\pi Af \quad (1.3)$$

Where,  $A$  is amplitude and  $f$  is frequency. If  $V < V_{cr}$ , periodic separation takes place between tool and workpiece, whereas in case of  $V > V_{cr}$ , the cutting action is continuous.

During the 1D UAM, the flank face rubs with the workpiece while machining, leading to severe tool wear at the flank face [19]. The 2D vibrations used elliptical motion, which improves the process efficiency by preventing the problem associated with 1D UAM. The characteristics equations of 2D UAM are shown in Table 1. The elliptical motion of the tool synchronized the two-directional vibration applied to the tool. The cutting edge of the tool forms an elliptical path for each cycle of vibration [20].

**Table 1.1** Different cutting mechanism in the UAT processes

Cutting type and process	Cutting mechanism	Trajectory
<b>1D UAM</b>		
 <p>1D UAM Vibration in cutting velocity direction</p>	$x(t) = A \sin(\omega t) + Vt$ $x'(t) = \omega A \cos(\omega t) + V$ <p>Where, angular frequency <math>\omega = 2\pi f</math></p>	
 <p>1D UAM Vibration in feed direction</p>	$x(t) = V_c t$ $z(t) = A \sin(\omega t) + V_f t$ <p>Where, <math>V_f</math> and <math>V_c</math> is velocity in feed and cutting direction</p>	
<b>2D UAM</b>		
 <p>2D UAM Elliptical vibration</p>	$x(t) = A \cos(\omega t) + Vt$ $z(t) = B \sin(\omega t)$ $x'(t) = -A\omega \sin(\omega t) + V$ $z'(t) = B\omega \cos(\omega t)$	

	Where, $A$ and $B$ are length of semi-major and semi-minor axis.	
<b>3D UAM</b>		
 <p>The side view diagram shows a tool cutting a workpiece. The workpiece is represented by a line with points A, B, and C. The tool is shown as a line with a cutting edge. The chip is the material being removed. The vibration amplitudes are labeled A and B. The angles are labeled alpha and phi. The top view diagram shows the tool and workpiece from above. The tool is shown as a rectangle. The workpiece is shown as a cylinder. The chip is shown as a curved line.</p>	$x(t) = A \cos(\omega t) - Vt \cos i$ $z(t) = B \cos(\omega t + \varphi_z)$ $y(t) = C \cos(\omega t + \varphi_y) + Vt \sin i$ <p>Where, <math>A</math>, <math>B</math> and <math>C</math> are vibration amplitude in <math>x</math>, <math>z</math> and <math>y</math> direction respectively. <math>i</math> is inclination angle in oblique cutting.</p>	

It is observed that conventional machining processes have been widely used for the machining of a wide range of materials including difficult-to-cut alloys. However, some external assistance is required to cut materials such as nickel-base superalloy, titanium alloy, hardened steel, etc. External assistance can be given in terms of heat, cooling and lubrication, and ultrasonic vibration. Several research groups are working on enhancing the machinability of hard materials using different external energies. Concerning this, the thesis is aimed to explore ultrasonic assistance, heat assistance, and sustainability in turning operations through experimentation and modeling.

As discussed in chapter 1, conventional machining is a widely explored area of research. Considering the poor machinability of difficult-to-cut materials, several modifications have been incorporated into the existing machining processes. Such incorporations are driven by analytical and FEM in some cases. For example, ultrasonic vibration assistance. In addition to this cooling and lubrication is another approach to assist the conventional processes. Researchers worldwide have been working on these assistances to enhance the machinability of difficult-to-cut materials. The following sections briefly review the literature in this context for turning, milling and drilling processes.

#### 2.1 Ultrasonic-assisted Machining Processes

Ultrasonic-assisted machining has been broadly investigated for several decades. The development of the ultrasonic-assisted system is a key that is beneficial in achieving high precision, accuracy, and applicability in manufacturing sectors. Frequency is a vital factor affecting the selection of the ultrasonic-assisted system. Based on the frequency, the system is classified into two types: Resonant and non-resonant systems. The non-resonant system operates at a discrete natural frequency, and the resonant system operates on a continuous frequency range. Thus, the resonant system can attain a higher operating frequency (above 20 kHz) and more energy efficient compared to a non-resonant system. The amplitude in the resonant system is usually low due to the nature of resonant vibration and the relationship between excitation and response [18]. In the UAM, the cutting characteristics of the tool and workpiece change from conventional machining (CM) to cyclic machining. This cutting characteristic changes the material removal mechanism of workpiece material, influencing the machining forces, surface integrity, and wear mechanisms of the tool. Several researchers have examined the effect of ultrasonic vibration on the machining responses in turning, milling and drilling processes.

Adnan et al. [21] implemented the vibrations of different amplitudes in a transverse direction (chip width direction) in the orthogonal turning of Al-2024 aluminium alloy. It was noted that cutting force, thrust force, chip thickness, and surface roughness decreased with increased amplitudes. This was attributed to the transverse vibration, which enhances the ductile fracture at the cutting edge, making chip formation easier, and results in a reduction in forces, chip thickness, and surface roughness. Muhammad et al. [22] developed  $\alpha+\beta$  titanium alloy Ti 6Al 7Zr 6Mo 0.9La (modified from Ti 6246) to compare the machinability with Ti 6246 under UAT and CT. The modified alloy formed short chips, higher chip formation ratio, lower cutting forces and surface roughness than Ti 6246 alloy under the UAT process. Amini et al. [23]



employed a quick stop device to analyze the shear angle and tool-chip contact length in the UAT of AISI 1060 and AISI 304 steel. The UAT increases the shear angle by 30% and decreases the contact length by 30%, compared to CT. It was also observed that as the feed increases, the shear angle and contact length increase, whereas a variation in cutting speed was ineffective. In a similar study of SS 304 stainless steel, Xu et al. [24] examined the chip formation mechanism in the UAT and CT processes. The chips produced during UAT were the loose spiral type with lower distortion and a larger curling radius than CT. The surface generated in the UAT was smoother and more regular than in the CT. Khanna et al. [16] investigated that a microchipping effect produced by the UAT lowered the cutting force and power consumption during the machining of Nimonic 90. The chips produced were fragmented and regular, helping to improve the surface quality in the UAT. Similar results in terms of power consumption were concluded for the UAT of Nimonic 90 by Airao et al. [17]. A pulsating cutting force reduced the average stress and forces on the cutting tool and thus reduced the power consumption and surface roughness.

Bai et al. [25] performed UAT on nickel-base superalloy Inconel 625 and Inconel 718 using TiAlN coated carbide tool and different machining parameters. Inconel 718 showed higher tool wear compared to Inconel 625 due to the higher strength of Inconel 718. The UAT improved surface topography and increased the compressive residual stresses compared to CT. Pei and Wu [26] performed ultra-precision diamond turning of Ti6Al4V at a frequency of 80 kHz. A higher surface finish and morphology, and lower machining forces, were achieved at a higher amplitude. Peng et al. [27] introduced a high-speed UAT of Ti6Al4V using the cutting speeds of 100-500 m/min, in which the vibration was given in the feed direction. High-speed UAT produced a surface with lower roughness and uniform texture than CT. The plastic deformation of the surface decreased, and microhardness improved with an increase in cutting speed for both processes. A similar study on the hardened steel GCr15 found that the high-speed UAT produced chip breaking with a decrease in cutting forces. The tool life was about 1.5 times longer in the UAT than in CT [28]. An ultrasonic-assisted diamond turning of high entropy alloy FeCrCoMnNi at a frequency of 101.68 kHz was performed by Zhang et al. [29]. The results disclosed that the tool wear, chip thickness, and cutting forces were decreased, and surface integrity was improved under ultrasonic vibration. It was explained that an impact-induced thin layer of material reduced the erosion wear of the tool. Moreover, due to ultrasonic vibration, the nanoscale burnishing effect completely eliminated scratch formation on the machined surface.

Muhammad [30] used a fuzzy logic model to analyze the UAT and CT of Ti-6Al7Zr3Nb4Mo0.9Nd titanium alloy. A model showed a reduction in cutting forces, temperature at the processing zone, average surface roughness and chip compression ratio compared to CT. Liu et al. [31] examined the surface characteristics of brass H62 processed by UAT using a polycrystalline diamond tool. It was investigated that the elastoplastic deformation of the

subsurface becomes larger under ultrasonic vibration. Moreover, surface roughness produced under ultrasonic vibration was higher, improving the friction performance and tribological properties. In a similar study on Ti6Al4V, Bertolini et al. [32] found that ultrasonic vibration did not affect the micro-hardness and wettability and improved surface properties. A composite SiCp/Al 2124 is machined using UAT and CT using polycrystalline diamond by Kim et al. [33]. An average tangential cutting force was reduced by 60.5% and surface roughness was improved by 33% in the UAT compared to CT.

The researchers have applied ultrasonic vibration to the milling processes to enhance the machinability of materials. Liu et al. [34] applied elliptical vibration in side milling of Ti6Al4V using TiAlN coated milling cutter. The surface roughness was decreased as the cutting speed increased under ultrasonic vibration and conventional milling. A cyclic mechanical load-induced due to ultrasonic vibration produced compressive residual stress in the feed direction. Moreover, the plastic deformation was significant under ultrasonic vibration at lower cutting speed and feed rate. Likewise, Zhang et al. [35] observed that vibration considerably improves subsurface deformation thickness and microhardness at a lower cutting speed. The hardening effect was found to decrease as the cutting speed increased. In a similar work on Ti6Al4V, it was found that using ultrasonic vibration, the cutting forces, chip curl angle, cutting temperature and surface roughness was reduced compared to conventional milling [36]. Chen et al. [37] performed longitudinal-torsional vibration-assisted milling of Ti6Al4V at different amplitudes varying from 1-9  $\mu\text{m}$ . The higher amplitudes damaged the micro-morphology of the surface, whereas the lower amplitude improved micro-morphology. Moreover, the simultaneous action of longitudinal and torsional amplitude reduced the formation of score marks and burrs, producing a uniform surface. In a study on TC 18 titanium alloy, Xie et al. [38] executed longitudinal vibration with a frequency of 33.9 kHz in the end milling process. Cutting forces and cutting temperature were reduced by 34.1% and 19.5%, respectively, whereas compressive residual stresses were increased by 50.9%, compared to conventional milling. In recent work, Su and Li [39] performed ultrasonic-assisted milling on selective laser-melted Ti6Al4V using a polycrystalline diamond tool, and compared the results with conventionally manufactured Ti6Al4V. The selective laser melted Ti6Al4V showed less surface roughness compared to conventional Ti6Al4V, attributed to lower plasticity, higher hardness and brittleness. In a similar study, Chen et al. [40] used C<sub>f</sub>/SiC composite to carry out ultrasonic-assisted milling using a polycrystalline diamond tool. Ultrasonic vibration lowered cutting temperature, surface roughness, and residual stresses.

Ultrasonic-assisted drilling (UAD) of Ti-6Al-4V/Al2024-T351 laminated material was executed using frequencies varying from 20 kHz to 40 kHz by Wei and Wang [41]. The chip length, thrust force, maximum temperature and equivalent stress were reduced significantly under UAD compared to conventional drilling. Moghaddas et al. [42] performed a study to measure the temperature in the UAD of aluminium 6061, alloy steel 4340, and stainless steel

316. The force was reduced, and the heat generated was increased for aluminium 6061 and alloy steel 4340, whereas, for SS304, the heat generation and thrust force were increased in the UAD. In a similar study of the UAD on Al6061-T6 alloy, Chu et al. [43] found that for a constant cutting speed, the UAD improved the drilling depth by up to two times the material removal rate by 1.5 times compared to conventional drilling. Moreover, the UAT produced a lower rubbing torque and amplitude of stick-slip torque, enhancing the machinability. Similar results in terms of a reduction in drilling force in the UAD were observed by Saffar and Abdullah [44]. In a recent study of the UAD on Al 6061 alloy, Moghaddas [45] noted that the trust force and chip size were reduced in the UAT due to intermittent cutting action. Moreover, it was also noted that at a lower feed rate, the effect of increasing amplitude on the increase of temperature is higher.

From the above literature, it can be noted that the assistance of ultrasonic vibration in turning, milling, and drilling can enhance the machinability of materials. Table 2.1 summarizes the work on ultrasonic-assisted turning, milling, and drilling of different materials. Just like ultrasonic vibration assistance to the conventional machining processes, the assistance of different cooling and lubrication strategies applied to machining processes can also enhance the machinability of different materials. Section 2.2 describes the literature review for different cooling and lubrication strategies used.

**Table 2.1** Summary of the review of UAT processes and their observations

Reference	Cutting process	Materials	Observations
Adnan and Subbiah, [21], 2010	Turning	Al-2024 Aluminium alloy	Reduced cutting forces, surface roughness, chip thickness
Muhammad et al., [22], 2014		Ti 6Al 7Zr 6Mo 0.9La	Reduced cutting forces, surface roughness, chip reduction coefficient
Amini et al., [23], 2017		AISI 1060 and AISI 304	Shear angle increases whereas tool-chip contact length decreased
Xu et al., [24], 2019		SS 304	Chips produced with lower distortion and loos spiral type
Khanna et al., [16], 2019		Nimonic 90	5-10% improvement in surface roughness and 8-10% reduction in power consumption
Airao et al., [17], 2020		Nimonic 90	75% reduction in surface roughness, 6-15% reduction in power consumption
Bai et al., [25], 2019		Inconel 718 and 625	Improved surface topography and increased the compressive residual stresses
Pei and Wu, [26], 2019		Ti6Al4V	Higher amplitudes produced a better surface finish and reduced the machining forces
Peng et al., [27], 2021		Ti6Al4V	High-speed UAT in the feed direction, Uniform textured surface and lower surface roughness
Peng et al., [28], 2021		Hardened steel GCr15	High-speed UAT in the feed direction, Improved chip breaking effect, longer tool life

Zhang et al., [29], 2021		FeCrCoMnNi	Reduced chip thickness, tool wear and improved surface integrity
Muhammad [30], 2021		Ti-6Al7Zr3Nb4Mo0.9Nd	Reduced processing zone temperature, chip compression ratio and machining forces
Liu et al., [31], 2021		Brass H62	Surface roughness and topography improved under ultrasonic vibration
Bertolini et al., [32], 2021		Ti6Al4V	Improved wettability and surface properties
Kim et al., [33], 2022		SiCp/Al 2124	Cutting force reduced by 60.5% and surface roughness reduced by 33%
Liu et al., [34], 2019	Milling	Ti6Al4V	Produced compressive residual stresses and higher plastic deformation of subsurface
Zhang et al. [35], 2020		Ti6Al4V	A high value of cutting speed and amplitudes resulted in a rougher surface
Liu et al. [36], 2020		Ti6Al4V	cutting forces, chip curl angle, cutting temperature and surface roughness reduced
Chen et al. [37], 2020		Ti6Al4V	Lower amplitude improved the surface morphology. Reduced tool wear and forces
Xie et al. [38], 2021		TC18 Titanium alloy	Increased surface roughness, morphology and plastic deformation
Su and Li, [39], 2021		Selective laser melted Ti6Al4V	Surface roughness and topography improved under ultrasonic vibration
Chen et al. [40], 2020		C <sub>f</sub> /SiC composites	Decreased surface roughness, cutting temperature and residual stresses
Wei and Wang, [41], 2019		Ti-6Al-4V/Al2024-T351	Thrust force, maximum temperature and chip length reduced
Moghaddas et al., [42], 2019	Drilling	Al 6061, 4340 alloy steel and SS 316	Reduction cutting temperature and thrust force for Al 6061 and 4340 alloy
Chu et al., [43], 2020		Al 6061-T6	lowered rubbing torque and amplitude of stick-slip torque
Saffar [44], 2021		Aluminium alloy	Reduction in thrust forces
Moghaddas, [45], 2022		Al 6061	Reduced the thrust force, chip size and cutting temperature

## 2.2 Cooling/lubrication Strategies

The cutting fluids have been used for several decades to remove heat and to improve the machinability of the materials. The cooling and lubrication effect provided by cutting fluid helps in reducing tool wear and friction. Moreover, the cutting fluid flushes chips and prevents the machined surface from corrosion [11]. A selection of the cutting fluids is vital as it affects machining forces, power consumption, geometrical tolerances and accuracy, tool wear, etc. The cutting fluids supplied to the cutting zone are categorized based on their characteristics. Table 2.2 gives a classification of cutting fluids and corresponding advantages and disadvantages. It is noted that neat oil-based cutting fluids have good lubrication properties and are desirable where cooling and lubrication are essential. This type of neat oil-based cutting fluid lubricates the tool

chip interface and reduces frictional heat. A water-miscible or soluble oil-based cutting fluid uses an emulsion of water and oil, typically in a ratio of 30:1 [45]. The stability of the emulsion is a vital property of soluble oils. Synthetic oil-based cutting fluids contain synthetic lubricants, corrosion inhibitors, high-pressure additives, etc. Poor lubrication is a major disadvantage, limiting their use in industries. Semisynthetic cutting fluids contain both chemical additives and mineral oil. They are more effective and cleaner in rust prevention than soluble oil [46].

**Table 2.2** Types of fluids used in machining operations

No	Cutting fluids	Advantages	Disadvantages	Remarks
1	<b>Neat oil</b> It is derived from vegetables, petroleum origins	Good lubricity	Poor cooling, fire hazards	Used at low cutting speeds and low temperatures
2	<b>Soluble oil</b> It is an emulsion or emulsified oil, Made by mixing oil (mineral or vegetable oil) with an emulsifier agent in water	Good lubricity and cooling	Rust formation due to water, fungi and bacteria growth	Used at higher cutting speeds
3	<b>Synthetic oil</b> Mixed with water and chemicals, It does not contain oil	Good cooling	Lubrication lesser than other fluid	Easily contaminated by other cutting fluids, used with high-cutting speeds
4	<b>Semisynthetic oil</b> It is a combination of synthetic cutting fluids and emulsion It contains less oil (2-30%)	Prevent rust, good cooling	Stability affected by water hardness	

It is observed that the conventional synthetic oil-based cutting fluids are not bio-degradable and entail expensive treatment for disposal. Moreover, it creates a rich environment for the growth of bacteria and fungi, reducing the lubricity of the fluids. It increases the risk of corrosion of machine tools and workpieces. On the other hand, it becomes dangerous for workers on the shop floor. The International Agency for Research on Cancer (IARC) reported that petroleum-based cutting fluids comprising heterocyclic and polyaromatic rings are carcinogenic and have exposure, resulting in occupational skin cancer [47]. Furthermore, cutting fluids comprising chlorine additives is not suitable for machining titanium alloys as it could enhance the corrosion on the machined surface. The vaporization and atomization of cutting fluid due to high temperature and pressure form a fluid mist, causing skin reactions and respiratory problems.

It has been noted that using conventional cutting fluids in machining operations becomes a severe problem due to the associated economic, health, and environmental issues. To minimize the use of conventional cutting fluids, some alternative cooling and lubrication strategies have been developed. These alternative strategies use vegetable oil, MQL (minimum quantity lubrication), and cryogenic cooling (LCO<sub>2</sub> and LN<sub>2</sub>). The following subsections present literature

containing vegetable oil, MQL, and cryogenic cooling as alternative and sustainable cooling strategies [48].

### 2.2.1 Vegetable oil-based cooling

Vegetable oils are extracted from plant seeds. The main source of these oils is palm, olive, rapeseed, coconut, canola, soybean, sunflower, etc. About 70-100% of the biodegradation of vegetable oil is possible [49]. Moreover, vegetable oils are environmentally friendly, nontoxic and renewable and thus are safe for human health. Their disposal is safe and does not impact the water bodies and atmosphere. Therefore, vegetable oils are a potential alternative for replacing conventional synthetic oil-based cutting fluids [50]. The vegetable oil-based cutting fluid is generally prepared by mixing vegetable oil with water and an emulsifier. The main component of vegetable oil is triglycerides, which are glycerol molecules with long-chain fatty acids and ester linkages. The fatty acid reacts with metals and produces sulfides and chlorides, limiting the friction in metal-cutting processes. Apart from that, typical physicochemical properties associated with vegetable oils are high flash point, high viscosity index, kinematic viscosity, high boiling point and molecular weight, etc. [47, 51]. Moreover, the strong intermolecular interactions provide a durable lubricating film, minimizing friction and wear. On the other hand, at extreme loads, vegetable oil-based cutting fluids become less effective. In a wide range of machining operations, it has been observed that the performance of vegetable oil-based cutting fluid is equal to or better than conventional cutting fluid. To supply the vegetable oil to the cutting zone, the MQL has been used for a long time. The details of the MQL are explained in the next section.

### 2.2.2 Minimum quantity lubrication (MQL)

Minimal Quantity Cooling Lubrication (MQCL)			
normal consumption per machine hour: 10 – 50 ml MQCL medium			
Minimal Quantity Cooling (MQC)	Minimal Quantity Lubrication (MQL)		
Emulsion (Water+Oil) Water $c_{p,water} = 4.18 \text{ kJ/kgK}$ Air $c_{p,air} = 1.04 \text{ kJ/kgK}$	Oil $c_{p,oil} = 1.92 \text{ kJ/kgK}$		
Medium	Cooling	Lubrication	Chip removal
Emulsion	excellent	good	excellent
Oil	good	excellent	good
Air pressure	little	no	little

**Figure 2.1** definition of minimum quantity cooling and lubrication (MQCL)

The minimum quantity lubrication (MQL) technique uses a minimal amount of cutting fluid, which is advantageous for sustainability and the economy. It is also termed a near-dry machining technique and mist lubrication technique. The minimum quantity lubrication is a cooling and lubrication technique in which a very less amount of cutting fluid (usually 20-100 ml/h) is supplied to the cutting zone. Weinert et al. [52] have defined minimum quantity cooling and lubrication (MQCL) as given in Figure 2.1.

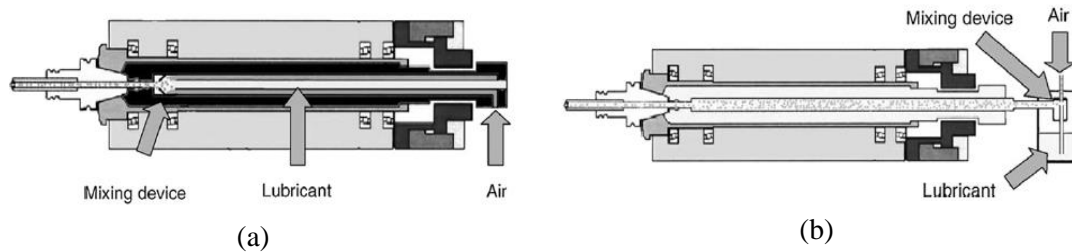


**Figure 2.2** MQL supply system (a) internal and (b) external [53]

The MQL can be provided to the machining zone in two ways: external supply through a nozzle and internal supply through channels made in the tool. The MQL supply system developed by Attanasio et al. [53] is shown in Figure 2.2. The external supply system is generally used for turning, end, and face milling operations, whereas the internal supply system is generally used for drilling, reaming, and tapping operations [54]. The compressed air and cutting fluid are mixed into a mixing device located outside the nozzle. The compressed air executes the cooling action, whereas the cutting fluid provides the lubricating action to the machining zone.

Using vegetable oil in machining applications reduces the machining cost and improves the machineability of difficult-to-cut materials. Lawal et al. [54] have shown that vegetable oil-based cutting fluids used during machining lower friction coefficient and improve the pitting resistance. Sharma et al. [55] have reported that the MQL with vegetable oil is more effective in improving machining responses, as it provides superior lubrication at high pressure. Chinchankar et al. [55] analyzed the flank tool wear of AISI 4340 steel under dry and MQL conditions with a carbide tool coated with three different materials, explicitly AlTiN, multi-layer TiAlN/TiSiN, and AlTiCrN. It was seen that the MQL improved tool life by 20-25% due to a decrease in cutting temperature compared to dry condition. Moreover, AlTiCrN coated carbide tool improved tool life by 30% due to the higher adhesive strength of the coating layer. Sivaiah et al. [56] studied the effect of a textured tool with MQL on the turning of AISI 52100 hardened steel. The results showed that the textured tool combined with MQL reduced the cutting temperature by 25%, flank wear by 40% and surface roughness by 42% compared to the non-textured tool with the wet cooling condition. Liu et al. [57] conducted experiments using 95% ethanol MQL (eMQL), vegetable oil MQL (vMQL), blended coolant MQL (bMQL), wet cooling and dry conditions in turning of AISI 304 steel. The bMQL demonstrated a considerable

improvement in tool life and surface roughness, as the blended coolant reduces the contact angle of coolant that causes an intrusion at the cutting zone and improves stability and cooling rate.

MQL is the process in which the nanoparticles can be added and used to enhance the machining performance. Different types of nanofluids, such as  $\text{TiO}_2$ ,  $\text{Al}_2\text{O}_3$ ,  $\text{MoS}_2$ ,  $\text{SiO}_2$ , carbon nanotubes, etc., are used with MQL [58, 59]. Nanija et al. [60] used  $\text{TiO}_2$  nanofluid with deionized water in MQL for end milling of AA6061T6 aluminium alloy to study the flank wear. It was seen that micro-abrasion, adhesion, and micro-attrition were the main wear mechanism in all cutting conditions. With nanofluid MQL, the transfer of aluminium (%) was higher, and tool edge chipping was lesser than with oil-based MQL. The turning experiments on Ti6Al4V steel with and without adding carbon nanotube in MQL were conducted by Shrma et al. [61]. The cutting temperature and tool flank wear were reduced, and the surface finish increased due to the increased thermal conductivity and heat-carrying capacity by adding carbon nanotubes. A nickel base super alloy Ti6Al4V was turned under MQL using hBN as a nanofluid volume concentration of 0.5% and 1%, pure MQL and dry condition with PVD TiAlN-TiN coated carbide tool [62]. It was observed that 0.5% nano MQL, 1% nano MQL, and pure MQL improved tool life by 68.8%, 105.9%, and 64.39% compared to dry conditions, respectively. Furthermore, 0.5% nano MQL improved surface finish, and 1% nano MQL reduced tool-chip interface temperature. Gaurav et al. [63] mixed  $\text{MoS}_2$  nanofluid (0.1, 0.5 and 0.9% by weight) with MQL and jojoba (vegetable oil) in turning of Ti 64 with PVD coated carbide tool. The cutting forces, surface roughness and flank wear reduced with 0.1%  $\text{MoS}_2$  nanofluid MQL compared to other conditions. It was noted that a higher concentration of  $\text{MoS}_2$  leads to the accumulation of nanoparticles, which increases the cutting forces and surface roughness. Pal et al. [64] carried out the drilling of AISI 321 with graphene nanofluid MQL with vegetable oil and found that MQL with graphene reduced the drilling forces, coefficient of friction, surface roughness, and tool wear. Sirin et al. [65] conducted experiments on nickel alloy X-750 under hBN nanofluid MQL with SiAlON ceramic tool. The hBN nanofluid MQL showed significant improvement in cutting force, tool wear, surface quality, surface defects, and microhardness.

The EMQL (electrostatic minimum quality lubricant) uses electrostatically charged oil droplets to be supplied to the target zone, as shown in Figure 2.3. The needle electrode is connected to a high negative voltage power supply through a wire connected to an oil tube. Highly compressed air is passed from an external nozzle to atomize the droplets.

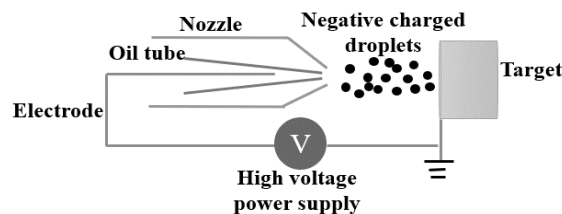


**Figure 2.3** Schematic of EMQL



Xu et al. [66] performed end milling of AISI-304 under dry, wet, MQL and EMQL with charging voltages of -5kV, -10kV and -20kV at different air pressure and oil flow rate. The low air pressure was more effective in terms of tool life, cutting forces and surface roughness due to the higher deposition rate of droplets. The charged voltage of -5kV and flow rate of 10 ml/h showed optimized results. A similar type of result was obtained in [67]. The nano graphene platelets in EMQL were used for end milling of AISI 304 by Lv et al. [68]. The nano-based EMQL showed better charging and physical properties than the oil-based EMQL. It also showed lower mist concentration and improved machining performance due to a better penetration at the interface, which reduced the coefficient of friction. Shah et al. [69] used 0-25 kV in EMQL for turning 15-5PH stainless steel and found that EMQL improved tribological properties and surface finish compared to conventional MQL. The SiO<sub>2</sub> nanoparticles used with EMQL for end milling of AISI-304 by Lv et al. [70]. It was observed that the SiO<sub>2</sub> exhibited lower surface tension and contact angle due to its charging capacity being higher than vegetable oil and resulting in better machining performance.

### 2.2.3 Cryogenic cooling

Cryogenics expresses the use of materials at a temperature below -150<sup>0</sup>C. Liquid nitrogen (LN<sub>2</sub>) is the most popular element in cryogenic applications. As LN<sub>2</sub> is nontoxic, it has been preferred as a coolant. The LN<sub>2</sub> as a coolant in machining applications was used by Hong et al. [71]. On the other hand, the LCO<sub>2</sub> is also used as a coolant in machining applications. The LCO<sub>2</sub> exists at atmospheric conditions, but it is stored at high pressure (approx. 6 MPa) for liquification. A dip tube is injected into the LCO<sub>2</sub> cylinder to eliminate the vaporization during delivery. When the LCO<sub>2</sub> is delivered to desired area through a nozzle, it expands and evaporates due to the joule-thomson effect [72]. Earlier Yildiz et al. [73] reviewed the cryogenic applications in machining to point out the effect of LN<sub>2</sub> on metal cutting performance compared to other cooling techniques. It was concluded that cryogenic cooling techniques could improve the machinability of metals by removing heat from the primary and secondary shear zones. Several studies have been carried out on cryogenic cooling in machining applications. Some recent studies and advancements in cryogenic-assisted machining of titanium alloy, superalloy, and other metals are described here.

Deshpande et al. [74] have briefly reviewed the cryogenic machining of nickel alloys. The effect of cryogenic coolant on surface quality, surface integrity, cutting forces, chip morphology, heat generation, tool wear analysis, etc., along with economic aspects and modeling, were briefly described. Courbon et al. [75] analyzed the tribological behavior of Inconel 718 with PVD coated carbide tool in cryogenic and dry conditions. It was seen that the friction coefficient significantly decreased with cryogenic cooling with better wear resistance. Cryogenic cooling substantially reduces the machining forces and tool wear compared to dry conditions. Krishnamurthy et al. [76] used cryogenic cooling and ethanol blended metal removal

fluid (MRF) during the orthogonal turning of Ti 64 to analyze the chip morphology. The chips formed during dry conditions demonstrate that successive chip segments cause adiabatic shear bands (ASB). During cryogenic cooling, a small section of the shear plane was attached and separated along most of the length. The ethanol-blended MRF reduced the friction at the chip-tool interface, decreased the cutting force by 65% and improved the surface finish. In a similar study, Kaynak et al. [77] performed experiments using LN<sub>2</sub> and liquid CO<sub>2</sub> (LCO<sub>2</sub>) on Ti-5553 alloy at high cutting speeds, constant feed and depth of cut. It was shown that LN<sub>2</sub> was better than LCO<sub>2</sub> in terms of cutting forces, tool wear, surface roughness, and chip formation. However, the results were far better with cryogenic coolants than with dry condition. A nickel-based super alloy Hastelloy C-276 showed similar surface roughness, cutting zone temperature, cutting forces and chip morphology when machined in dry and using LN<sub>2</sub> with TiAlN coated tool [78]. Jadhav et al. [79] optimized process parameters with neuro- genetic algorithm TOPSIS-based ANN-GA for turning of Nimonic C-263 with a multi-layer coated carbide insert during cryogenic and dry conditions. It was found that the improvement in surface roughness, tool wear, and cutting forces was significant with cryogenic cooling compared to dry condition. Amigo et al. [80] conducted high-feed turning experiments for Inconel 718 and Haynes 263 with an insert of low cutting-edge angle using wet and cryogenic cooling. The mechanistic model was proposed and results were compared with the results of reference material AISI 1045 steel. Good agreement was found between the results of AISI 1045 and Haynes 263, whereas Inconel 718 inhibited some errors. The tool wear, along with energy consumption and surface roughness for Inconel 718 during cryogenic, dry and wet cooling conditions, were examined by Khanna et al. [81]. In dry conditions, abrasion due to high temperature was observed, whereas, in the case of flood and cryogenic cooling conditions, adhesion and chipping were observed; however, the length of flank wear was less in cryogenic cooling. Moreover, cryogenic coolant reduced energy consumption by 8% and 13% compared to dry and wet conditions.

Halim et al. [82] analyzed tool wear in the milling of Inconel 718 with ball nose insert at high cutting speeds during dry and LCO<sub>2</sub> cooling conditions. The BUE was present in dry conditions and became severe with an increase in flank wear on the other side; BUE was less prominent due to heat dissipation with LCO<sub>2</sub>. The wear pattern in both the conditions was similar, and modes of tool wear were abrasion, chipping and adhesion; however, the tool life was increased by 70% during cryogenic cooling compared to dry condition. Wang et al. [83] investigated the oxidation wear effect in cryogenic and wet milling of Ti 64. In cryogenic cooling, a small breakage part of TiAlN was exposed, and hence oxidation was weaker, whereas, in conventional cooling, WC-Co was exposed without coating, due to which a large amount of oxygen was observed, and hence more oxidation reactions were observed. The plastic deformation resistance was increased on the tool and workpiece surface and hence reduced oxidative wear by using cryogenic coolant. In a similar study on the milling of Ti 64, Wang et al. [84] used a jet of cryogenic coolant with different pressure, flow rate and optimized jet

parameters by using response surface methodology (RSM). Similar results in terms of surface roughness and chip formation were noted. The heat transfer efficiency of LN<sub>2</sub> and CO<sub>2</sub> snow was studied in turning Ti 64 by Jamil et al. [85]. The results showed that the heat transfer ability of CO<sub>2</sub> snow was 87% higher than LN<sub>2</sub> on a flat surface for a specific injection time of coolant. Furthermore, CO<sub>2</sub> snow showed 14%-20% lower temperature in cutting zone than LN<sub>2</sub>. A similar type of experimental analysis on drilling of pseudo- $\alpha$ -Ti alloy, namely VT- 20 with LN<sub>2</sub>, LCO<sub>2</sub>, wet and dry conditions, was performed by Shah et al. [86, 87]. The LN<sub>2</sub> was better in terms of the number of drilled holes, cylindricity and circularity of drilled holes and microhardness, whereas LCO<sub>2</sub> was better in terms of surface roughness, torque and thrust force. In a similar study on the drilling of Inconel 718 under wet and LN<sub>2</sub>, Attanasio et al. [88] found that the LN<sub>2</sub> significantly improved hole circularity and cylindricity, and reduced the torque compared to wet conditions.

From the literature on MQL and cryogenic cooling, it can be noted that cooling and lubrication are very important to lessen the cutting temperature, attain sustainability issues and maintain the ecological balance. The results show an improvement in the machinability and surface integrity of different hard-to-cut materials. The improvements attributed to a substantial reduction in cutting temperature at the deformation zone and improvement in tribological properties. Cryogenic cooling is very promising as it improves machining performances without any post-processing of machined parts. Furthermore, nanofluids-based MQL and electrostatic MQL further enhance the performance than conventional vegetable-based MQL. Table 2.3 summarizes the above literature on MQL and cryogenic cooling approaches.

**Table 2.3** Summary of the review of MQL and cryogenic cooling in machining processes

Reference	Cutting process	Workpiece material	Observations
<b>MQL</b>			
Chinchani et al., [55], 2014	Turning	AISI 4340	Improved tool life by 20-25% in MQL compared to dry condition
Sivaiah et al., [56], 2020		AISI 52100	Reduction in cutting temperature by 25%, flank wear by 40% and surface roughness by 42%
Liu et al., [57], 2020		AISI 304	blended coolant reduces the contact angle of the coolant, improving the stability and cooling rate
Sharma et al. [61], 2015 MQL+carbon nanotube		Ti6Al4V	The cutting temperature and tool flank wear reduced, and the surface finish increased by adding the carbon nanotubes
Yildirim et al. [62], 2019 MQL+ hBN		Ti6Al4V	0.5% nano MQL improved surface finish and 1% nano MQL reduced tool-chip interface temperature
Gaurav et al. [63], 2020 MQL+ MoS <sub>2</sub>		Ti6Al4V	higher concentration of MoS <sub>2</sub> leads to an accumulation of nanoparticles which increase the cutting forces and surface roughness

Shah et al. [69], 2021 EMQL		15-5PH SS	EMQL improved tribological properties and surface finish compared to conventional MQL
Nanija et al. [60], 2015 MQL+ TiO <sub>2</sub> nanofluid	Milling	AA6061T6	With nanofluid MQL, the transfer of aluminium (%) was more, and tool edge chipping was lesser compared to oil-based MQL.
Sirin et al. [65], 2021 MQL+ hBN		Nickel alloy X-750	hBN nanofluid MQL significantly improved cutting force, tool wear, surface quality, surface defects and microhardness
Xu et al. [66], 2018 EMQL		AISI-304	The charged voltage of -5kV and flow rate of 10 ml/h improved tool life and reduced cutting forces and surface roughness
Lv et al. [68], 2018 EMQL+graphene nanofluid		AISI 304	The nano-based EMQL showed a better charging properties and physical properties compared to oil-based EMQL
Lv et al. [70], 2021 EMQL+SiO <sub>2</sub>		AISI 304	SiO <sub>2</sub> exhibited lower surface tension and contact angle due to its charging capacity was higher than vegetable oil, and resulted in a better machining performance
Pal et al. [64], 2020 MQL+graphene nanofluid	Drilling	AISI 321	MQL with graphene reduced the drilling forces, coefficient of friction, surface roughness and tool wear
<b>Cryogenic cooling</b>			
Courbon et al. [75], 2013	Turning	Inconel 718	The friction coefficient significantly decreased with cryogenic cooling with better wear resistance
Krishnamurthy et al. [76], 2017		Ti6Al4V	Cryogenic cooling reduced the friction at tool-chip interface, decreased cutting force by 65% and improved surface finish
Kaynak et al. [77], 2019		Ti-5553	LN <sub>2</sub> was better than LCO <sub>2</sub> in terms of surface roughness, tool wear, cutting forces and chip formation
Dhananchezian [78], 2019		Hastelloy C-276	surface roughness, cutting zone temperature, cutting forces and chip morphology are significantly lowered using LN <sub>2</sub>
Jadhav et al. [79], 2020		Nimonic C-263	Improvement in cutting forces, tool wear, surface roughness was significant with cryogenic cooling compared to dry condition
Amigo et al. [80], 2020		Haynes 263, Inconel 718	Good agreement was found between results of AISI 1045 and Haynes 263 whereas Inconel 718 inhibited some errors in cryogenic cooling
Khanna et al. [81], 2021		Inconel 718	energy consumption reduced by 8% and 13% with cryogenic coolant compared to dry and wet conditions respectively
Halim et al. [82], 2019	Milling	Inconel 718	Tool life was increased by 70% during cryogenic cooling compared to dry condition
Wang et al. [83], 2019		Ti6Al4V	Plastic deformation resistance was increased on the tool and workpiece surface and hence reduced oxidative wear by using cryogenic coolant
Wang et al. [84], 2021			

Jamil et al. [85], 2021			heat transfer ability of CO <sub>2</sub> snow was 87% higher than LN <sub>2</sub> on a flat surface for a specific injection time of coolant
Shah et al. [86, 87], 2020	Drilling	$\alpha$ -Ti alloy, VT- 20	LN <sub>2</sub> was better in terms of the number of drilled holes, cylindricity and circularity of drilled holes, microhardness whereas, LCO <sub>2</sub> was better in terms of thrust force, surface roughness and torque
Attanasio et al. [88], 2021		Inconel 718	LN <sub>2</sub> significantly improved hole circularity and cylindricity. It reduced the torque compared to wet conditions

## 2.3 Modelling of Ultrasonic-assisted Turning Processes

Machining processes are the most widespread manufacturing area in terms of volume and expenditure. Machined products are used in almost every type of manufactured component. In this regard, advances in machine tools and cutting tools are being carried out to improve manufacturing productivity and part quality and reduce costs [89]. These requirements include selecting optimum cutting conditions, cooling and lubrication, cutting tools, etc. In order to achieve all those requirements, predictive models need to be developed and integrated with the process planning.

On the other hand, the machining processes involve a large plastic deformation near the cutting edge of the tool. Moreover, even at a moderate cutting speed, the strain rates are significantly high, almost of the order of  $10^4$ - $10^5$  per unit time. The localized temperature generation is also quite higher. Therefore, the viscoplasticity, temperature softening effect, and strain hardening become important to analyze in the machining process. All these phenomena happen very near to the cutting edge [90, 91]. Thus, to understand all these phenomena happening around the cutting edge, modeling of the machining processes is needed.

Researchers have developed various modeling methods for the past several decades, including analytical modeling, empirical modeling, numerical modeling, and slip-line field modeling. Concerning to the ultrasonic-assisted turning process, the recent modeling study, including analytical and finite element analysis, is given in the following subsections.

### 2.3.1 Analytical modeling

Research in the field of the analytical model is still being carried out since the analytical model gives more insight into the physical behavior of the metal-cutting processes. Various researchers have developed analytical models to predict different machining responses, such as machining forces, friction behavior, etc., for ultrasonic-assisted machining processes.

Bai et al. [92] developed an analytical model for chip formation in ultrasonic-assisted orthogonal cutting of Ti6Al4V, considering the Calamaz-modified Johnson-cook model. Moreover, the non-equidistance shear zone model was used to determine shear strain and strain

rate at the primary shear zone. The developed analytical model closely agreed with the experimental results. It was observed that the cutting forces, tool-chip contact length, coefficient friction and shear strain reduced with cutting speed. Zhang et al. [93] developed a model for predicting cutting force in a high-speed ultrasonic-assisted turning process, considering elastic recovery on the flank face and plowing effect. The frequency was employed in the feed direction. The predicted values of cutting force closely agreed with the experimentally obtained values. In an ultrasonic elliptical vibration cutting, Huang et al. [94] developed a ductile regime model to predict the critical depth of cut in the machining of brittle materials. Predicted critical chip thickness match well with the experimentally obtained critical chip thickness. Moreover, it was noted that the critical chip thickness increased with amplitudes of vibration. In another study, an analytical approach to estimate the cutting temperature in an orthogonal cutting of Ti6Al4V considering Komanduri-Hou and the Huang-Liang model was performed by Shan et al. [95]. The temperature characteristics obtained by the predictive model were consistent with the temperature distribution obtained by the thermocouple in experiments. Moreover, the authors claimed that the developed model was more accurate than the Huang-Liang model for the given range of process parameters. In a recent study, Bai et al. [96] developed an analytical model to predict shear angle and frictional behavior using non-equidistant shear zone and tool-chip sliding-sticking zone theories. The theoretical results of effective shear angle under conventional and ultrasonic vibration were in good agreement with the results of the experiments. It was noted that the shear angle under ultrasonic vibration was larger compared to conventional condition. The shear angle increased with an increase in the amplitude of vibrations. Arefin et al. [97] performed modeling to estimate the chip formation during the vibration-assisted cutting process. The results showed that an elastic recovery and strain-hardened shear zone were responsible for higher shear angle and smaller chip thickness in vibration-assisted cutting compared to conventional cutting. Moreover, the tool-chip contact length and friction at the secondary zone were reduced by using ultrasonic vibration.

Verma and Pandey [98] developed a statistical model to evaluate the effect of process parameters on the cutting forces in the ultrasonic-assisted milling process. The results showed that axial ultrasonic vibration reduced machining forces for the given parameters. Moreover, it was noted that the most effective parameter for cutting force was feed rate, followed by ultrasonic power. In a similar study for ultrasonic-assisted milling, Verma et al. [99] developed an analytical model to estimate the cutting force considering acoustic softening using a modified Johnson-Cook model. The developed model predicted the machining force within 15% of deviation with experimentally produced cutting forces. It was noticed that the cutting forces reduced with an increase in ultrasonic power. Yan et al. [100] estimated the penetration length of lubricants based on the capillary rise theory for ultrasonic-assisted machining under MQL condition. The developed model showed a close agreement with the results of the experiments. It was found that high-frequency vibrations reduced the capillary rise during machining. The MQL along with

ultrasonic vibration, reduced the friction coefficient and tool-chip contact length. Feng et al. [101] estimated machining temperature using a physics-based analytical model during ultrasonic-assisted milling of Al 6063 alloy. The predicted model was able to estimate the temperature with an average error of 5.22%. Moreover, it was observed that the temperature decreased with an increase in vibration frequency and amplitude. In another study on analytical modeling, Ying et al. [102] predicted residual stresses during longitudinal-torsional ultrasonic-assisted milling of Ti6Al4V. Theoretical results were well agreed with the results of experiments. The results showed that the residual stresses fluctuate with ultrasonic vibrations. The absolute value of mechanical stresses was larger, and thermal stresses were lesser in vibration-assisted machining than in conventional machining. In a similar study on longitudinal-torsional ultrasonic-assisted milling of Ti6Al4V, a cutting force model based on tool flank wear was developed by Gao et al. [103]. The developed model predicted the cutting force relatively well by experimentally obtained results with an average error of 12-19%. The ultrasonic vibration decreased the cutting force by approximately 7-29% compared to conventional machining. It was also noted that the flank wear was decreased by increasing the amplitude of vibration up to a certain limit.

Zai et al. [104] developed an analytical model to determine the burr height, considering acoustic softening in the high-speed ultrasonic-assisted drilling (UAD) process. Analytically achieved burr height values were consistent with experimental results with a relative error of 5.35% and 4.9% for conventional and ultrasonic-assisted drilling. It was noted that the burr height was mainly affected by uncut chip thickness. Under ultrasonic vibration, the morphology of the hole was better compared to conventional drilling. In a similar study on burr formation, Zhu et al. [105] estimated burr height during UAD of DD6 superalloy. The predicted burr height showed an error of 4.5-17.7% with experimentally obtained burr height. The burr height was reduced with an increment in vibration frequency and amplitudes. Recently, Li et al. [106] proposed a model to calculate the delamination factor and thickness for CFRP during the UAD process. The predicted values of the delamination factor, thrust force, and thickness were in good agreement with the results of the experiments. In a similar study on UAD of CFRP, Huang et al. [107] predicted tool wear using a data-driven physics-based model. The estimated tool wear values closely agreed with the experimentally obtained tool wear.

### **2.3.2 Finite element modeling**

Finite element modeling or numerical modeling of machining different types of analysis, namely (i) Eulerian (ii) Lagrangian, and (iii) Arbitrary Lagrangian-Eulerian (ALE). This procedure uses two different types of time integration, namely implicit and explicit. The Lagrangian approach uses continuous updating and automatic remeshing, but it is computationally intensive. The Eulerian approach uses a predefined steady-state mesh structure but is computationally efficient. On the other hand, the ALE approach requires a predefined chip geometry, fixed Eulerian boundaries, and free Lagrangian boundaries as the mesh deform [91].

It is observed that the Fem has been fruitful in estimating stress, strain, temperature, force, and tool wear during machining processes. Moreover, the FEM can use several friction models to predict the friction at the secondary shear zone. Phenomena related to microstructures, such as residual stresses, microhardness, etc., can be simulated using FEM. Some recent works performed to simulate the ultrasonic-assisted machining processes using FEM are reviewed here.

Recently, Lotfi and Akbari [108] have briefly reviewed the FEM of ultrasonic-assisted machining processes. Lotfi and Amini [109] performed the FEM of 1D and 2D UAT using the Johnson-Cook plasticity model and Cockcroft and Latham's damage model for chip separation. An updated Lagrangian approach was used to remesh the workpiece. Predicted cutting forces were consistent with the experimentally measured cutting forces. Moreover, it was observed that the shear angle increased and chip thickness decreased by implementing ultrasonic vibrations. Lotfi et al. [110] carried out 3D FEM for rotary ultrasonic turning to predict flank wear rate using Usui's wear rate model. The experiments were conducted using AISI 4140 steel and results were compared for conventional, rotary and ultrasonic-assisted rotary turning. The ultrasonic vibration along with rotary motion, reduced cutting force by 30-50% and surface roughness by 50% compared to conventional turning. In a similar work, Gholamzadeh and Soleimanimehr [111] used the ALE approach for the prediction of cutting force and temperature using the FEM of UAT. A thermo-mechanical coupling with reduced integration elements was used for simulation. The results showed a good agreement between the values obtained by experiments and FEM. It was noted that the temperature decreased when lower amplitude and higher frequency were used in the UAT. Likewise, Shuang and Ma [112] used the coupling Eulerian-Lagrangian approach to model chip formation for UAT of Ti6Al4V. The results of FEM were compared with the results obtained from the analytical model. High-frequency vibration suppressed periodic shear band instability, producing continuous chips instead of serrated chips. Moreover, it was also observed that high-frequency vibration transferred shear deformation energy into tensile deformation energy, resulting in a transition of the serrated chip to a continuous chip. Khajehzadeh et al. [113] predicted residual stresses during UAT of AISI 4140 using FEM. The simulation results showed approximately 91% agreement with cutting force, and 87% for residual stresses, obtained experimentally. The UAT produced more compressive residual stresses compared to CT. A reduction in cutting speed and an increment in vibration amplitude increased the compressive residual stresses. In a similar study on the surface integrity of Ti6Al4V in UAT, Lotfi et al. [114] performed 3D FEM using Johnson-Mehl-Avrami-Kolmogorov to predict grain size in the UAT of Ti6Al4V and Inconel 100. The predicted value of grain size and cutting forces were in good agreement with the results obtained from experiments. The UAT produced 5% smaller grain and 20-30% lower cutting forces than CT. Moreover, the UAT increased the hardness and reduced the surface roughness of the machined surface compared to CT. Kurniawan et al. [115] used FEM for ultrasonic-assisted micro-grooving of AISI 1045 to predict cutting forces and residual stresses. The ultrasonic vibration decreased the cutting forces and tensile residual stresses.



Moreover, the residual stresses generated under ultrasonic vibration were having more depth compared to conventional conditions.

Elhami et al. [116] performed 3D FEM for ultrasonic-assisted milling to predict temperature field and cutting forces. Along with FEM, an analytical model was also developed and results were compared. To predict the temperature, a concentrated heat source was used. Experimental results showed a good agreement with the results of the FEM and analytical model. The FEM gave a closer result to the experiment compared to the analytical model. Chen et al. [117] studied tool-workpiece separation in vibration-assisted milling using kinematic equations and FEM. It was observed that periodic tool-work separation occurred when vibration was applied in the feed direction. Both the parameters, namely vibration frequency, and amplitude, affected the tool-work separation. Inappropriate values of parameters resulted in the generation of a larger cutting force, decreasing the surface quality. Xiang et al. [118] conducted FEM to investigate a particle rupture process and temperature variation during ultrasonic-assisted milling of SiCp/Al composites. The simulations were performed considering a single particle milling model, multiparticle milling model, and homogeneous model. Results of the single particle model showed that ultrasonic vibration improved the particle breakage effect. Results of the multiparticle model showed that when the amplitude was too high, the surface quality deteriorated. The results of the homogenous model showed that an increase in amplitude reduced the cutting temperature. In a similar study on vibration-assisted milling, Chen et al. [119] performed FEM and compared the results obtained from experiments. The vibration improved the surface quality and reduced the tool wear. An increment in vibration frequency shifted the crack initiation direction to the cutting region. As a result, the cutting force was found to reduce under ultrasonic vibrations. Ying et al. [120] performed 3D FEM to predict cutting force, temperature and residual stresses for longitudinal-torsional ultrasonic-assisted milling of Ti6Al4V. The results of FEM were in close agreement with the results of the experiments. Moreover, it was observed that ultrasonic vibration significantly reduced the cutting force, residual stresses and temperature compared to the conventional milling process.

Lotfi and Amini [121] performed the FEM of 3D ultrasonic assisted drilling (UAD) using Lagrangian formulation and Cockcroft and Latham's criterion. The effect of ultrasonic vibration on the drilling process, tool wear, thrust force and temperature were investigated. The simulated model was in good agreement with the experiments. It was noted that the UAD reduced the thrust forces, heat generation on the flank face, adhesion and built-up edge (BUE) formation compared to conventional drilling. Similar work on the FEM of UAD was performed by Paktinat and Amini [122, 123] and found that the theoretical results deviated by 18% from the experimental results. The UAD reduced BUE and improved the circularity compared to conventional drilling. Wang and Wang [124, 125] conducted the FEM of UAD of Ti6Al4V using 3-flute drills. The results obtained from FEM deviated by 3-7% with the results obtained from experiments. Moreover, it

was noticed that the UAD reduced the thrust force by 13-22%, cutting temperature by 7-15%, and improved the chip morphology compared to conventional drilling.

Table 2.4 summarizes the recent works being performed using analytical and finite element modeling of ultrasonic-assisted machining processes.

**Table 2.4** Summary of the recent work being performed in modeling of ultrasonic-assisted machining processes

<b>Analytical modeling</b>			
<b>Reference</b>	<b>Cutting process</b>	<b>Consequences</b>	<b>Remark</b>
Bai et al. [92], 2017	Turning	Prediction of chip geometry using Calamaz-modified Johnson-cook model	Cutting forces, tool-chip contact length, coefficient friction and shear strain are reduced with cutting speed
Zhang et al. [93], 2018		Prediction of cutting forces in high-speed machining	Predicted values of cutting force were closely agreed with the experimentally obtained values
Huang et al. [94], 2018		A ductile regime model was developed to predict the critical depth of cut	Predicted critical chip thickness match well with the experimentally obtained critical chip thickness
Shan et al. [95], 2019		Cutting temperature prediction in an orthogonal cutting considering Komanduri-Hou and the Huang-Liang model	Authors claimed that the developed model was more accurate than Huang-Liang model for the given range of process parameters
Bai et al. [96], 2021		Prediction of shear angle and frictional behaviour using non-equidistant shear-zone and tool-chip sliding-sticking zone theories	The shear angle under ultrasonic vibration was larger compared to conventional condition.
Arefin et al. [97], 2021		Estimate the chip formation during vibration assisted orthogonal cutting process	Elastic recovery and strain hardened shear zone were responsible for higher shear angle and smaller chip thickness in vibration assisted cutting
Verma and Pandey [98], 2018	Milling	Developed a statistical model to evaluate the effect of process parameters on the cutting forces	Axial ultrasonic vibration reduced machining forces
Verma et al. [99], 2018		Developed analytical model to estimate the cutting force considering acoustic softening	The developed model predicted the machining force within 15% of deviation
Yan et al. [100], 2018		Estimated penetration length of lubricants based on capillary rise theory, during machining under MQL condition	The developed model showed a close agreement with the results of experiments
Feng et al. [101], 2020		Estimated machining temperature using physics-based analytical model	The predicated model was able to estimate the temperature with an average error of 5.22%

Ying et al. [102], 2020		Predicted residual stresses for longitudinal-torsional vibration assisted milling	Theoretical results were well agreed with the results of experiments. The residual stresses fluctuate with ultrasonic vibrations
Guo et al. [103], 2021		Developed model for predicting cutting force based on tool flank wear	The model predicted the cutting force relatively well by experimentally obtained results with an average error of 12-19%
Zai et al. [104], 2021	Drilling	Developed an analytical model to determine the burr height, considering acoustic softening	Analytically achieved burr height values were consistent with experimental results with a relative error of 5.35% and 4.9% for conventional and UAD
Zhu et al. [105], 2022		Estimated burr height during UAD of DD6 superalloy	Predicted burr height showed an error of 4.5-17.7% with experimentally obtained burr height
Cau et al. [106], 2022		Proposed a model to calculate the delamination factor and thickness for CFRP	Predicted values of delamination factor, thrust force, thickness were in good agreement with the results of experiments
Huang et al. [107], 2022		Predicted tool wear for CFRP using data-driven physics-based model	Estimated tool wear values are closely agreed with the experimentally obtained tool wear.
Finite Element modelling			
Lotfi and Amini [109], 2017	Turning	FEM of 1D and 2D UAT using Johnson-Cook plasticity model and Cockcroft and Latham’s damage model for chip separation	Predicted cutting forces were consistent with the experimentally measured cutting forces
Lotfi et al. [110], 2018		3D FEM for rotary ultrasonic turning to predict flank wear rate using Usui’s wear rate model	Ultrasonic vibration and rotary motion reduced cutting force by 30-50% and surface roughness by 50%
Gholamzadeh et al. [111], 2019		Used ALE approach for prediction of cutting force and temperature using FEM of UAT	Results showed a good agreement between the values obtained by experiments and FEM
Shuang and Ma [112], 2019		Used coupling Eulerian-Lagrangian approach to model chip formation for UAT of Ti6Al4V	The high-frequency vibration suppressed periodic shear band instability, producing continuous chip, instead of serrated chip
Khajehzadeh et al. [113], 2020		Predicted cutting forces and residual stresses during UAT of AISI 4140	Simulation results showed approximately 91% agreement with cutting force, and 87% for residual stresses
Lotfi et al. [114], 2020		Performed 3D FEM using Johnson-Mehl-Avrami-Kolmogorov to predict grain size for Ti6Al4V and Inconel 100	UAT produced 5% smaller grain and 20-30% lower cutting forces, compared to CT

Kurniawan et al. [115], 2021		Used FEM for ultrasonic-assisted micro-grooving of AISI 1045 to predict cutting forces and residual stresses	Ultrasonic vibration decreased the cutting forces and tensile residual stresses
Elhami et al. [116], 2015	Milling	Performed 3D FEM for ultrasonic assisted milling for predicting temperature field and cutting forces. An analytical model was also developed	FEM gave a closer result to experiment, compared to analytical model
Chen et al. [117], 2018		Studied tool-workpiece separation in vibration-assisted milling using kinematic equations and FEM	Periodic tool-work separation occurred when vibration was applied in the feed direction
Xiang et al. [118], 2019		Conducted FEM to investigate a particle rupture process and temperature variation of SiCp/Al composites	Ultrasonic vibration improved the particle brakeage effect, reduced the cutting temperature
Chen et al. [119], 2019		Performed FEM and compared the results obtained from experiments	Increment in vibration frequency shifted the crack initiation direction to the cutting region, reducing the cutting forces
Ying et al. [120], 2020		Performed 3D FEM to predict cutting force, temperature and residual stresses, for longitudinal-torsional vibrations	Ultrasonic vibration significantly reduced the cutting force, residual stresses and temperature compared to conventional milling process
Lotfi and Amini [121], 2017	Drilling	Performed FEM of 3D ultrasonic assisted drilling (UAD) using Lagrangian formulation and Cockcroft and Latham's criterion	UAD reduced the thrust forces, heat generation on the flank face, adhesion and built-up edge formation
Paktinat and Amini [122, 123], 2017		Performed FEM of 3D ultrasonic assisted drilling (UAD)	Theoretical results deviated by 18% from the experimental results
Wang and Wang [124, 125], 2019		Conducted the FEM of UAD of Ti6Al4V using 3-flutes drills	Results obtained from FEM were deviated by 3-7% from the results obtained from experiments

## 2.4 Research Gaps

Above discussed literature shows that the ultrasonic-assisted machining process significantly improves the machinability of different hard-to-cut materials. Furthermore, sustainable cooling strategies such as MQL, cryogenic cooling, and vegetable oil-based cutting fluids are very useful in removing the heat from the machining zone during the machining of those materials. Apart from experimental work, some researchers have developed analytical and FEM to predict the various process parameters considering ultrasonic vibrations in the machining processes. Although several researchers have explored ultrasonic assisted machining process, some research gaps are identified as follows:

- Despite the significant volume of work performed to examine the surface quality, machining forces, chip morphology, power consumption and surface integrity, the tool wear behavior during machining under ultrasonic vibration has not been studied comprehensively.
- Very less number of literature work was found explaining a combined effect of ultrasonic vibration and cutting fluids such as vegetable oil-based cutting fluid, MQL, and cryogenic coolants such as LCO<sub>2</sub> and LN<sub>2</sub> on the machinability of difficult-to-cut materials.
- Several studies have been performed on the analytical modeling of ultrasonic-assisted machining processes. But analytical modeling of ultrasonic vibration-assisted machining using specific cutting energy has not been analyzed yet.
- Although several studies have been performed using FEM in the ultrasonic-assisted machining process, the tool wear behavior using FEM has not been explored much.

## 2.5 Objectives

For several decades, ultrasonic vibration, and cooling and lubrication assistances to conventional machining have been of interest to researchers exploring the machinability of difficult-to-cut materials. With the invention of novel materials, the process has also emerged with advancement in the mentioned assistance as the conventional machining processes are still irreplaceable by any particular process due to their unmatched capabilities. Thus, to investigate further into the conventional machining area, and to fulfil the above-mentioned research gaps, the following objectives are set to achieve;

1. To develop an analytical model considering ultrasonic vibration in the turning process, for analysing machinability in terms of cutting forces and tribological behaviour.
2. To develop a finite element model to simulate the cutting forces and tool wear in ultrasonic assisted turning process.
3. To design and develop a UAT setup to validate the analytical model and FEM developed in objectives 1 and 2, respectively. Moreover, analyzing the machinability of different materials with and without ultrasonic vibrations is also set as part of it.
4. To investigate a combined effect of ultrasonic vibration and cooling approaches such as flood cooling, MQL and LCO<sub>2</sub> to analyze the machinability of difficult-to-cut materials experimentally.
5. To explore the machinability of the materials at micro-scale cutting.

A details description of the experimental setup, cutting parameters, cooling strategies, measurement and characterization, are explained in chapter 3.

This chapter describes the development of experimental setup to perform the UAT operation, selection of process parameters, cooling and lubrication strategies implemented and measurement and characterization of the responses.

The main components of the Ultrasonic assisted turning process are the frequency generator, piezoelectric transducer, and horn. The frequency generator generates the electrical signal, which is then converted into a mechanical signal by piezoelectric transducers. These mechanical signals propagate through the ultrasonic horn to the cutting tool. The primary requirement to develop the setup is to design the ultrasonic horn. The machinability improvement in the UAT process is directly linked to proper horn design, which ensures the easy delivery of vibration to the cutting tool and increases the chip removal rate. An incorrect horn design can produce undesirable heat generation. A precise horn design reduces vibrational energy waste and improves the cutting operation [126]. Before going into the details of ultrasonic horn, some theoretical aspects of the acoustics are explained in section 3.1.1

### 3.1 Horn Design

#### 3.1.1 Longitudinal Waves in Solids

A mechanical wave is a physical quantity (energy or pressure) that propagates in a supporting medium. It may be characterized by the relative displacement of particles of the supporting medium from the position of equilibrium. One can say it is the form of distortion together with the speed and direction of propagation of distortion [127].

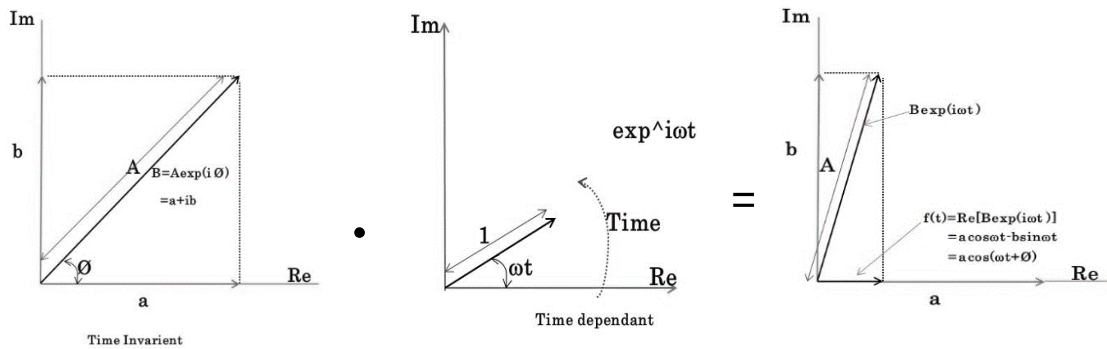


**Figure 3.1** complex exponential representation of  $f(t) = A \cos(\omega t + \phi)$

Simple harmonic variations in time are most conveniently described mathematically using a complex exponential representation. The basis of the representation is a simple harmonic variation of a quantity with time, which may be expressed as

$$f(t) = A \cos(\omega t + \phi) \quad (3.1)$$

In equation (3.1),  $A$  is the amplitude,  $\phi$  is the phase, and  $\omega$  is an angular frequency in rad/s. The above equation can also be represented as,

$$f(t) = \text{Re}[B \exp(i\omega t)] \quad (3.2)$$

In equation (3.2),  $B$  is the complex number, say  $a + ib$  and  $\text{Re}$  means 'real part of'.  $B$  is termed as the complex amplitude, which can also be expressed in the exponential form as,

$$B = A \exp(i\phi) \quad (3.3)$$

Where,

$$A = (a^2 + b^2)^{1/2}$$

$$a = A \cos \phi, b = A \sin \phi, \phi = \arctan(b/a)$$

Hence,  $f(t)$  may be represented graphically in the complex plane by a rotation vector which rotates at angular speed  $\omega$  as shown in Figure 3.1. The projection of the vector  $B \exp(i\omega t)$  on the real axis is the real harmonic function  $f(t)$

In pure longitudinal wave motion, the direction of particle displacement is purely in the direction of wave propagation; such waves can propagate in large volumes of solids. Two parallel planes in an undisturbed solid elastic medium, which are separated by a small distance  $\delta x$ , may be moved by different amounts during the passage of a longitudinal wave, as shown in Figure 3.2

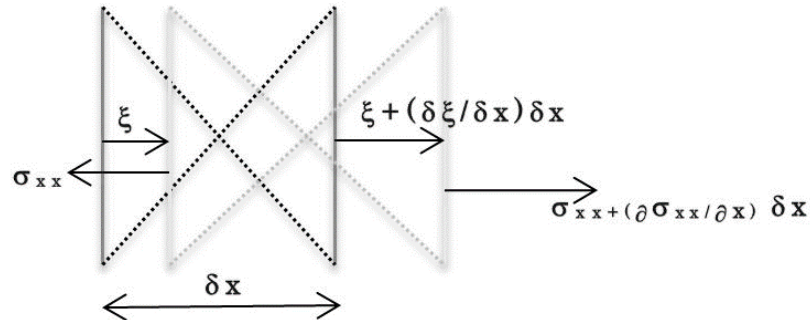


**Figure 3.2** Displacement from equilibrium and stresses in a pure longitudinal wave

Hence the element undergoes a strain  $\epsilon_{xx}$  given by,

$$\epsilon_{xx} = \partial \xi / \partial x \quad (3.4)$$

Where,  $\xi$  is the displacement of the parallel planes in the  $x$  direction

The longitudinal stress  $\sigma_{xx}$  is, according to the Hook's law, proportional to  $\epsilon_{xx}$ .

$$\sigma_{xx} = E \times \partial \xi / \partial x \quad (3.5)$$

Where,  $E$  is the modulus of elasticity or young's modulus.

The resulting equation of motion of element,

$$(\rho \delta x) \partial^2 \xi / \partial t^2 = \left[ \sigma_{xx} + (\partial \sigma_{xx} / \partial x) \delta x - \sigma_{xx} \right]$$

$$(\rho \delta x) \partial^2 \xi / \partial t^2 = (\partial \sigma_{xx} / \partial x) \delta x \quad (3.6)$$

Where  $\rho$  is the material mean density. Equations (3.5) and (3.6) can be combined into a wave equation,

$$\partial^2 \xi / \partial x^2 = (\rho / E) \partial^2 \xi / \partial t^2 \quad (3.7)$$

The general solution of the equation (3.7), which is the same form as the one-dimensional acoustic wave equation, shows the speed is,

$$c = (E / \rho)^{1/2} \quad (3.8)$$

The above equation presents the speed of the sound wave in the solid material. It can be noted that the speed of the sound mainly depends upon the modulus of elasticity and density of the material. The higher the stiffness of the material, the faster the sound wave propagates because in the stiffer material, each molecule is interconnected to other molecules, so any disturbance can transmit faster. The denser the medium slower the sound wave propagation for given materials because more density means more mass per volume, so more inertia, it is sluggish in the movement or oscillation. The value of the sound speed in different materials are shown in Table 3.1

**Table 3.1** Different types of materials used for acoustic horn [128]

Material	Speed of sound (m/s)	Length (mm)	Density(g/cm <sup>3</sup> )	E (GPa)
Steel	5300	133	7.8	210
Aluminium	5440	129	2.7	80
Titanium	4970	124	4.4	120
Monel Metal	4220	106	8.8	180
Brass	3370	84	8.4	97

### 3.1.2 Design of ultrasonic horn

Horn is a tapered waveguide for sound, and the shape of the waveguide supports the impedance matching between a sound source and free air, increasing sound amplitude. Mechanical impedance is a measure of how much a structure resists motion when subjected to a harmonic force. It relates forces with velocities acting on a mechanical system. The mechanical impedance of a point on a structure is the ratio of the force applied at a point to the resulting velocity at that point. Horns are such examples that are used to increase the efficiency of sound



propagation from source to free or end surface. The following points are considered in designing the horn [129]:

1. The largest diameter of a horn should be less than or equal to one-fourth of the vibration wavelength in the corresponding frequency. If this condition is not satisfied, the effect of the lateral vibration on the horn becomes considerable, leading to a waste of energy.
2. The diameter of the transducer attached to the side of the horn should be greater or equal to the diameter of the horn. This prevents the air from contacting the transducer end. Otherwise, at any point when air contacts the transducer, all the waves will return, and acoustic energy will be transformed into heat. Because of a rough interface between the transducer and horn surface and the possibility of air penetration, a connector such as a grease, aluminium foil, polymer, washer, etc., should be placed in their interface to fill the roughness.
3. Horn material should be such that it has a minimum amount of energy loss. For example, cast iron contains a small number of graphite particles that absorb the sound, so sound transmission in the medium is weak.
4. From the wavelength point of view, there are two types of horn viz. (1) the half wave; the length of the horn is half of the vibration wavelength, and (2) the full wave; the length of the horn is equal to the vibrational wavelength. It was noticed that half wavelength horn has lower energy loss and a better clamping option. In the present thesis work, the half-wavelength is considered.
5. The amplification or magnification of the vibration energy depends on the shape of the horn. The vibration energy remains constant through the horn length, indicating that energy density decreases with the decrease in the cross-section.
6. The correct clamping of the equipment, including the transducer, horn, and tool plays an important role. Clamping is generally done at the vibrational node point so that vibration cannot be transferred to the clamping system. However, the transfer of the ultrasonic vibration to the clamping system cannot be completely avoided.

Consider the wave equation:

$$\frac{\partial^2 p}{\partial x^2} = \frac{1}{c^2} \frac{\partial^2 p}{\partial t^2} \quad (3.9)$$

The above wave equation is the linear lossless wave equation for sound propagation in fluid with speed  $c$ . When a wave travels in a medium, some sound energy reflects after colliding with medium particles. It means that when a wave travels forward in a medium, some parts get reflected and travel in a backward direction. So, the total sound pressure at that boundary will be

a combination of forward and backwards travelling waves. Pressure function travelling in the  $x$  direction represented by

$$p = p^+ + p^- = Ae^{i(\omega t - kx)} + Be^{i(\omega t + kx)} \quad (3.10)$$

$A$  and  $B$  are constants.  $p^+$  stands for forward travelling wave and  $p^-$  stands for a backward travelling wave. As presented in Figure 3.3, consider a small strip of area  $dA$  and length  $dx$  at a distance  $x$  from the inlet. The wave is propagating in the  $x$ -direction;  $v$  is the particle velocity of the wave.

Let,  $p = p_0 e^{i(\omega t - kx)}$

$$\frac{\partial^2 p}{\partial t^2} = -\omega^2 p_0 e^{i(\omega t - kx)} = -\omega^2 p \quad (3.11)$$

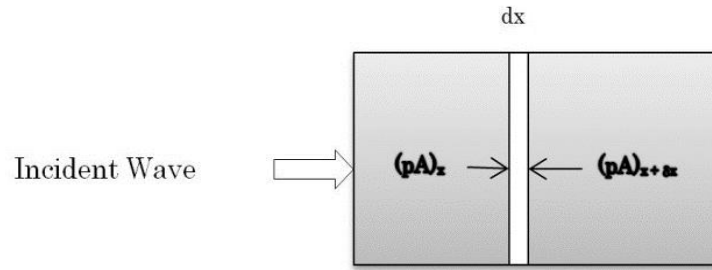


**Figure 3.3** A horn showing pressure force on a small elemental strip [130]

#### 1) Force Balance

Total elastic force is equal to the inertia force

$$\begin{aligned} (pA)_x - (pA)_{x+\delta x} + p dA &= \rho_0 A dx \frac{\partial v}{\partial t} \\ pA - (pA + \delta p A) + p dA &= \rho_0 A dx \frac{\partial v}{\partial t} \\ -\frac{\partial(pA)}{\partial x} + p \frac{\partial A}{\partial x} &= \rho_0 A \frac{\partial v}{\partial t} \\ -\left( A \frac{\partial p}{\partial x} + p \frac{\partial A}{\partial x} \right) + p \frac{\partial A}{\partial x} &= \rho_0 A \frac{\partial v}{\partial t} \\ -A \frac{\partial p}{\partial x} &= \rho_0 \frac{\partial(Av)}{\partial t} \\ -\frac{\partial}{\partial x} \left( A \frac{\partial p}{\partial x} \right) &= \rho_0 \frac{\partial^2(Av)}{\partial x \partial t} \end{aligned} \quad (3.12)$$

#### 2) Mass Balance

$$\begin{aligned}
(\rho_0 A v)_x - (\rho_0 A v)_{x+\delta x} &= A dx \frac{\partial \rho}{\partial t} \\
\rho_0 A v - (\rho_0 A v + \rho_0 \partial A v) &= A dx \frac{\partial \rho}{\partial t} \\
\rho_0 \left( \frac{\partial A v}{\partial x} \right) &= -\frac{A}{c^2} \frac{\partial p}{\partial t} \\
\left( \frac{\partial p}{\partial \rho} = c^2 \right) \\
\rho_0 \left( \frac{\partial^2 A v}{\partial x \partial t} \right) &= -\frac{A}{c^2} \frac{\partial^2 p}{\partial t^2}
\end{aligned} \tag{3.13}$$

Combining the equation (3.11), (3.12) and (3.13)

$$\frac{\partial}{\partial x} \left( A \frac{\partial p}{\partial x} \right) = \frac{A}{c^2} (-\omega^2 p) \tag{3.14}$$

$$\frac{\partial^2 p}{\partial x^2} + \frac{1}{A} \frac{\partial A}{\partial x} \frac{\partial p}{\partial x} + \frac{\omega^2}{c^2} p = 0$$

$$\frac{\partial^2 p}{\partial x^2} + \frac{d}{dx} (\ln A) \frac{\partial p}{\partial x} + \frac{\omega^2}{c^2} p = 0 \tag{3.15}$$

Here A is a function of x. this equation is given by A. G. Webster [130], which is named Webster's horn equation.

The general differential equation can be solved after substituting the shape function A(x). Four shape functions A(x) are available for acoustic horns, which are as follows:

- Cylindrical stepped horn
- Exponential horn
- Conical horn
- Hyperbolic horn

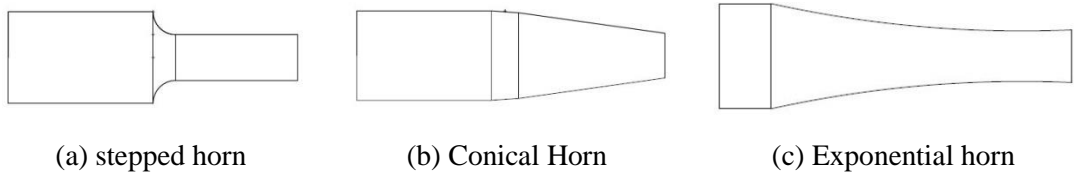


**Figure 3.4** Different types of horn

The choice of the shape function A(x) controls the magnification factor R. however, exponential and stepped types are frequently used. The conical and hyperbolic horns are difficult to design. Here, A is the function of x, this equation was given by A.G. Webster and the equation is named Webster's Horn Equation [131].

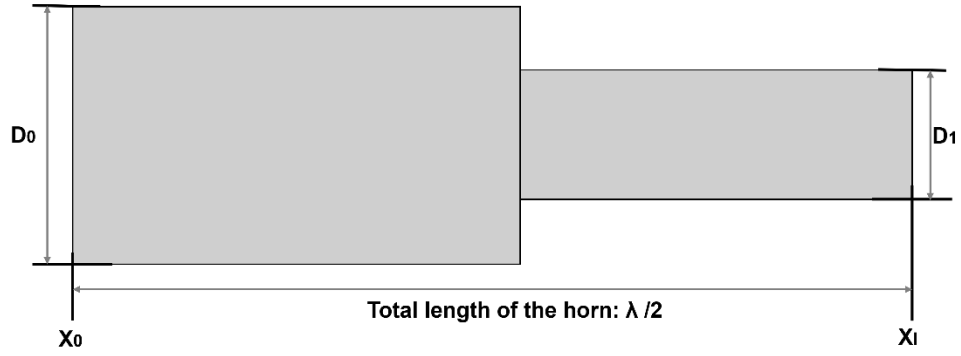


**Figure 3.5** Schematic of stepped horn

For constant area duct, change in cross-section area will be 0

$$\frac{\partial^2 p}{\partial x^2} + \frac{\omega^2}{c^2} p = 0 \quad (3.16)$$

This equation is called Helmholtz equation of wave.

For the amplitude, the above equation can be rewritten as follows:

$$\frac{\partial^2 \xi}{\partial x^2} + \frac{\omega^2}{c^2} \xi = 0 \quad (3.17)$$

$$\frac{\partial^2 \xi}{\partial t^2} = \frac{\partial}{\partial t} \left( \frac{\partial \xi}{\partial t} \right) = \frac{\partial}{\partial t} (\xi \omega) = \omega \left( \frac{\partial \xi}{\partial t} \right) = \xi \omega^2$$

$$\xi \omega^2 = \frac{\partial^2 \xi}{\partial t^2} \quad (3.18)$$

By combining the equation no (3.17) and (3.18), the following result will come

$$\frac{\partial^2 \xi}{\partial x^2} = \frac{1}{c^2} \frac{\partial^2 \xi}{\partial t^2} \quad (3.19)$$

The solution to the above equation can be written as follows.

$$\xi = \left( B \cos \frac{\omega x}{c} + C \sin \frac{\omega x}{c} \right) (D \cos \omega t + E \sin \omega t) \quad (3.20)$$

The boundary conditions are as follows:

- At  $x=0$  and  $x=l$ ,  $d\xi/dx=0$

$$\sin \frac{\omega l}{c} = 0$$

$$\sin \frac{\omega l}{c} = \sin n\pi$$

$$\frac{\omega l}{c} = n\pi$$

$$\omega_n = \frac{n\pi c}{l} \quad (3.21)$$

Equation no. (3.21) is the equation of **natural frequency** for the solid bar, where n is the number of modes and this,

For the two modes of vibration, put n=2 in the equation (3.21)  
the final displacement equation:

$$\xi = \xi_{\max} \cos\left(\frac{\omega x}{c}\right) \cos(\omega t) \quad (3.22)$$

$\xi_{\max}$  is the maximum displacement at x=0

Particle velocity is given by equation (3.23),

$$v = \frac{\partial \xi}{\partial t} = -\omega \xi_{\max} \cos\left(\frac{\omega x}{c}\right) \sin(\omega t) \quad (3.23)$$

Acceleration,

$$a = \frac{\partial^2 \xi}{\partial t^2} = -\omega^2 \xi_{\max} \cos\left(\frac{\omega x}{c}\right) \cos(\omega t) = -\omega^2 \xi \quad (3.24)$$

- **Location of the nodal point:**

The nodal point is the point where the amplitude is zero; by putting the  $\xi=0$  and  $x=x_n$  in the above equation,

$$\begin{aligned} \xi &= 0 \\ \cos\left(\frac{\omega x_n}{c}\right) &= 0 \\ \frac{\omega x_n}{c} &= \frac{n\pi}{2} \\ \frac{2\pi f x_n}{c} &= \frac{n\pi}{2} \\ x_n &= \frac{nc}{4f} \end{aligned} \quad (3.25)$$

For the horn, n=2 because there are three node points for two-mode

So,

$$\begin{aligned} x_2 &= l \\ l &= \frac{2c}{4f} \\ l &= \frac{c}{2f} \end{aligned} \quad (3.26)$$

Equation (3.26) is used to find out the length of the ultrasonic horn

- **Magnification factor for stepped horn:**

$$R_m = \frac{\xi_l}{\xi_0} = \left( \frac{D_0}{D_l} \right)^2 \quad (3.27)$$

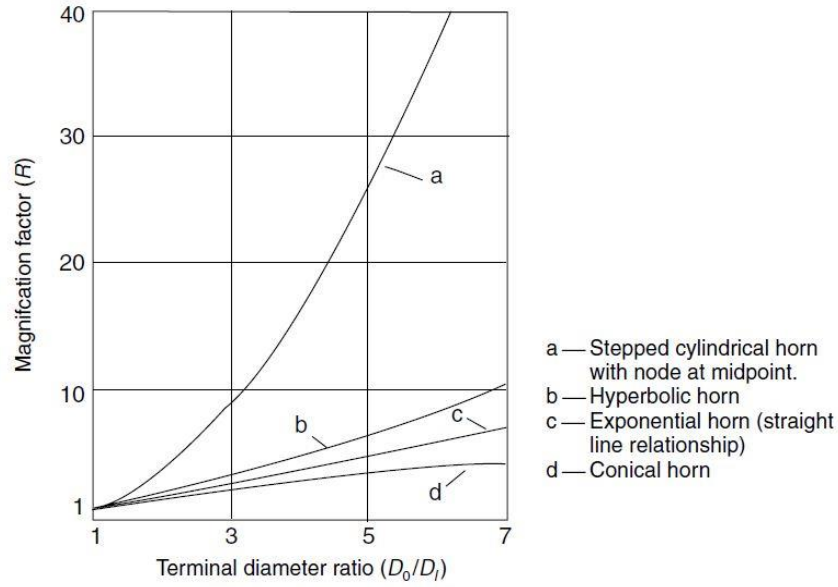


**Figure 3.6** Effect of terminal diameter ratio and shape function on the magnification factor [127]

From Figure 3.6, it is clear that for the stepped horn, the magnification factor is maximum for the same terminal diameter ratio.

Figure 3.7 shows the amplitude distribution of the stepped horn, assuming  $f_r=20$  KHz,  $D_0/D_1=5$  so that the magnification factor  $R_m$  can be calculated using-

$$R_m = \frac{\xi_l}{\xi_0} = \left( \frac{D_0}{D_l} \right)^2 \quad (3.28)$$

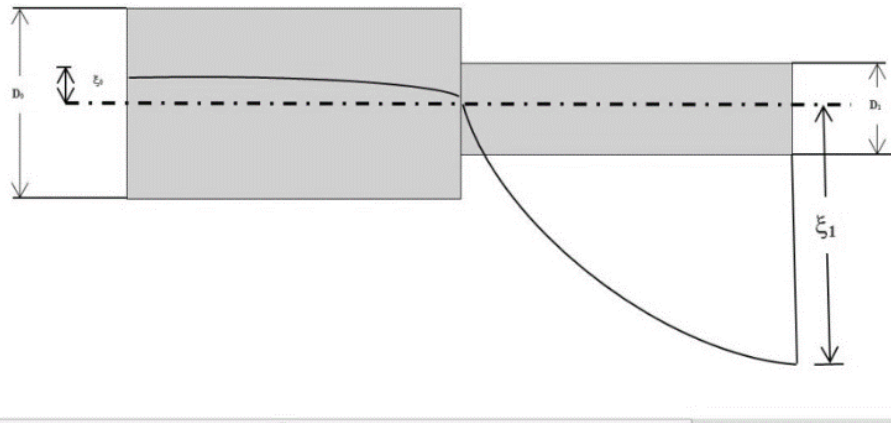


**Figure 3.7** A schematic shows the magnification of the amplitude in the stepped horn

From the above procedure, it can be concluded that

1. The magnification factor  $R_m$  is independent of the horn material.
2. In the case of an exponential circular acoustic horn, the magnification factor  $R_m$  depends upon the diameter ratio  $D_0/D_1$ .
3. For a given diameter ratio,  $D_0/D_1$ , the stepped horn possesses the highest magnification factor  $R_m$ , followed by the hyperbolic, the exponential, and finally, the conical type.

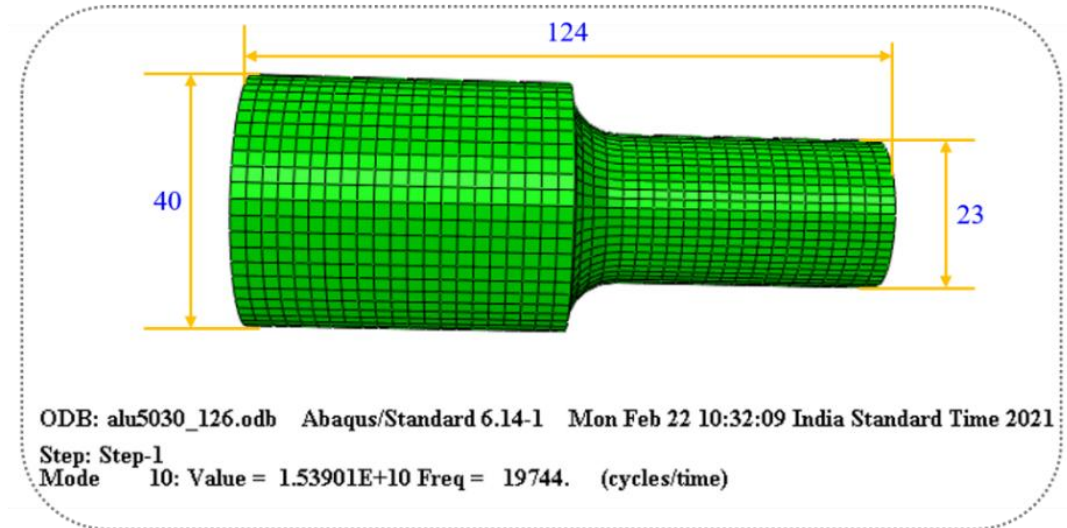


**Figure 3.8** A model of the horn prepared by FEM

The numerical analysis of the UAT process was performed using ABAQUS, a FEM software. The horn length calculated from equation (3.26) and resonance frequency of 20 kHz are given as input in the FEM. The model developed for the horn is shown in Figure 5. The element type used is C3D8R, eight nodes, and reduced integration. It is seen from Figure 3.8 that, at mode 10, the resonance frequency is around 19744 Hz. It is very near to the actual resonance frequency, 20000 Hz. The optimum length of the horn is 124 mm and the input and output diameters are 40 mm and 23 mm, respectively. Figure 3.9 presents the horn fabricated based on the diameter and length determined from theoretical and FEM.



**Figure 3.9** Horn used for conducting UAT experiments

## **3.2 Components for the UAT Setup**

The UAT setup consists frequency generator, piezoelectric transducer, booster and horn. The following sections briefly describe the each of the components used for preapright he UAT setup.

### **3.2.1 Frequency generator**

A frequency generator is an electronic equipment that generates different types of electrical waveforms over a wide range of frequencies. Some of the common waveforms are sine, square, and triangular shapes. A typical function generator can provide frequencies up to 20 MHz. A frequency generator is used to generate different types of electrical waveforms over a wide range of frequencies and regulates it as per requirement. A frequency generator is connected with a piezoelectric transducer attached to an ultrasonic horn by high-frequency cable, as shown in Figure 3.10. The frequency generated by the generator is transmitted to the cutting tool by an ultrasonic horn, and a vibro impact turning process is started.

### **3.2.2 Piezoelectric transducer**

Crystalline materials such as Quartz, Rochelle salt, and Barium Titanate produce the EMF (electromotive force) when they are placed under the force. This property is used in the piezoelectric transducer, where a crystal is placed between a solid base and force. An externally applied force enters the transducer through its pressure ports. Applied pressure to the top of the crystal produces the EMF across the crystal proportional to the magnitude of applied pressure. Power applied to the transducer at 20kHz can range from less than 50 Watts up to 3000 Watts. The transducer supplies the ultrasonic vibrations through piezoelectric converters, which transform electrical energy into mechanical movement. The transducer is made from a number of polycrystalline ceramic elements separated by thin metal plates clamped together under high pressure. When an alternating voltage is applied to the converters (or ceramics), a corresponding electric field is produced, which results in a variation in the thickness of the ceramic elements. This variation in thickness induces a pressure wave. Because the molecules or atoms of a solid are elastically bound to one another, the pressure wave propagates through the material, which is reflected by the ends of the metal mass of the converter. When the length of the assembly is tuned to its frequency of excitation, it resonates and becomes a source of standing waves. The output amplitude from a 20kHz transducer is only about 20 microns, so this amplitude needs to be amplified by the horn (and possibly a booster) to do useful work.



### 3.2.3 Booster

The primary function of a booster is to alter the amplitude of the probe. A booster amplifies if its amplitude is greater than one and reduces if its gain is less than one. Amplitudes at 20kHz typically range from less than one-half to about three. A booster designed to be mounted in a fixture between the transducer and horn is shown in Figure 3.10. Since the horn cannot be clamped, only the transducer and booster can be secured. Therefore, a secondary function (and sometimes sole purpose) of a booster is to provide an additional mounting location without altering the amplitude when the stack is secured in a press. The neutral (1:1) or coupling booster is added between the transducer and horn and mounted in the press by its mounting ring, which is placed at the nodal point (where the standing wave has minimal amplitude). Note that the maximum stress occurs at the nodal points.

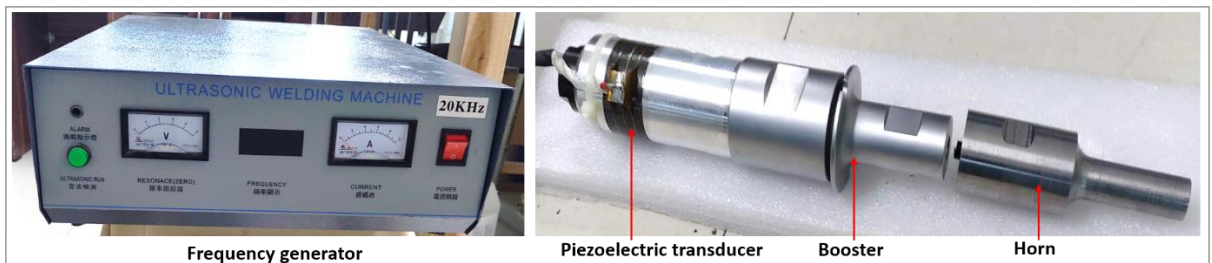


**Figure 3.10** Components used for UAT setup

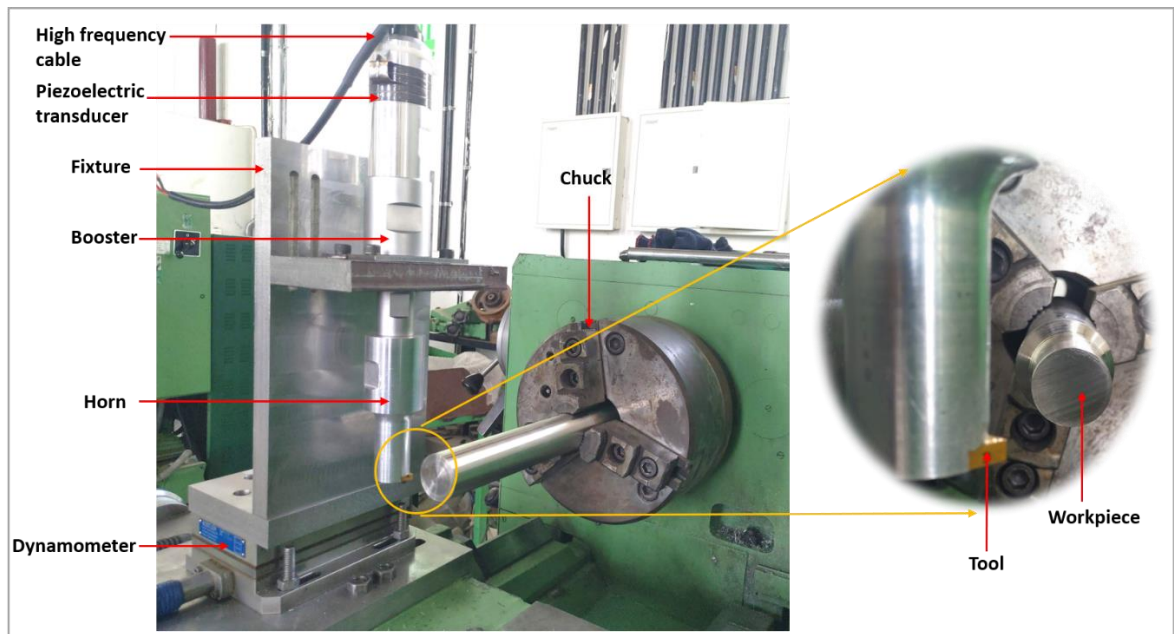


**Figure 3.11** UAT setup mounted on a conventional lathe for performing experiments

Once the horn is fabricated, the UAT setup is prepared and assembled on the conventional lathe, as shown in Figure 3.11. Figure 3.11 shows that the compound rest is replaced

with the UAT setup. The fixture is mounted on the dynamometer. The assembly of the horn, booster and piezoelectric transducer is mounted on the horizontal plate. The piezoelectric transducer is connected to a frequency generator. The frequency generator produces an electrical signal which is then converted into mechanical displacement through a transducer. This mechanical displacement is transferred to the horn in terms of frequency and amplitude. The vibration and frequency are finally transferred to the cutting tool, which is bolted at the end of the horn. The vibration is imposed in a vertical direction i.e., in the cutting velocity direction of the workpiece. Those vibrations are superimposed on the cutting action of the cutting tool, and thus ultrasonic vibration-assisted cutting is taken place.

### 3.3 Materials and Methods

As discussed in chapter 2, the machining of Titanium and Nickel base super alloy is difficult compared to mild steel, aluminum alloy and different soft metals. Ti6Al4V, Nimonic 90 and Inconel 718 are chosen as workpiece materials to analyze the machinability under ultrasonic vibration.

#### 3.3.1 Workpiece materials

##### (1) Ti6Al4V

Ti6Al4V includes in the category of  $\alpha+\beta$  titanium alloys. That is, the microstructure of Ti6Al4V consists of  $\alpha$  and  $\beta$  phases. The crystal structure of the  $\alpha$  phase is HCP (hexagonal close-packed), whereas the  $\beta$  phase is BCC (body-centred cubic). The Ti6Al4V uses over 50% of global consumption [132]. Due to its higher corrosion resistance, specific weight, elastic modulus, fatigue and creep resistance, the Ti6Al4V is widely used in aerospace, automotive, medical and biomedical, and nuclear sectors. The properties of Ti6Al4V and chemical structure are given in Table 3.2 and 3.3, respectively.

**Table 3.2.** Mechanical properties of Ti6Al4V

Property	Density	Hardness	Modulus of elasticity	Ultimate Tensile strength	Melting point
Value	4400 kg/m <sup>3</sup>	320 HV	110-115 Gpa	1170 Mpa	1660 °C

**Table 3.3.** Chemical structure of Ti6Al4V

Element	Ti	V	O	Fe	C	N
% weight	Balance	4.33%	5.92%	0.13%	0.032%	0.012%

## (2) Nickel base super alloy: Nimonic 90 and Inconel 718

Nickel base superalloys such as Nimonic 90 and Inconel 718 are used to perform experiments. The microstructure of both alloys consists of FCC (face-centered cubic) structure. The mechanical properties of both the alloys are given in Table 3.4. Tables 3.5 and 3.6 show the chemical compositions of Nimonic 90 and Inconel 718, respectively. Nimonic 90 is a precipitation-hardened nickel-chromium-cobalt alloy strengthened by an addition of aluminum and titanium. It has a high-stress rupture strength and creep resistance at elevated temperatures. It is generally used in high-temperature applications such as turbine blades, hot working tools, reheaters and springs [133].

Inconel 718 is made up of 50-55% nickel+cobalt (with cobalt limited to 1% max) and 17-21% chromium. This combination gives the material its corrosion-resistance properties. This includes good oxidation resistance, enabling it to withstand corrosive environments present in many applications. It is often used in the aviation and aerospace industries. It's imperative to use materials that can retain their strength and resistance to corrosion in the hottest sections of these engines [133].

**Table 3.4.** Mechanical properties of Nimonic 90

Property	Density	Hardness	Modulus of elasticity	Ultimate Tensile strength	Melting point
Nimonic 90	8180 kg/m <sup>3</sup>	300 HV	213 Gpa	1175 Mpa	1350 °C
Inconel 718	8200 kg/m <sup>3</sup>	350 HV	205 Gpa	1375 Mpa	1300 °C

**Table 3.5.** Chemical structure of Nimonic 90

Element	C	Si	Mg	S	Cr	Ni	Ti	Al	Co	Fe
% weight	0.084	0.137	0.018	0.004	18.17	58.03	2.4	1.09	18.57	0.814

**Table 3.6.** Chemical structure of Inconel 718

Element	Ni	Cr	Fr	Nb	Mo	Ti	Al	Si	Co	Mg
% weight	54.8	17.7	17	4.9	3.86	0.85	0.372	0.205	0.12	0.12

### 3.3.2 Tool material: Coated Tungsten Carbide (WC)

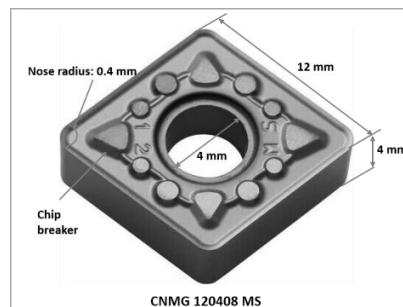


**Figure 3.12** Cutting insert used to perform the experiments

As shown in Figure 3.12, a PVD-coated WC insert (Make: Kyocera), CNMG 120408 MS, is chosen to perform the experiments. Table 3.7 presents the specifications of the cutting insert. According to the manufacturer, this cutting insert is used to perform the machining of heat-resistant alloys for finishing and roughing operations. The tool is coated with multiple nanolayers of TiAlN. The TiAlN is a chemical compound of the three elements titanium, aluminum, and nitrogen. The coating thickness is in the range of 1-4  $\mu\text{m}$ . The coating offers high resistance to heat and oxidation. This enables working with a higher cutting speed and thus accelerating working processes. Compared to uncoated tools, TiAlN coating, depending on the application, increases service life by up to ten times. TiAlN has superior ductility, and it is stable at higher temperatures.

**Table 3.7** Cutting inserts designation

Designation	Meaning
C	80° Rhombic
N	Relief angle (N=0°)
M	Tolerance symbol (M= $\pm 0.08\text{mm}$ ~ $\pm 0.18\text{mm}$ )
G	Types of inserts (G=with hole and chip breaker)
12	Edge length, 12.70 mm
04	Thickness symbol, 4.76 mm
08	Corner radius, 0.8mm
MS	Manufacture's opinion, for finishing and medium roughing

### 3.3.3 Machine tool

It is clear from chapter 2 that the study on ultrasonic-assisted turning needs a dedicated setup, producing ultrasonic vibration to be given to the cutting tool. Thus, it is decided to assemble the UAT setup on a conventional lathe to perform the turning experiments. The conventional lathe used for experimentation is shown in Figure 3.13. The specification of the lathe is presented in Table 3.8.



**Figure 3.13** Machine tool used to perform the experiments

**Table 3.8** Specifications of the machine tool used for experiments

Parameter	Specification
Machine tool	Convectional lathe (Make: HMT, Model: NH 22)
Spindle power	11 kW
Height of centers	220 mm
Swing over bed	500 mm
Swing over cross slide	270 mm
Distance between centers	1000 mm
Spindle speed range	Maximum 2040 rpm forward, Maximum 1430 rpm reverse
Feed	0.04-2.24 mm/rev (longitudinal), 0.02-1.12 mm/rev (cross)

### 3.4 Processes Parameters

The experiments are performed using UAT and CT at different process parameters. Cutting speeds, feed, depth of cut, frequency, and vibration amplitude are considered input parameters. The values of the cutting speed can be chosen based on a value of critical cutting speed ( $V_c$ ), which is given by equation 31, as follows

$$V < V_{cr} = 2\pi af \quad (3.29)$$

Where  $V$  is cutting speed,  $a$  is amplitude, and  $f$  is frequency. If equation (3.29) is not satisfied, the cutting action results in a conventional turning. Considering equation (3.29), the cutting speed used for the machining should be lesser than the critical cutting speed, 75 m/min for the resonance frequency and amplitude of 20 kHz and 10 $\mu$ m, respectively. The feed and depth of cut are chosen based on previous literature and industrial requirements. Table 3.9 represents the range of process parameters used for CT and UAT of different materials.

**Table 3.9** Process parameters used for experiments

Parameter	Range
Cutting speeds	50-75 m/min
Feed rate	0.1-0.3 mm/rev
Depth of cut	0.3-0.5 mm
Frequency	20 kHz
Amplitude	10 $\mu$ m

### 3.5 Cooling Strategies

The experiments are performed under different conditions using the developed UAT setup. The conditions are dry, wet, vegetable oil-based cutting fluid, MQL and LCO<sub>2</sub>. The following subsections explain various cooling and lubricating conditions used for machining.

#### 3.5.1 Dry cutting

Dry-cutting methods eliminate the use of coolant and thus minimize the machining cost and environmental issues arising from the use of coolants. The dry condition also ensures the workers' health by preventing contact with harmful chemicals with humans. However, it is noted that the friction and temperature generated in the dry condition are significantly high, accelerating the tool wear and degrading the surface quality. Since the titanium and nickel base superalloys are in the category of difficult-to-cut materials, the heat and friction generated during machining are extremely high while machining under dry condition. Furthermore, the chemical reactivity of those alloys promotes the adhesion of the workpiece with the tool, enhancing the tool wear [134]. Due to the problems mentioned earlier, it is desirable to use cooling and lubrication during the machining of difficult-to-cut materials. In this study, dry machining is performed for comparison purposes.

#### 3.5.2 Flood cooling

Wet cooling is the conventional approach for applying cutting fluid in machining processes. The schematic of wet cooling is shown in Figure 3.14. This approach uses petroleum-based fluids that are harmful to the environment and health and thus are not considered sustainable. Still, wet cooling is the most commonly used lubrication approach in machining processes. It has been seen that the conventional cooling approach does not give the best results when different metals are machined. However, it is observed that wet cooling is compatible with almost all materials, achieving good productivity [135]. In the current work, the machining responses are compared during machining under wet and other cooling and lubrication strategies.



**Figure 3.14** Schematic of conventional wet cooling approach used during machining

### 3.5.3 Vegetable oil-based cutting fluid

In the present research, vegetable oil, i.e., canola oil, is used during the machining all the materials. It is observed that canola oil has excellent biodegradability, lubrication properties, viscosity and thermal stability [136]. As discussed in chapter 2 that vegetable oil-based cutting fluid is influenced by its chemical properties during machining processes. Moreover, it prevents tool and workpiece from corrosion. The properties of the canola oil are given in Table 3.9. In the current work, 10% canola oil is mixed with water. The emulsion of canola oil mixed with water is delivered to the rake face of the tool.

**Table 3.10** Properties of canola oil

Property	Value
Specific heat (J/g)	1.91-1.92 (at 20 <sup>0</sup> C)
Flash Point ( <sup>0</sup> C)	275-290
Kinematic viscosity (mm <sup>2</sup> /s)	78.2
Relative density (g/cm <sup>3</sup> )	0.914-0.917
Thermal conductivity (w/m K)	0.18-0.185

### 3.5.4 MQL (Minimum quantity lubrication)

Minimum quantity lubrication (MQL) is considered near dry machining (NDM) as it consumes much less cutting fluid during machining. This approach is considered sustainable due to a reduction in cutting fluid consumption. The MQL setup used for machining is shown in Figure 3.15. It contains an air compressor, FRL (filter regulator and lubricator) unit, a hose pipe, and a nozzle. The compressed air from the compressor enters the FRL unit. The FRL unit filters out the dust particles and vapours. After that, the pressure is pressurized by a pressure regulator equipped with a pressure gauge. The lubricator unit mixes the oil particles with the compressed air by the venturi effect. A venturi ring is fitted in the lubricator unit, increasing the velocity of the air for generating a vacuum, drawing the oil particles from the oil collector to an upper part of the lubricator by pressure difference. Finally, a mixture of oil and compressed air i.e., the mist comes out from another side of the FRL unit. The mist is passed through a hose pipe connected to the other side of the FRL unit. Ultimately, the mist comes out from the nozzle connected with the hose pipe and flows over the rake face of the tool. The specification of the MQL setup is presented in Table 3.10.

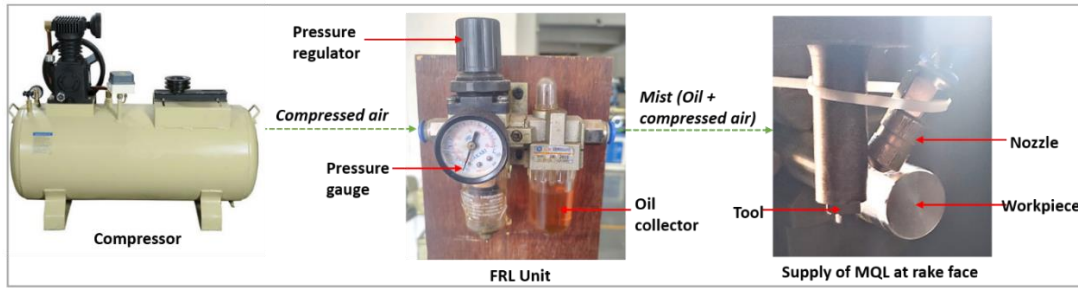


**Figure 3.15** Setup used for MQL in machining

### 3.5.5 Liquid carbon dioxide (LCO<sub>2</sub>)

The machining under LCO<sub>2</sub> is an alternative approach to using LN<sub>2</sub>. The LCO<sub>2</sub> is stored in a pressure of 57 bar at atmospheric temperature to make it in liquid form. At atmospheric pressure, a sudden pressure drop causes the LCO<sub>2</sub> to cool down and expand due to the Joule-Thomson effect. When the LCO<sub>2</sub> is delivered to the machining zone, it absorbs the heat due to sudden vaporization and expansion. Heat extraction is mainly dependent on the convective heat transfer coefficient. An LCO<sub>2</sub> cylinder used, in the present study, is shown in Figure 3.16. A dip tube is inserted into the cylinder to ensure the delivery of LCO<sub>2</sub> without evaporation. The LCO<sub>2</sub> comes out from the nozzle attached at the end of the hose pipe. The parameter used for LCO<sub>2</sub> is mentioned in Table 3.10.

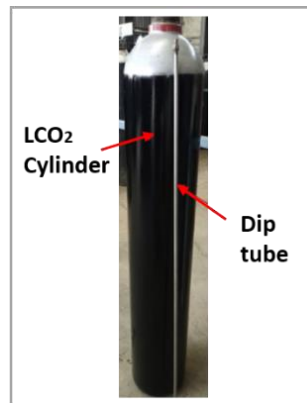


**Figure 3.16** Liquid carbon dioxide (LCO<sub>2</sub>) cylinder

**Table 3.11** Details of cooling strategies employed

Parameter	Attributes
Wet cooling	Fluid: Emulsion of synthetic oil in water, Pressure: 3 bar, Flow rate: 21 l/min, Nozzle diameter: 10 mm,
MQL	Oil: Canola oil



	pressure: 5 bar Flow rate: 7-8 ml/hr Nozzle diameter: 2 mm
LCO <sub>2</sub>	Pressure of the cylinder: 57 bar, Flow rate: 27 l/hr, Nozzle diameter: 2 mm
Distance of nozzle tip from rake face	20 mm for all the cooling strategies

### 3.6 Measurement and Characterization

The machinability of different materials is examined using different responses such as machining forces, surface quality, power consumption and tool wear. The machining forces and power consumption are measured during machining, whereas the surface roughness and tool wear are measured after machining. The components used to measure various responses are explained in the following subsections.

#### 3.6.1 Force measurement

During machining, the machining forces are measured using a Dynamometer (Make: Kistler, Model: 9257B). As shown in Figure 3.11, the dynamometer is placed under the fixture on which the UAT setup is mounted. The force measuring system is shown in Figure 3.17. The dynamometer consists of quartz three-component transducers for measuring three orthogonal components of the forces. Four three-component force sensors are fitted under high preload between the base plate and the top plate. Each sensor includes three pairs of quartz plates. One plate is sensitive to pressure in the X direction, and the other two are in the Y and Z directions. The force components are measured practically without displacement. The outputs of four force sensors are connected inside the dynamometer to allow multi-component measurement of forces and moments to be performed. The dynamometer has a natural frequency of 3.5 kHz. The piezoelectric sensors inside the dynamometer convert the mechanical displacement into an electrical signal. The connecting cable transfer those electrical signals to the charge amplifier. The connecting cable has high insulation and impedance (low current and high voltage). The charge amplifier produces a voltage as an output proportional to the input current, or a total charge is given. The charge or current produced by the piezoelectric sensor is difficult to access. It is proportional to the load or applied pressure. The charge amplifier converts the charge to the voltage. The selection of a charge amplifier is mainly depended upon the size of the signal and the type of sensor. The sensitivity is a ratio of charge to a physical quantity. That means to measure a very small signal; the amplifier has a very low noise floor; thus, the quality of the signal is still high. On the other hand, to measure a very large signal, the amplifier should cope

with big charge signals. The next important criterion is the frequency range, i.e., the lower and upper cut-off value of frequency. The piezoelectric sensors deliver relatively small charges as a signal. The slower the signal is, the more difficult it is not to lose any electrons to poor insulation. Measuring a very low signal, i.e.,  $<0.1$  Hz (quasistatic signal) or dynamic signal, i.e.,  $>0.1$  Hz, requires a different configuration of an amplifier. In the present study, the charge amplifier used is 5070A, which contains 0-45 kHz frequency. For the present work, the charge amplifier used is 5070. This charge amplifier is connected to the data acquisition (DAQ) system consisting DynoWare via low-impedance cable. The DAQ system consists of a connection box and a DynoWare program. The DAQ interfaces and controls charge amplifiers, signal conditioners, and cutting force applications using component sensors and dynamometers. The DAQ system is connected through a USB port and is controlled by DynoWare software. It digitizes the analogue output data. The DAQ has excellent resolution and a very high sampling rate of up to 125 kS/s with eight measuring channels, enabling the measurement of highly dynamic data of a very broad range.

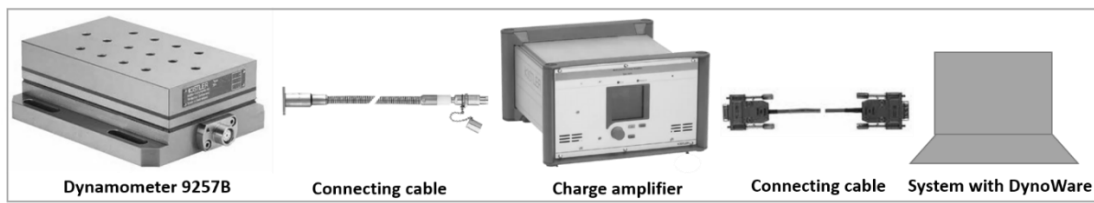


**Figure 3.17** Force measurement using dynamometer

### 3.6.2 Surface roughness measurement

The surface roughness of the machined surface is measured using a contact-type surface roughness tester (Make: Taylor Hobson, Model: Surtronic S128). Figure 3.18 shows a schematic, whereas Table 3.12 shows details of the surface roughness tester. The surface roughness tester includes a stylus that can lift up to 50 mm and travel more than 70 mm on the surface horizontally. It has a measurement capability of  $2\%+0.004\text{ }\mu\text{m}$  for standard roughness measurement ( $R_a$ ). This standard roughness can be used to calibrate the instrument and stylus wear. The surface roughness is measured, keeping a cut-off length of 0.8 mm and an evaluation length of 4 mm, as per ISO 4288-1996.



**Figure 3.18** Taylor Hobson Surtronic S128 surface roughness tester

**Table 3.12** Details of surface roughness tester

Characteristics		Value
Gauge	Range	400 $\mu\text{m}$ , 100 $\mu\text{m}$ , 10 $\mu\text{m}$
	Resolution	50 nm, 10 nm, 5 nm
	Repeatability	0.5 % of value + noise
	Gauge force	150-300 mg
	Stylus tip radius	5 $\mu\text{m}$
Calibration	Process	Automated software calibration routine
	Standards	Able to calibrate to ISO 4287 roughness standards
Analysis	Filter cut-off	0.25 mm / 0.8 mm / 2.5 mm
	Filter type	2CR / Gaussian
	Evaluation length	0.25 mm - 25.0 mm
	Max X axis range	25.5 mm
Speed	Measuring speed	1 mm / sec
	Returning speed	1.5 mm / sec
Parameters	Standards	ISO 4287, ISO 13565-1, ISO 13565-2, ASME 46.1, JIS 0601, N31007
	ISO basic	Ra, Rv, Rp, Rz, Rt, Rq, Rsk, Rmr, Rdq, Rpc, RSm, Rz1max

### 3.6.3 Power consumption measurement

Power consumption during machining is an essential factor in achieving sustainability. For the present study, a power quality and energy analyzer (Make: Fluke, Model: 435 series II) is used to measure the power consumption during machining. The schematic view of the power analyzer is shown in Figure 3.19. The device is connected to 3 phase distribution system, as given in Figure 3.19. Four BNC (Bayonet neill concealma) type connectors are used for current and voltage drew by the machine tool. Multiple parameters such as phase voltages, phase current, crest factor, frequency, energy loss and power inverter efficiency can be measured using this device. Moreover, it helps in minimizing downtime, finding out troubleshoot, and power quality issues. Thus, detailed information is used to improve the performance of the machine, minimizing the energy waste due to electrical systems.

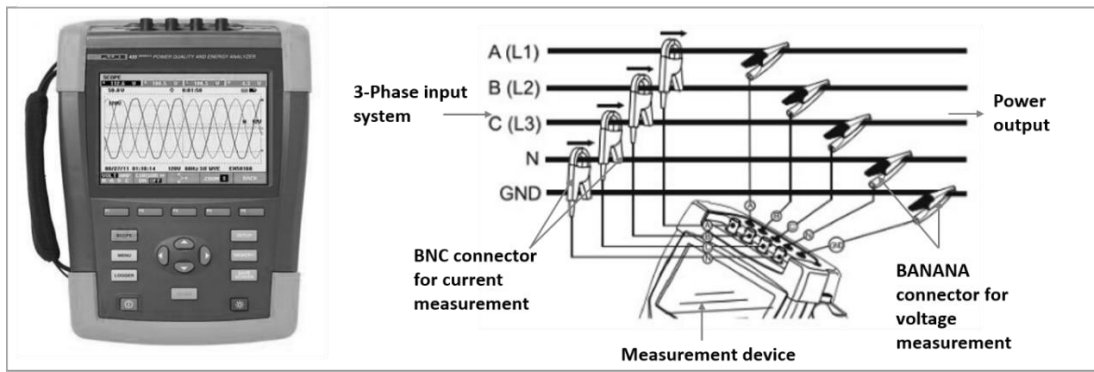


**Figure 3.19** Fluke 435 power quality and energy analyzer

**Table 3.13** Details of power analyzer

Characteristics	Range
Number of inputs	4(3 phase + neutral) DC-coupled
Maximum input voltage	1000 Vrms (Root mean square voltage)
Nominal voltage range	Selected 1V to 1000V
Maximum peak measurement voltage	6 kV
Resolution	16 bit analog to digital converter on 8 channels
Bandwidth	>10 kHz

### 3.6.4 Tool wear and chip morphology assessment

Tool wear is an important criterion for deciding the machinability of workpiece materials. To examine the tool wear morphology, the tools are collected and observed using an optical and scanning electron microscope, as shown in Figure 3.20. The following tool wear criteria given by ISO 3685:1993 are considered for analysis [138].

- The maximum width of flank wear land ( $VB_b \text{ max}$ )  $\geq 0.6$  for non-regular wear pattern
- The average width of flank wear land ( $VB_b \text{ avg}$ )  $\geq 0.3$  for regular wear pattern
- The maximum notch wear at the relief face of the tool ( $VB_N$ )  $\geq 0.6$  for non-regular wear pattern
- The average notch wear at the relief face of the tool ( $VB_N$ )  $\geq 0.3$  for regular wear pattern
- Crater depth  $\geq 0.06 + 0.3f$ , where  $f$  is feed in mm/rev
- Catastrophic failure of cutting edge

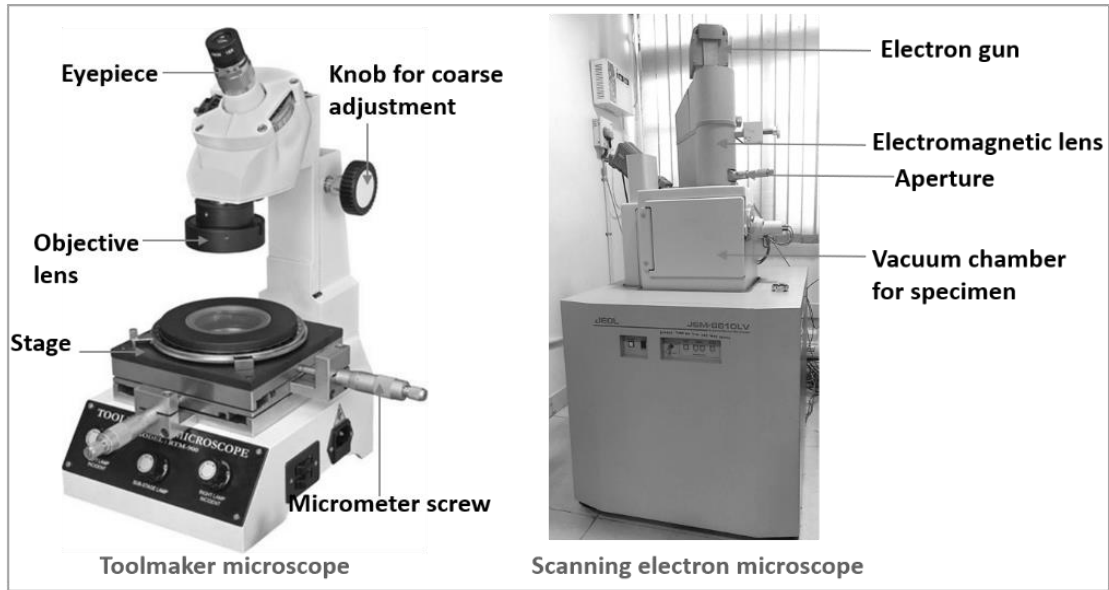


**Figure 3.20** Optical and scanning electron microscopes

The flank wear is analyzed using a toolmaker microscope (Make: Radical, Model: RTM 900). The specifications of the toolmaker microscope are given in table 3.14. The morphology of the tool wear and chips can not be visualized using an optical microscope as long as the light is used. An electron beam is employed whose wavelength is smaller than the light to observe something smaller than the light. Thus, it is possible to examine a structure down to several nm in scale using an electron beam. The scanning electron microscope uses an electron beam to observe a very small structure of a specimen. Moreover, it captures images with deeper focal length compared to an optical microscope.

**Table 3.14** Details of optical and scanning electron microscopes

Parameter	Specification
<b>Optical microscope:</b> Radical RTM 900 Supplied with Standard Micrometre, Least Count 0.01mm. & Tungsten Lights	
<b>Observation Tube</b>	Monocular, inclined at 30° Coupled with graduated Eyepiece Protractor
<b>Base</b>	Large and heavy base provides extra overall rigidity
<b>Illumination</b>	Sub-stage lamp emits transmitted light from a bottom source equipped with collimated green filter halogen light. Oblique illuminator with an adjustable inclination for surface illumination of the sample with relief structure
<b>Objective</b>	2x Achromatic
<b>Eyepiece</b>	WF 15 x with Cross reticle
<b>Scanning electron microscope:</b> JEOL 6610LV	

Resolution mode	3.0 nm (30 kV), 8 nm (3 kV), 15 nm (1 kV)
Magnification	3,00,000
Accelerating voltage	0.3 kV to 30 kV
Filament	Factory pre-cantered filament
Electron gun	Fully automated
Maximum specimen	200 mm diameter
LV pressure	10 to 270 Pa

### Modelling of Ultrasonic-assisted Turning Process

---

Manufacturing of a wide range of components for aerospace, automotive, medical, etc., depends on the high surface quality, accuracy and productivity of the conventional machining processes. Researchers in academia and industries have increased their effort in enhancing the quality and productivity of the components, seeking sustainability in terms of environmental impact, manufacturing cost and resource consumption [139]. Modelling of the machining processes helps in optimizing the process parameters and predicting the responses such as machining forces, chip geometries, power consumption, tool wear and surface integrity. Different types of modelling approaches such as empirical, analytical, mechanistic, numerical and artificial intelligence, are being used for predicting the responses. Advances in cutting technology have changed the interest in predictive machining modelling. In the early days, tool wear was of utmost importance but nowadays the interest has shifted to heat generation, accuracy of the surface finish and cutting forces etc. Thus, modelling of the conventional machining processes is of significance in digital manufacturing age, enabling the concurrent product design and creating digital twins of the processes.

#### 4.1 Analytical Modelling

The complex mechanics of machining process has been simplified to model the chip formation using various approaches. Such approaches are shear plane [140] and parallel shear zone models [141], slip line field models [142, 143], universal slip line field models [144-146], etc. Using them, different machining responses such as cutting forces, tribological conditions, tool wear, chip geometry and surface integrity are predicted. In the present study, the analytical model is developed considering the ultrasonic vibration to predict the machining forces and friction characteristics.

To implement these models in the UAT process, a combination of mechanics of metal cutting and kinematics of vibration should be considered. The mechanics of metal cutting includes the effect of cutting speed, feed rate, depth of cut, tool geometries etc. On the other hand, the kinematics of vibration includes the effect of frequency, amplitude, and relative speed between tool and work-piece. The analytical modeling of cutting forces and friction characteristics in the UAT process has been carried out by considering conventional metal cutting theories. As the tool is not in continuous contact with the work-piece, a vibration cycle was considered to analyze the machining responses. The schematic of a single point turning with

ultrasonic vibration is shown in Figure 4.1, in which the tool is vibrating in a cutting velocity direction. The analysis is made assuming the shear zone as a plane. A kinematic is explained in section 2.1 to understand the behavior of UAT process.

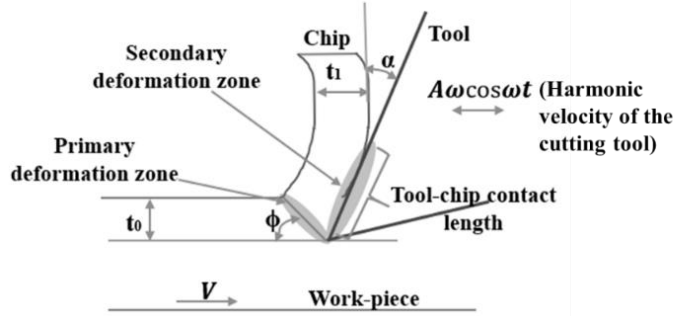


**Figure 4.1** Schematic of UAT process

#### 4.1.1 Kinematics of UAT process

The behaviour of UAT process can be realised by considering a vibration cycle for a given frequency  $F$ . The schematic of tool displacement and velocity for a cycle of vibration is shown in Figure 4.2. The tool vibrates in a cutting velocity direction with a frequency of  $F$ , and amplitude of  $A$ . It comes in contact with the work-piece at time  $t_y$  and disengages at  $t_z$  in the positive half cycle. The phenomenon repeats, and the tool comes in contact with the work-piece again at  $t_{y1}$ . For the entire contact duration, the velocity of the tool continuously decreases.

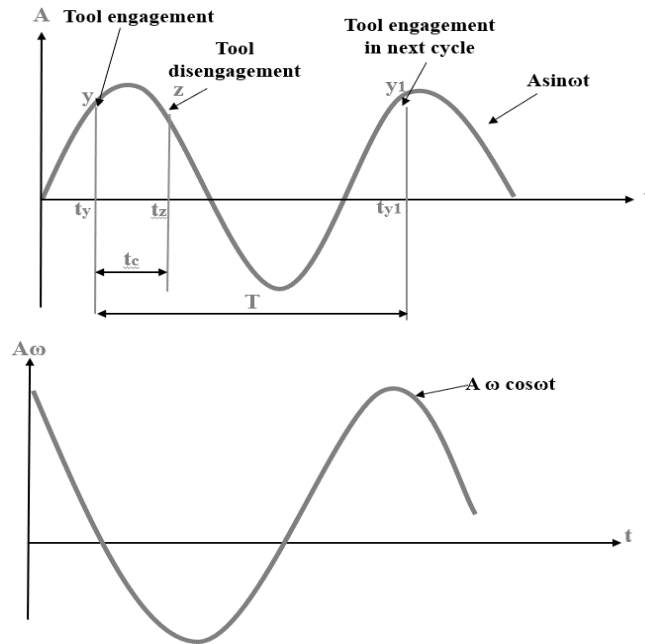


**Figure 4.2** Tool displacement and velocity in UAT process

A displacement of the tool with frequency  $F$  and amplitude  $A$  is given as follow



$$y = A \sin(\omega t) \quad (4.1)$$

Where  $\omega$  is the angular frequency ( $\omega=2\pi F$ ) and  $t$  is time.

The velocity of tool ( $V_t$ ) can be expressed by Eq. (4.2)

$$y' = V_t = A\omega \cos(\omega t) \quad (4.2)$$

The relative cutting velocity between tool and work-piece is described by Eq. (4.3)

$$\begin{aligned} V_R &= V + V_t \\ V_R &= V + A\omega \cos(\omega t) \end{aligned} \quad (4.3)$$

Where  $V$  is the cutting velocity and  $V_R$  is the relative cutting velocity.

The intermittent cutting action is only fulfilled when a  $V$  should be less than a critical cutting velocity ( $V_{cr}$ ) [17, 129]. The separation criteria to achieve UAT is described as follows.

$$V < V_{cr} = \omega A = 2\pi AF \quad (4.4)$$

If the above condition is not satisfied, the cutting action becomes continuous and conventional turning takes place. If a tool vibrates with a maximum cutting velocity ( $2\pi FA$ ) and it disengages with work-piece at a time  $t_z$ , the following expression can be made.

$$V + A\omega \cos(\omega t_z) = 0 \quad (4.5)$$

The tool remains disengaged from the work-piece until the next cycle begins at a time  $t_{y1}$ . The displacement of the tool and work-piece is equal in an interval from  $t_z$  to  $t_{y1}$ . It can be expressed by an Eq. (4.6).

$$A \sin(\omega t_{y1}) - A \sin(\omega t_z) = V(t_{y1} - t_z) \quad (4.6)$$

Where,  $t_{y1} = T + t_y$

In the one cycle of vibration, if the tool remains engaged with the work-piece for time  $t_c$ , then a tool work-piece contact ratio (TWCR) is given by Eq. (4.7) [147].

$$R = \frac{t_c}{T} \quad (4.7)$$

Where  $R$  is TWCR and  $t_c = t_z - t_y$ .

From Eq. (4.5), Eq. (4.6) and Eq. (4.7), the following expression is made [129].

$$\frac{AF}{V} = \frac{1-R}{2\sin(\pi R)\cos\left[\cos^{-1}(-V/\omega A)-\pi R\right]} \quad (4.8)$$

The Eq. (4.8) gives a relation between  $A$ ,  $F$  and  $V$ . It also shows that the  $R$  depends upon all three parameters. It can be said that the value of  $R$  reduces with an increment in  $F$  and  $A$ , whereas it increases with a reduction in  $V$ . In a vibration cycle, effective cutting is taken place from  $t_y$  to  $t_z$ , since the tool is not in contact with work-piece for a duration from  $t_z$  to  $t_{y1}$ . The effective cutting velocity ( $V_{EF}$ ) to analyse the machining responses is divided in two regions, viz. cutting and non-cutting. The effective cutting velocity can be expressed as follows.

$$V_{EF} = \begin{cases} V_R, t_y \leq t \leq t_z \\ 0, t_z < t < t_{y1} \end{cases} \quad (4.9)$$

The  $V_{EF}$  has been considered to analyse the machining responses for a vibration cycle. The analytical modelling of cutting and feed forces and frictional properties has been carried out for a vibration cycle considering contacting and not contacting regions. The material's elasticity has not been considered for chip formation in this study. The conventional machining theories developed by Merchant [148, 149] and Oxley [150] have been used for analytical modelling. A model to predict machining forces and frictional characteristics has been described in a subsequent section.

#### 4.1.2 Prediction of cutting forces

The machining forces are mainly depending upon cutting speed ( $V$ ), feed rate ( $f$ ), depth of cut ( $a$ ), rake angle ( $\alpha$ ), shear angle ( $\phi$ ) and shear strength of work-piece material. The specific cutting energy (SCE) of a work-piece material is primarily affected by the machining forces induced during the machining process. The SCE is consumed in different ways, such as shear energy at the primary zone, frictional energy at the secondary zone, surface energy at the machined surface etc., [151]. The total energy per unit volume (SCE) can be expressed as follows.

$$SCE = \frac{F_{csp}}{at_0} \quad (4.10)$$

Where  $F_{csp}$  is cutting force obtained from SCE,  $a$  is width or depth of cut and  $t_0$  is the thickness of cut. By knowing the SCE,  $a$  and  $t_0$ , the cutting force can be calculated by Eq. (4.11).

$$F_{csp} = SCE \times at_0 \quad (4.11)$$

The values of SCE for different metallic materials have been given in [152], which are generally used to estimate the value of cutting forces.

The relative cutting velocity ( $V_{EF}$ ) estimated by equation (9) is used to determine a value of shear angle ( $\phi$ ). Here, the  $\phi$  is divided based on contacting and non-contacting regions using the following expression:

$$\phi_{EF} = \begin{cases} \phi_c, t_y \leq t \leq t_z \\ \phi_{nc}, t_z \leq t < t_{y1} \end{cases} \quad (4.12)$$

where  $\phi_{EF}$  is the effective shear angle,  $\phi_c$  and  $\phi_{nc}$  are the shear angles at contacting and non-contacting regions, respectively. Toropov and Ko [153] have given a relation to find out the  $\phi$  based on thermo-mechanical properties of the material as follows

$$\phi = \frac{5}{8}\alpha + \frac{1}{2}\cos^{-1}\left[\exp\left(-52.5 \times 10^{-3}\left(\frac{\sigma_{uts}}{100\rho C}\right)^{0.8}\left(\frac{V_{EF}t_0 \times 10^{-3}}{K_t \times 60}\right)^{0.4}\right)\right] \quad (4.13)$$

Where  $\alpha$  is rake angle,  $\sigma_{uts}$  is ultimate tensile strength,  $\rho$  is density,  $C$  is specific heat,  $t_0$  is undeformed chip thickness and  $K_t$  is temperature conductivity. The above equation was used to predict the value of  $\phi$  during contacting and non-contacting regions. The  $\phi$  varies during the contacting regions as the cutting velocity varies whereas, it remains constant during the non-contacting region. The friction angle ( $\beta$ ) associated with both regions can be calculated using Merchant theory [149] as

$$\beta_{EF} = 90 + \alpha - 2\phi_{EF} \quad (4.14)$$

The friction angle is time dependent as the  $\phi_{EF}$  varies with time. The shear force ( $F_{sh}$ ) and shear velocity ( $V_{sh}$ ) are calculated using Eq. (4.15) and Eq. (4.16), respectively.

$$F_{sh} = \frac{F_{csp}(\cos(\phi_{EF} + \beta_{EF} - \alpha))}{\cos(\beta_{EF} - \alpha)} \quad (4.15)$$

$$V_{sh} = \left( \frac{V_{EF} \cos \alpha}{\cos(\phi_{EF} - \alpha)} \right) \quad (4.16)$$

The shear stress required to form the chip ( $\tau_p$ ) is calculated by Eq. (4.17)

$$\tau_p = F_{sh} / A_{sh} \quad (4.17)$$

Where,  $A_{sh}$  is the area of shear stress. A model can determine the shear strain at the primary zone as explained in [154, 155].

$$\gamma_p = \tan(\phi_{EF} - \alpha) + \cot \phi_{EF} \quad (4.18)$$

Oxley and Hastings [156] have determined the shear strain rate distribution on the primary zone using slip line field theory. The average value of the shear strain rate can be determined by Eq. (4.19).

$$\dot{\gamma}_p = \frac{C_1 V_{EF} \sin^2 \phi_{EF}}{\sqrt{3} t_0} \quad (4.19)$$

where,  $C_1$  is constant.

Boothroyd [157] explained the temperature distribution at the machining zones. The average temperature rises at the primary zone ( $\theta_p$ ) can be expressed as

$$\theta_p = \frac{(1-\lambda) V_{sh} F_{sh}}{\rho C V_{EF} t_0 a} \quad (4.20)$$

Where  $\lambda$  is a fraction of heat conducted back to the work-piece,  $C$  is specific heat, and  $\rho$  is the density of work-piece material. It has been found that the fraction  $\lambda$  is a unique function of  $N * \tan \phi$ , where  $N$  is the thermal number that can be determined from Eq. (4.21).

$$N_p = \frac{\rho C V_{EF} t_0}{k} \quad (4.21)$$

Where  $k$  is thermal conductivity. A relation between  $\lambda$  and  $N$  is determined from Boothroyd's experimental graph, as shown in Figure 4.3. It is seen that the  $\lambda$  decreases as the  $N * \tan \phi$  increases. It also shows that the portion of the  $\lambda$  is not less than 50% for very low rate of material removal. Some results obtained by other researchers, from experiments and theory, are also shown in Figure 4.3. It was found that the temperature of the chip is not highly influenced by cutting speed. The value of  $\lambda$  decreases as the cutting speed increases, and it increases the temperature because less heat flows into the work-piece, but the chip temperature tends to remain constant at high speed [156].

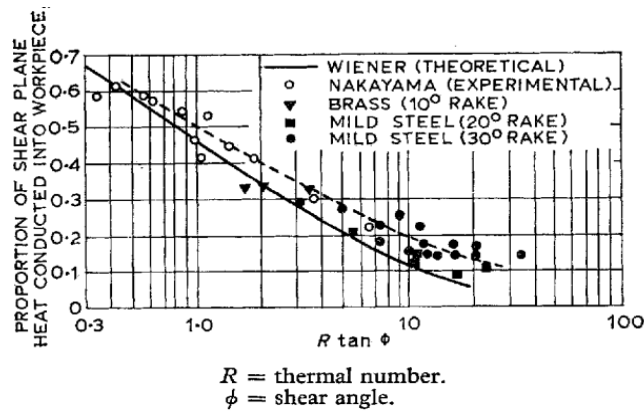


**Figure 4.3** Relation between thermal number and heat conducted back to work-piece [157]

Using the known shear strain, shear strain rate and temperature at the primary zone, the flow stress can be determined using Johnson and Cook model [158], as given in Eq. (4.22).

$$K_p = \left[ A_p + B_p (\gamma_p)^n \right] \left[ 1 + C_p \ln \left( \frac{\dot{\gamma}_p}{\dot{\gamma}_0} \right) \right] \left[ 1 - \left( \frac{\theta_p - T_0}{T_m - T_0} \right)^m \right] \quad (4.22)$$

Where,  $K_p$  is flow stress,  $\gamma_p$  is strain,  $\dot{\gamma}_p$  is the strain rate ( $s^{-1}$ ),  $\dot{\gamma}_0$  is reference strain rate ( $s^{-1}$ ),  $\theta_p$  is the temperature ( $^{\circ}C$ ) at primary zone,  $T_0$  is room temperature,  $T_m$  is the melting temperature of the work-piece material. Coefficient  $A_p$  (Mpa) is the yield strength;  $B_p$  (MPa) is hardening modulus,  $C_p$  is strain rate sensitivity coefficient,  $n$  is the hardening coefficient, and  $m$  is the thermal softening coefficient.

The cutting force ( $F_c$ ) and thrust force ( $F_t$ ) can be obtained by following equations [92],

$$(F_c)_{EF} = \begin{cases} \frac{K_p t_0 a \cos(\beta_{EF} - \alpha)}{\sin(\phi_{EF}) \cos(\phi_{EF} + \beta_{EF} - \alpha)}, & t_y \leq t < t_z \\ 0, & t_z \leq t < t_{y1} \end{cases} \quad (4.23)$$

$$(F_t)_{EF} = \begin{cases} \frac{K_p t_0 a \sin(\beta_{EF} - \alpha)}{\sin(\phi_{EF}) \cos(\phi_{EF} + \beta_{EF} - \alpha)}, & t_y \leq t < t_z \\ 0, & t_z \leq t < t_{y1} \end{cases} \quad (4.24)$$

The cutting force and feed force varies during contacting zone, whereas their value is zero during the non-contacting zone. These machining forces are further used to determine the frictional characteristics, i.e., coefficient of friction and tool-chip contact length at secondary zone or tool-chip interface. The analytical model to determine the friction characteristics is described in section 4.1.3.

#### 4.1.3 Prediction of friction characteristics

The chips slide over the tool's rake face while machining is responsible for the secondary shear zone. The friction-induced at the secondary zone is accountable for the shear angle and friction force produced during machining [159]. The normal and shear stresses induced on the tool rake face during machining are shown in Figure 4.4. Zorev [160] has primarily conveyed the theory to describe a normal and shear stress distribution over the tool's rake face. Roth and Oxley [161] have used slip line field theory to obtain the stress distribution at the tool-chip interface. It was found that the normal stress is maximum at the main cutting edge of the tool, and it progressively goes to zero where the chip separates from the tool. On the other hand, the shear stress is maximum at the tooltip, and gradually, it goes to zero. In this article, dual contact zone theory

has not been considered; however, the analytical modelling for the coefficient of friction ( $\mu$ ) has been carried out by considering the shear and normal stress produced at the tool-chip interface.

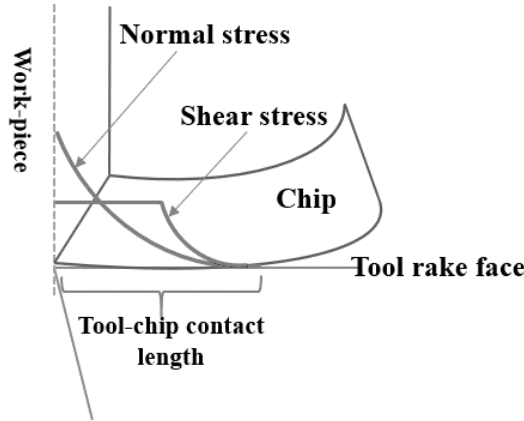


**Figure 4.4** Stresses induced on rake face of the tool during machining

An earlier study to find out the tool-chip contact length ( $L_{tc}$ ) was carried out with slip line field theory by Lee and Shaffer [142]. The model was a function of shear angle ( $\phi$ ), rake angle ( $\alpha$ ) and undeformed chip thickness ( $t_0$ ). It can be expressed as follows [162]

$$L_{tc} = \frac{t_0 \sqrt{2}}{\sin(\phi_{EF}) \sin(45 + \phi_{EF} - \alpha)} \quad (4.25)$$

From Eq. (4.25), it can be said that the thicker the undeformed chip thickness, the larger the tool-chip contact length. Moreover, the smaller the rake angle, the larger the contact length. For the UAT process, the  $L_{tc}$  is a function of time, i.e., contact and non-contact zone in vibration cycle. Bai et al [96] analysed tool-chip contact behaviour by considering the different values of effective cutting velocity during a vibration cycle. Here, the effective value of tool-chip contact length ( $L_{tcef}$ ) is determined by considering the contact and non-contact zone as follows.

$$L_{tcef} = \begin{cases} L_{tc}, & t_y \leq t < t_z \\ 0, & t_z \leq t < t_{y1} \end{cases} \quad (4.26)$$

Next, the chip velocity ( $V_{ch}$ ) and chip thickness ( $t_1$ ) can be calculated by using Eq. (4.27) and Eq. (4.28), respectively [151].

$$V_{chip} = \frac{V_{EF} \sin(\phi_{EF})}{\cos(\phi_{EF} - \alpha)} \quad (4.27)$$

$$t_1 = \frac{t_0 V_{EF}}{V_{chip}} \quad (4.28)$$

Based on the chip thickness, the empirical relation to find out secondary shear zone thickness ( $t_{ss}$ ) can be expressed as follows [150, 163]

$$t_{ss} = 0.049t_1 \quad (4.29)$$

Guo [164] determined shear strain and shear strain rate at the secondary shear zone by using Eq. (4.30) and Eq. (4.31), respectively.

$$\gamma_s = \frac{0.5L_{tef}}{\sqrt{3}t_1} \quad (4.30)$$

$$\dot{\gamma}_s = \frac{V_{chip}}{L_{tef}} \quad (4.31)$$

Based on temperature generation at primary zone, tool-chip contact length, and chip thickness, Boothroyd [157] has given a relation to find the temperature ( $\theta_s$ ) at the secondary zone as follows.

$$\theta_s = 1.13\theta_p \frac{L_{tef}}{t_1} \quad (4.32)$$

Knowing the shear strain, the shear strain rate and the temperature at the secondary zone, the flow stress can be determined using Johnson and Cook as follows [158].

$$K_s = \left[ A_p + B_p (\gamma_s)^n \right] \left[ 1 + C_p \ln \left( \frac{\dot{\gamma}_s}{\dot{\gamma}_0} \right) \right] \left[ 1 - \left( \frac{\theta_s - T_0}{T_m - T_0} \right)^m \right] \quad (4.33)$$

Moufki et al [165] has formulated the normal stress distribution along the secondary shear zone ( $\sigma_s$ ) considering the shear stress. The mathematical expression for  $\sigma_s$  is as follows.

$$\sigma_s = K_s \frac{t_1 (\xi - 1)}{t_{ss} \sin(\phi_{EF}) \cos(\phi_{EF} + \beta_{EF} - \alpha)} \frac{\cos(\beta_{EF})}{\cos(\phi_{EF} + \beta_{EF} - \alpha)} \quad (4.34)$$

Where  $\xi$  is stress distribution characteristics at the secondary zone. The value of  $\xi$  is assumed to be 2 [166].

The normal force ( $F_{sn}$ ) and friction force ( $F_{sf}$ ) on the secondary zone can be calculated based on a model developed by Ozlu et al. [167]

$$F_{sn} = \frac{\sigma_s a L_{tef}}{\xi + 1} \quad (4.35)$$

$$F_{sf} = F_{sn} \tan(\beta_{EF}) \quad (4.36)$$

The coefficient of friction ( $\mu$ ) is the ratio of friction force ( $F_{sf}$ ) to normal force ( $F_{sn}$ ) which can express as,

$$\mu = F_{sf} / F_{sn} \quad (4.37)$$

For finding out the machining forces and friction characteristics analytically, an iterative scheme was employed in MatLab. The modelling was carried out by considering one vibration cycle. The time for contact and non-contact zone were calculated. The machining forces for the contact zone were determined by iterating specific cutting energy (SCE) values for the given input conditions. The cutting force calculated using SCE and JC flow stress model was compared for a particular value of SCE. If the absolute difference between the cutting forces calculated by each method was less than 10%, it was taken as a final value. The flow chart of the analytical modelling is shown in Figure 4.5.

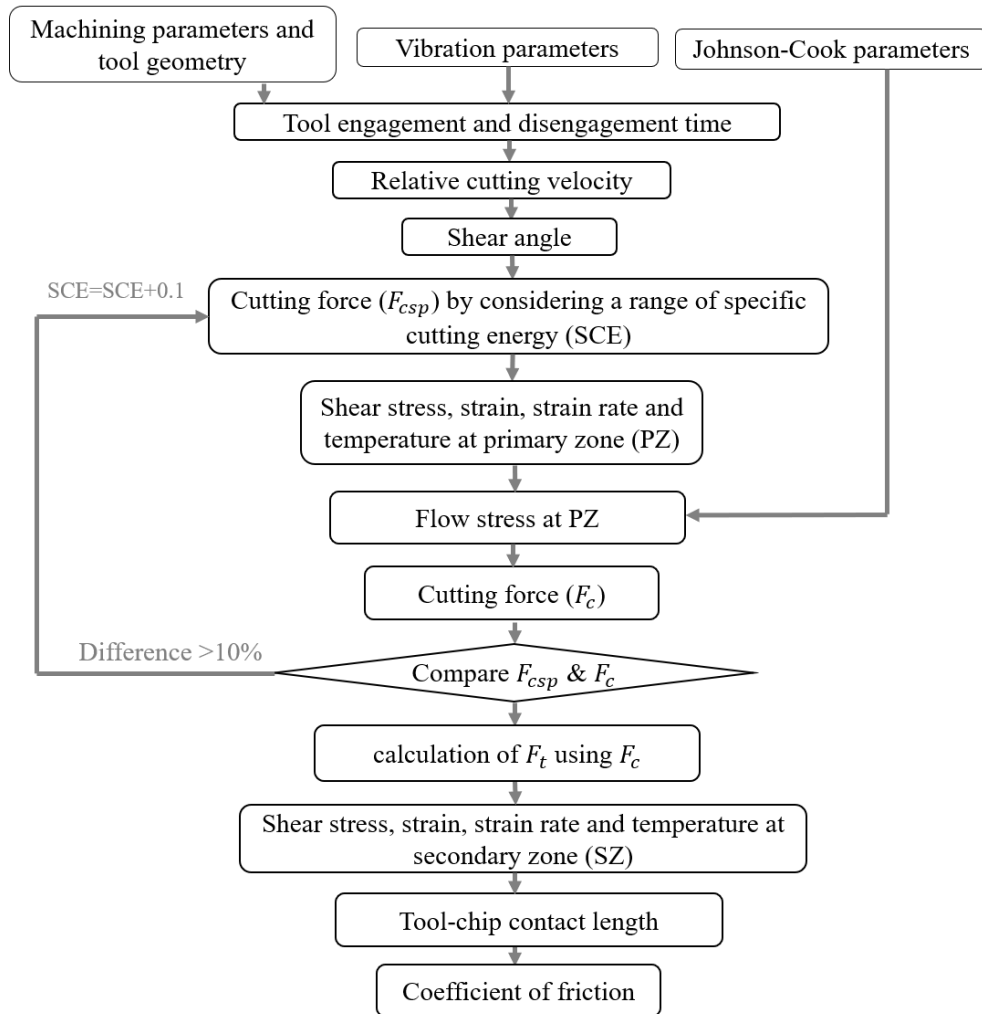


**Figure 4.5** Flow chart for analytical modelling of machining forces and friction characteristics



#### 4.1.4 Results of analytical modeling

The results for TWCR and maximum shear angle obtained from the analytical modeling are described in this section. Theoretically, in ultrasonic-assisted turning, the shear angle value does not remain constant during the engagement period. The values of shear angle during the engagement period are calculated using Eq. (4.13), and the maximum value of the shear angle is taken for analysis purpose. These values have been considered for different frequencies and amplitudes. A variation in TWCR and max. shear angle with frequencies is shown in Figure 4.6(a) and Figure 4.6(b), respectively. It can be seen that as the frequency increases, TWCR decreases and max. shear angle increases. This is attributed to a reduction in engagement time of tool and workpiece at higher values of frequencies. As the frequency increases, the engagement time decreases, reducing the TWCR and increasing the shear angle. On the other hand, as the frequency decreases, the cutting action of UAT tends to appear as a CT, increasing the TWCR and reducing the shear angle. The slope of TWCR and max shear angle reduces at higher values of frequency. It means that the effect of UAT process is higher when the frequency is approximately in the range of 10-20 kHz. A similar result for a variation of TWCR with frequency is given by Nath et al. [147].

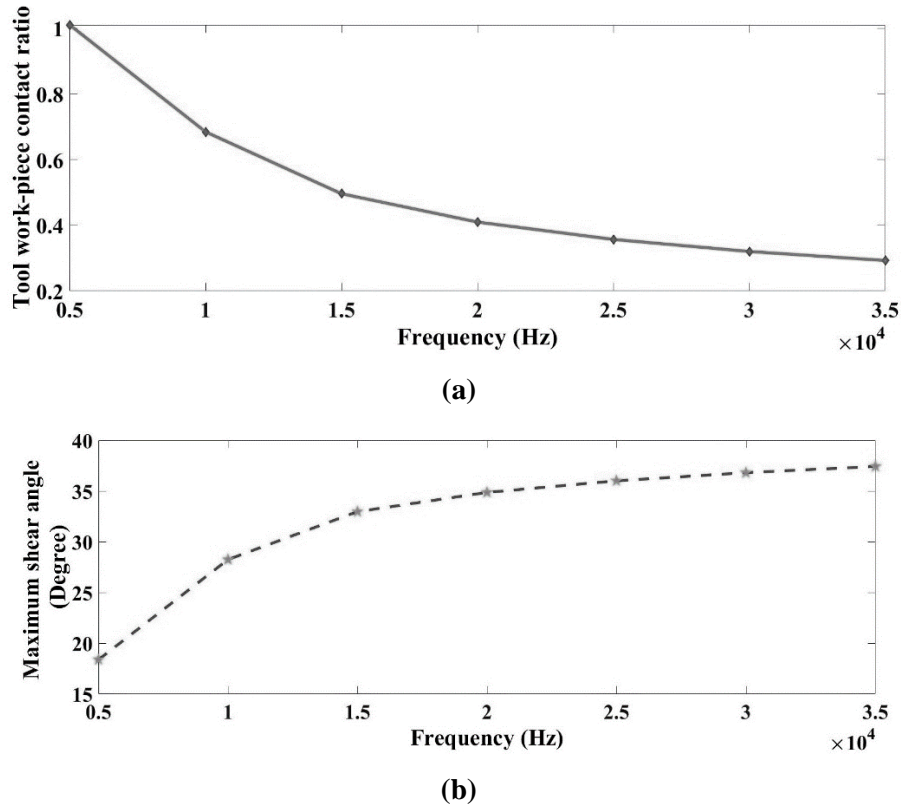


**Figure 4.6** Variation in (a) TWCR and (b) maximum shear angle with frequencies ( $A=10\mu\text{m}$ )

A variation in TWCR and max. shear angle with amplitudes is shown in Figure 4.7(a) and Figure 4.7(b), respectively. It can be seen that as the amplitude increases, TWCR decreases

and max. shear angle increases. This is due to a reduction in engagement time of tool and workpiece at higher amplitudes. As the amplitude increases, the engagement time decreases, reducing the TWCR and increasing the shear angle. On the other hand, as the amplitude decreases, the cutting action of UAT appears as a CT, which increases the TWCR and reduces the shear angle. The slope of TWCR and max shear angle reduces at higher amplitudes. It means that the effect of UAT process is higher when the amplitude is approximately in the range of 10-20  $\mu\text{m}$ .

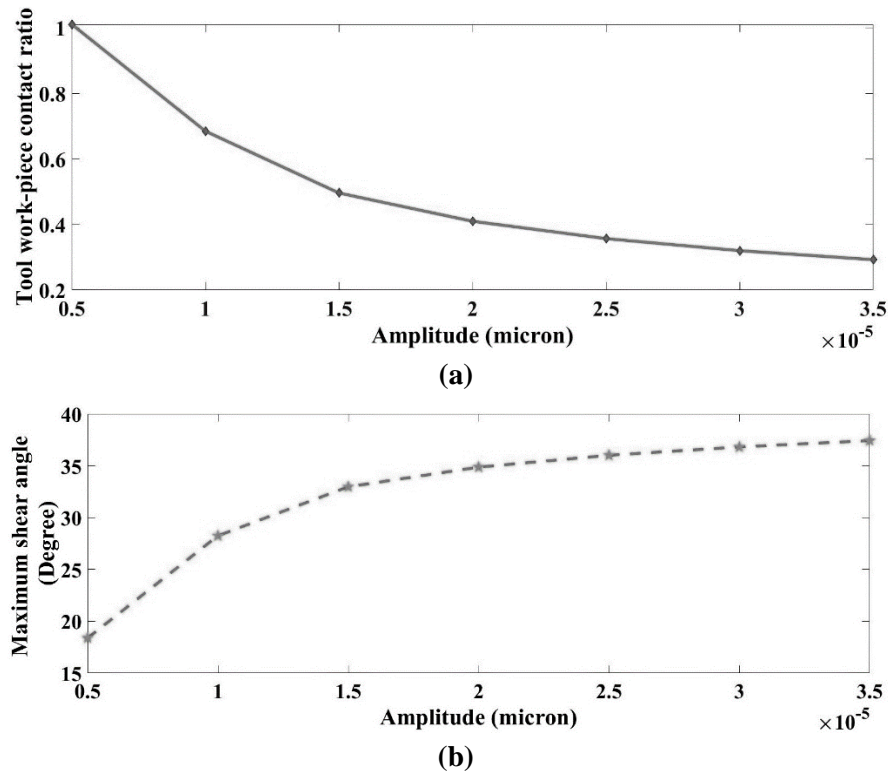


**Figure 4.7** Variation in (a) TWCR and (b) maximum shear angle with amplitudes ( $F=20$  kHz)

From the above results for TWCR and maximum shear angle, the UAT process's performance can be enhanced by maintaining an optimum value of frequency and amplitude. Moreover, the value of the shear angle depends upon the value of TWCR for a given frequency and amplitude. It is seen that the performance of machining increases with an increase in shear angle as it reduces the machining forces by lowering the friction at the tool-chip interface [17].

#### 4.1.5 Experimental validation of the model

An experimental analysis has been carried out to validate the developed analytical model. An in-house developed UAT setup (Figure 3.11) was used to carry out the experiments. The experiments have been carried out by using different process parameters, as shown in Table 4.1. Tool geometry, depth of cut ( $a$ ), frequency of vibration and amplitude are taken as constants, whereas cutting speed and feed rate are varied. Three different values of cutting speed

and feed rate are considered for experimentation of CT and UAT process. A SS304 is taken as a workpiece material. The physical properties and JC constants of SS304 used for analytical modelling are given in Table 4.2. The insert was of CVD coated WC with a layer of TiCN, Al<sub>2</sub>O<sub>3</sub> and TiN. The CVD coated grade provides a good combination of wear resistance and toughness for turning steel workpieces.

**Table 4.1** Input process parameters for experimentation

Parameter	Specification
Workpiece material	SS 304 steel
Tool	Coated WC
Coating	TiCN-Al <sub>2</sub> O <sub>3</sub> -TiN
Rake angle (°)	5
Horn material	Al 7075
Input/Output diameter of horn (mm)	40/25
Radius of horn (mm)	10
Cutting speed (m/min)	30, 50, 70
Feed rate (mm/rev)	0.1,0.2,0.3
Depth of cut (mm)	0.2
Frequency (Hz)	20,000
Amplitudes (μm)	10
Machining condition	Dry

**Table 4.2** Johnson-cook and thermo-mechanical constant of SS304 steel [153, 41]

Properties	A (Mpa)	B (Mpa)	C	n	m	$\dot{\epsilon}_0$ (s <sup>-1</sup> )	UTS (Mpa)	$\rho$ (Kg/ m <sup>3</sup> )	$K_t^{*10^{-6}}$ (m <sup>2</sup> /s)	Specific cutting energy (J/Kg °C)
Value	310	1000	0.07	0.65	1	1	837	7800	5.07	2-5

The cutting force and thrust force-induced during machining are measured by a dynamometer (make: Kistler, Model: 9121). For validation purposes, average values of cutting and thrust forces have been considered. The coefficient of friction at the tool-chip interface is calculated by using merchant theory as follows [141].

$$\mu_e = \frac{F_{te} + F_{ce} \tan \alpha}{F_{ce} - F_{te} \tan \alpha} \quad (4.38)$$

Where,  $\mu_e$ ,  $F_{ce}$ ,  $F_{te}$  are the coefficients of friction, cutting force and thrust force obtained from experiments.

The tool-chip contact length was measured using an optical microscope (Make: Dino-lite, Model: AM4515). The rake face of the tool was examined for any apparent alteration which defines the tool-chip contact length. The experiments were repeated twice, and the average values have been considered for comparison purposes.

#### ***4.1.5.1 Variation in cutting force***

The values of cutting force obtained from the analytical model are compared with the experimental values, as shown in Figure 4.8. The variation in cutting force with cutting speed at a constant feed rate (0.1mm/rev) is shown in Figure 4.8(a). It can be seen that at a higher cutting speed, cutting forces obtained from the analytical model are a bit higher in UAT, whereas they are comparatively lesser in CT. The results are not showing a significant difference in cutting force at a lower cutting speed (30m/min). It may be due to the ultrasonic softening effect. The flow stress of the material decreases with the application of ultrasonic vibration. This reduction in flow stress is termed as ultrasonic softening effect [169]. have shown that due to ultrasonic softening, the flow stresses reduce and the cutting forces decrease. The ultrasonic softening effect has not been considered in the developed model. As the cutting speed increases, the cutting force increases in CT whereas, it decreases in UAT. In the CT, it is observed that the SS 304 forms a built-up edge during machining at cutting speed lower than 60 m/min [155], and leading to enhanced cutting forces in the CT. On the other hand, in the UAT, as the cutting action is intermittent, the tendency of built-up edge reduces, decreasing the cutting forces. In UAT, at a higher cutting speed, the TWCR increases, which increases the cutting force [147]. Moreover, under the action of ultrasonic vibration, the friction at the tool-chip interface reduces, which increases the shear angle resulting in a lower cutting force. It can also be seen that the cutting forces are higher in CT compared to UAT due to the intermittent cutting nature of the UAT. An approximate error in the cutting forces is 1-10% for CT, and 2-15% for UAT for the given range of the cutting speed.

The variation in cutting force with feed rate at a constant cutting speed (50 m/min) is shown in Figure 4.8(b). It can be observed that the results obtained from analytical modelling are in good agreement with the results obtained from the experiment in UAT, whereas the results somehow differ in CT. The cutting force obtained from the experiment in CT is higher compared to theoretically obtained values. It may be attributed to the material anisotropy that increases the cutting force during experiments. The cutting force increases with the feed rate in both the processes due to an increase in the uncut chip thickness, which requires a higher cutting force to remove the material at a higher feed rate. Due to the repetitive cutting action of UAT, the

cutting force obtained from the experiments is lesser as compared to that of CT. An approximate error in the cutting forces is 14-17% in CT, and 6-7% for UAT for the given range of the feed rate.

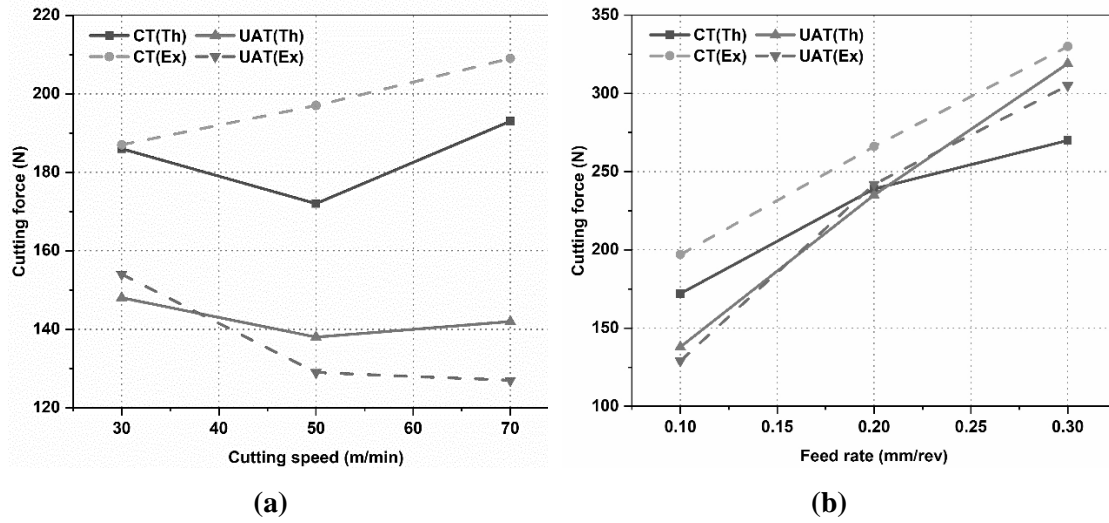


**Figure 4.8** Variation in cutting force with (a) cutting speed at a feed rate of 0.1 mm/rev and (b) feed rate at a cutting speed of 50 m/min (Th: Theoretical, Ex: Experimental)

#### 4.1.5.2 Variation in thrust force

The values of thrust force obtained from the analytical model are compared with the experimental values, as shown in Figure 4.9. The variation in thrust force with cutting speed at a constant feed rate (0.1mm/rev) is shown in Figure 4.9(a). It can be seen that the nature of the thrust force obtained from experiments in UAT and CT is almost similar. It first increases and then decreases with cutting speed. It is observed that when the cutting speed increases from 30 m/min to 50 m/min, the built-up edge formation takes place, which increases the thrust force. On the other hand, when the cutting speed increases from 50 m/min to 70 m/min, the built-up edge reduces, which decreases the thrust force [17]. The built-up edge is not severe in UAT due to its intermittent cutting characteristics. The thrust force is lower in UAT than in CT at a lower feed rate whereas, it is higher in UAT at a higher feed rate. It is attributed to the lower value of TWCR at a lower cutting speed which reduces the thrust force. But at a higher speed, the cutting action in UAT replicates the cutting action in CT, which increases the thrust forces. An approximate error in the values of thrust forces is 5-20% in CT, and 10-15% in UAT for the given range of the cutting speed.

The variation in thrust force with feed rate at a constant cutting speed (50 m/min) is shown in Figure 4.9(b). It can be observed that the results obtained from the model follow the same trend as the results obtained from experiments. As the feed rate increases, the thrust force increases for both the processes due to an increase in uncut chip thickness, which requires higher

force at a higher feed rate. The thrust force is lesser in UAT than CT due to the higher shear angle, reducing the thrust force in UAT. An approximate error in thrust force values is 5-15% in CT, and 15-20% in UAT for the given range of the feed rate.

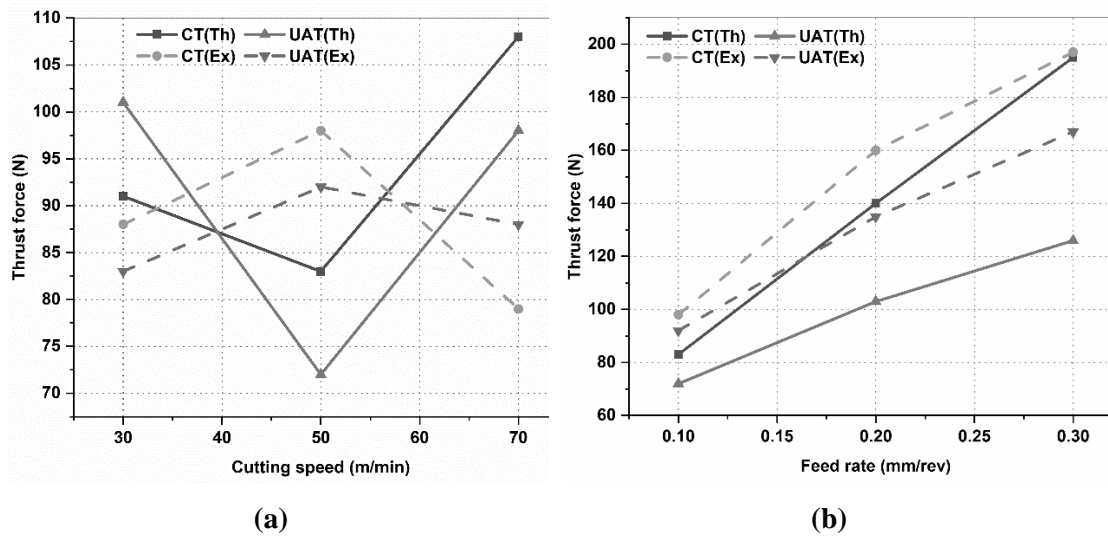


**Figure 4.9** Variation in thrust force with (a) cutting speed at a feed rate of 0.1 mm/rev and (b) feed rate at a cutting speed of 50 m/min (Th: Theoretical, Ex: Experimental)

#### 4.1.5.3 Variation in friction coefficient

The values of coefficient of friction ( $\mu$ ) for different cutting speeds and feed rates obtained from the analytical model are compared with the experimental values, as shown in Figure 4.10. The variation in  $\mu$  with cutting speed at a constant feed rate (0.1 mm/rev) is shown in Figure 4.10(a). It can be observed that the difference between  $\mu$  obtained from experiments and model is higher in CT, whereas it is lesser in UAT. The value of  $\mu$  obtained from the model is higher than the value obtained from the experiment for both machining conditions. As the cutting speed increases, the  $\mu$  decreases due to a reduction in friction force at a higher cutting speed. Moreover, the thermal softening of workpiece also takes place at a higher cutting speed reducing the forces and resulting in a lesser  $\mu$  [16]. The results also show that the values of  $\mu$  obtained from experiments are lesser in CT compared to UAT. It would be due to tool edge wear by a cyclic motion of the tool, which increases the friction between tool and chip. An approximate error in  $\mu$  is 17-25% in CT, and 7-13% in UAT for the given range of the cutting speed.

The variation in  $\mu$  with feed rate at a constant cutting speed (50 m/min) is shown in Figure 4.10(b). It is seen that the difference between the  $\mu$  obtained from the experiment and model is higher at a low feed rate in CT, whereas it is lesser in UAT. As the feed rate increases, the difference reduces in CT and increases in UAT. The  $\mu$  obtained from experiments initially increases with feed rate and decreases with a further increase in feed rate. The variation can be

explained with the help of chip thickness. The uncut chip thickness increases with an increase in the feed rate, which increases the force required to remove the material and results in a higher value of  $\mu$  in CT. On the other hand, the ultrasonic softening effect in UAT reduces material hardness and forces, reducing friction at tool-chip contact. It can be noted that the  $\mu$  is lesser in UAT compared to in CT. An approximate error in the  $\mu$  is 5-22% in CT and 5-20% in UAT for the given range of the feed rate.

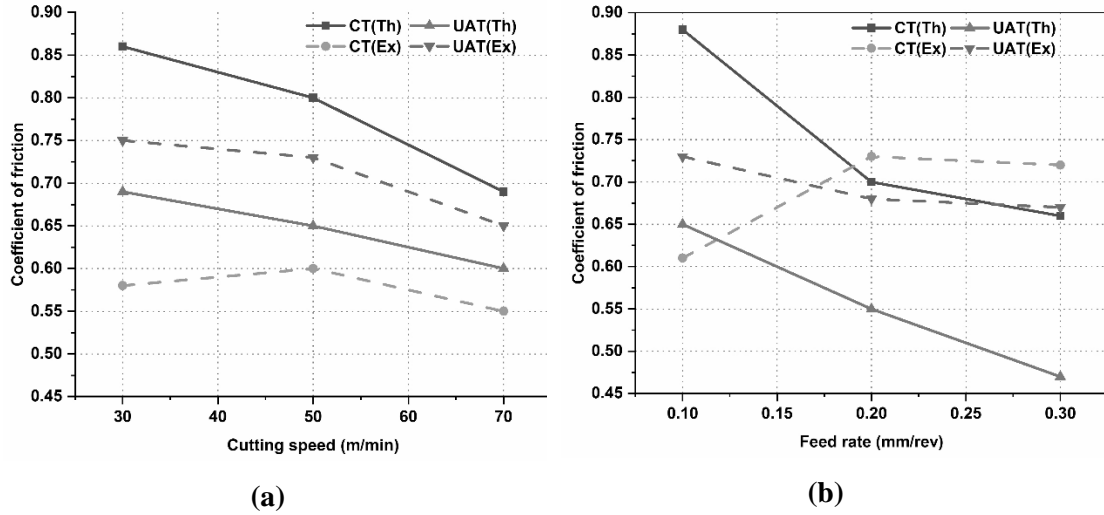


**Figure 4.10** Variation in coefficient of friction with (a) cutting speed at a feed rate of 0.1 mm/rev and (b) feed rate at a cutting speed of 50 m/min

#### 4.1.5.4 Variation in tool-chip contact length

The values of tool-chip contact length ( $L_c$ ) obtained from the analytical model are compared with the experimental values as shown in Figure 4.11. The variation in  $L_c$  with cutting speed at a constant feed rate (0.1 mm/rev) is shown in Figure 4.11(a). It can be seen that the  $L_c$  obtained from the experiment differs much from the modelling of the CT at lower cutting speed, whereas the difference reduces with increasing speed. For the UAT, the  $L_c$  obtained from the experiment is in close agreement with the values obtained from the model. The  $L_c$  obtained from the model is higher than that of the experiments in CT, whereas it is lower in UAT. As the cutting speed increases, the  $L_c$  decreases due to an increase in shear angle [162]. The results show that the  $L_c$  increases with the cutting speed in CT process. It may be attributed to the tool-wear at a higher cutting speed which increases the  $L_c$ . It can be observed that the  $L_c$  is lower in UAT compared to in CT due to the cyclic motion of the tool, which reduces the contact between chip and tool. An approximate error in the values  $L_c$  is 16-20% in CT and 13-20% in UAT for the given range of the cutting speed.

The variation in  $L_c$  with feed rate, at a constant cutting speed (50 m/min), is shown in Figure 4.11(b). It is observed that the difference between the values of  $L_c$  obtained from

experiments and model is higher in CT, whereas it is not significant in UAT. As the feed rate increases, the  $L_c$  increases due to a higher value of uncut-chip thickness at a higher feed rate. The values of  $L_c$  obtained from experiments are lower in CT compared to UAT. This may be attributed to the tool wear that happens due to its repetitive contact with workpiece, which increases the contact between tool and chip. However, the difference between the  $L_c$  obtained from the experiment in UAT and CT is not significant. An approximate error in the  $L_c$  is 20-25% in CT and 15-20% in UAT for the given range of the feed rate.

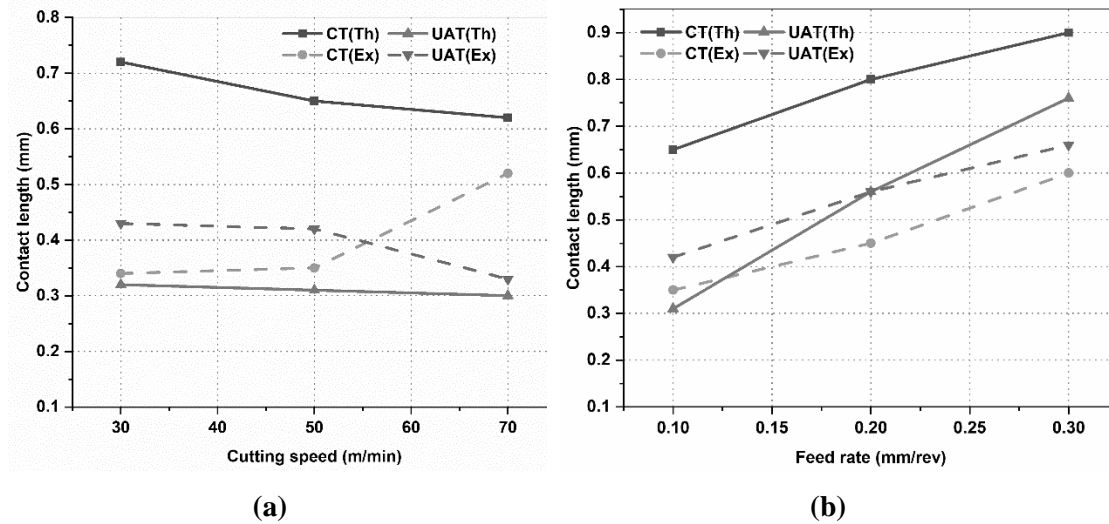


**Figure 4.11** Variation in tool-chip contact length with (a) cutting speed at a feed rate of 0.1 mm/rev and (b) feed rate at a cutting speed of 50 m/min

#### 4.1.6 Conclusions for analytical modeling

The analytical model was developed to obtain the output responses in terms of cutting force, thrust force, coefficient of friction and tool-chip contact length for UAT and CT processes. The experiments were carried out at different cutting speeds and feed rates using SS304 stainless steel for validation. The results obtained from the model are compared with the results obtained from the experiments. The following conclusions can be made from the comparisons:

- The shear angle increases and the TWCR decreases, with increasing frequency and amplitude of the vibrations.
- The cutting forces obtained from the model and experiments are in good agreement with an approximate error of 1-17% for CT and 2-15% for UAT for different cutting speeds and feed rates. The cutting forces are lower for the UAT compared to the CT process due to the cyclic nature of the tool.



- The thrust forces obtained from the model and the experiments are in close agreement with an approximate error of 5-20% for CT and 10-20% for UAT for different cutting speeds and feed rates. The thrust forces are lower for the UAT compared to the CT process.
- The coefficient of friction obtained from the model and experiments are in close agreement with an approximate error of 5-22% for CT and 5-20% for UAT for different cutting speeds and feed rates. The difference is higher for CT compared to UAT, at different cutting speeds. It is also seen that the coefficient of friction obtained from experiments is lesser for CT compared to UAT due to tool edge wear in a cyclic motion of the tool, increasing the friction between the tool and the chip.
- An approximate error in the tool-chip contact length obtained from the model and experiments is higher compared to other output responses. It is around 16-25% for CT and 13-20% for UAT for different cutting speeds and feed rates.

The model developed to predict output responses show a very good agreement at a lower value of cutting speed and feed rate. As the cutting speed and feed rate increase, the error also increases. It may be due to the parameters such as material anisotropy, ultrasonic softening effect, constant values of material properties, etc. The error can be minimised by incorporating those parameters.

## 4.2 Finite Element Modelling

The finite element method (FEM) is the most used simulation technique employed for solving the problems for the various manufacturing processes such as machining, forging, abrasive processes, etc. In the FEM, a continuum body is replaced by finite elements. The FEM includes the formulation of the model, generation of mesh, determination of boundary conditions, etc. [170]. Problems in metal cutting processes are dynamic and non-linear and need heat and stress analysis considering material microstructure, friction, cutting fluid action, etc. It is noted that the FEM of the machining process could predict machining forces, stress, strain, temperature, tool wear etc.

### 4.2.1 Development of the model

The FEM for UAT is carried out using DEFORM 3D, a commercial finite element software. Models used for the workpiece and tool are revealed in Figure 4.12. X, Y and Z are in the direction of depth of cut ( $a_p$ ), cutting speed ( $V$ ) and feed ( $F$ ), respectively. A Lagrangian implicit approach is used to simulate chip formation and re-meshing criteria. As shown in Table

1, two sets of cutting parameters are considered for machining. The tool is supposed to be rigid, and the workpiece is plastic. The cutting tool has a nose radius of 0.4 mm, a rake angle of  $0^\circ$  and a relief angle of  $5^\circ$ . The cylindrical workpiece, in general, is considered rectangular for FEM simulation, and hence the dimension of the workpiece in this work is taken as 10 mm x 5 mm x 3 mm. An uncut chip thickness ( $t_0$ ) is considered equal to the feed for each set of process parameters. The three-node triangular, thermally coupled elements are used for both tool and workpiece. The number of elements for the tool is taken as 12000 whereas, for the workpiece, it is 30000. The mesh density for the tool and workpiece is non-identical and non-uniform as a high-density mesh is required on the shear zone of the workpiece where a large plastic deformation occurs [171]. The element size is smaller at the contact zone where the chip formation occurs. It is larger on the remaining parts. The element edge length is  $12\text{ }\mu\text{m}$  which is much smaller than the uncut chip thickness. The simulation time was set to 0.01 s.

**Table 4.3** Input process parameters used for FEM

Set 1	$V = 30\text{ m/min}$ , $a_p = 0.4\text{ mm}$ , $F = 0.2\text{ mm/rev}$
Set 2	$V = 70\text{ m/min}$ , $a_p = 0.2\text{ mm}$ , $F = 0.1\text{ mm/rev}$
Cutting condition	CT, UAT, HUAT
Frequency	20 kHz
Amplitude	$10\text{ }\mu\text{m}$
Temperature	$200^\circ\text{C}$ for HUAT
Room temperature	$25^\circ\text{C}$

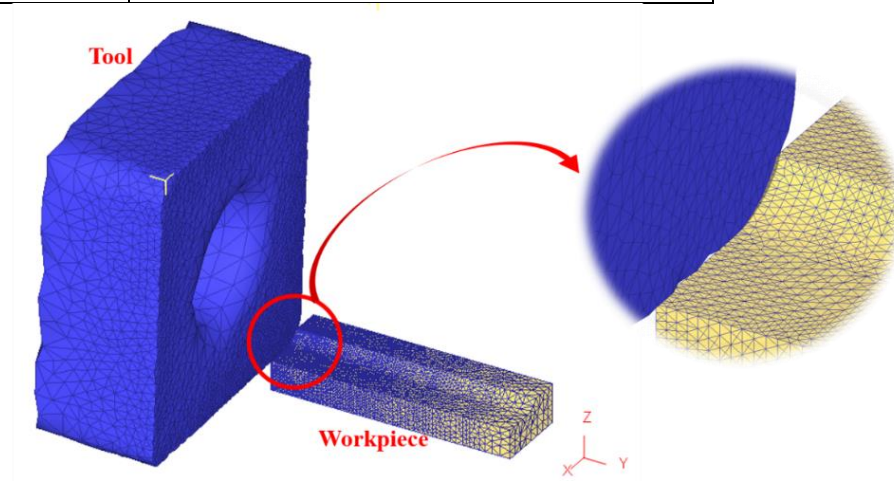


**Figure 4.12** Finite element model of the tool and workpiece

#### 4.2.2 Material properties

The machining process involves plastic deformation at large strain and heat generation. The flow stress is involved in the plastic deformation that takes place in the machining operations.

The flow stress is mainly affected by temperature, strain rate, and strain, during the deformation process. Hence, it is needed to use a consistent model to simulate the behavior of the materials during the dynamic condition of machining. In this regard, the Johnson-cook (JC) plasticity model (Eq. 4.22) can be employed to achieve the thermoplastic behavior of the machining process as it simultaneously contemplates the effect of temperature, strain rate, and strain. The flow stress for the material is generally obtained by doing a tensile test at different strain and strain rates. In this work, the workpiece material considered is Nimonic 90. The JC constants used for workpiece material are specified in Table 4.4. The tool material considered is coated tungsten carbide (WC). The coating materials used are TiCN, Al<sub>2</sub>O<sub>3</sub>, and TiN with a coating thickness of 1-4 μm. The properties considered for workpiece and tool materials are presented in Table 4.5. The thermos-mechanical properties used for coating materials are given in Table 4.6. Moreover, to analyse, the damage and chip formation during machining, Cockcroft and Latham model [172] is used, which is given by equation (4.39)

$$\int_0^{\varepsilon_f} \sigma_1 d\varepsilon = D \quad (4.39)$$

where,  $\varepsilon_f$  is effective strain,  $D$  is material constant and  $\sigma_1$  is maximum principal stress. Concerning this criterion, when the integral of maximum principal stress over the plastic strain is equal to damage value  $D$ , the chip segmentation starts, or fractures take place. In this regard, the critical damage value is determined for each element during deformation at each time step [173]. Once the damage value equals the critical damage value, the crack will be initiated.

**Table 4.4** Johnson-cook parameters for Nimonic 90 [174]

Parameters	$A$ (MPa)	$B$ (MPa)	$C$	$n$	$m$
Value	762	1812	0.01	0.5	1

**Table 4.5** Properties considered for FEM

Properties	Workpiece	Tool
Material	Nimonic 90	Tungsten carbide (WC)
Modulus of elasticity (GPa)	215	650
Poisson's ratio	0.3	0.25
Thermal conductivity (W/m °C)	11.5	59
Coefficient of thermal expansion (°C <sup>-1</sup> )	12×10 <sup>-6</sup>	4.98×10 <sup>-6</sup>
Heat capacity (J/°C)	6	15

**Table 4.6** Properties of coating material [175]

Parameters	Coating Materials					
	TiCN		Al <sub>2</sub> O <sub>3</sub>		TiN	
Density (kg/m <sup>3</sup> )	4180		3780		4650	
Elastic modulus (GPa)	448		415		600	
Poisson's ratio	0.23		0.22		0.25	
Heat capacity (N/mm <sup>2</sup> °C)	2.5		3.42		3	
Thermal expansion coefficient (10 <sup>-6</sup> * °C <sup>-1</sup> )	8		8.4		9.4	
Thermal conductivity (W/m °C)	Temp (°C)	Value	Temp (°C)	Value	Temp (°C)	Value
	30	26	30	33	30	20
	100	27	100	28	100	21
	300	28	300	19	300	22
	500	30.5	500	13	500	23.5
	1000	33.5	1000	7	1000	26

#### 4.2.3 Boundary conditions

As appeared in Figure 4.13, boundary conditions related to cutting velocity, preheating temperature, frequency and amplitude are given to the tool and workpiece. Initially, the workpiece is fixed in all three directions, whereas it moves while machining with a cutting velocity  $V$ , which is shown by black arrows at the bottom of the workpiece. The tool vibrates with a harmonic velocity  $V_t$ . An ultrasonic-assisted cutting is attained through a harmonic velocity to the tool provided with a frequency ( $f$ ) of 20 kHz and amplitude ( $a$ ) of 10  $\mu$ m in the direction of the cutting velocity. For the CT process, the  $V_t$  is zero. A velocity applied to the cutting tool is specified by equation (4.40) [17],

$$V_t = a\omega \cos \omega t \quad (4.40)$$

Where,  $\omega$  is the angular frequency,  $V_t$  is harmonic velocity given to the tool,  $a$  is amplitude, and  $t$  is time. To fulfil the ultrasonic cutting action, the  $V$  should be lesser than a critical cutting velocity ( $V_t$ ). Mathematically, it is given by equation (4.41).

$$V < V_t = \omega a = 2\pi af \quad (4.41)$$

Violation of the above condition results in a conventional cutting. In this study, the cutting speeds were considered as 30 m/min and 70 m/min to satisfy equation (4.41).

The area which is far from the processing zone is kept at room temperature ( $T_0$ ). The heat transfer takes place from these areas according to the following equation (4.42) and equation (4.43) [176]

$$q_w = h(T_w - T_0) \quad (4.42)$$

$$q_t = h(T_t - T_0) \quad (4.43)$$

where,  $q_w$  is heat flux at the work-environment interface,  $q_t$  is heat flux at the tool-environment interface,  $h$  ( $20 \text{ W/m}^2 \text{ } ^\circ\text{C}$ ) is heat convection coefficient,  $T_w$  and  $T_t$  are workpiece and tool temperatures respectively. At the processing zone, the heat transfer is determined using equation (4.44):

$$q_p = h_p(T_w - T_t) \quad (4.44)$$

where,  $h_p$  ( $10^5 \text{ W/m}^2 \text{ } ^\circ\text{C}$ ) is heat transfer coefficient at the processing zone. The CT and UAT processes are simulated at room temperature, whereas for the HUAT process, the workpiece is preheated at  $200 \text{ } ^\circ\text{C}$ .

The friction at the tool-chip contact depends upon various parameters such as cutting speed, rake angle, uncut chip thickness, etc. Friction at the secondary contact zone is difficult to estimate. A widely accepted model to simulate friction is to use normal and friction stress. The friction at the tool-chip contact zone is not constant and is a function of friction and normal stress distribution. At the tool-chip contact area, sticking friction occurs, and the friction stress is equivalent to the flow stress at the secondary zone. Conversely, when the sliding friction occurs, the friction stress is determined using the coefficient of friction. The condition of friction at the tool-chip contact zone can be given by equation (4.45a) and equation (4.45b) [177]

$$\tau = m_f \sigma \quad \text{when } \mu \sigma_{nn} \geq \sigma \quad (4.45a)$$

$$\tau = \mu \sigma_{nn} \quad \text{when } \mu \sigma_{nn} < \sigma \quad (4.45b)$$

where,  $\sigma$  is flow stress of work material,  $\tau$  is shear stress, and  $m_f$  is a constant of shear friction and equal to 0.6,  $\sigma_{nn}$  is normal stress and  $\mu$  is the friction coefficient.

There are numerous models to evaluate the tool wear available in the literature. In this study, to simulate the tool wear for the given materials, the Usui's wear law is used, which is given as equation (4.46) [178],

$$\frac{dw}{dt} = c_1 \sigma_n V_s \exp\left(-\frac{c_2}{T_i}\right) \quad (4.46)$$

Where,  $dw/dt$  is the tool wear rate,  $\sigma_n$  is contact normal pressure,  $T_i$  is the temperature at the tool-chip contact zone and  $V_s$  is sliding velocity.  $w$  is crater wear, and,  $c_1$  and  $c_2$  are coefficient. The value of  $c_1$  is  $7.8 \times 10^{-9}$  and  $c_2$  is 2500 K diffusion temperature of WC.

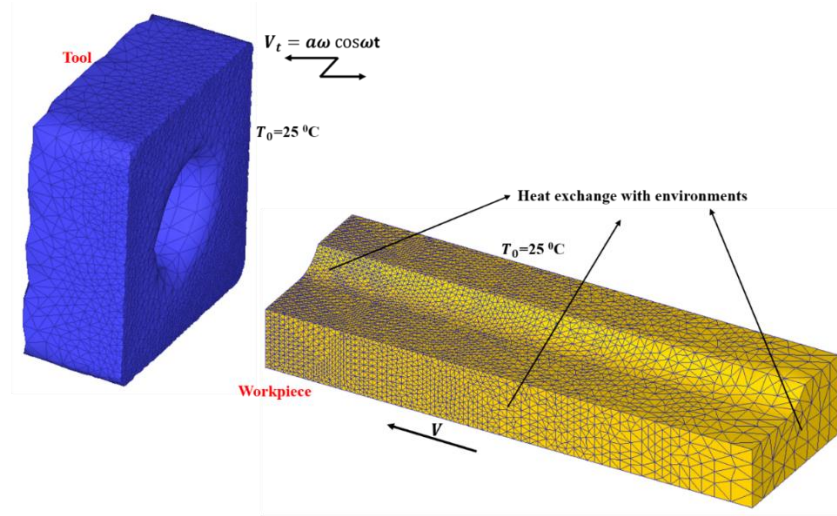


**Figure 4.13** Boundary conditions used for tool and workpiece

#### 4.2.4 Experimental validation

The experiments are performed on a conventional lathe (Figure 4.14(a)), using Nimonic 90 as a workpiece and coated WC as a tool. The cutting tool was CVD coated with a coating of TiCN,  $\text{Al}_2\text{O}_3$  and TiN. The CT, UAT and HUAT are conducted at a given set of process parameters under dry conditions. The HUAT is achieved by preheating the workpiece at  $200^\circ\text{C}$ , as shown in Figure 4.14(b). In the induction heating, the heat source is located in front of tool to heat work-piece material before tool cut the heated part. The high frequency current is used in induction heating. For each set, values of cutting speed, feed and depth of cut are mentioned in Table 4.3. Each experiment is repeated twice to consider the average responses.

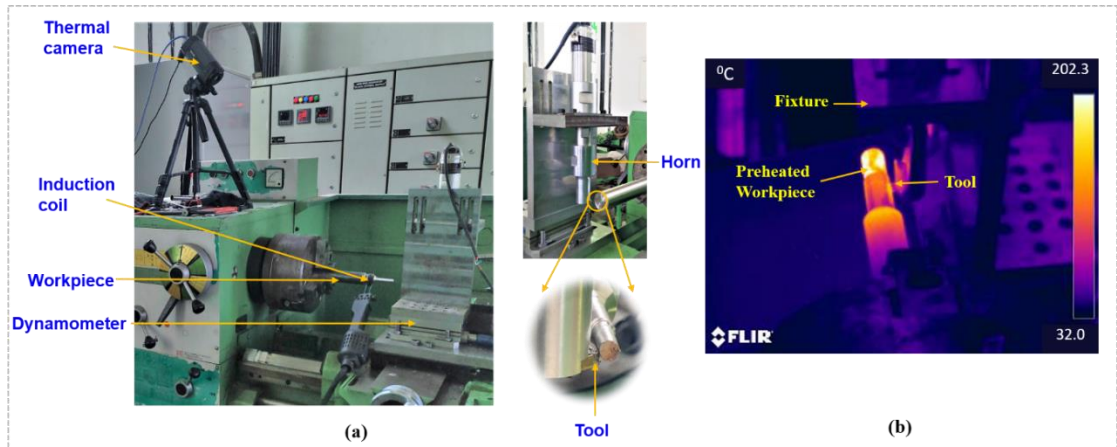


**Figure 4.14** (a) Inhouse developed UAT setup and (b) Workpiece preheated at  $200^\circ\text{C}$  just before HUAT

Experimental outcomes such as tool wear, machining forces and tool-chip contact length are investigated for CT, UAT and HUAT. For the HUAT, the workpiece is heated using an induction coil. The temperature of the workpiece is measured using a thermal camera. A dynamometer is utilized to measure the cutting and feed forces. The worn tools are examined and characterized after each experiment. A scanning electron microscope is employed to examine the morphology of the tool wear. The following criteria are considered to decide the tool wear as specified by ISO 3685:1993 [179]. (1) The average flank wear width ( $VB$ ) is not exceed 0.3 mm, and (2) Sudden deformation of the cutting edge.

#### 4.2.3.1 Tool crater wear

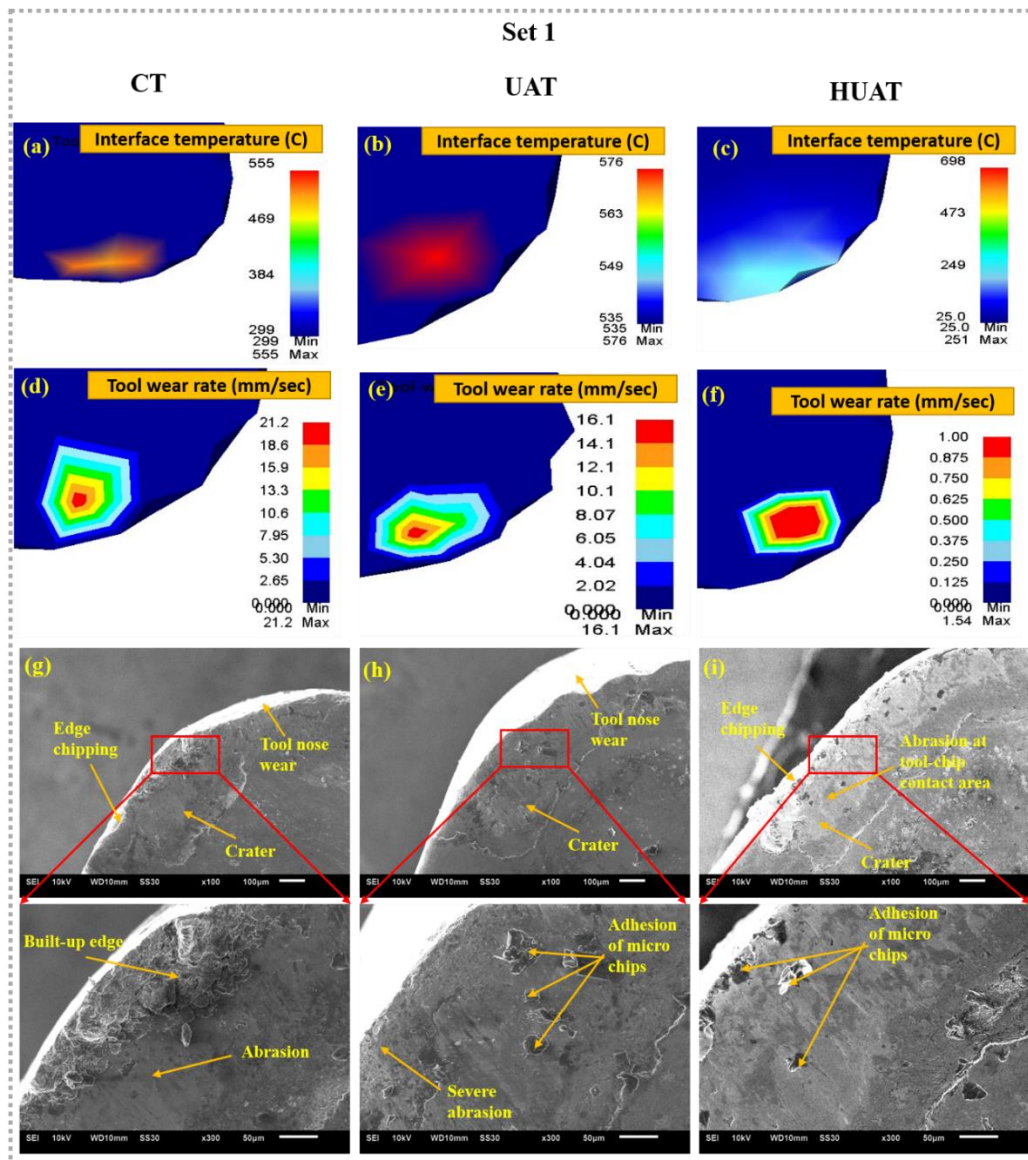


**Figure 4.15** Results of tool crater wear obtained from FEM and experiments at set 1 (30 m/min, 0.2 mm/rev, 0.4 mm)



Tool wear is a critical issue during the machining of superalloys. Here, FEM and experiments for CT, UAT and HUAT of Nimonic 90 are performed. As the wear depth is not possible measure in the FEM, temperature and wear rate are considered to estimate the tool rake face wear. On the other hand, the flank wear is evaluated based on the wear depth and temperature. Moreover, to appreciate the mechanism of tool wear, SEM has been performed, and results of tool wear are compared for all three conditions.

The tool crater wear obtained from experiments and FEM for set 1 is shown in Figure 4.15. As said earlier, the measurement of the crater depth is not possible in the FEM; the tool-chip interface temperature and wear rate are considered for analysis. On the other hand, in the experiment, the morphology of crater wear is taken into consideration. Figure 4.15(a) displays that the temperature at tool-chip contact is the highest in the CT (555 °C), whereas it is lowest in the HUAT (300 °C). The UAT generates slightly higher temperatures than the CT (576 °C), as exposed in Figure 4.15(b). Similarly, it can be realized that the wear rate in the CT is the highest, as revealed in Figure 4.15(d). Alternatively, the HUAT shows the lowest tool wear rate, as shown in Figure 4.15(f). The UAT offers a lower tool wear rate than CT, as given in Figure 4.15(e). From the results of FEM, it can be said that the tool wear is lesser in the HUAT, followed by UAT, whereas the wear is higher in the CT. Similar results are also noted in experiments. Analysing the experimental results, the CT shows edge chipping, tool nose wear, built-up edge (BUE), crater formation and abrasion, as presented in Figure 4.15(g). The BUE is projecting during the machining of Nimonic 90 due to its chemical affinity [180]. During the machining of Nimonic 90, the temperature and pressure at the cutting edge are very high, peeling off the coatings and formation of crater take place. Hard carbide particles in Nimonic 90 sandwiched between tool and chip at higher pressure, causing the abrasion. The UAT suppresses the BUE formation; instead, small microchips adhered to the rake face are observed in Figure 4.15(h). The intermittent cutting action of UAT reduces the formation of BUE by decreasing the pressure at the cutting edge [179]. Alternatively, the cyclic load is applied on the tool nose due to ultrasonic vibration in UAT, leading to deform the tool nose. The size of crater is slightly reducing in UAT compared to CT. The HUAT prevents forming a BUE and lowers the adhesion of microchips, as given in Figure 4.15(i). In the HUAT, simultaneous action of ultrasonic and heating energy lowers the hardness of the workpiece, decreasing the crater wear. However, a small edge chipping and abrasion are noted. Similar results are obtained for induction-assisted machining of Inconel 718 by Choi and Lee [181].

The tool crater wear obtained from experiments and FEM at set 2 are given in Figure 4.16. The interface temperature raises with the cutting speed in all three cases. The maximum interface temperature is observed for CT, whereas, it is lowest for the HUAT. The UAT produces a slightly lower temperature than CT. Furthermore, it is noticed that the tool wear rate



considerably rises as the cutting speed increases. The CT shows the highest tool wear rate, as appeared in Figure 4.16(d). The wear rate is almost similar for UAT and HUAT. At a cutting speed of 70 m/min, tool wear significantly increases although the feed and depth of cut are lower

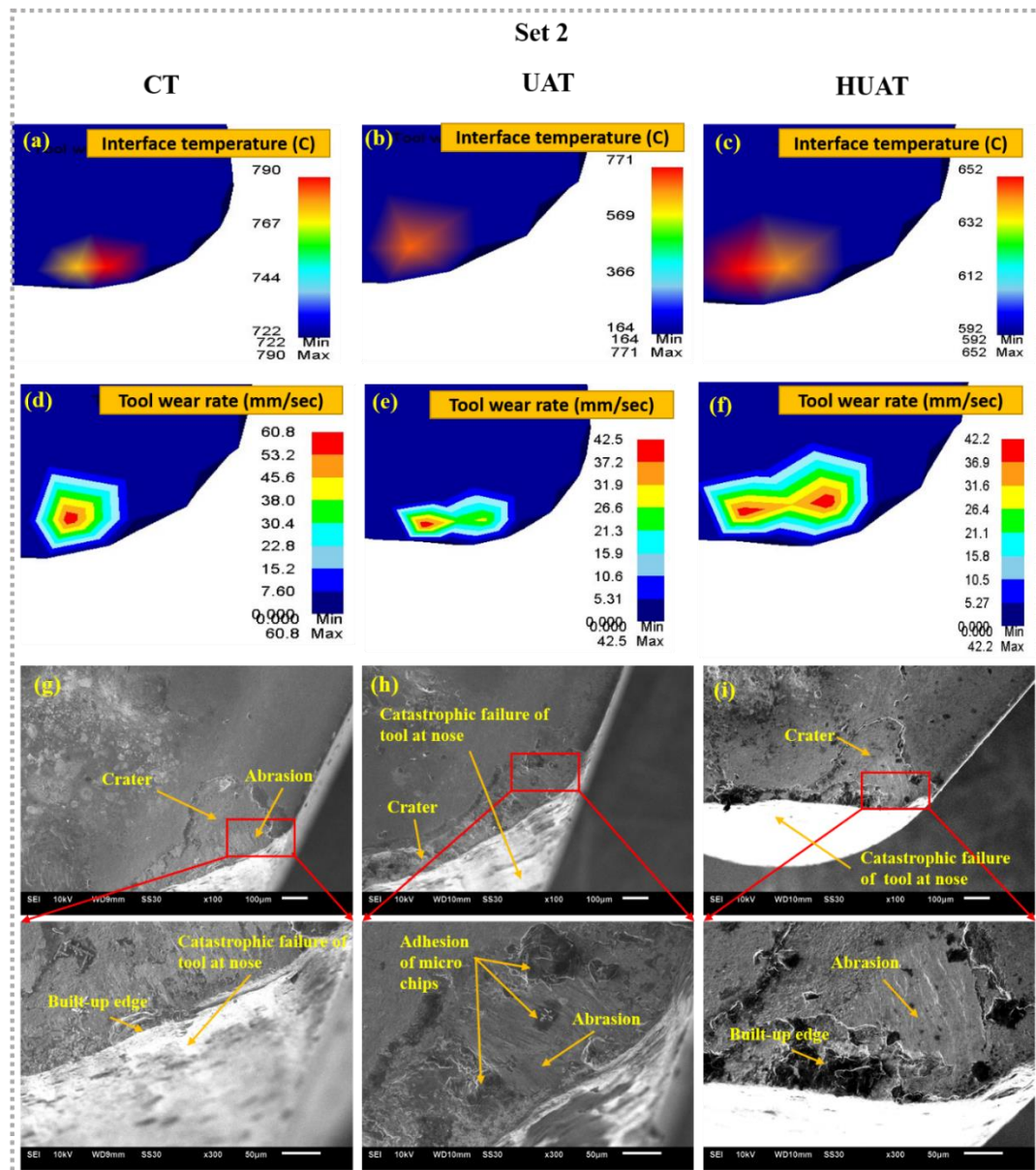


**Figure 4.16** Results of tool crater wear obtained from FEM and experiments at set 2 (70 m/min, 0.1 mm/rev, 0.2 mm)

compared to set 1. The rate of tool wear also increases at higher cutting speed. At a higher cutting speed, chip-tool contact length increases the friction. The CVD coating no longer sustains the stresses imposed on the tool edge, accelerating the tool wear rapidly. Alternatively, in the UAT, at a higher cutting speed, cyclic load acting on the tool also increases, wear out tool rapidly. The HUAT also increases the tool wear rate at the set 2. It can be thought that, the heat reduces the flow stress of the materials, decreasing the wear rate. However, the wear rate in the

HUAT does not much differ from the UAT. The interface temperature is reduced in the HUAT compared to, CT and UAT. A similar trend can also be observed in the results obtained from experiments. As shown in Figure 4.16(g), the CT displays a disastrous failure of the tool nose because of very high pressure and temperature at the tool nose [155]. The WC tool losses the hardness at the temperature above 600 °C, accelerating the tool wear. The BUE formed near the cutting edge is very small. The UAT and the HUAT also show such type of catastrophic failure of tool nose, as exposed in Figure 4.16(h) and Figure 4.16(i), respectively. From FEM results, it can be visualized that the wear rate in all three conditions is much higher even if the machining has been performed only for 0.01 s. In the experiments, machine tool rigidity, vibration, and material anisotropy are also part of tool wear. Even after a sudden failure of the tool nose, a crater is formed in all three conditions. It is observed that during machining of Nimonic 90 the hard carbide particles interrupted between the chip and tool caused the abrasion, forming a crater. Ezugwu et al. [182] has also shown that coated carbide tools fail if Nickel-based superalloys are machined at high cutting speed. In the case of UAT and HUAT, ultrasonic vibration is overlapped with the cutting action of the tool, enhancing the tendency of tool failure. In the case of HUAT, heat cannot be transferred to the shear zone to lower the shear strength of the workpiece, even if the workpiece is preheated. Thus, the tool crater wear does not reduce significantly at a higher cutting speed. Similar observations for a decrease in tool wear for hot turning of manganese steel are obtained by Ozler et al. [183].

#### **4.2.3.2 Tool flank wear**

An average flank wear width ( $VB$ ) obtained from experiments for CT, UAT, and HUAT, and for both the sets are given in the Figure 4.17. The  $VB$  is the highest for the CT, whereas it is the lowest for the HUAT for both the sets. As the cutting speed increases from 30 m/min to 70 m/min, the  $VB$  increases, although the feed and depth of cut are lower for set 2. For set 1, the  $VB$  in the UAT and HUAT is approximately reduced by 13% and 40%, respectively, compared to that in the CT. The CT makes continuous contact between tool and workpiece, increasing friction at the secondary zone, increasing the cutting force and hence the tool wear. Alternatively, in the CT and UAT, intermittent contact lowers the chip-tool contact area and average cutting force imposing the tool, lowering the tool wear. Moreover, the chemical affinity of Nimonic 90 reacts with the tool coating, accelerating the tool wear in the CT.

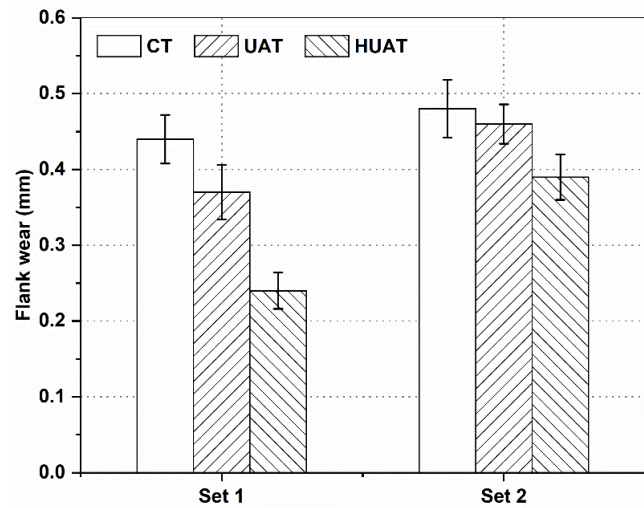


**Figure 4.17** Width of the flank wear obtained for both the sets Experimentally

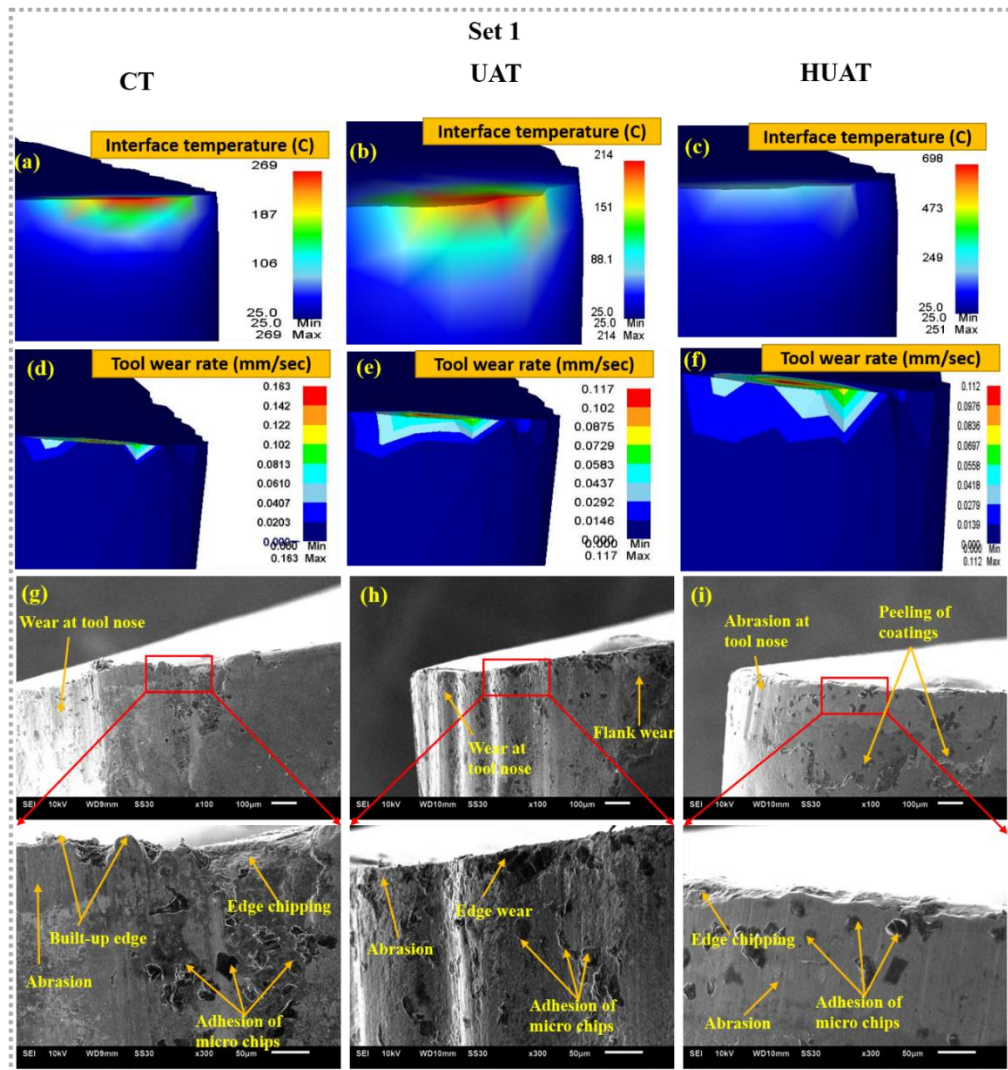


**Figure 4.18** Results of tool flank wear obtained from FEM and experiments at set 1 (30 m/min, 0.2 mm/rev, 0.4 mm)

For the set 2, the tool wear increases significantly for all the three conditions. It is noted that, the UAT does not show a significant reduction in tool wear whereas the HUAT shows a comparable reduction. The UAT and HUAT lower the  $VB$  approximately by 5% and 15 %, respectively, compared to that in CT. At 70 m/min., the temperature-induced at the deformation zone is very high during machining of Nimonic 90, rapidly decreasing the strength of tool coating and enhancing the tool wear. Zhu et al. [184] studied that the major cause of the tool wear is cracking occurred due to the cutting edge exposing a high level of thermal shock and temperature variation at high cutting speed. It is also examined that during machining of superalloys at a higher cutting speed, chips get welded to the tool, which retarded the flow, raising the cutting temperature drastically and increasing the wear rate. However, the temperature-induced in the UAT is lower than the CT; the ultrasonic vibration imposes the fatigue loading at tool nose, accelerating the tool wear. In the case of HUAT, the heating temperature is insufficient to lower the flow stress and thus requires more resistance to cut the material, increasing the tool wear even in HUAT.

The tool flank wear observed from FEM and experiments for set 1 are shown in Figure 4.18. In the study of the flank wear, the wear depth and the temperature on the flank face obtained from the FEM, are considered for the analysis. The results display that the temperature produced on the flank face is 270°C for the CT, 215°C for the UAT and 250°C for the HUAT. Although the temperature is slightly higher in the HUAT than UAT, the wear depth is lower in the HUAT. However, the CT shows the highest depth of wear. On the other hand, the results of experiments show a similar trend as that in FEM. The CT shows a failure of tool nose, BUE, abrasion, adhesion of microchips and edge chipping, as exposed in Figure 4.18 (g). Because of the low heat conductivity of Nimonic 90 and higher temperature and pressure near the cutting edge, BUE adheres to the cutting edge. The BUE is not always stable, and when it breaks, it carries a tool fragment with it, leading to an edge chipping [155]. When the worn tool starts rubbing with a machined surface, it produces frictional heat and causes abrasion. An abrasion is due to rubbing between the machined surface and tool flank face just behind the cutting edge. The coating of  $Al_2O_3$  and TiN is not sufficient to withstand the abrasion at a high temperature. In the UAT, an intermittent cutting action suppresses BUE formation, as shown in Figure 4.18 (h). However, tool nose wear and abrasion are significant but lesser than CT. Ultrasonic vibrations reduce a rubbing between tool flank face and machined surface, decreasing the abrasion. Adhesion of microchips on the flank face is accredited to the chemical affinity of workpiece material [178]. As shown in Figure 4.18 (i), the HUAT shows a significant reduction on the flank face compared to CT and UAT. An adhesion of microchips decreases due to a reduction of chemical affinity in HUAT. Peeling of the coatings occurs due to the abrasion of carbide particles. It is observed that a preheat temperature reduces the susceptibility of tool to



abrasive and adhesive wear. A similar result is obtained in the machining of Inconel 718 with coated carbide tool by Devillez et al. [185]. It can be said that HUAT significantly reduces the tool flank wear at a given set of process parameters.

The tool flank wear observed from FEM and experiments for set 2 are shown in Figure 4.19. From the FEM itself, it is observed that tool flank wear is very severe during machining of Nimonic 90 at set 2. Although the depth of cut and feed are lesser in set 2 compared to set 1, a higher cutting speed, i.e., 70 m/min, significantly affects the tool wear. It is observed that the temperature on the flank face raises up to 520°C which is almost double the value for set 1 in the CT. On the other hand, this temperature difference is comparatively lesser in the UAT and HUAT. It can also be observed that the temperature rise in the HUAT is almost similar to that in UAT. However, the flank wear seems lesser in the HUAT than in UAT. The wear depth is the highest in the CT. The results of experiments also show a similar trend as that in FEM. The tool nose wears out severely in all the three conditions. As shown in Figure 4.19(g), in the CT, a combination of high stresses and temperature generates the cracks, leading to cause the fracture during machining at a higher cutting speed [155]. It is also seen that the segment chips formed during machining of Nimonic 90 imposing very high shear stress on the tool and drastically reduce the strength of tool, resulting in plastic deformation [186]. Severe abrasion is owing to the rubbing between the work-hardened surface of the workpiece and tool flank face. As realized in Figure 4.19(h) and Figure 4.19(i), the UAT and HUAT also show substantial wear on the flank face. The preheated temperature is not sufficient to lower the flow stress of the tool. In contrast, the UAT action does not affect the tool wear at a higher cutting speed. A sudden failure of the tool is attributed to higher hardness and toughness of the Nimonic 90 [179]. Moreover, adhesion of microchips, abrasion, and coating peeling are also observed in the UAT. The HUAT also shows an edge chipping. An increase in cutting speed, enhancing the temperature, and reducing the hardness and shear strength of the tool coating and/or substrate [182]. Ultimately, it results in an edge chipping in UAT and HUAT. It can be said that the HUAT is not effective at a higher speed, although it reduces wear depth during machining of Nimonic 90.

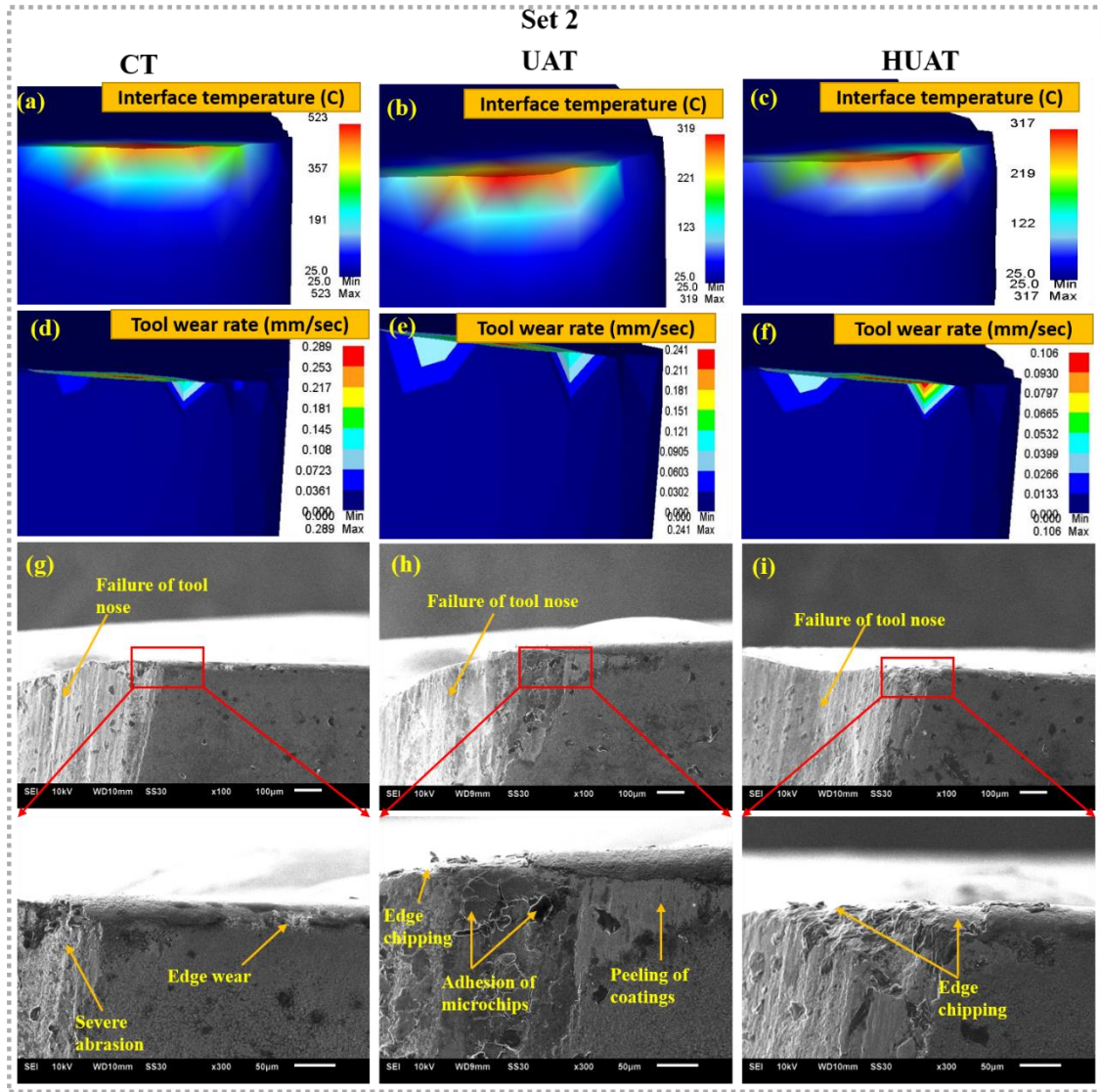


**Figure 4.19** Results of tool flank wear obtained from FEM and experiments at set 2 (70 m/min, 0.1 mm/rev, 0.2 mm)

#### 4.2.3.3 Tool-chip contact length

The tool-chip contact length ( $L_c$ ) is the length between chip and tool. The metal cutting is extremely dependent upon the  $L_c$ , since the  $L_c$  directly affects the tool wear and ultimately tool life. In the experiments, three different values of  $L_c$  are measured and the average is considered for the analysis. The values of  $L_c$  obtained from FEM are compared with experimentally obtained values.

The tool chip contact length ( $L_c$ ) obtained from experiments and FEM, for set 1, is given in Figure 4.20(a). The values of  $L_c$  obtained from experiments are in close agreement with the values obtained from FEM. The CT shows a maximum deviation, whereas UAT and HUAT are not showing much. The UAT from FEM displays a bit higher value of  $L_c$  than experimental. It is noted that the  $L_c$  is lower in HUAT than in CT and UAT, in FEM and experiments. As

discussed earlier, the tool-chip contact length plays a significant role in tool wear. The CT shows the highest value of the  $L_c$  due to high frictional heat, adhering the chips of Nimonic 90 to the rake face of the tool, showing a larger  $L_c$ . It can also be said that, high ductility of Nimonic 90 produces a higher  $L_c$  mainly in the CT. These results agree with the results for turning Nimonic 90 under dry condition by Chetan et al. [187]. Due to the repetitive cutting action, the  $L_c$  decreases in the UAT and HUAT. It is believed that the preheating of the workpiece might reduce the ductile nature, lowering the  $L_c$  in the HUAT. In this study, an average reduction in the  $L_c$  for HUAT is 21.8% and 9.3% compared to CT and UAT, respectively, for a given set of process parameters. When comparing the results obtained from experiments and FEM, an approximate error in the  $L_c$  is 8.3%, 2.9% and 3.3%, for CT, UAT and HUAT, respectively.

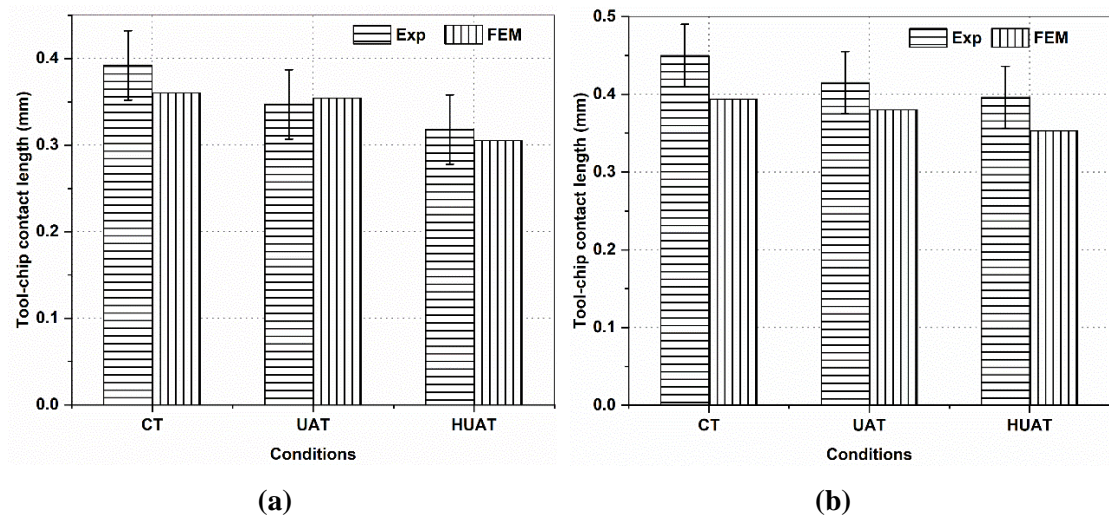


**Figure 4.20** Average value of tool-chip contact length measured for (a) set 1 (30 m/min, 0.2 mm/rev, 0.4 mm) and for (b) set 2 (70 m/min, 0.1 mm/rev, 0.2 mm)

The tool chip contact length ( $L_c$ ) obtained from experiments and FEM, for set 2, is presented in Figure 4.20(b). The results show a considerable difference in the values of  $L_c$  obtained from experiments and FEM. This difference is due to an effect of tool wear. Although the feed used for set 2 is lower compared to set 1, the  $L_c$  is higher for set 2. The tool wear is found severe at 70 m/min, as revealed in previous study. A fracture at the tool nose in all three conditions makes the cutting condition worst, producing a larger value of  $L_c$ . It can be observed that the  $L_c$  is higher for set 2 than set 1. It means that, the  $L_c$  raises as the cutting speed increases, although the trend remains the same for set 2. However, the  $L_c$  mainly depends upon the uncut chip thickness [186]. Moreover, a high contact pressure at nose region helps the chip to be adhered with rake face of the tool at a higher cutting speed, producing more  $L_c$ . Here, it depends upon the tool wear, which is higher at 70 m/min, showing a higher value of  $L_c$ . The UAT and HUAT do not much differ in the values of  $L_c$ , due to severe tool wear. An average reduction in the  $L_c$  for HUAT is 12.5% and 5% than in CT and UAT, respectively, for a given set of process

parameters. When comparing the results obtained from experiments and FEM, an approximate error in the  $L_c$  is 12.5%, 10.5% and 14.3%, for CT, UAT and HUAT, respectively.

#### 4.2.3.3 Machining forces

Machining forces are the parameters to analyze the machinability of materials. They depend upon the tool wear, workpiece and tool material, machine tool rigidity, tool geometry, etc. Due to the poor machinability of superalloys, large cutting forces generate during machining. In this work, based on the tool wear analysis, the higher machining forces can be experienced. The machining forces obtained from FEM and experiments are compared for all three conditions.

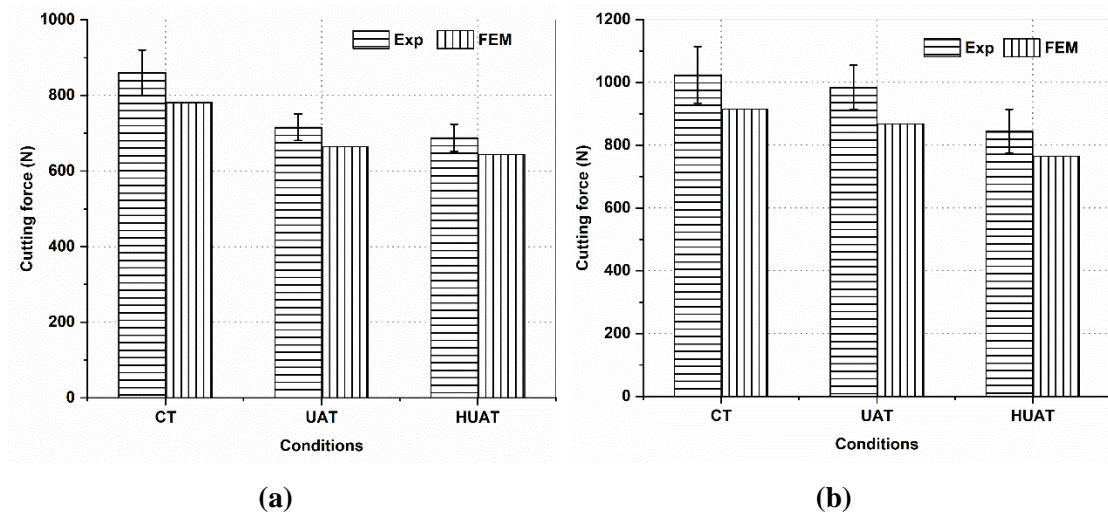


**Figure 4.21** Average cutting forces generated for (a) set 1 (30 m/min, 0.2 mm/rev, 0.4 mm) and for (b) set 2 (70 m/min, 0.1 mm/rev, 0.2 mm)

The cutting force ( $F_c$ ) gained from experiments and FEM, for set 1, is given in Figure 4.21(a). The results of  $F_c$  obtained from experiments are in good agreement with the results obtained from FEM. Compared to CT, the  $F_c$  is lower in UAT and HUAT. However, the difference in  $F_c$  is not noteworthy in UAT and HUAT. A lower value of  $F_c$  is attributed to the cyclic nature UAT. The tool separates from a workpiece during the disengagement, making the cutting force zero and dropping the average value [175]. Continuous contact between tool and workpiece produces a larger tool-chip contact length, increasing friction and cutting force. Alternatively, pulsating cutting force lessens the average cutting force in the UAT and HUAT. Furthermore, along with ultrasonic energy, heat also contributes to reducing the  $F_c$  in HUAT. Similar results are obtained by [188]. An average reduction in the  $F_c$  for HUAT is 25% and 5% compared to CT and UAT, respectively, for a given set of input parameters. When comparing the results obtained from experiments and FEM, an approximate error in the  $L_c$  is 15%, 14% and 12%, for CT, UAT and HUAT, respectively. The cutting force ( $F_c$ ) obtained from



experiments and FEM, for set 2, is given in Figure 4.21(b). The results show a significant difference in the values of  $F_c$  obtained from experiments and FEM. This difference is one of the results of tool wear. Even if the feed and the depth of cut is lower in set 2, the  $F_c$  increases. At a 70 m/min, the tool wear is very severe, generating a very high cutting force. The worn tool starts rubbing with a machined surface, producing large friction and hence cutting forces. Moreover, the chip produced during machining with the worn tool, becoming strain hardened, affecting the cutting force severely. Due to fracture of tool nose, producing a very high  $F_c$  in UAT. The HUAT shows a small reduction in cutting force than in UAT. However, the preheating temperature is not sufficient to lower the flow stress of the Nimonic 90. An average reduction in the  $F_c$  for HUAT is 22% and 15% compared to CT and UAT, respectively, for a given set of parameters. When comparing the results obtained from experiments and FEM, an approximate error in the  $L_c$  is 19%, 17% and 14%, for CT, UAT and HUAT, respectively.

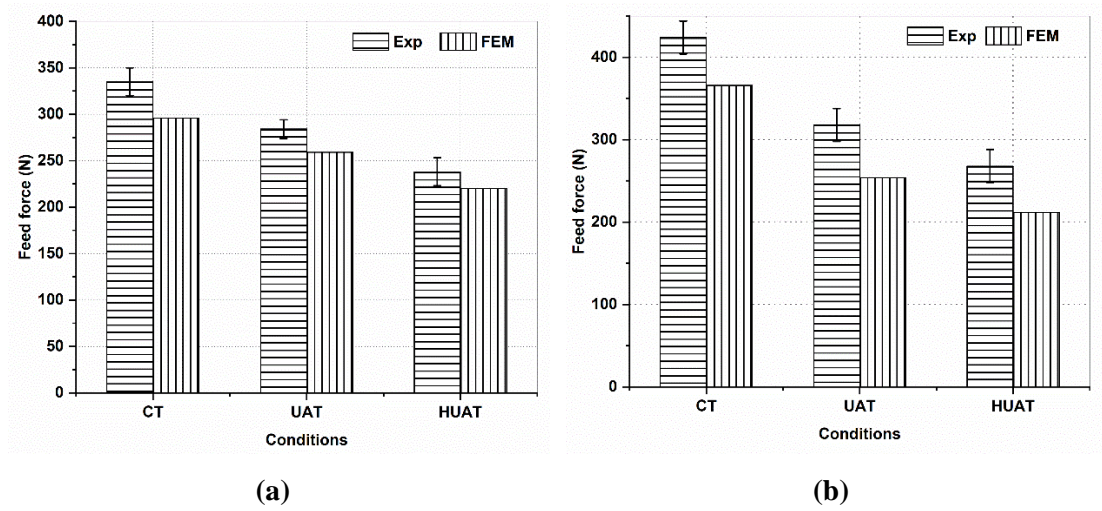


**Figure 4.22** Average feed forces generated for (a) set 1 (30 m/min, 0.2 mm/rev, 0.4 mm) and for (b) set 2 (70 m/min, 0.1 mm/rev, 0.2 mm)

The feed forces ( $F_f$ ) obtained from the experiments and the FEM analysis, for set 1 and set 2, are appeared in Figure 4.22(a) and Figure 4.22(b), respectively. The values of  $F_f$  obtained from experiments show a significant difference compared to the values obtained from FEM. However, the trend is similar for both, the experiments, and the FEM. The values of  $F_f$  for set 1 are not much different than set 2. This is due to a large feed rate value and a small value of cutting speed used for set 1. Whereas the former is lower and the latter is higher for set 2. A reduction in  $F_f$  at a lower feed rate is compensated by a higher cutting speed for set 2. Moreover, tool flank wear also contributes to an increment of  $F_f$ . The UAT and HUAT show a reduction in  $F_f$ , for both the sets. Due to intermittent cutting characteristics, the average feed force decrease. It is seen that the UAT reduces the chip thickness by increasing the shear angle, lowering the  $F_f$  [17]. The heat energy further reduces the  $F_f$  in HUAT. An average reduction in

the  $F_f$  in HUAT is 36% and 17% for set 1, and 35% and 14% for set 2, respectively, compared to CT and UAT. While comparing the results obtained from experiments and FEM, an approximate error in the  $F_f$  is 20%, 24% and 23%, for set 1, and 20%, 26% and 27% for set 2, in CT, UAT and HUAT, respectively.

#### 4.2.4 Conclusions for FEM

The finite element model was established to examine the tool wear along with the chip-tool contact length and machining forces for CT, UAT and HUAT. The experiments were performed at two different sets (refer to table 1 for set1 and set 2) of input parameters on Nimonic 90 using FEM-based designed and developed horn. SEM characterization of tool wear was accomplished, and the results obtained were compared with the FEM. The conclusions upon the comparisons are as follows:

- The results of tool crater and flank wear obtained from FEM are in close agreement with the results of the experiments for set 1. Moreover, the HUAT showed a significant improvement in tool wear. For set 2, significant wear is observed in all three conditions.
- The main tool wear mechanisms detected are edge chipping, abrasion, adhesion of BUE, and fracture of tool nose. The HUAT showed a reduction in abrasion, adhesion and edge chipping during machining for set 1. Whereas, for set 2, fracture of the tool nose is observed in all three conditions.
- The results of tool-chip contact length show a good agreement with the results of experiments with an approximate error of 2-6% for set 1, and 12-15% for set 2. The HUAT reduces the tool-chip contact length by approximately 9-21% for set 1, and 5-12% for set 2, compared to CT and UAT.
- The results of machining forces show a close agreement with the results of experiments with an estimated error of 12-19% for cutting force and 20-27% for feed force. The HUAT reduces the cutting force by 5-25%, and feed force by 14-36%, compared to CT and UAT.

The FEM developed to predict output responses shows a very good agreement at a lower value of cutting speed. As the cutting speed increase, the error also increases. It may be due to the parameters such as material anisotropy, ultrasonic softening effect, constant values of material properties, etc.

### Experimental analysis on the combined effect of ultrasonic vibration and cutting fluids

---

In order to fulfil the objective 4, i.e, Experimental investigation on a combined effect of ultrasonic vibration and cooling approaches to analyse the machinability, the experiments have been performed combining ultrasonic vibration and cutting fluid, on the Inconel 718 and Ti6Al4V. The outcomes such as surface roughness, power consumption, chip morphology and tool wear are examined. The results for Inconel 718 and Ti6Al4V are discussed separately.

#### 5.1 Experimental analysis for Inconel 718

##### 5.1.1 Methodology

A cylindrical bar of Inconel 718 with a diameter of 35 mm is used to perform the experiments. The experiments are performed for CT and UAT using different strategies such as dry, wet, MQL, and LCO<sub>2</sub>. The dry condition is considered the cheapest way of machining. However, during machining of Inconel 718, the heat generation is very high, resulting in rapid tool wear. To remove the heat and increase the tool life, the coolant could be used. As discussed earlier, the conventional cutting fluids are not sustainable since more energy is required to recycle it. In contrast, the MQL and LCO<sub>2</sub> are considered clean and sustainable, minimizing emulsion-based cutting fluid. Cutting speeds, feed, depth of cut, frequency, and vibration amplitude are considered as input parameters. All the experiments are repeated twice to minimize the parameter error. Table 5.1 and Table 5.2 represent the conditions employed for the machining, and cooling and lubrication, respectively.

Machining performances such as tool crater and flank wear, power and specific cutting energy consumption, surface quality, and chip morphology are examined. At the end of machining, worn tools are examined using a SEM. Tool wear assessment includes an average width of flank wear ( $VB_b$ ) and morphology of crater and flank. According to the criteria given by ISO 3685:1993, the maximum width of the flank wear should not be greater than 0.3 mm [179]. Furthermore, the power consumption is measured using a fluke 435 (Series II) 3-phase energy and power analyzer. For the present study, the power consumption by spindle during the machining operation is considered for the analysis. A Taylor Hobson contact-type surface roughness tester is utilized to evaluate the surface roughness, keeping cut-off length of 0.8 mm

and evaluation length of 4 mm, as per the given in ISO 4288-1996 [180]. The surface roughness is measured thrice in a feed direction for each cutting condition and at different location and an average value is considered for analysis. Three different measurements are performed for each cutting condition, and an average is taken for evaluation. The chips have been collected after each experiment and examined using SEM.

**Table 5.1.** Conditions used to perform the experiment

Parameters	Attributes
Workpiece	A cylindrical bar of Inconel 718 of 35 mm diameter
Tool	CNMG 120408 with a nose radius of 0.8mm
Coating	PVD multilayer coating of TiAlN
Cutting condition	Conventional and Ultrasonic assisted turning
Frequency	20,000 Hz
Amplitude	10 $\mu\text{m}$
Cutting speed	66 m/min
Feed	0.22 mm/rev
Depth of cut	0.3 mm
Cutting length	500 mm
Cooling strategies	Dry, Wet, MQL and LCO <sub>2</sub>

**Table 5.2** Details of cooling strategies employed

Parameter	Attributes
Wet cooling	Fluid: Emulsion of synthetic oil in water, Pressure: 3 bar, Flow rate: 21 l/min, Nozzle diameter: 10 mm,
MQL	Oil: Canola oil, Pressure of air: 5 bar, Flow rate: 8 ml/hr, Nozzle diameter: 2 mm,
LCO <sub>2</sub>	Pressure of the cylinder: 57 bar, flow rate: 27 l/hr, Nozzle diameter: 2 mm
Distance of nozzle tip from rake face	20 mm for all the cooling strategies

### 5.1.2 Tool crater wear

The tool wear is a crucial factor affecting the surface quality and integrity, cutting forces and power consumption, cost, etc. The tool wear occurs due to the chemical, physical and mechanical reactions that happened at the deformation zone. It also depends upon tool and workpiece material, input parameters, and cooling conditions. During machining of Nickel base superalloys, high temperature-induced at secondary and tertiary deformation zone making the

process unstable due to thermo-mechanical loading, enhancing the tool wear rapidly. This section analyzes the morphology of tool wear under different cooling strategies using both the processes.

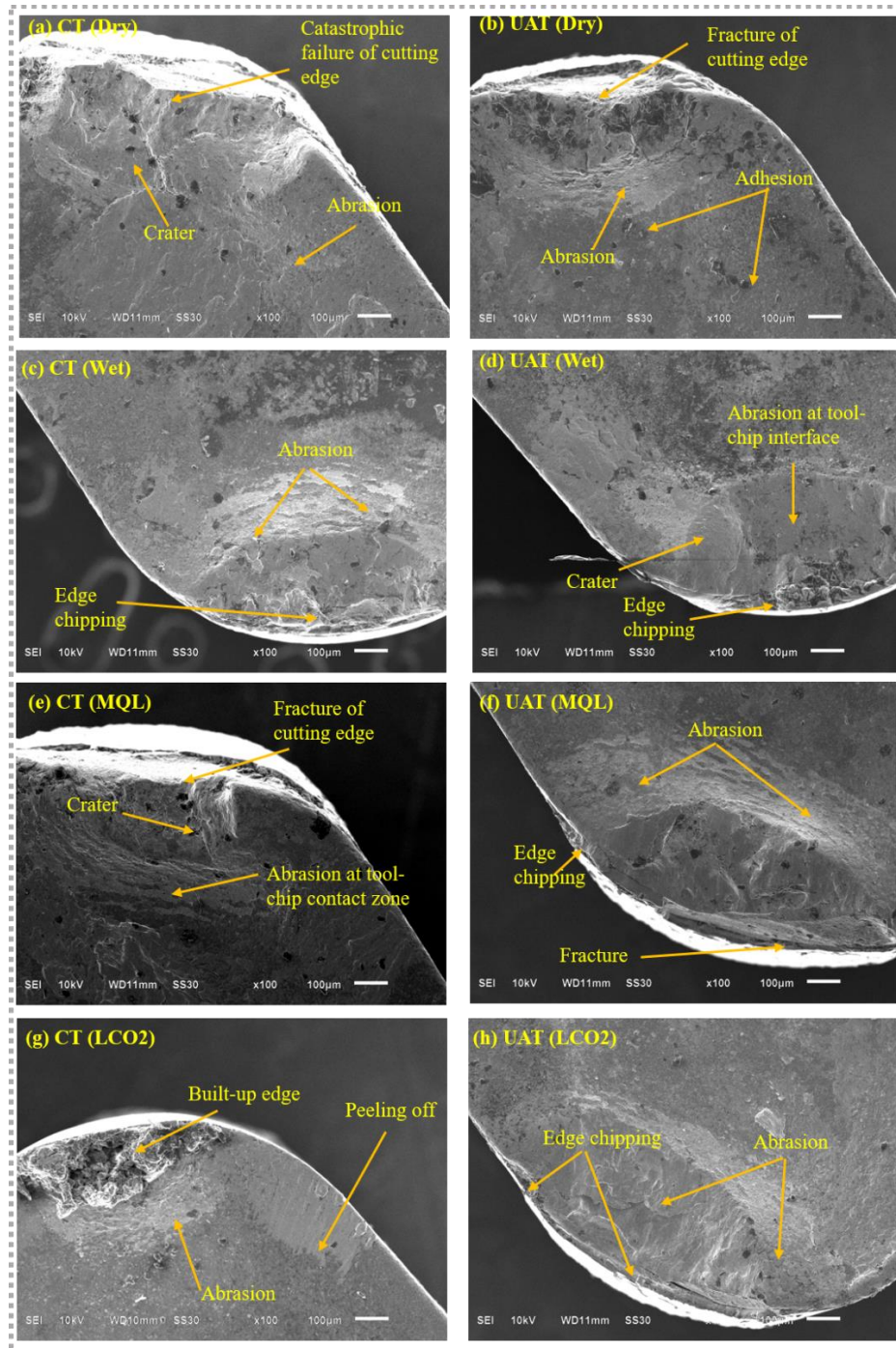


**Figure 5.1** Morphology of tool crater wear observed in CT and UAT, under different conditions

Crater wear appears on the tool rake face, owing to the contact between tool and chip. The chip passes over the rake face, generating a heat and friction, resulting in a tool crater wear. Morphology of crater wear observed in CT and UAT under different cooling strategies are shown in Figure 5.1.

The CT shows a severe tool wear of the rake face, as revealed in Figure 5.1(a). It appears a catastrophic failure of the cutting edge due to plastic deformation. A similar failure of cutting edge is also observed during UAT under dry condition, as presented in Figure 5.1(b). The reason for the plastic deformation is the high stresses and forces imposed on the cutting edge. Thakur et al. [189] claimed that the plastic deformation is due to the weakening of the tool under high forces and stresses enforced during machining of Inconel 718. It is also seen that during machining of Inconel 718, a shrinkage of the seizure zone takes place even for PVD coated tools, resulting in plastic deformation of the tool nose [190]. The ultrasonic vibration further enhances the plastic deformation due to the repeated action of the tool, and hence failure of the cutting edge takes place rapidly. Apart from cutting edge failure, crater and abrasion are also observed on the rake face in the CT. When the chip flows on the rake face, the coating of TiAlN wears out under high Pressure and temperature, causing abrasion and crater. The crater could be formed due to the built-up edge (BUE). The instability of BUE results in removing the tool material from the rake face, producing a crater. Partial adhesion of microparticles is mainly observed in the UAT. It is due to a variation in temperature and Pressure due to the periodic motion of the tool in UAT. During the UAT, the chips flown over the rake face reduce the contact between with the tool, reducing the mechanical load and hence the crater formation. Nath et al. [191] have explained that during the disengagement period in the UAT, the tool-workpiece contact removes the heat, helping in reducing the tool wear in the UAT. Thus, it can be said that the dry condition is not beneficial to improving the machinability of Inconel 718.

As shown in Figure 5.1(c), the CT under wet condition eliminates the sudden breakage of the cutting edge, unlike in the dry condition. Yet, the abrasion and edge chipping seem severe in the same condition. The cutting fluid help in removing the heat from the deformation zone, preventing the fracture of the cutting edge. However, high temperature near the cutting edge reduces the strength of the tool, leading to chipping of the cutting edge. Additionally, in subsequent machining, when the adhered BUE is brought out through the chip flowing over the rake face, it brings a small fragment of the tool material, causing the chipping [192]. The chemical reactivity of Inconel 718 with the cutting tool causes the built-up layer, which is unstable in nature, causing the chipping in subsequent machining. During machining of Nickel base superalloy under wet condition, chipping is usually due to the combination of cyclic thermal and mechanical loading. Under the fluctuation of the thermal and mechanical load, the coating of TiAlN loses its strength, leading to an edge chipping. Minor chipping is noted in case of the UAT under wet condition, as shown in Figure 5.1(d). The UAT reduces the abrasion and adhesion by allowing the cooling fluid very near the cutting edge during the separation of tool and chip, as shown in Figure 4. A capillary action takes place between tool and chips, helps in removing the heat from the secondary zone by cutting fluid, reducing the abrasion and adhesion.

On the other hand, an abrasion is severe at the tool-chip contact zone in the CT. The abrasion is primarily caused by the inclusion of hard carbide particles sandwiched between tool and chip, removing TiAlN coating and causing the abrasion. Besides, high temperature at the deformation zone causes the strain hardening of the chip, removing the coating by abrasive action rapidly [193]. It can be said that the CT and UAT perform better in terms of crater wear under wet conditions compared to dry condition.

The CT under MQL indicates a catastrophic failure of the cutting edge, as shown in Figure 5.1(e). A crater is also formed under the same condition. The MQL does not provide sufficient cooling to remove the heat from the deformation zone. The lubrication provided by oil particles is insufficient to eliminate crater wear. Thus, the MQL shows higher tool wear compared to wet condition. A similar result is observed for UAT under MQL, as presented in Figure 5.1(f). The cutting-edge fracture takes place when the tool is unable to resist the Pressure and temperature at secondary shear zone [193]. According to Cantero et al. [194], the fracture is associated with attrition wear and thermo-mechanical cracking at high Pressure and temperature during the machining of Nickel-base superalloy. The fracture is also associated to thermal cracking, strain hardening of the chips and diffusion from the rake face, even under MQL [190]. Adhesion of the workpiece materials could also be caused the peeling off the coating s and fracture of the cutting edge. The ultrasonic vibration minimizes the fracture; instead, severe edge chipping and abrasion are noted. It may be due to sufficient cooling at the cutting edge during the disengagement of the tool, allowing the air and oil particles to penetrate, enabling the heat dissipation, and reducing the fracture. It can be said from Figure 5.2 that in the UAT, the lubricating film formed by mist particles at tool chip contact zone reduces the friction, lowering the heat interaction between tool and chip, lessening the tool wear in the UAT. A similar result was obtained for UAT of Ti6Al4V under MQL by Yan et al. [195]. However, the load imposed by ultrasonic vibration enhances the edge chipping. Uneven chips flowing over the rake face remove the coating by abrasion in both the processes. Thus, it can be said that the MQL is not much effective in lowering the tool wear in both the processes.

Figure 5.1(g) shows that the LCO<sub>2</sub> significantly reduces the crater wear in the CT compared dry, wet and MQL conditions. An effective cooling provided by LCO<sub>2</sub> suppresses the edge chipping and plastic deformation, unlike in other cutting conditions. The LCO<sub>2</sub> absorbs considerable volume of heat from the deformation zone, diminishing the tool wear. An accretion of strained workpiece material on the cutting edge forms a BUE. It is believed that the materials heated up during machining cool down rapidly by the pressurized jet of LCO<sub>2</sub>, causing the strain hardening and forming of BUE [196]. This BUE eliminates the crater formation by preventing the tool-chip contact. The abrasion and peeling of the coating are primarily observed at the tool-chip contact zone. It is believed that strain hardened chip passes over the rake face, removing the

TiAlN coating by abrasive wear. However, the abrasion and peeling off is not severe under the LCO<sub>2</sub>. A high value of heat transfer coefficient enhances heat dissipation by forced convection, reducing the friction and ultimately tool wear. Furthermore, a gaseous cushion formed by LCO<sub>2</sub> prevents the sticking zone, limiting the friction and tool wear [197]. Similar observations of the tool wear in the machining of Inconel 718 are made by Khanna et al. [81]. In case of the UAT, the edge chipping and abrasion are noted, as shown in Figure 5.1(h). The chipping is attributed to the thermo-mechanical loading caused by LCO<sub>2</sub> and ultrasonic vibration, resulting in a reduction in strength of the cutting edge, appearing the edge chipping. It is believed that the force of LCO<sub>2</sub> help in reducing the BUE in the UAT by penetrating at tool-chip contact area. Khanna et al. [196] have found that the UAT of Ti6Al4V under LCO reduces the load imposed by shear localized chip on the cutting edge, reducing the heat interaction between chips and cutting edge, lowering the adhesion and crater formation. Nevertheless, the UAT shows a reduction in tool wear under LCO<sub>2</sub> compared to other strategies. Thus, it can be said that an effective cooling offered by LCO<sub>2</sub> substantially reduces the tool wear compared to other cooling strategies.

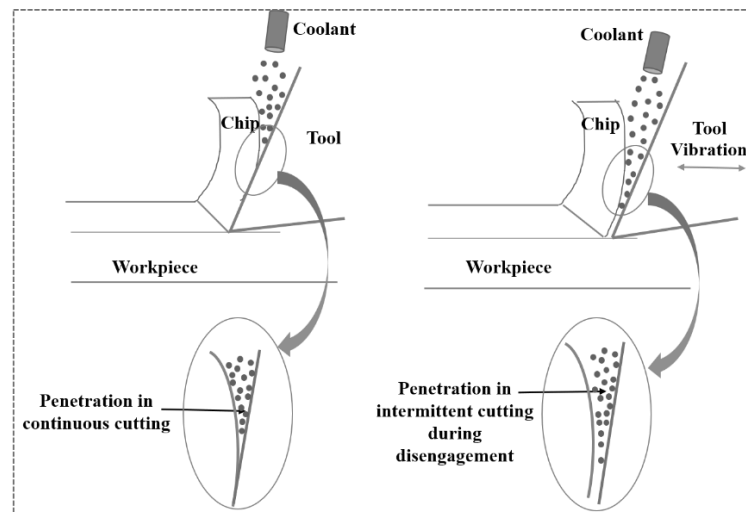


**Figure 5.2** Penetration of the cutting fluid in conventional and ultrasonic assisted turning

### 5.1.2 Tool flank wear

The flank wear occurs at the tool-workpiece contact area. A small part of the tool nose intersects with the workpiece during machining, generating the heat at the tool-workpiece interface and producing flank wear.

An average width of flank wear ( $VB_b$ ) measured in CT and UAT under dry, wet, MQL, and LCO<sub>2</sub>, are shown in Figure 5.3. The flank wear is determined at three different places using SEM and average value is taken for assessment. The error bar is representing a standard deviation from the mean value of flank wear. The standard deviation is calculated for each cutting



condition and for CT and UAT. It can be said that the  $VB_b$  is substantially influenced by cooling strategies. The dry condition indicates the highest wear whereas, the  $LCO_2$  indicates the lowest wear for both the processes. During the machining under dry condition, heat generation at the deformation zones are high, increasing the thermal load on the tool, enhancing the tool wear. A similar result is observed during milling of Inconel 718 under dry condition by Halim et al. [82]. In case of the UAT, during disengagement of the tool, some heat dissipates and reduces the  $VB_b$ . Nath et al. [147] found that during the UAT, pulsating cutting force reduces the load on the tool, retain the strength for a longer duration, and reduces the tool wear. The wet condition reduces the  $VB_b$  appreciably, in both the processes. The coolant absorbs the heat from the deformation zone, reducing the temperature and thermal load on the tool, decreasing the tool wear. The UAT under wet condition shows a slightly higher value of tool wear compared to CT. The MQL does not indicate much difference in the  $VB_b$  compared to wet conditions. However, the  $VB_b$  increases in the CT, whereas it decreases in the UAT, compared to wet condition. Insufficient cooling provided by MQL could be the reason to increase the  $VB_b$  in the CT. However, the oil droplets presented in the MQL form lubricating film between tool and workpiece, lowering the wear rate compared to the dry condition. In the UAT, tool allows the pressurized air and oil droplets to enter at tool-workpiece interface, further decreasing the  $VB_b$ . The  $LCO_2$  significantly reduces the  $VB_b$  compared to all the other cooling strategies. The pressurized jet of  $LCO_2$  enables the convective heat dissipation from the tool-work interface, removing the heat rapidly and reducing the tool wear. According to Patil et al. [198], a low temperature provided by  $LCO_2$  decreases the stickiness of the chip of Inconel 718, reducing the friction and wear. The UAT does not show a much difference in  $VB_b$  compared to CT. For the CT under  $LCO_2$ , an average reduction in the  $VB_b$  is 60%, 28%, and 32% compared to dry, wet, and MQL conditions, respectively. For the UAT under  $LCO_2$ , an average reduction in the  $VB_b$  is 53%, 39%, and 32% compared to dry, wet, and MQL conditions, respectively.

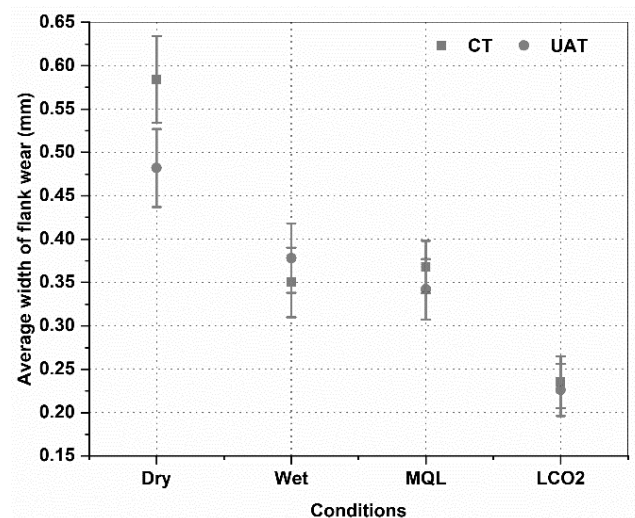


**Figure 5.3** Average width of flank wear measured under different cutting environments

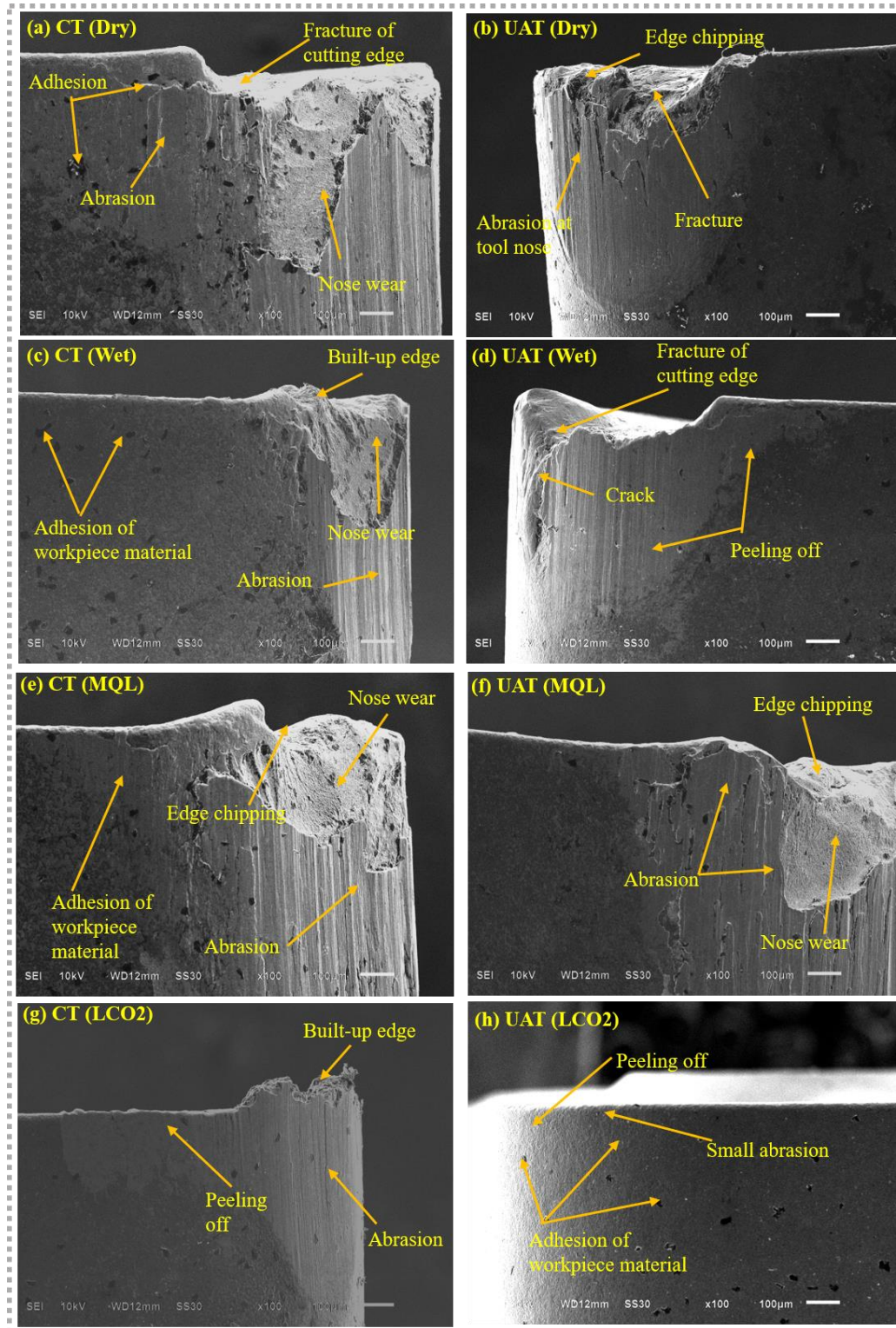


**Figure 5.4** Morphology of tool flank wear observed in CT and UAT, under different conditions

The morphology of flank wear observed in the CT and UAT, under different cooling strategies are shown in Figure 5.4. The dry condition creates severe tool wear compared to other conditions. Figure 5.4(a) shows that the CT reveals intense flank wear under dry conditions. The flank wear is associated with the tool nose wear as well. An abrasion and adhesion appear on the

flank face. In case of the UAT, the nose wear is associated to the abrasion, as indicated in Figure 5.4(b). In the dry condition, the heat gets concentrated at the tool nose part, increasing the thermal load on the cutting edge and enhancing fracture possibility. Initially, the TiAlN coating wears off due to frictional heat, exposing the tool substrate directly in contact with the machined surface, speeding up the wear of tool. The nose wear is primarily due to hard carbide particles pressurized between the tool and the workpiece at elevated temperatures. Additionally, the compressive stresses acting on the flank face are much higher than on the rake face, leading to plastic flow of the coatings from the flank and tool nose, resulting in nose wear [199]. The hard inclusions of carbide particles scratch the flank face, resulting in abrasion and peeling off the coating takes place. An adhesion of microparticles of work materials is noted on the flank face. The UAT reduces the nose wear by disconnecting the tool with the workpiece during cyclic motion. However, ultrasonic vibration accelerates edge chipping by imposing fatigue on the tool. An Inconel 718 has high strength, toughness, creep resistance, imposing the fatigue loading on the tool, reducing the strength of the tool and plastic deformation takes place in the UAT [147]. Moreover, it is also believed that at a cutting speed of 66 m/min, that is very near to the critical cutting speed (75 m/min), a number of impacts in the UAT is also high, leading to fail the tool by fatigue loading. Eventually, it can be said that the main tool wear mechanism is nose wear, fracture, and abrasion in CT and UAT processes.

The flank wear seems less severe under wet condition for CT and UAT, as revealed in Figure 5.4(c) and Figure 5.4(d), respectively. The CT shows nose wear accompanying abrasion, BUE formation, and adhesion of microparticles on the flank face. The BUE formation is due to sticking contact between tool and chip under high Pressure, not allowing the cutting fluid to enter at secondary deformation zone. The BUE formation is considerably affected by the adhesion mechanism. However, it prevents the tool from plastic deformation in the CT. On the other hand, the BUE in the UAT is unstable due to repetitive cutting action, enhancing the tool wear rapidly by flaking. When the hard carbide particles mixed with cutting fluid enter the tool-work interface, it wears off the coating due to erosion, exposing the tool substrate with a newly generated machined surface. It raises the temperature at the tool-work interface, accelerating the nose wear [200]. In case of the UAT, a crack propagating from the cutting edge is shown at the tool nose. The tool starts cracking when the principal stress equals the ultimate stress of the tool material. It is thought that, when the coolant penetrates between tool and workpiece, the heat dissipation takes place, simultaneously when the worn tool continues the machining, accumulating the heat takes place, which generates the thermal load on the tool, arising the possibility of catastrophic failure [201]. A reduction abrasion is noted in the UAT; instead, peeling of the coating is observed. Ultrasonic vibration reduces the Pressure at the tool-workpiece contact zone, reducing friction and temperature and decreasing abrasive wear. Thus,

it can be said that flood cooling is not beneficial much in reducing the flank wear in the machining of Inconel 718.

The MQL shows drastic flank wear in the CT, as shown in Figure 6(e). Compared to dry and wet conditions, the MQL shows higher flank wear in both the processes. The UAT shows an edge chipping, nose wear, and abrasion, as shown in Figure 6(f). The MQL is not sufficient in removing the heat from the tool-workpiece interface. Low amount of the cutting fluid used in MQL compared to flood cooling, providing the conducive condition for the workpiece and hard carbide particles broken from the tool to cause the abrasion, mainly at tool nose. Similar results of tool wear are observed in machining 15-5 PH hardened steel with carbide tool by Khanna et al. [87]. Initially, the TiAlN protects the tool from the high temperature and friction. Additionally, the MQL also provides a lubricating layer, reducing the friction at interface zone. However, in the subsequent machining, the oil particles get evaporated, exposing the tool at high temperature, enhancing the tool wear. On contrary, in the UAT, some oil particles are penetrated inside the tool-workpiece interface, delaying the tool wear compared to CT. The chipping of the cutting edge is primarily attributed to the thermo-mechanical loading exerted by high temperature and pressure. The UAT shows a higher edge chipping due to the excessive mechanical load imposed by ultrasonic vibration to the cutting edge. Nath et al. [147] investigated that at a higher cutting speed, the number of cycles also increases in the UAT, raising the temperature at the tool-workpiece contact zone. The oil particles in the mist get evaporate when exposed to the high temperature, becoming ineffective in providing lubrication even in the UAT, resulting in high tool wear. Thus, it can be said that MQL is inefficient in improving the tool flank wear during machining of Inconel 718.

The LCO<sub>2</sub> decreases the flank wear significantly compared to other cooling strategies for both the processes. As shown in Figure 6(g), the CT shows a BUE, abrasion at the tool nose, and peeling of the coating at the flank face. On the other hand, the UAT offers a partial peeling of the coating at the cutting edge and a minor adhesion of microparticles on the flank face, as shown in Figure 6(h). An adhesion of BUE is attributed to the welding of the microchips at the cutting edge. During machining of Nickel-base superalloys, adhesion is an active wear mechanism in all the cooling conditions. Excessive adhesion of microparticles leads to a formation BUE even under cryogenic condition. An adhesion of BUE prevents the tool from edge chipping and abrasion. An effective cooling provided by LCO<sub>2</sub> significantly reduces the nose wear, unlike in other strategies. However, a squeezing of hard carbide particles between tool and workpiece induces friction, producing smooth wear marks on the tool nose due to abrasion [202]. The wear observed on the nose part looks smooth without any deep abrasion. The LCO<sub>2</sub> prevents abrasion by providing effective cooling very near to the cutting edge. Peeling of the coating takes place also due to abrasion. Similar results are observed for the UAT. The

UAT provides the gap between tool and workpiece, enhancing the heat dissipation by LCO<sub>2</sub>, lowering the tool wear. Moreover, the effective removal of the heat minimizes the adhesion and abrasion on the flank face in the UAT. However, a chemical affinity of Inconel 718 results in the adhesion of small microparticles with the tools. It can be said that the LCO<sub>2</sub> is more effective with the UAT in preventing tool wear. Thus, the UAT enhances the heat transfer taken place by forced convection and helps to reduce the tool wear.

### 5.1.3 Power consumption

Power consumption during machining is an essential factor in achieving sustainability. The power consumption should be reduced without hampering machining performance and product quality. The power consumption is considered for machining perspective for the present analysis. For each experiment, the value of apparent power is noted and the average value of apparent power is considered for the analysis. The error bar is representing a standard deviation from the mean value of power consumption. The standard deviation is calculated for each cutting condition and for CT and UAT processes. An average power consumption obtained for CT and UAT under different cooling strategies is shown in Figure 5.5. It can be noticed that dry and LCO<sub>2</sub> consume less power than wet and MQL conditions for both the processes. The power consumption is highest for the MQL, whereas it is lowest for the LCO<sub>2</sub>. The UAT and CT, both follow the same trend. The UAT consumes more power than CT under dry and wet conditions, whereas it consumes less than CT under MQL and LCO<sub>2</sub>. The dry condition does not use cutting fluid, i.e., no external equipment is required, thus lesser power consumption, in both the processes. A plastic deformation of the cutting edge in the UAT increases the friction at the tool-chip interface, enhancing the cutting forces and power consumption under dry conditions. However, the power consumption also depends upon the tool wear. The tool wear during machining under dry condition is larger than in LCO<sub>2</sub>, hence more power consumption is noted for the dry condition. The wet condition uses an external pump to supply the cutting fluid to the desired area, consuming more power. Moreover, the UAT has shown a higher flank wear value than CT, under wet condition, hence more power consumed by UAT. The MQL shows the highest power consumption due to the external use of a compressor. The MQL requires pressurized air to be compressed before supplying to the cutting zone. Thus, machining power and compressor power give the total power during machining under MQL. Additionally, the tool wear is higher for MQL than wet condition, enhancing the power consumption. Relatively lower power consumption in the UAT than the CT is attributed to efficient heat removal from the deformation zone. It is in agreement with the results obtained for machining of Nimonic 90 by Khanna et al. [203]. The LCO<sub>2</sub> is effective cooling provided by LCO<sub>2</sub> drastically lessens the tool wear in both the processes. Additionally, the UAT allows to dissipate the heat from the

deformation zone, reduces the average cutting forces and hence power consumption under LCO<sub>2</sub>. Eventually, power consumption is lower in LCO<sub>2</sub> compared to dry, wet, and MQL conditions. Quantitatively, an average reduction in power consumption for the CT under LCO<sub>2</sub> is 4%, 15%, and 41% compared to dry, wet, and MQL conditions. Similarly, an average reduction in power consumption for the UAT under LCO<sub>2</sub> is 11%, 26%, and 40% compared to dry, wet and MQL conditions.

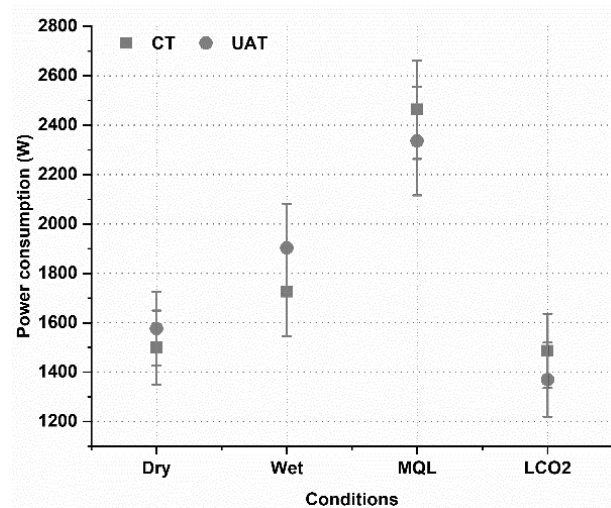


**Figure 5.5** Average power consumption measured in CT and UAT under different conditions

#### 5.1.4 Surface roughness

The machined surface quality is mainly influenced by workpiece material, tool material and geometry, cutting zone temperature, chip geometry, cutting fluid, etc. Higher surface quality reduces the rejection of the part. Typically, average surface roughness ( $R_a$ ) is used to check the quality of the machined surface. The error bar is representing a standard deviation from the mean value of average surface roughness. The standard deviation is calculated for each cutting condition and for CT and UAT. The  $R_a$  is quantified on the machined surface in the CT and UAT under different cooling strategies conditions and, the results are shown in Figure 5.6. It is clear that, the  $R_a$  is the highest for the dry condition, whereas it is the lowest for LCO<sub>2</sub>, for both the processes. The  $R_a$  does not show much variation in CT and UAT, except wet condition. It is said that higher flank wear obtained in the dry condition deteriorates the surface quality. As discussed earlier, the heat generation at the tool-workpiece interface is higher in dry conditions, decreasing the surface quality. When the worn tool comes in contact with a newly machined surface, degrading the surface quality [204]. The  $R_a$  does not show a much variation in the UAT under dry condition since the tool wear is severe and hence the  $R_a$  is higher. The wet condition significantly reduces the  $R_a$  in both the processes. The CT shows a slightly lower value of surface roughness compared to UAT. It is seen that the cutting fluid helps to remove the heat from the

deformation zone, reduce the thermal load. On the other hand, erosive action taken place at the tool-workpiece interface by hard carbide particles enhances tool nose and flank wear, increasing the  $R_a$  [193]. The reason for the higher value of  $R_a$  in the UAT is the high tool wear, as shown in Figure 3(b). The fracture occurs on the cutting edge in the UAT, producing heat when rubbing with the machined surface, reducing the surface quality. Higher flank wear increases the heat at the tool-workpiece interface, increasing the adhesion of microparticles diminishing the surface quality. The MQL reduces the  $R_a$  in the UAT, whereas it increases in the CT, compared to wet conditions. A worn tool observed for CT under MQL could be responsible for lowering the surface quality in the CT. On the other hand, the UAT allows the air and oil particles to enter at the tool-workpiece interface, lowering the friction and hence  $R_a$ . Nath et al. [147] observed that, the generation of thicker chips in the CT, producing frictional heat and cutting instability, deteriorating the surface quality. on the contrary, in the UAT when an intermittent cutting action reduces the frictional heat and forces, enhancing the surface quality. Additionally, the cooling provided by pressurized air, and lubrication provided by oil particles, further reduce the  $R_a$  compared to dry condition. The  $R_a$  reduces during machining under LCO<sub>2</sub> for both the processes. The LCO<sub>2</sub> offers an effective cooling that enforces the convective heat dissipation from the cutting zone. In addition to that, the tool wear observed for LCO<sub>2</sub> is low compared to other strategies, lessening friction and heat generation at the tool-work interface, enhancing the surface quality. The UAT under LCO<sub>2</sub> is much more effective in improving the surface quality. Due to the cyclic cutting nature of the UAT, it reduces the stresses imposed on the tool and chip breakability, which reduces the frictional heat and improves the surface quality. A similar observation is made in machining of Inconel 718 using UAT by Nath et al. [147]. Quantitatively, an average reduction in  $R_a$  for the CT under LCO<sub>2</sub> is 31%, 5% and 9% compared to dry, wet, and MQL conditions. Similarly, an average reduction in  $R_a$  for the UAT under LCO<sub>2</sub> is 31%, 18%, and 5% compared to dry, wet, and MQL conditions.

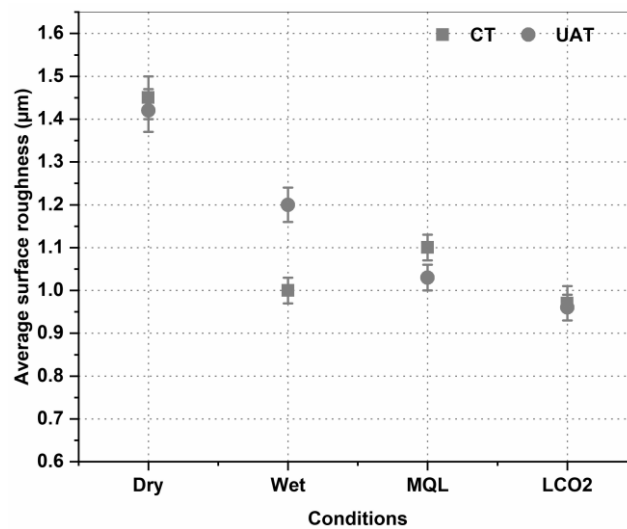


**Figure 5.6** Average surface roughness measured in CT and UAT under different conditions.

### 5.1.5 Variation in specific cutting energy and surface roughness with tool wear

Energy consumption during machining affects the sustainability goals. Thus, it is necessary to lower the energy consumption achieving good machinability of the materials. The specific cutting energy (SCE) criterion provides a measure of energy require to remove the unit volume of the material [205]. As given by Groover [206], The SCE is a ratio of power consumption during machining to the material removal rate, as given by equation (5.1),

$$SCE = \frac{P_M}{MRR} \quad (5.1)$$

Where,  $P_M$  is power consumed during actual machining in watt. It is determined by subtracting the idle power of machine from total power, as follows,

$$P_M = P_T - P_I \quad (5.2)$$

Where,  $P_T$  is the power require during cutting operation and  $P_I$  is power required when the machining tool is running without contact between tool and workpiece. The MRR is a product of cutting speed, width of cut and uncut chip thickness,

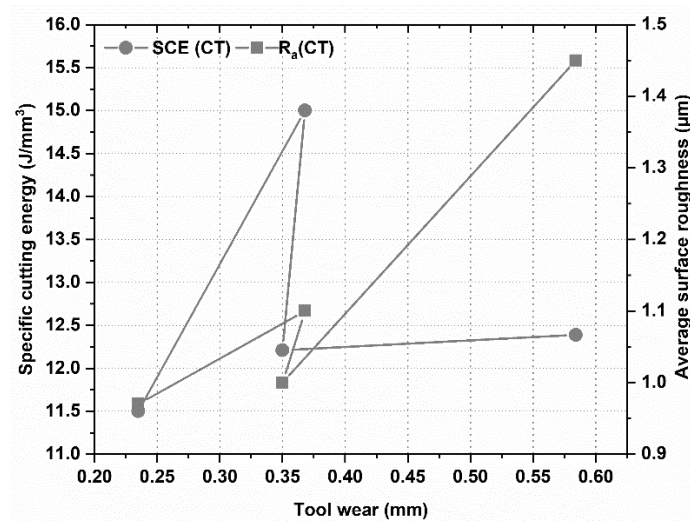
$$MRR = V t_0 a_p \quad (5.3)$$

Where,  $V$  is cutting speed,  $t_0$  is uncut chip thickness and  $a_p$  is width of cut. The specific cutting energy is affected by tool geometry, cutting speed and cutting fluids used during machining. It has been seen that when the cutting fluid is used, the SCE is reduced.

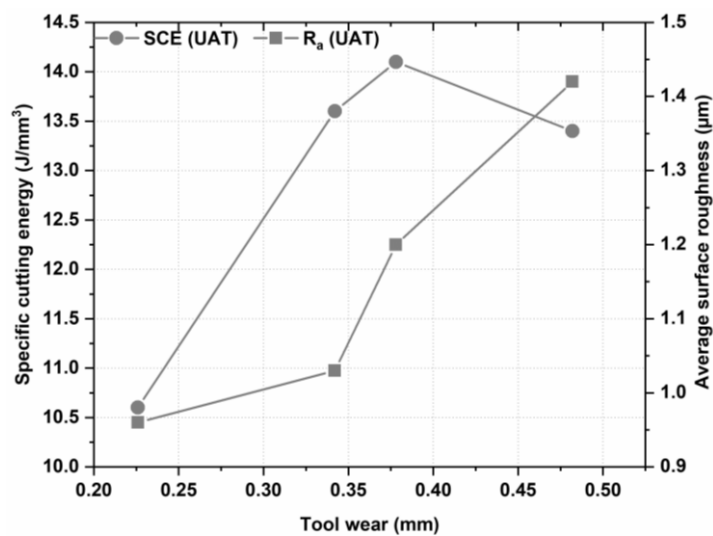
A variation in SCE and average surface roughness ( $R_a$ ) with tool wear for CT and UAT is presented in Figure 5.7(a) and 5.7(b), respectively, for different cooling strategies. The tool wear significantly affects specific cutting energy and surface roughness. The dry condition requires more SCE than wet and LCO<sub>2</sub> during CT and LCO<sub>2</sub> during the UAT. The fracture of the cutting edge takes place in the UAT considerably increases the friction between tool-workpiece and the tool-chip, increasing the SCE. Higher tool wear reduces the surface quality of part, showing a higher surface roughness. This agrees with the results obtained for machining Ti6Al4V by Ji et al. [207]. The tool wear is reduced during machining under wet conditions for both the processes. However, it needs a slightly higher specific cutting energy compared to the dry condition in the UAT. The surface roughness decreases in both the processes under wet condition. The wet condition effectively removes the heat from the tool-chip interface, decreasing the friction reducing the SCE. On the other hand, In the UAT, a severe fracture of cutting edge of the tool increases the temperature, increasing the friction. A coolant might not be sufficient to remove the heat, increasing the SCE. The MQL significantly increases the SCE during the CT, whereas it slightly reduces the SCE in the UAT. A small increment in tool wear enhances the specific cutting energy and surface roughness, in the CT. In case of UAT, a reduction in tool wear lowers the specific cutting energy and surface roughness. As discussed



previously for the UAT, the oil particles produce a lubrication layer at the tool-chip and tool-workpiece interface during the disengagement period, minimizing the friction, reducing the SCE. However, due to a lower thermal conductivity of Inconel 718, the heat gets accumulated at the tool nose where the cooling is insufficient, resulting in a cutting-edge fracture, increasing the SCE in the MQL compared to LCO<sub>2</sub> for both the processes [208]. The LCO<sub>2</sub> needs the least specific cutting energy since the tool wear is the lowest among all the cooling strategies. It also reduces the surface roughness in both the processes. It is thought that the LCO<sub>2</sub> effectively removes the heat from the deformation zone, reduces the contact length and friction. This results in reducing the SCE in both the processes. The effectiveness of LCO<sub>2</sub> in turning Inconel 718 leads to achieving a lower specific cutting energy without hampering the surface roughness, promoting sustainability in machining Inconel 718.



(a)



(b)

**Figure 5.7** Variation in (a) specific cutting energy and (b) average surface roughness with tool wear during CT and UAT under different cooling strategies

### 5.1.6 Chip morphology

The chip produced during machining depends upon the material properties, cutting conditions, cutting environments, input parameters, tool geometries, etc. The chips produced during machining in the CT and UAT under dry, wet, MQL, and LCO<sub>2</sub> are collected and observed microscopically. The chip geometry and morphology are displayed in Figure 5.8. The poor thermal conductivity of Inconel 718 leads to produce shear localized chips during machining. The chips formed in the CT under dry condition are long, continuous, plastically deformed, and non-uniform, as shown in Figure 5.8(a). The UAT reduces the

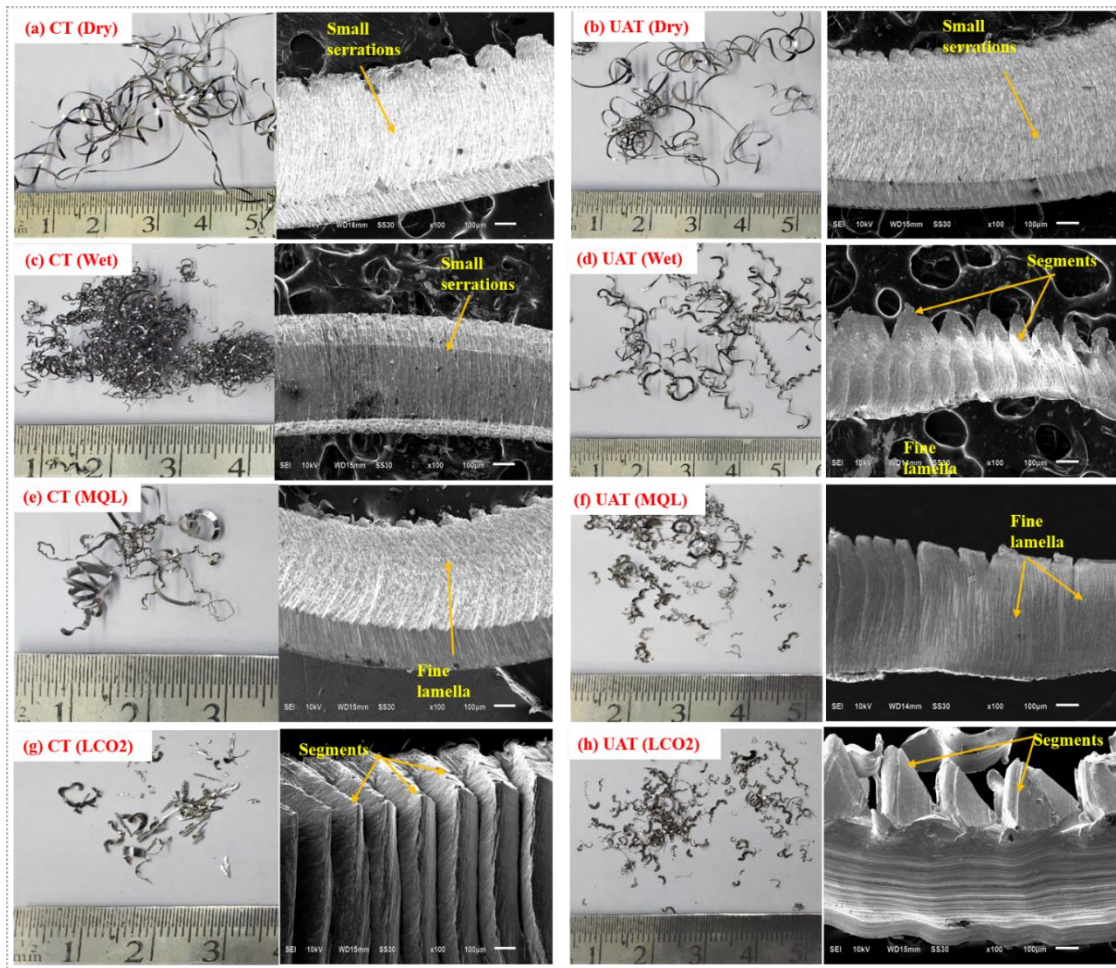


**Figure 5.8** Chips geometry and morphology observed in CT and UAT under different cooling strategies

plastic deformation by imposing ultrasonic vibration, producing shorter chips, as shown in Figure 5.8(b). The micrograph of the chip shows that the serrations are very small and have a lamella structure. This serration is the adiabatic shear band or shear localization in the chip. These chips formed are contained many segments together, forming continuous chips in both the processes [209]. The chips generated during CT and UAT under wet conditions are shown in Figure 5.8(c) and Figure 5.8(d), respectively. Cutting fluid used in wet condition increases the

chip breakability and produces shorter and thinner chips. The segments still look jointed together in the CT despite the cooling provided. At the same time, the UAT shows a clear difference in chip segments compared to CT. It is due to an ultrasonic vibration, which helps to propagate the crack in the chip, producing semi-continuous chips. The chips look thinner in the UAT as compared to that in the CT. The thinner chips in the UAT reduces the friction and forces and hence the high regenerative chatter, improving the surface finish. The CT and UAT under MQL, produce the chips with fine lamella, as shown in Figure 5.8(e) and Figure 5.8(f), respectively. Here, the effect of ultrasonic vibration can clearly be differentiated in terms of segmentation. The chips are thin and continuous in the CT, whereas they are shorter and discontinuous in the UAT. The cooling and lubrication offered by MQL decrease the friction at the tool-chip contact zone, producing uniform chips. Similar observations of chips during machining of alloy 625 are observed by Yildirim et al. [210]. The UAT enhances the cooling and lubricating effect provided by MQL during the disengagement of the tool with the workpiece. Thus, the chips isolate the shear band and form individual segments, i.e., semi-continuous chips. Moreover, a layer formed by oil particles reduces the friction and hence the plastic deformation, enhancing the surface quality in the UAT. The chips produced during machining under LCO<sub>2</sub> are distinct compared to other conditions. A pressurized flow of LCO<sub>2</sub> boosts the heat transfer from the deformation zone, tending to reduce the friction, producing the uniform chips. Moreover, the pressurized jet facilitates isolation of the shear band even in the CT, unlike in wet and MQL. The segments are evidently visible in the CT, as shown in Figure 5.8(g). The UAT further reduces the strain localization in the segment and producing the chips almost discontinuous, as shown in Figure 5.8(h). Thus, it can be said that the LCO<sub>2</sub> improves the chip morphology, increasing the surface quality and tool life.

### 5.1.7 Summary

Table 5.3 describes the comparison of LCO<sub>2</sub> with dry, wet and MQL for CT and UAT of Inconel 718. It can be noted that the LCO<sub>2</sub> performs better than other strategies in reducing flank and crater wear, surface roughness, power consumption and specific cutting energy, and improving the chip morphology. Moreover, the UAT under LCO<sub>2</sub> performs better than CT for all the outcomes. Thus, it can be said that the LCO<sub>2</sub> with UAT is more favorable to attain sustainability in the machining of Inconel 718.

**Table 5.3** Comparison of LCO<sub>2</sub> with other cooling strategies for CT and UAT of Inconel 718

<b>Machining Evaluation criteria</b>	<b>% Reduction with LCO<sub>2</sub></b>				<b>Effect of ultrasonic vibration</b>	<b>Remark</b>
	<i>Cutting strategy</i>	<i>Dry</i>	<i>Wet</i>	<i>MQL</i>		
<b>Crater wear</b>	Wet and LCO <sub>2</sub> reduce the abrasion, adhesion, and chipping				UAT is effective when used with wet and LCO <sub>2</sub>	Wet and LCO <sub>2</sub> perform better than dry and MQL
<b>Flank wear</b>	<i>CT</i>	60	28	32	UAT reduces the flank wear when used with LCO <sub>2</sub>	LCO <sub>2</sub> is better in reducing the flank wear compared to dry, wet and MQL
	<i>UAT</i>	53	39	32		
<b>Power consumption</b>	<i>CT</i>	4	15	41	UAT does not significantly affect the power consumption	Dry and LCO <sub>2</sub> reduce power consumption compared to wet and MQL
	<i>UAT</i>	11	26	40		
<b>Surface roughness</b>	<i>CT</i>	31	5	9	Wet and LCO <sub>2</sub> produce a better surface finish with ultrasonic vibration	CT with wet and LCO <sub>2</sub> and UAT with LCO <sub>2</sub> can be used
	<i>UAT</i>	31	18	5		
<b>Specific cutting energy</b>	Specific cutting energy requirement for LCO <sub>2</sub> is lesser compared to other strategies for CT and UAT				Reduced specific cutting energy without compromising performance compared to CT	UAT under LCO <sub>2</sub> performs better in reducing the specific cutting energy
<b>Chip morphology</b>	Chips formed are of scaly structure and fine lamella almost in all the strategies. LCO <sub>2</sub> helps in isolating the shear band				Ultrasonic vibration facilitates to enhance the chip breakability and segmentation frequency	UAT under LCO <sub>2</sub> gives better chip morphology than other strategies

### 5.1.8 Conclusions

A hybrid UAT+ cryogenic / MQL system has been presented in this research for decreasing tool wear and increasing machinability of Inconel 718. The novelty of this work is in terms of a combination of lubrication (MQL) and cooling (LCO<sub>2</sub>) the ultrasonic vibration. A comparison of different cooling/lubricating methods, namely dry, wet MQL, and LCO<sub>2</sub> was made to explore the machining performance in terms of tool wear, power consumption, average surface

roughness, and chip morphology. Significant results show:

- Abrasion, chipping, plastic deformation of cutting edge, are the main mechanisms observed for tool crater wear in dry, wet, and MQL conditions. The effective cooling provided by LCO<sub>2</sub> significantly minimizes the crater wear for CT and UAT.
- The main flank wear mechanisms observed are abrasion, chipping, and nose wear in the CT and UAT. The LCO<sub>2</sub>, along with CT and UAT, eliminates chipping and abrasion. The CT under LCO<sub>2</sub> reduces an average width of flank wear by 60%, 28% and 32%, and the UAT under LCO<sub>2</sub> reduces by 53%, 39%, and 32%, compared to dry, wet, and MQL conditions.
- The power consumption is the highest for the MQL condition whereas it is lowest for the LCO<sub>2</sub>. The LCO<sub>2</sub> reduces the tool flank and crater wear significantly, lowering the power consumption. An average reduction in power consumption for the CT under LCO<sub>2</sub> is 4%, 25%, and 41% compared to other strategies. Similarly, for the UAT under LCO<sub>2</sub>, it is 11%, 26% and 40% compared to other strategies.
- The intermittent cutting nature of the UAT produces a lower surface roughness compared to the CT, mainly under dry, MQL and LCO<sub>2</sub>. An average reduction in average surface roughness for the CT under LCO<sub>2</sub> is 31%, 5% and 9% compared to other strategies. Similarly, for the UAT under LCO<sub>2</sub>, it is 31%, 18% and 5% compared to other strategies.
- The LCO<sub>2</sub> with UAT significantly reduces specific cutting energy without compromising tool wear and surface quality. The LCO<sub>2</sub> may attain the sustainability goal without compromising the machinability of Inconel 718.
- The chips produced under LCO<sub>2</sub> are shorter and discontinuous. The LCO<sub>2</sub> enhances the chip breakability and reduces strain localization. The UAT makes chips shorter and reduces the plastic deformation, improving the chip breakability and segmentation frequency.

## 5.2 Experimental analysis for Ti6Al4V

### 5.2.1 Methodology

A cylindrical bar of Ti6Al4V with a diameter of 35 mm is used to perform the experiments. The experiments are performed for CT and UAT using different strategies such as dry, wet, MQL, and LCO<sub>2</sub>. Cutting speeds, feed, depth of cut, frequency, and vibration amplitude are considered as input parameters. All the experiments are repeated twice to minimize the parametric error. Machining performances such as tool crater and flank wear, power and specific cutting energy consumption, surface quality, and chip morphology are examined. Table 5.1 and Table 5.2 represent the conditions employed for the machining, and cooling and lubrication, respectively.

### 5.2.2 Tool flank wear

A maximum width of the flank wear ( $VB$ ) is measured at three different locations of the tool using a scanning electron microscope. An average value of  $VB$  is considered for analysis. An average value of  $VB$  in CT and UAT under different cooling environments is revealed in Figure 5.9. Compared to the CT, the UAT shows an approximate reduction of 27%, 26% and 31% in  $VB$  under wet, MQL and LCO<sub>2</sub>. The CT shows an approximate reduction of 29% and 53% in  $VB$  under MQL and LCO<sub>2</sub>, compared to dry condition. The UAT shows an approximate reduction of 35%, 54% and 70% in  $VB$  under wet, MQL and LCO<sub>2</sub>, compared to dry condition. The CT shows a lower value  $VB$  than UAT, under dry condition. On the other hand, the UAT is better than CT, under wet, MQL and LCO<sub>2</sub>. It can also be detected that, the  $VB$  is slightly higher in CT under wet condition than dry condition, whereas it is significantly lower in UAT under wet condition than dry condition. Under MQL and LCO<sub>2</sub>, the  $VB$  shows a significant reduction compared to dry and wet conditions, in both the processes. Due to higher cutting temperature in the dry condition, the  $VB$  is higher in the UAT under dry condition [211]. Moreover, due to vibration in UAT, extra heat is also added, enhancing the wear rate in dry condition. Alternatively, in CT, the  $VB$  is slightly lesser in dry condition than in wet condition. It may be attributed to a chemical affinity of Ti-6Al-4V with coolant used for wet condition, progressing the wear rate and showing the higher value of  $VB$  [14]. In UAT, during the disengagement period, heat dissipates from cutting zone and lessens the temperature, lowering the tendency of chemical reaction of Ti-6Al-4V with the coolant. A reduction in the  $VB$  is due to the effect of cooling and lubrication under both the conditions. Oil particles in MQL form a lubricative layer at the tool-workpiece interface, lowering the interaction and reducing the  $VB$ . The LCO<sub>2</sub> drops the cutting

temperature significantly and retains the hardness of the tool for a longer time. Therefore, the  $VB$  is lesser under  $LCO_2$  under both the processes.

The morphology of flank wear observed in CT and UAT under different cooling strategies is exposed in Figure 5.10. The CT under dry condition shows a built-up edge (BUE), abrasion, adhesion, and peeling off the coating on the flank face, as revealed in Figure 5.10(a). On the other hand, in UAT under dry condition, the BUE and adhesion are not severe. However, abrasion and chipping of cutting edge are observed, as shown in Figure 5.10(b). Low heat conductivity and chemical reactivity of Ti-6Al-4V with the tool material, generating a high temperature and causing a BUE formation and adhesion. When the adhered material is removed, it brings a tool material with it, resulting in an edge chipping, as shown in UAT. According to Biksa et al. [212], the BUE is associated with attrition, resulting in chipping of the cutting edge, mainly in intermittent cutting. The tool repetitively separates with the workpiece generating an interrupted mode of cutting, increasing the tendency of edge chipping. A high heat generation in the deformation zone, in dry condition, peeling off the coating of TiAlN at high temperature, exposing the substrate to a workpiece. Exposure of substrate to workpiece causes abrasion, increasing the flank wear. The abrasion observed in the UAT seems less severe than in CT. The vibrations add additional heat but lessen the tool-workpiece contact area, decreasing the abrasion. Ultimately, it can be noted that abrasion and adhesion are the main tool wear mechanism observed in machining of Ti-6Al-4V under dry condition.

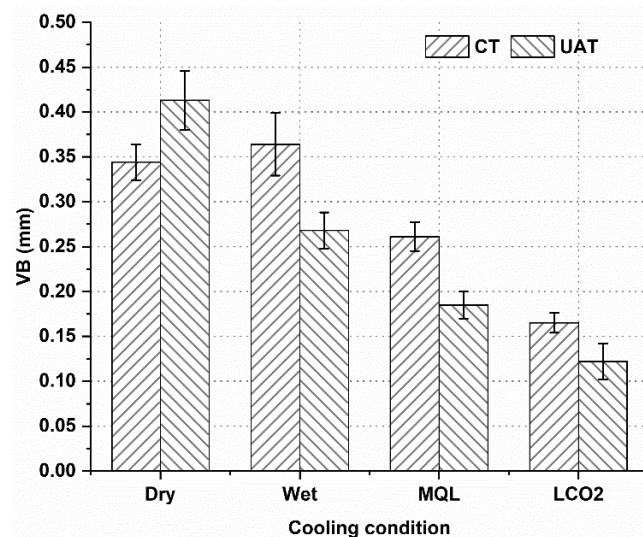


**Figure 5.9** Average width of flank wear measured under different cooling strategies

The CT shows substantial flank wear under wet condition, as observed in Figure 5.10(c). The flank wear is higher under wet conditions than dry conditions. On the other hand, the UAT shows a drastic lessening in flank wear compared to dry and the CT under wet conditions. A



BUE, adhesion of workpiece material and abrasion, are severe in the CT, whereas they look mild in the UAT, as shown in Figure 5.10(d). Some microparticles adhere on the flank face and peeling

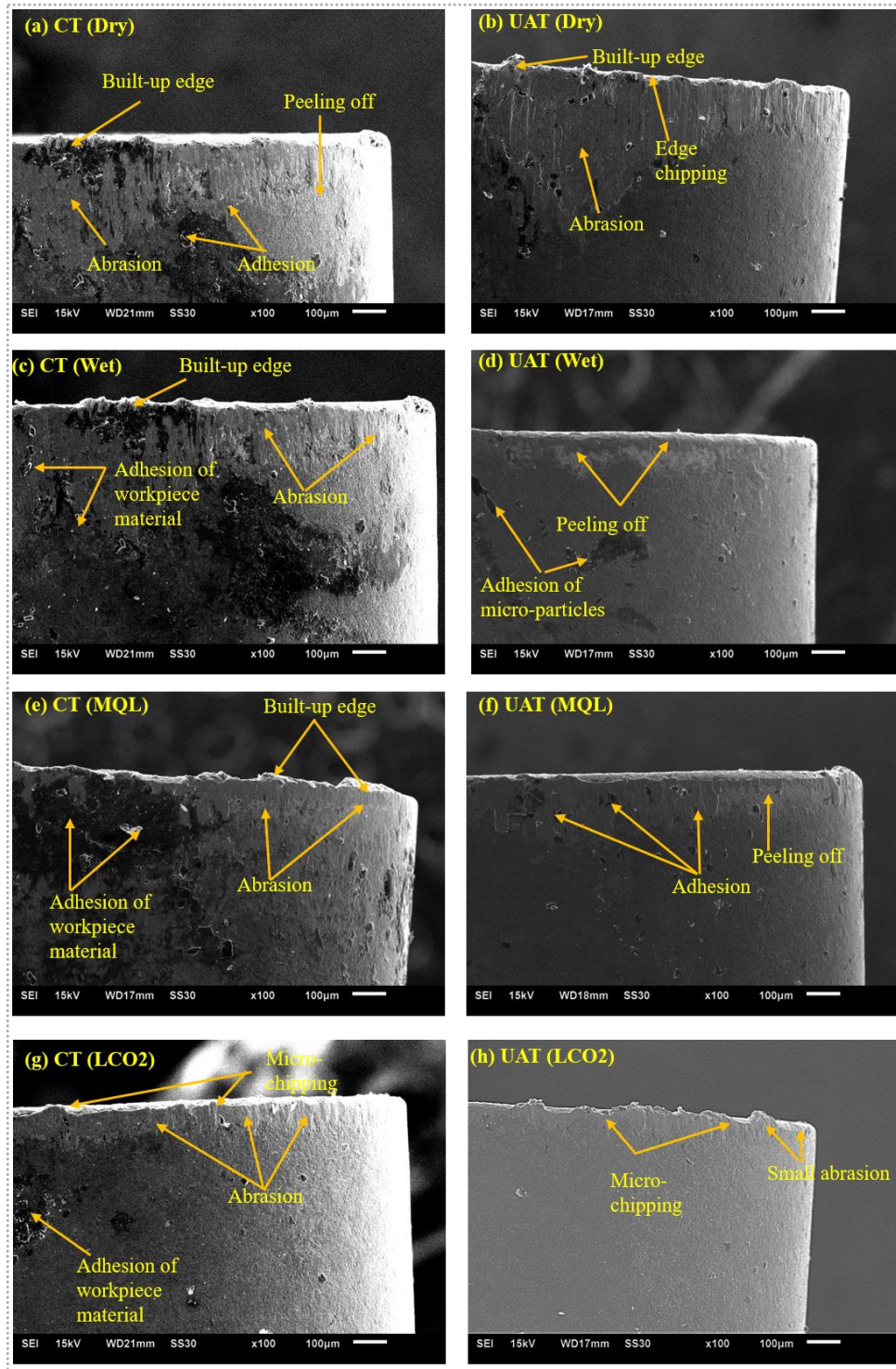


**Figure 5.10** Morphology of flank wear observed in CT under (a) dry, (c) wet, (e) MQL and (g) LCO<sub>2</sub>, and UAT under (b) dry, (d) wet, (f) MQL and (h) LCO<sub>2</sub>

of coating is taken place near the cutting edge. The wet condition could not prevent the adhesion of workpiece material due to the reactivity of titanium with the tool. It is found that during the



machining of titanium alloy, the additives in the cutting fluid react with the titanium. This chemical reaction causes abrasion on the flank face [180]. Additionally, the aluminum of TiAlN coating also reacts with the oxygen from the atmosphere and creates aluminum oxide, reacting rapidly with the titanium. As aluminum oxide has the least resistance of abrasion causing abrasive wear [214]. In the UAT, the chemical reaction is not as severe as in CT, eliminating the abrasion. Moreover, cutting fluid lowers the temperature in the deformation zone and decreases the adhesion due to ultrasonic vibration in the UAT. Thus, using ultrasonic vibration, the flank wear can significantly be reduced than CT even under flood cooling condition.

The CT under MQL shows almost a similar nature of flank wear as that in wet condition. On the other hand, the UAT shows a reduction in flank wear compared to dry and wet conditions. In the CT, the BUE formation, adhesion and abrasion are observed, as exposed in Figure 5.10(e). The size of BUE seems reduced under MQL than under wet condition. Furthermore, the adhesion and abrasion appear near the cutting edge and at the tool nose, respectively. As displayed in Figure 5.10(f), a small adhesion and peeling off the coatings are noted in the UAT compared to the CT. The MQL reduces the abrasion due to oil particles between the tool and workpiece, lowering the friction and heat [215]. However, the MQL is insufficient to minimize the adhesion, particularly in the CT due to the continuous contact. Owing to the poor heat conductivity of Ti-6Al-4V, the temperature at the cutting zone is very high, activating the ions of the oil particles. These ions then react with freshly generated workpiece surface, increasing the possibility of adhesion [216]. The lack of cutting fluid near the cutting edge and tool nose provides the conducive condition for workpiece and micro fragments to cause the abrasion. Ultrasonic vibrations combined with MQL significantly suppress adhesion and abrasion. This is attributed to an improvement in cooling and lubrication of MQL because of intermittent cutting. During the disengagement period in UAT, the oil particles can penetrate into the cutting zone, removing the heat and lowering the tool wear.

The LCO<sub>2</sub> shows a substantial reduction in flank wear as compared to other strategies, in both the processes. It also eliminates BUE formation in the CT, unlike in dry, wet and MQL. A small adhesion on the flank face and a minor abrasion and edge chipping are noted in the CT, as shown in Figure 5.10(g). On the other hand, a minor abrasion and edge chipping at the cutting edge are realized in the UAT, as given in Figure 5.10(h). The chipping is attributed to the thermo-mechanical load fluctuation at the cutting edge. Poor heat conductivity of Ti-6Al-4V generates a large heat; simultaneously, the LCO<sub>2</sub> reduces the temperature, producing a thermal load at the cutting edge and causing an edge chipping [217]. Furthermore, the segmented chips formed during machining of Ti-6Al-4V induce very high stresses at the cutting edge, causing an edge chipping. The TiAlN is insufficient to sustain a thermal and mechanical load and wears out rapidly by abrasion, mainly in CT. In the UAT, the ultrasonic vibration further enhances the

mechanical stresses imposed on the cutting edge and increases the chipping. Thus, the edge chipping seems a bit larger in the UAT than the CT. Similar observations have been made for the machining of Ti-6Al-4V under cryogenic cooling by Agrawal et al. [72]. Eventually, it can be said that LCO<sub>2</sub> is much more effective in machining Ti-6Al-4V in CT and UAT processes.

### 5.2.2 Tool crater wear

The chips sliding over the rake face significantly damages the rake face by causing high friction, stress and temperature. Thus, the rake face wear takes place. The morphology of crater wear observed in CT and UAT under different cooling strategies are presented in Figure 5.11.

As exposed in Figure 5.11(a), the CT under dry condition produces BUE, severe abrasion and crater. Unlike in the CT, the UAT suppresses the BUE, as shown in Figure 5.11(b). However, the abrasion, adhesion and peeling off the coatings are observed in both the condition in almost all the strategies. The chemical reactivity and poor heat conductivity of Ti-6Al-4V lead to BUE formation and adhesion on the rake face. Moreover, segmented chip formation during machining imposes higher stresses at the cutting edge, and welding of the chip with the rake face takes place. In the subsequent machining, when the chip adheres to the cutting edge is removed, it brings particles of tool materials and the formation of a crater occurs. Moreover, the coating of TiAlN no longer sustains such high stresses and temperature (up to 900°C [218]), allowing to diffuse the carbon into the chip, forming a crater. Thus, a crater is also formed due to the diffusion mechanism, mainly during the machining of titanium in dry condition. As long as the temperature is very high at the cutting edge, the coating becomes soft and wears out more rapidly with abrasion. Ultrasonic vibration reduces the adhesion and formation of BUE by improving the chip breakability. However, the tool particles sandwiched between chip and tool form wear by abrasion under high pressure and temperature, even in UAT. The peeling of the coating is mainly noted at a sleeping zone of the tool-chip contact area.

The wet condition minimizes the BUE formation, abrasion, and adhesion compared to that in dry condition, in both the processes. As shown in Figure 5.11(c), an abrasion, a small BUE and a crater are observed in the CT, whereas adhesion of small microchips and peeling off the coating are observed in the UAT, as shown in Figure 5.11(d). Thus, the UAT lowers the abrasion and adhesion compared to the CT. The wet condition provides sufficient cooling and eliminates the heat from the machining zone, reducing stresses and temperature and eventually lowering the wear than in dry condition [219]. Yet, the coolant is not effectively reached at the cutting edge, forming a small BUE. Due to uneven cooling near the cutting edge, thermal stresses are imposed, reducing the strength of the coating and cobalt binder. Therefore, the tool materials remove by the chips flow over the rake face, forming a crater by abrasion. Additionally, the chip

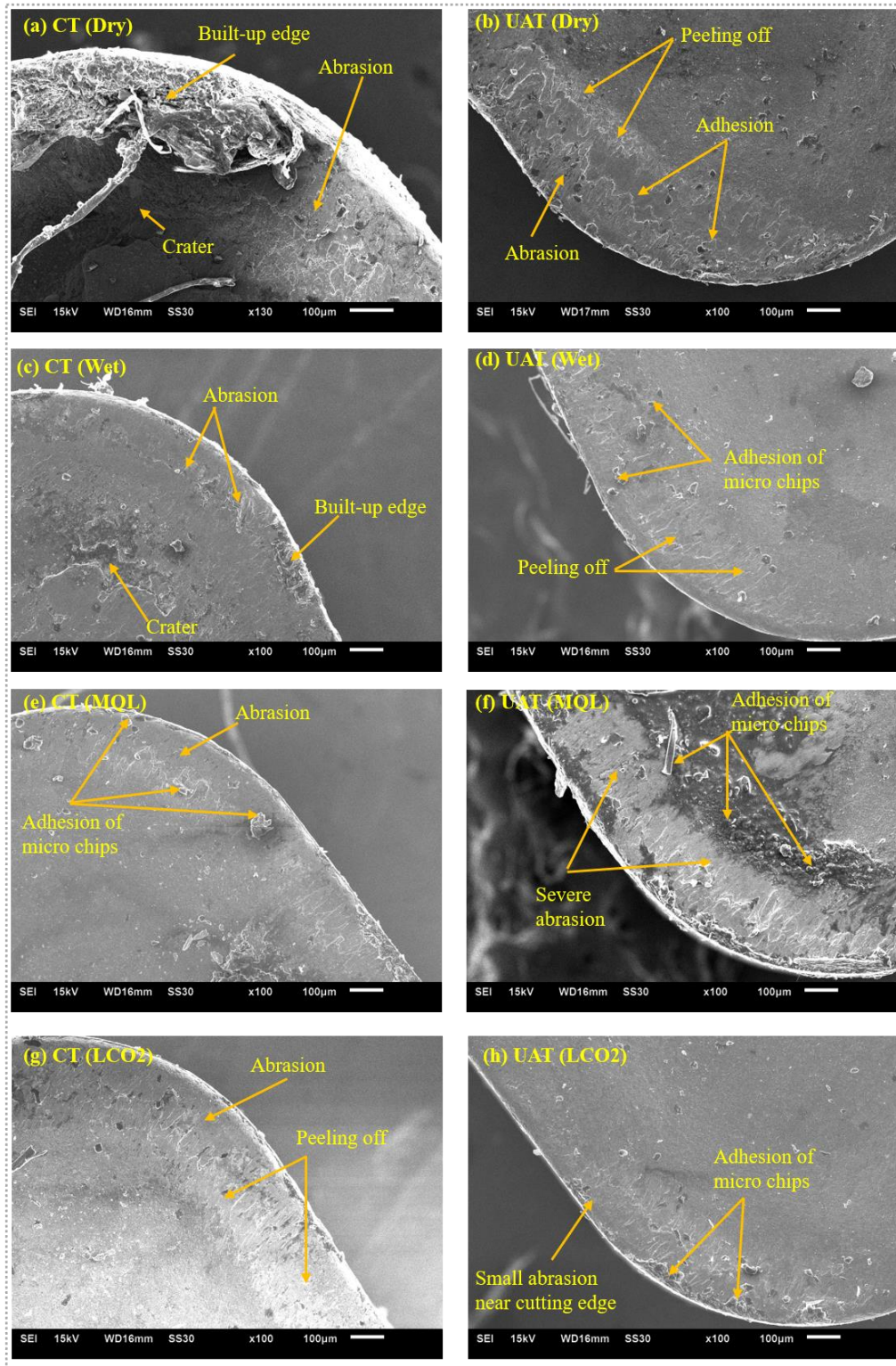


**Figure 5.11** Morphology of rake face wear observed in CT under (a) dry, (c) wet, (e) MQL and (g) LCO<sub>2</sub>, and UAT under (b) dry, (d) wet, (f) MQL and (h) LCO<sub>2</sub>

chemically reacts with the carbon in the tool, forming an interlayer of titanium carbide. This interlayer strongly bonds with chip and tool, endorsing seizure by the diffusion and producing a crater [214]. The UAT allows the cutting fluid to reach near the edge, dissipating the heat during the disengagement period. Furthermore, in the UAT, pulsating forces and stresses imposed on

the tool, reducing the average stresses and pressure on the rake face. Thus, the strength of the tool retains for a longer time, reducing the crater wear.

As shown in Figure 5.11(e), the MQL shows better results of tool wear on the rake face than in dry and wet conditions for the CT. On the contrary, the tool wear significantly increases in the UAT under MQL, as shown in Figure 5.11(f). The abrasion, adhesion and formation of BUE are decreased in the CT, whereas they are significantly higher in the UAT. The oil particles in MQL form a lubricating layer at interface area, lowering the friction and heat in the machining zone. According to Chetan et al. [187], the contact angle made by biodegradable oil on the surface of Titanium is relatively lower than other surfaces, improving the wetting capability and enhancing the lubrication. Therefore, an abrasion and adhesion decrease under the MQL. In the case of UAT, implying ultrasonic vibration itself generates heat and mechanical load at the cutting edge. Moreover, less quantity of fluid used in MQL is insufficient to disperse the heat from the tool-chip interface. Additionally, the compressed air used in MQL, might produce more friction at tool-chip contact zone, showing more abrasion compared to dry condition. Eventually, the cutting edge becomes soft due to a large heat generation and wear of coating occurs due to abrasion. Similar observations are made for ultrasonic-assisted side milling of Ti-6Al-4V under MQL by Ni et al. [220]. Thus, it can be said that the UAT is inferior under MQL in reducing tool crater wear than CT.

The LCO<sub>2</sub> shows a superior performance in terms of abrasion, adhesion and BUE compared to other strategies, in both the processes. Figure 5.11(g) shows that small abrasion and peeling off the coatings is mainly observed at the tool-chip contact area. Alternatively, the UAT greatly losses the abrasion and adhesion compared to the CT, as shown in Figure 5.11(h). The abrasion and adhesion of small microchips are primarily noted at the cutting edge and tool nose part. The LCO<sub>2</sub> lowers the cutting temperature retaining the hardness of the tool lowering the abrasion [221]. However, the shear localized chip formation in titanium machining induces a larger load at a cutting edge and tool nose. Eventually, the abrasion and peeling of the coating happen. In the UAT, the cyclic cutting nature of the tool reduces the load imposed by the shear localized chip on the cutting edge, decreasing tool-chip contact length and seizure zone. Moreover, it also allows the LCO<sub>2</sub> to penetrate at tool-chip interface, removing the heat and lessening the thermal load to the cutting edge. Ultimately, it reduces abrasion and adhesion on the rake face. In this regard, Sadik and Isakon [217] have noted in the milling Ti-6Al-4V that LCO<sub>2</sub> eliminates chipping and abrasion due to effective cooling. Ultimately, it can be said that LCO<sub>2</sub> is superior in decreasing the tool wear compared to other strategies, for both the processes. Additionally, the UAT further decreases the tool wear under LCO<sub>2</sub> attributed to intermittent cutting characteristics.

### 5.2.3 Power consumption

The power consumption during machining provides the stability of the process and helps to categorize optimum parameters for reducing energy consumption. To achieve sustainability in the machining process, the power consumption during machining should be minimized. This section analyzes the power consumed by machine tools during CT and UAT under different cutting environments. Figure 5.12 represents the power consumed in CT and UAT under different cooling strategies. The dry and LCO<sub>2</sub> conditions show a lower power consumption value than wet and MQL conditions. The UAT does not show a significant variation in power consumption in all the conditions. In the dry conditions, it is observed that the BUE formation is higher than in other conditions, acting as another cutting edge, lowering the tool-chip contact length and forces and ultimately power consumption. A reduction in machining force in UAT is owing to the pulsating cutting forces, reducing the average machining forces and power consumption [16]. The wet condition uses an external pump to flow the cutting fluid at the rake face during machining. Thus, adding the power required for machining and the external pump gives the total power for the wet condition. In the case of MQL, the power required to run the compressor is used to blow the air along with oil particles at the cutting zone. Thus, the total power required for machining under MQL becomes higher than in other conditions. When it comes to LCO<sub>2</sub>, no external component is used other than a cylinder of LCO<sub>2</sub>. In this regard, the power consumption could be lesser in machining under LCO<sub>2</sub>. On the other hand, an effective cooling provided by LCO<sub>2</sub> deliberately reduces the tool-chip contact length, friction at the cutting zone and heat, decreasing the power consumption in CT and UAT under LCO<sub>2</sub>. Quantitatively, an average drop in power consumption for the CT under LCO<sub>2</sub> is 15%, 30% and 60% compared to dry, wet and MQL conditions. Similarly, an average reduction in power consumption for the UAT under LCO<sub>2</sub> is 10%, 32% and 58% compared to dry, wet and MQL conditions.

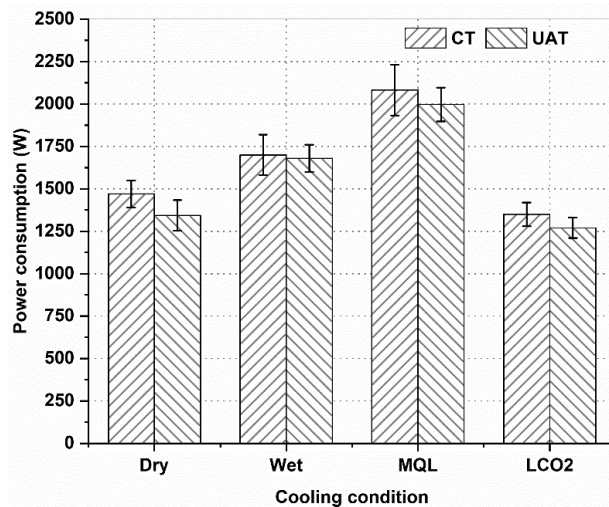


**Figure 5.12** Power consumption measured in CT and UAT under different cooling strategies

#### 5.2.4 Surface roughness

The machined surface quality is mainly influenced by workpiece material, tool material and geometry, cutting zone temperature, chip geometry, cutting fluid, etc [222]. Higher surface quality reduces the rejection of the part. Typically, average surface roughness ( $R_a$ ) is used to check the feature of the machined surface. In the present study, the  $R_a$  is measured on the machined surface at the end of machining in all the conditions and, the results are revealed in Figure 5.13. It can be observed that the  $R_a$  is maximum in dry conditions compared to wet, MQL and LCO<sub>2</sub> for both the processes. The UAT shows a significant reduction in  $R_a$  mainly under wet and LCO<sub>2</sub>. The  $R_a$  does not much differ both the processes, under dry and MQL conditions. Moreover, under dry and wet conditions, the difference between the  $R_a$  in CT is not significant, whereas, it is significant in case of the UAT. The tool wear is higher in dry conditions, deteriorating the surface quality. Moreover, the adhesion and abrasion take place on the tool, increasing the friction at tool-workpiece interface, raising the heat and lowering the surface quality. Compared to dry condition, the wet condition slightly reduces the  $R_a$  in the CT, whereas it reduces deliberately in the UAT. This is ascribed to the tool wear, which is more in the case of CT than in UAT. The higher tool wear in the CT reduces the surface quality and increases the  $R_a$ . The abrasion and adhesion of microparticles are responsible for degrading the surface quality in the CT. On the other hand, very less amount of tool wear in the UAT reduces the  $R_a$ . During the ultrasonic vibration, the cutting fluid can penetrate between the tool-workpiece and tool-chip contact area, removing the heat from the machining zone, improving the surface quality [17]. The MQL shows better results of  $R_a$  Compared to dry and wet conditions. However, the difference between  $R_a$  in CT and UAT is not noteworthy. A reduction in  $R_a$  is owing to evaporative cooling and lubricating properties. The former makes the tool-chip and tool-workpiece interface cooler, and the latter lowers the coefficient friction at secondary and tertiary shear zone. In addition to that, the pressurized airflow enforcing the chips to remove from the newly generated machined surface, improving the surface quality [223]. An ultrasonic vibration further enhances the surface quality by improving cooling and lubrication at the cutting zone during machining. The LCO<sub>2</sub> is superior in improving the surface quality compared to other strategies for both the processes. A drastic lessening in tool wear resulted in an improved surface quality under LCO<sub>2</sub>. Besides, the tool-chip contact length is much lesser during machining under LCO<sub>2</sub> than under dry, wet, and MQL lessening the friction at the secondary zone and reducing the heat and forces. Eventually, the surface quality improves under LCO<sub>2</sub> [224]. Moreover, LCO<sub>2</sub> provides sufficient cooling, which prevents thermal softening of the tool, chipping of the cutting edge, and ultimately reduces the  $R_a$ . The UAT under LCO<sub>2</sub> is much more effective in improving the surface quality. Due to the intermittent cutting characteristic between tool and workpiece in the UAT, it reduces the stresses imposed on the tool and chip breakability, which reduces the

frictional heat and improves the surface quality. Quantitatively, an average reduction in  $R_a$  for the CT under LCO<sub>2</sub> is 30%, 25% and 12% compared to dry, wet and MQL conditions. Similarly, an average reduction in  $R_a$  for the UAT under LCO<sub>2</sub> is 43%, 24% and 22% compared to dry, wet and MQL conditions.

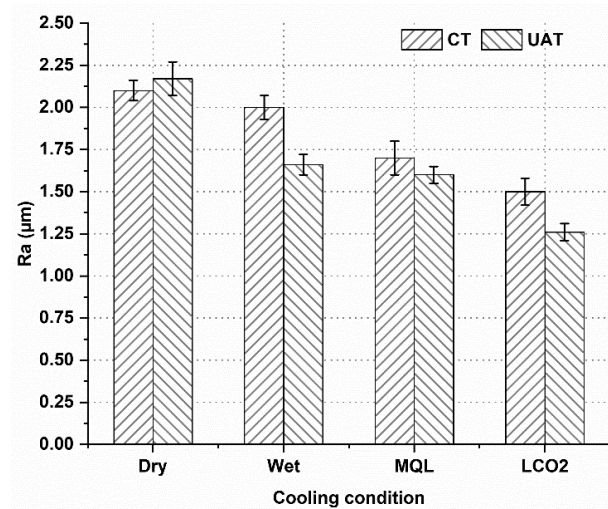


**Figure 5.13** Average surface roughness measured in CT and UAT under different cooling strategies

### 5.2.5 Variation in specific cutting energy and surface roughness with tool wear

A variation in SCE and average surface roughness ( $R_a$ ) with tool wear for CT and UAT is noted in Figure 5.14. It is noted that the SCE is the lowest and  $R_a$  is higher in CT and UAT under dry condition. The dry condition does not use fluid; thus, no external equipment is needed to lower the SCE. At the same time, the higher value of  $R_a$  is noted due to higher tool wear. The UAT requires a slightly less SCE though the tool wear and  $R_a$  is slightly higher than CT under dry condition. The wet condition has a higher SCE than dry condition due to more power consumption. The CT increases the SCE as the tool wear increases. Conversely, the UAT also raises the SCE though the tool wear decreases. The  $R_a$  is slightly reduced in CT though the tool wear increases, whereas the UAT shows a considerable reduction in  $R_a$  with tool wear [225]. The SCE in the MQL is highest among all the cooling strategies for both processes. An increment in SCE is due to the power consumption, which is highest for MQL in both the processes. On the other hand, MQL shows a substantial lessening in tool wear and  $R_a$ , yet the SCE is the highest. A reduction in  $R_a$  and tool wear in machining under MQL is already discussed in the previous subsections. The LCO<sub>2</sub> reduces the need drastically in both the processes. Additionally, it also decreases the tool wear and  $R_a$ , with a reducing in SCE. The LCO<sub>2</sub> system does not require any external equipment other than a cylinder of LCO<sub>2</sub>. Moreover, the effectiveness of LCO<sub>2</sub> in reducing the  $R_a$  and tool wear has been already discussed previously. The UAT along with



LCO<sub>2</sub> further reduces a requirement of SCE without the cost of tool wear and  $R_a$ . Thus, to attain sustainability, the LCO<sub>2</sub> and ultrasonic vibration are better among all other cooling strategies. A similar conclusion is also made during the machining of Ti-6Al-4V under LN<sub>2</sub> by Agrawal et al. [226].

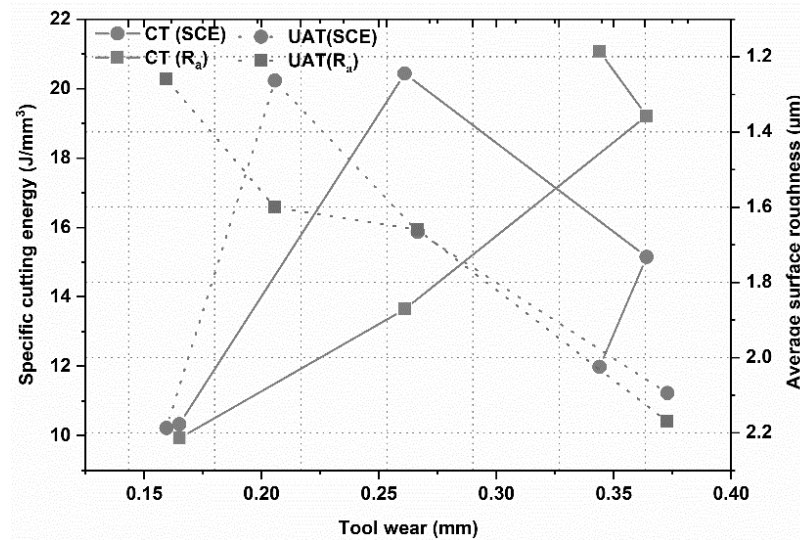


**Figure 5.14** Variation in specific cutting energy and average surface roughness with tool wear during CT and UAT under different cooling strategies

## 5.2.6 chip morphology

Segmented chips formation is a typical characteristic of titanium alloy. Segmented chips are mainly responsible for a periodic variation in cutting force and stresses, reducing the tool life and surface quality. This segmentation or shear localization in the chips could be due to an instability of plastic deformation, variation in physical and metallurgical changes, etc. In this study, the chips formed during CT and UAT of Ti-6Al-4V under dry, wet MQL and LCO<sub>2</sub> are collected and analyzed. As shown in Figure 5.15, the chip geometry is examined macroscopically, whereas; morphology is examined under SEM. As shown in Fig 5.15(a), the chips seem very long, irregular, and nonuniform in the CT under dry condition. In the dry condition, the heat generation at primary and secondary deformation zone is higher due to lack of cooling, increasing tool-chip contact length and friction producing nonuniform chips. Unlike the CT, the UAT produces discontinuous chips, as shown in Figure 5.15(b). An ultrasonic vibration lowers the tool-chip contact length due to the periodic disengagement of the tool and workpiece, reducing the friction and producing discontinuous chips. Moreover, it is also noted that chips formed in the UAT have fine lamella structure compared to CT. The vibration helps to propagate the crack produced, producing the chips with uniform fracture. The wet condition shows continuous spiral chips in the CT, whereas the chips are comparatively shorter with a large curling radius in the UAT. As shown in Figure 5.15(c), the chips show nonuniform fracture with



a fine lamella structure in the CT. The cutting fluid facilitates the shear band formation enhancing the chip morphology and producing the chips with fine lamella [217]. It can be depending upon the heat generation and friction at deformation zone. A reduction in temperature and friction produces the chips with a fine lamella. In the UAT, the cutting fluid penetrates between tool and chip, further lowering the friction and improving the chip

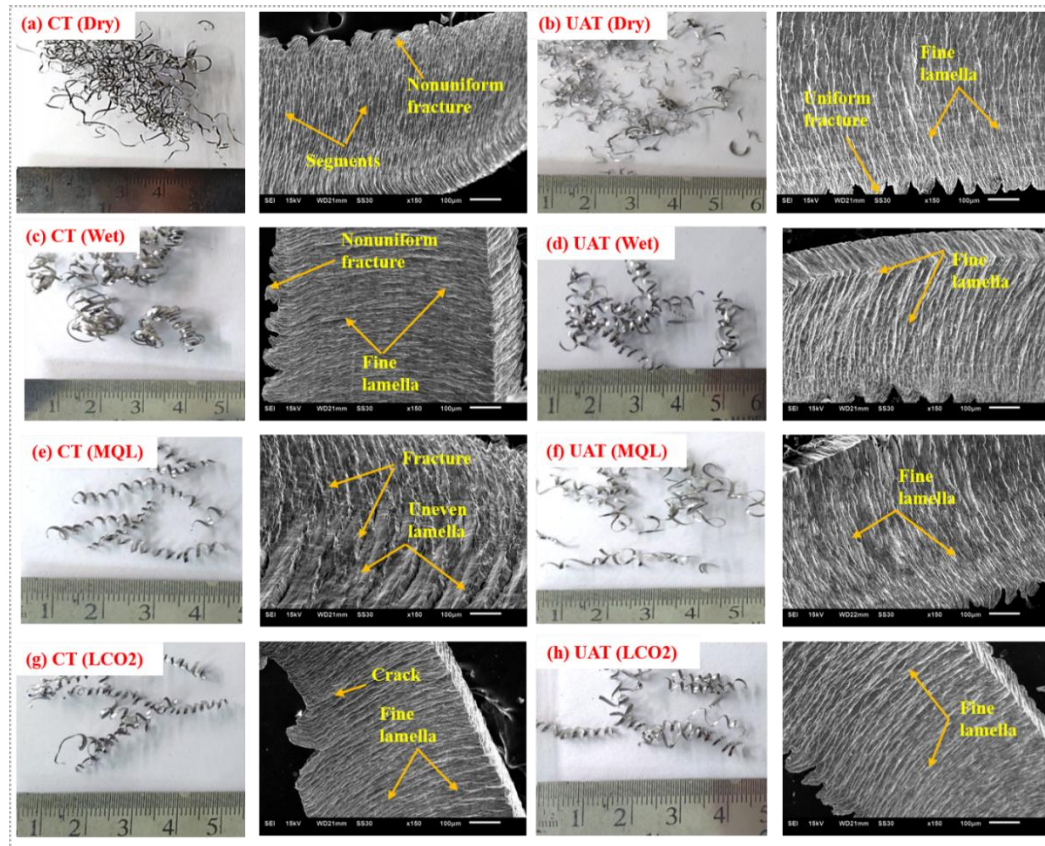


**Figure 5.15** Chips geometry and morphology observed in CT under (a) dry, (c) wet, (e) MQL and (g) LCO<sub>2</sub>, and UAT under (b) dry, (d) wet, (f) MQL and (h) LCO<sub>2</sub>

morphology. In the case of MQL, the chips produced are of lower curling radius and short length in the CT, as shown in Figure 5.15(e). The MQL makes chip removal easier by providing a high-pressure airflow between tool and chip. Moreover, the oil particles decrease the friction by forming a lubricating layer between tool and chip, making chip removal easy. However, due to insufficient cooling at the tool-chip contact length in the CT, the chips show an uneven lamella structure with a fractured surface. In the MQL due to insufficient cooling the friction is higher, increasing the temperature, producing fractured chips with uneven lamella. The UAT formed the chips with a shorter length and curling radius than CT, as shown in Figure 5.15(f). Ultrasonic vibration and pressurized air improve the chip breaking effect, producing chips with a fine lamella. A similar observation has been made in ultrasonic-assisted milling of Ti-6Al-4V by Ni et al. [220]. The CT and UAT, under LCO<sub>2</sub> produce the chips with shorter length. As presented

in Figure 5.15(g), the CT shows a chip with a fine lamella structure. The crack shown may be due to the thermal load generated due to the heat and cooling effect of LCO<sub>2</sub>. It can be explained by a reduction in tool-chip contact length due to the pressurized flow of LCO<sub>2</sub>, extracting the heat from the secondary shear zone. Therefore, less heat is dissipated to the tool, reducing the tool wear and forming the chips with a fine lamella structure. This mechanism is more effective in the UAT due to the intermittent cutting characteristic between tool and workpiece, producing very fine structured chips, as shown in Figure 5.15(h). Thus, it can be said the machining performance can be upgraded using the simultaneous effect of ultrasonic vibration and LCO<sub>2</sub>.

## 5.2.6 Summary

Table 5.4 describes the comparison of LCO<sub>2</sub> with dry, wet and MQL for CT and UAT of Ti-6Al-4V. It may be noted that the LCO<sub>2</sub> performs better than other strategies in reducing flank and crater wear, surface roughness, power consumption and specific cutting energy, and improving the chip morphology. Moreover, the UAT under LCO<sub>2</sub> performs better than CT for all the outcomes. Thus, it can be said that the LCO<sub>2</sub> with UAT is more favorable to achieve sustainability in the machining of Ti-6Al-4V.

**Table 5.4** Comparison of LCO<sub>2</sub> with other cooling strategies for CT and UAT of Ti-6Al-4V

<b>Machining Evaluation criteria</b>	<b>% Reduction with LCO<sub>2</sub></b>				<b>Novelty with UAT</b>	<b>Remark</b>
	<b><i>Cutting strategy</i></b>	<b><i>Dry</i></b>	<b><i>Wet</i></b>	<b><i>MQL</i></b>		
<b>Flank wear</b>	<b><i>CT</i></b>	53	56	38	Except for wet condition, it performed better than CT	Reduced adhesion and abrasion
	<b><i>UAT</i></b>	68	52	28		
<b>Crater wear</b>	Crater wear was lesser in LCO <sub>2</sub> compared to dry, wet and MQL, in CT and UAT				Except for MQL, it performed better than CT	Reduced diffusion, chipping, and adhesion
<b>Power consumption</b>	<b><i>CT</i></b>	15	30	60	Improved surface quality than CT	Improved surface quality
	<b><i>UAT</i></b>	10	32	58		
<b>Surface roughness</b>	<b><i>CT</i></b>	30	25	12	Reduced power consumption compared to CT	Reduced power consumption
	<b><i>UAT</i></b>	43	24	22		
<b>Specific cutting energy</b>	Specific cutting energy requirement for LCO <sub>2</sub> was				Reduced specific cutting energy without compromising	Lowest specific cutting energy

	lesser compared to other strategies for CT and UAT	performance compared to CT	among all the strategies
<b>Chip morphology</b>	Chips produced during machining under LCO <sub>2</sub> were comparatively thin and shorter	Improved chip breakability and morphology compared to CT	Better chip morphology due to efficient cooling

### 5.2.7. Conclusions

The machining of Ti-6Al-4V using conventional and ultrasonic-assisted turning was performed under dry, wet MQL and LCO<sub>2</sub>. The morphology and behavior of tool wear were analyzed and compared for CT and UAT under different cooling strategies. The effect of tool wear on the machinability of Ti-6Al-4V in terms of power consumption, average surface roughness and chip morphology was also studied. Based on the results discussed above, the following is concluded:

- The main flank wear mechanisms observed are abrasion, adhesion and BUE in the CT and UAT. The LCO<sub>2</sub>, along with ultrasonic vibrations, eliminates the BUE formation and flank wear. The UAT shows an approximate reduction of 35%, 54% and 70% in average width of flank wear under wet, MQL and LCO<sub>2</sub>, compared to dry condition.
- Diffusion, abrasion, adhesion, and chipping are the main mechanisms observed for tool crater wear in dry conditions. The wet, MQL and LCO<sub>2</sub> deliberately reduce the crater wear by enabling heat dissipation. The effective cooling provided by LCO<sub>2</sub> significantly minimizes the crater wear for CT and UAT.
- An average reduction in average surface roughness for the CT under LCO<sub>2</sub> is 30%, 25% and 12% compared to dry, wet and MQL conditions. Similarly, for the UAT under LCO<sub>2</sub>, it is 43%, 24% and 22% compared to dry, wet and MQL conditions.
- An average reduction in power consumption for the CT under LCO<sub>2</sub> is 15%, 30% and 60% compared to dry, wet and MQL conditions. Similarly, for the UAT under LCO<sub>2</sub>, it is 10%, 32% and 58% compared to dry, wet and MQL conditions.
- The chips produced under LCO<sub>2</sub> are shorter and have fine lamella structured in both the conditions. It is owing a reduction in tool-chip contact length and friction during machining under LCO<sub>2</sub>.
- The LCO<sub>2</sub> with UAT significantly reduces specific cutting energy without any compromise in tool wear and surface quality. The LCO<sub>2</sub> may attain the sustainability goal without compromising the machinability of Ti-6Al-4V.

- The UAT under LCO<sub>2</sub> shows a substantial enhancement in the machinability. It is attributed to the intermittent cutting characteristic between tool and workpiece, reducing average cutting forces, tool-chip contact length and improving chip breakability. Thus, it can be concluded that the UAT under LCO<sub>2</sub> promotes sustainability in the machining of Ti-6Al-4V.

## 5.3 Surface integrity analysis for Ti6Al4V

### 5.3.1 Methodology

In order to examine the surface integrity, i.e., surface roughness and topography, subsurface deformation, microhardness, the experiments are performed on Ti6Al4V using UAT and CT, under dry and VCF conditions. Cutting speeds, feed, depth of cut, frequency and amplitude of vibration are taken as input parameters. The range of process parameters are given in Table 5.5. All the experiments are carried out under dry and vegetable oil-based cutting fluid (VCF). Canola oil is used as vegetable oil. An emulsion of 10% Canola oil mixed with mineral water is used as cutting fluid. Each experiment is performed using a new cutting edge and was repeated two more times to reduce the experimental error. The average of three responses is considered for analysis.

The specimens used to measure the responses are cut using wire electro discharge machining. The surface roughness and surface topography are measured at three different locations and, average response is taken for analysis. Machined surface hardness is examined by Vickers indenter with a load of 1 kN for a dwell time of 10 s. To observed microstructures, each specimen is polished and etched in Kroll's reagent (H<sub>2</sub>O+HF+HNO<sub>3</sub>). The microstructures are observed using optical microscopy.

**Table 5.5** Components and process parameters used for experiments

Component/parameter	Attributes
Workpiece	Ti6Al4V- A cylindrical bar of 35 mm dia.
Tool	WC with CVD coating of TiCN-Al <sub>2</sub> O <sub>3</sub> -TiN, Nose radius: 0.8mm
Cutting parameters	Cutting speed: 50 m/min, Feed: 0.2 mm/rev, Depth of cut: 0.3 mm
Cutting action	CT and UAT
Operation	Axial turning
Frequency	20000 Hz
Amplitude	10 µm
Cutting condition	Dry and VCF (10% emulsion of Canola oil in mineral water)

### 5.3.2 Surface roughness

Surface roughness is considered the most typical parameter which prefers for surface irregularities generated during machining. The surface roughness is measured twice in a feed direction for each cutting condition and an average value is considered for analysis. It has been observed the surface roughness is mainly affected by feed rate and nose radius. However, it is also affected by cutting speed and depth of cut. An average surface roughness ( $R_a$ ) measured for CT and UAT under dry and VCF conditions is shown in Figure 5.16. The CT under dry condition shows the highest value of  $R_a$ , whereas it is the lowest for the UAT under VCF. due to an insufficient cooling and poor heat conductivity of Ti6Al4V, the heat generated at the cutting zone gets accumulated under the dry condition. Therefore, adhesion occurs on the tool under high temperature and pressure, deteriorating the surface roughness. On the other hand, under the VCF condition, some amount of heat gets removed from the cutting zone, minimizing the tool wear and hence the surface quality [179]. However, the difference in surface roughness is not significant in case of UAT under dry and VCF conditions. The UAT shows a significant reduction in  $R_a$  compare to that in CT, under dry condition. It is due to a lower duration of pulsating cutting force during UAT, improving surface quality, and reducing  $R_a$ . The use of VCF further reduces the  $R_a$  by decreasing the friction between tool and workpiece in both the processes. In the UAT, during disengagement period, the VCF penetrates at the deformation zones by capillary action, forming a lubricating layer and enhancing the surface quality [63]. A reduction in surface roughness in the UAT compared to CT, is also observed by Airao et al. [17]. The UAT under VCF shows an approximate reduction of 47%, 25%, and 10 % in  $R_a$ , as compared to in CT under dry, CT under VCF and UAT under dry condition, respectively.

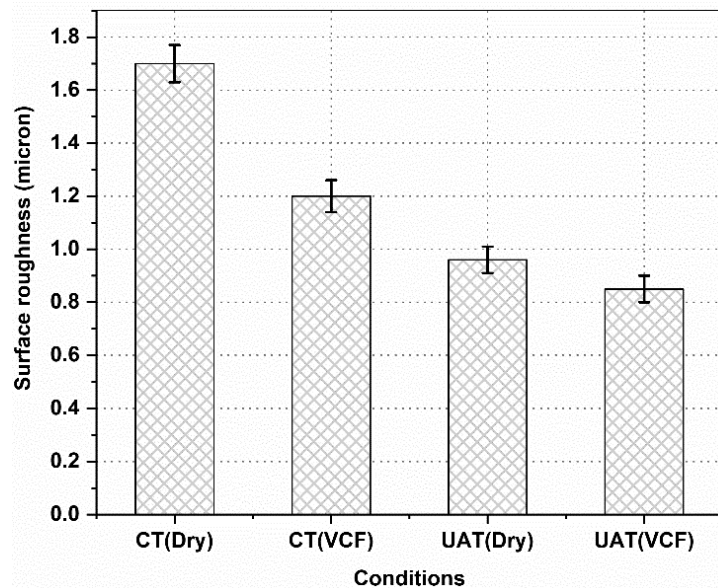


**Figure 5.16** Average surface roughness measured in CT and UAT and dry and VCF conditions

### 5.3.3 Surface topography

In order to characterize the finished surface topographies in CT and UAT, 3D optical images have been taken, as shown in Figure 5.17. Stepped or ridged textures with uniform spacing along the feed direction are observed in CT and UAT under both the conditions. The CT clearly highlights the ridges under dry conditions, as shown in Figure 5.17(a). Few small pits are also observed in the same condition. These may be attributed to adhesion of small microchips to the machined surface due to continuous contact in the CT. Similar peaks are also observed during dry turning of AISI 1045 steel by Maruda et al. [227]. As shown in Figure 5.17(c), the UAT under dry condition produces lower ridges decreasing the value of  $R_a$  as discussed in section 3.1. Due to ultrasonic vibrations, the ridges produced are uniform and regular, even in dry condition. Chen et al. [228] claimed during ultrasonic vibration helical milling of Ti-6Al-4V that the vibrations might generate a combined effect of friction and compression, reducing larger peaks produced during UAT. The use of VCF improves the surface topography in both the processes. As shown in Figure 5.17(b), the CT under VCF reduces the waviness of ridges compared to dry condition. As shown in Figure 5.17(d), The UAT produces more uniform ridges than CT under VCF and thus improves the surface topography. It can be explained by the improved lubricating properties of cutting fluid, reducing the friction at the tool-workpiece interface. In the UAT, during the disengagement period, penetration of the VCF is more than in CT, enhancing the lubrication, which lowers the peak height of ridges. The UAT under VCF shows an approximate reduction of 62%, 12%, and 7 % in the maximum peak height of ridges compared to that in CT under dry, CT under VCF and UAT under dry condition, respectively.

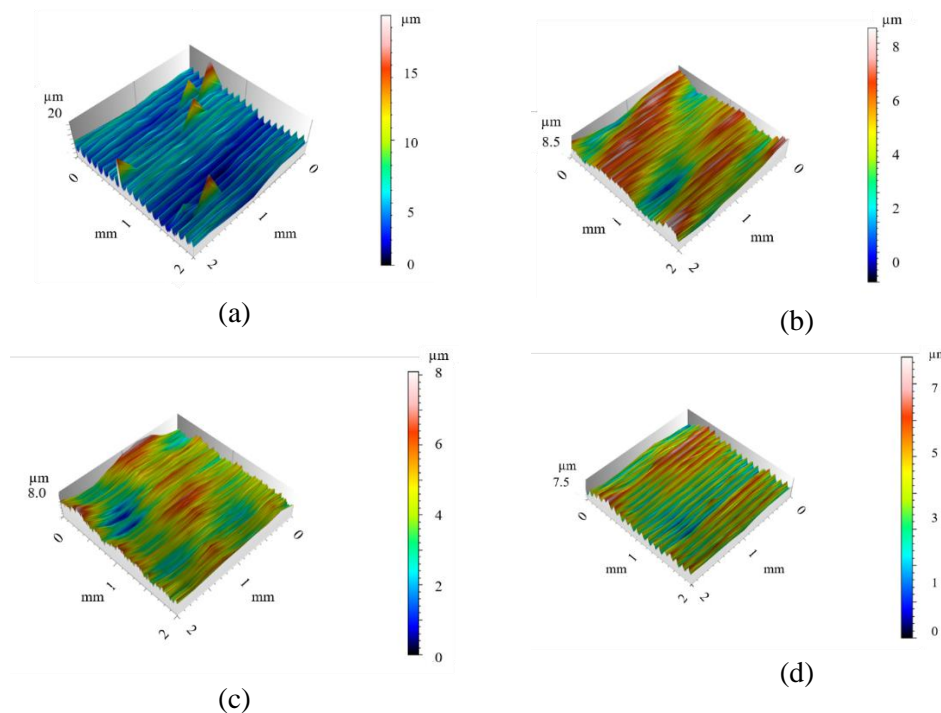




**Figure 5.17** Surface topography measured in (a) CT under dry, (b) CT under VCF, (c) UAT under dry and (d) UAT under VCF conditions

### 5.3.4 Microstructure of machined surface

The machining surface is affected by high thermal and mechanical load during machining. The machined surface could be divided into two different zones: plastic deformation zone and bulk material zone. The former contains distorted or affected grains, whereas the latter contains unaffected grains. Cross-section of machined surface in CT and UAT, under dry and VCF conditions, observed under a scanning electron microscope, are shown in Figure 5.18. For the CT, the machined surface zone, under dry and VCF conditions, is shown in Figure 5.18(a) and Figure 5.18(b), respectively. The CT under VCF shows a thicker deformation zone than the dry condition. The grain boundaries of the undeformed grains are clearly visible. The plastically deformed grains might be refined grains. The VCF reduces the microstructure alteration beneath the machined surface. The grain refinement under the VCF is due to a reduction in surface temperature, prevailing the microstructure behavior. According to Rotella et al. [229], less deformed grain in the vegetable oil is attributed to the prevention of grain growth after dynamic recrystallization, resulting from severe plastic deformation. In the case of the UAT, the depth of deformation zone is almost similar in both dry and VCF. However, the deformation is higher in the UAT compared to CT.

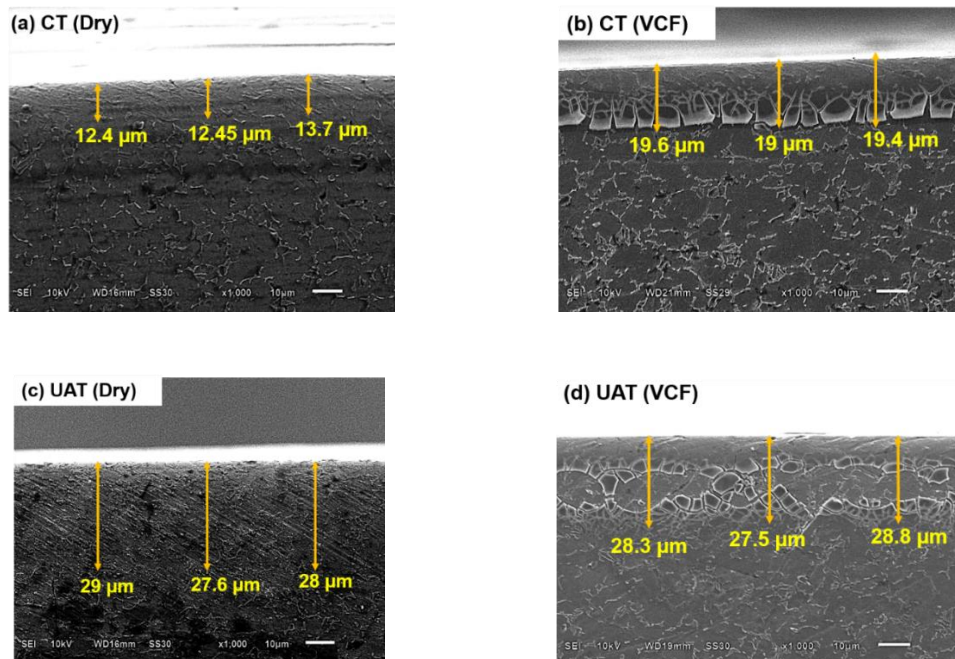


**Figure 5.18** Cross section of deformed layer under (a) CT under dry, (b) CT under wet, (C) UAT under dry and (d) UAT under VCF conditions

An increment in the depth of deformation zone is also observed for Ti6Al4V by Zhang et al. [35]. It is attributed to an impulse enhancement effect caused by high-frequency ultrasonic vibration, increasing the plastic deformation beneath the surface. The grains just below the deformation zone seem cracked in the UAT under VCF. It is noted that the CT under VCF shows a single layer of grain distortion, whereas the UAT under VCF shows double layers of grain distortion. It might be thought that due to the ultrasonic vibration and cooling impose the thermos-mechanical loading and hence, the cracks are generated. Due to the thermo-mechanical loading, the surface layer of the workpiece becomes soft. Therefore, the cracks generated propagated to another layer of the grain. It can also be said that more penetration of the VCF in the UAT than in the CT, significantly reduces the surface and sub-surface temperature, reducing the degree of plastic deformation under VCF than dry condition. A similar observation is made for the subsurface deformation for rotary ultrasonic elliptical vibration machining of Ti6Al4V by Liu et al. [34]. In addition to that, Willert et al. [230] have examined that in the UAT, the materials yield strength decreases due to the ultrasonic softening effect, causing the plastic deformation in a large depth. Thus, it can be said that the subsurface microstructure can severely affected by ultrasonic vibration and cutting fluid.

### 5.3.5 Microhardness

Measurement of hardness indicates the plastic deformation on the surface of the workpiece during machining. A degree of hardening is represented by the thickness of the plastic deformation layer [34]. Vicker hardness measurement is performed beneath the machined surface at three different locations, and an average is considered for analysis. The depth used for analyses is 250  $\mu\text{m}$  beneath the machined surface. The results obtained for CT and UAT under dry and VCF conditions are shown in Figure 5.19. The trend of the graph is almost similar for all the conditions. The hardness of the machined surface is much higher than bulk material hardness. The hardness values decrease gradually with the machined surface depth and approach the average value of bulk material. It can be said that high microhardness values beneath the machined surface are associated with strain hardening, plastic deformation, and dislocation density. In case of CT, the dry condition shows a high value of hardness compared to the VCF condition. It can be noted that the UAT gives a higher value of hardness than CT. A larger value of hardness is attributed to a higher strain hardening of a machined surface due to ultrasonic vibration. Moreover, the vibration may produce the rubbing effect on the machined surface leading to a distorted  $\beta$  phase on the surface and causing more strain hardening [228]. In case of the UAT, the hardness under dry condition is slightly higher compared to VCF condition, up to the depth of 50  $\mu\text{m}$ . On the other hand, when the depth increases beyond 50  $\mu\text{m}$ , the hardness for the VCF is significantly higher compared to dry condition for the UAT. The heat accumulation



at the contact zone provides a thermal softening effect, decreasing the hardness in the dry condition compared to VCF, in the UAT. Moreover, the ultrasonic softening effect also contributes in reducing the hardness. Furthermore, the VCF can reduce the temperature by applying cooling and lubrication on the machined surface. A higher hardness value under VCF is attributed to heating and cooling effects. Rahim and Sasahara [231] have reported that rapid cooling and heating increases work hardening during machining and enhances hardness. It can also be explained by the contact angle made by a fluid on the surface. A droplet of cutting fluid makes a smaller angle of contact on the surface of the titanium workpiece, increasing wettability, enhancing heat transfer, and reducing plastic deformation and increasing the hardness [232].

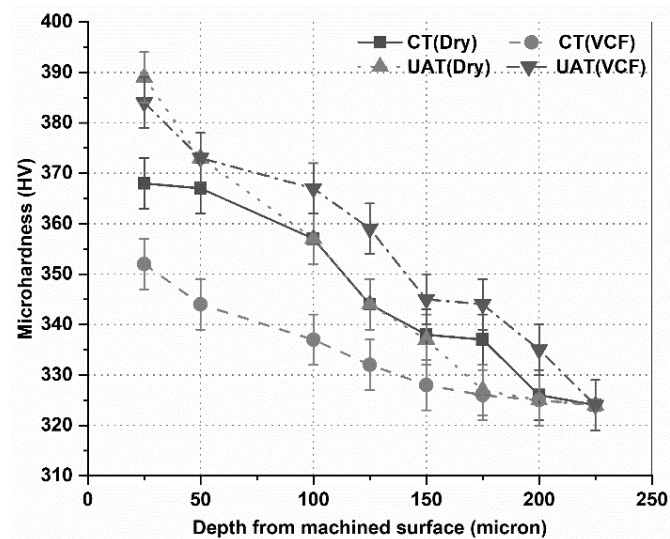


**Figure 5.19** Average variation in microhardness for different machining conditions

### 5.3.6 Conclusions

The surface integrity of Ti6Al4V has been analyzed in conventional and ultrasonic-assisted turning under dry and Canola oil-based cutting fluid. Eventually, the UAT under VCF gives better results for the surface integrity, promoting sustainability in the machining of Ti6Al4V.

The conclusions are summarized as follows:

- The UAT under VCF reduces an average surface roughness approximately by 47%, 25%, and 10% than CT under dry, CT under VCF and UAT under dry condition, respectively.
- The use of VCF improves the surface topography in both processes. The UAT under VCF shows an approximate reduction of 62%, 12%, and 7 % in the maximum peak height of ridges compared to that in CT under dry, CT under VCF and UAT under dry conditions, respectively.
- The plastic deformation and depth in the UAT are more than in the CT. It is attributed to the effect of ultrasonic vibration and thermal softening.
- The UAT under VCF gives a higher micro hardness value than in other conditions. A higher value is attributed to strain hardening due to ultrasonic vibration.

## Experimental investigation on the downscale of machining

Demand for the miniaturized components or products is increasing in the field of optics, medicines, biotechnology, electronics, avionics etc. The miniaturization of the components is required to reduce the energy and materials consumptions and to enhance the action of the devices. It also reduces the cost and increases the reliability, sensitivity and performance [233]. Considering the importance of the miniaturization of the components, it is necessary to explore the microfabrication processes. Additionally, the development of new engineering materials, offering high strength, has enforced the manufacturing industries to develop new microfabrication processes.

In order to respond the demand of miniaturized products, various microfabrication techniques such as, lithography, mechanical micromachining, thermoelectric micromachining and chemical micromachining processes. The aim of the micromachining processes is to create micro features and to generate micro or nano level finished products. The mechanical micromachining involves micro-turning, micro-milling, micro-drilling, micro-grinding etc. The mechanical micromachining processes are capable for producing complex miniature parts, 3D cavities and curvatures [234]. It is observed that the micromachining performance is greatly affected by microstructure of work materials, tool geometry, process stability, and specific cutting force imposing on the tool during machining [235].

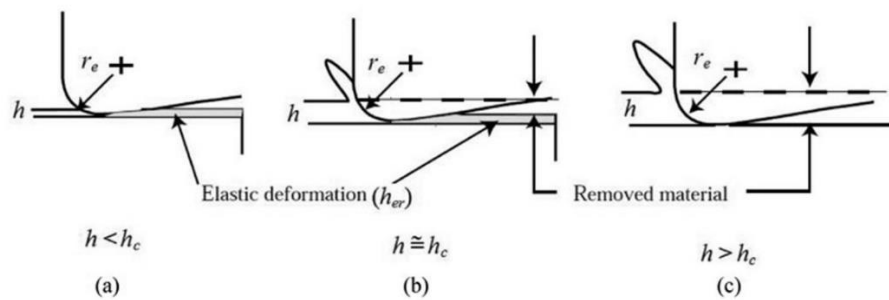


**Figure 6.1** Size effect in micro-scale machining process

Chae et al. [236] have explained the chip formation mechanism in micromachining as shown in Figure. 6.1. When the uncut chip thickness ( $h$ ) is less than the minimum chip thickness ( $h_c$ ), the material is formed elastically. Therefore, no material is removed from workpiece surface, as presented in Figure. 6.1 (a). When the uncut chip thickness is equal to minimum chip thickness, the chip forms through the shearing of the workpiece coupled with elastic deformation

and recovery. Thus, the amount of deformed material is less than the desired ones, as shown in Figure. 6.1(b). When the chip thickness is larger than the minimum chip thickness, material is removed and is produced a chip, as shown in Figure. 6.1(c). Thus, it is essential to determine the ratio of minimum chip thickness to the cutting-edge radius in micromachining, to avoid the size effect.

In this study, the micro-turning of different workpiece materials is performed to analyses the micro-scale cutting performance on the outcomes such as tool wear, chip morphology and surface quality.

## 6.1 Experimental analysis for Nimonic 90 in micro-turning

### 6.1.1 Methodology

In order to carry out in-dept analysis of tool wear for  $\mu$ -turning and a comparative study of tool wear for micro turning of Nimonic 90 under dry, wet and vegetable oil-based cutting fluid (VCF) conditions, three different combinations of cutting speed, feed rate and depth of cut are used for experiments. The values of process parameters are given in Table 6.1. These values of input process parameters are categorically decided based on reported in the literature.

**Table 6.1** Experimental conditions used in micro-turning of Nimonic 90

Parameter	Specification
Machine tool	Hybrid micromachine tool, Make: MIKROTOOLS, Model: DT110i
Workpiece	Nimonic-90
	Diameter: 5 mm
Tool	Tungsten carbide CCMT 060204
	Nose radius: 0.4 mm
	Rake angle: 0°
Vegetable oil	Canola oil
Cooling strategies	Dry, Wet (conventional cooling) and VCF (Emulsion of 10% Canola oil in mineral water)
Microscopic analysis	Scanning electron microscope
Set 1	$V$ : 10 m/min, $F$ : 0.03 mm/rev, $a_p$ : 0.06 mm
Set 2	$V$ : 25 m/min, $F$ : 0.02 mm/rev, $a_p$ : 0.05 mm
Set 3	$V$ : 40 m/min, $F$ : 0.01 mm/rev, $a_p$ : 0.04 mm

**Table 6.2** Chemical composition of Nimonic 90

element	C	Si	Mg	Cr	Ni	Ti	Al	Co	Fe
% weight	0.08	0.13	0.018	18.1	Balance	2.4	1.09	18.5	0.82

All the experiments have been carried out on a three-axis Multipurpose hybrid machine tool (Make: Mikrottools Pvt Ltd., Model: DT110i). The machine tool has an accuracy of  $\pm 1 \mu\text{m}$  in its axial movements with  $0.1 \mu\text{m}$  of resolution in linear optical scale in three axes. The experimental setup used for  $\mu$ -turning is shown in Figure. 6.2. The workpiece material used is Nimonic 90, a nickel-base superalloy. It is precipitation-hardened and consists of high mechanical properties and corrosion resistance. It is strengthened by adding Titanium and Aluminum with 16–20% chromium to enhance the corrosion resistance. It is used for components subjected to high-temperature environments. The chemical composition of the workpiece material is listed in Table 2. Similarly, for turning experiments, tungsten carbide inserts, CCMT 060204 (Make: WIDIA) is used. The length of the cut used is 15 mm and, for each cut, a new cutting edge is used.

Fatty acid and triglyceride are the main components of vegetable oil. Due to these components, polar groups like -COOR and -COOH is present in the vegetable oil, as shown in Figure.6.3(a). These polar groups are responsible for the lubrication properties of vegetable oil. The reason being a formation of a lubricating film on the surface of a workpiece, shown in Figure. 6.3(b), due to the magnetic property of the polar groups, reducing the friction [46]. In this study, Canola oil is used as vegetable oil. An emulsion of 10% Canola oil mixed with mineral water is used as a cutting fluid.

The worn tools are examined and characterized after each experiment. The flank wear on a flank face and the crater wear on a rake face is analyzed. For the characterization, the worn tools are etched in dilute Hydrochloric acid (HCl) to remove the adhered material. It was shown that HCl-based solution does not affect the WC grains [179]. A scanning electron microscope (Make: Jeol, Model: 6610 LV) is used to examine the tool wear and its pattern.

### 6.1.2 Flank wear

The flank wear observed on the flank face of the tool is measured using a scanning electron microscope, as shown in Figure. 6.4(a). The width is measured at three different points on the flank face, and an average value is considered for analysis. It is estimated at each set of machining parameters under dry, wet and VCF conditions. An average value of the width of flank wear at the end of machining is shown in Figure. 6.4(b). The highest width of flank wear is observed for set 2, followed by set 3 and set 1. The  $\mu$ -turning under VCF shows better results

for each set of machining. Except for set 1, the wet condition shows a higher width compared to dry and VCF conditions. Due to the chemical reactivity of Nimonic 90 with conventional cutting

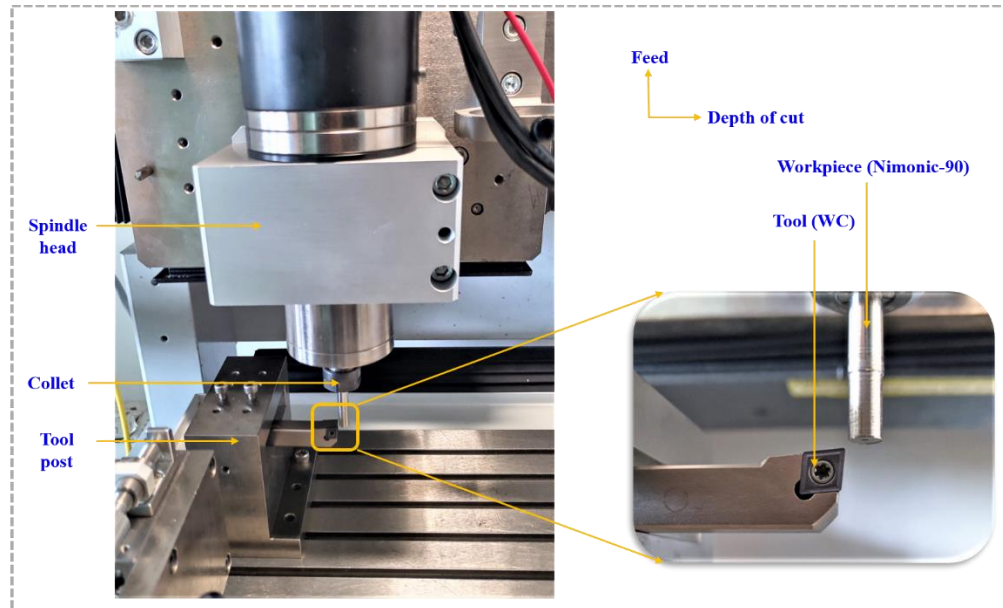


**Figure 6.2** Experimental setup used for  $\mu$ -turning

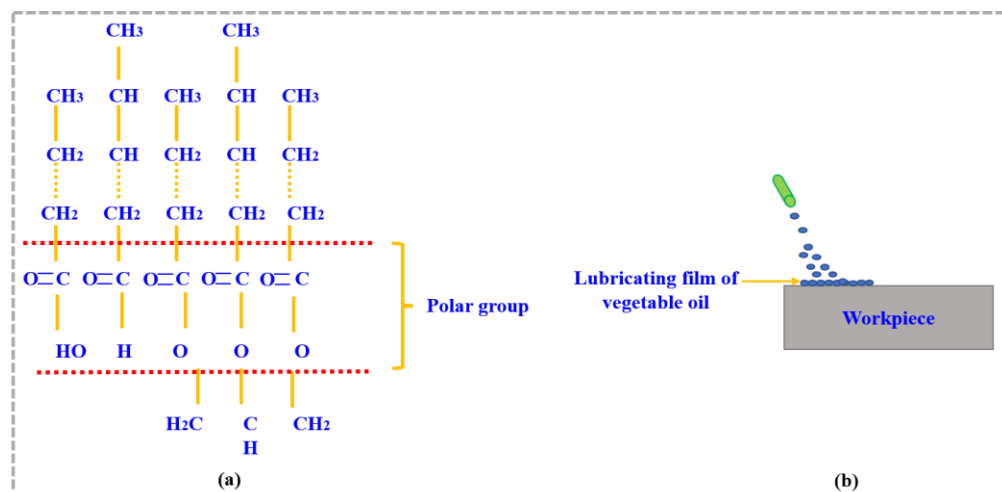


**Figure 6.3** Arrangement of molecule in vegetable oil and lubrication film of vegetable oil formed on a surface of workpiece

fluid, the width is higher than dry and VCF conditions. A similar observation was made for conventional turning of Nimonic 90, using coated carbide tool, under dry and wet conditions, by Airao et al. [178]. The difference in the width for VCF and the other two conditions is the highest at a lower cutting speed i.e., set 1. This difference reduces for set 2, followed by set 3. It is attributed to an increment in cutting speed that reduces the effectiveness of cutting fluid at the shear zone, reducing the difference in flank wear width. It is seen that the tool wear is mainly influenced by cutting speed followed by feed rate and depth of cut. At a higher value of cutting

speed, tool-chip contact length increases and, cutting fluid does not have sufficient time to penetrate between tool and chip, increasing the tool wear. On the other hand, as the feed rate decreases, the effect of size effect increases, enhancing the plowing force, which increases friction between tool and workpiece, enhancing the tool flank wear. The VCF reduces the width of flank wear due to forming a lubricating layer on the workpiece, reducing friction and wear of the tool. Moreover, the heat generated at the deformation zone is dissipated by VCF, reducing the strain hardening properties of Nimonic 90 and decreasing tool wear. A similar observation was made for micro-milling of Inconel 718 under MQL condition by Uzun et al. [237]. The VCF reduces flank wear width approximately by 52%, 19% and 12%, for set 1, 2 and 3, respectively, compared to dry condition. Moreover, the VCF reduces the width of flank wear approximately by 42%, 26%, and 25%, for set 1, 2 and 3, respectively, compared to wet condition.

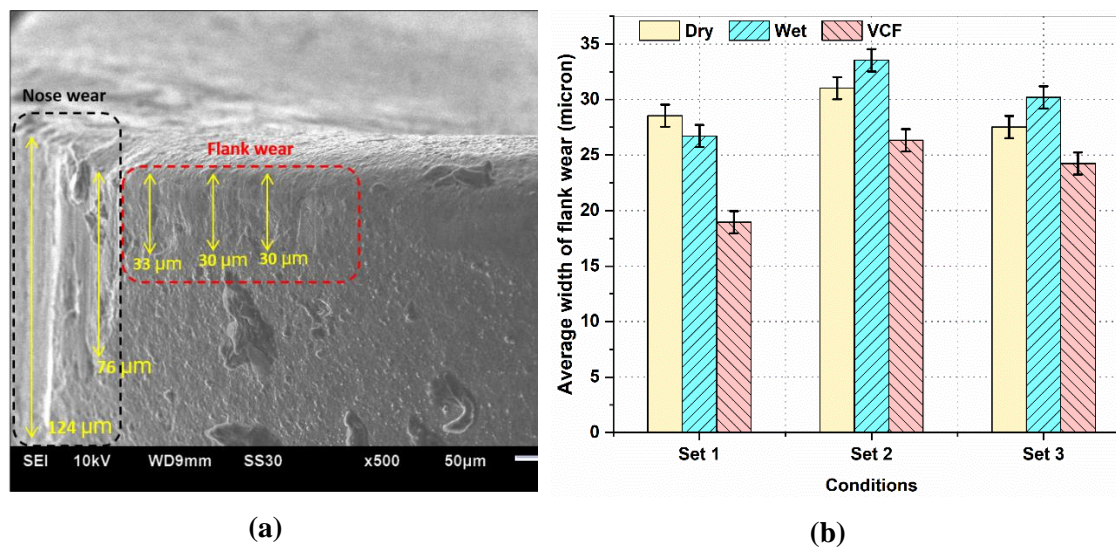


**Figure 6.4** (a) A typical flank wear and (b) average width of flank wear for each set under different conditions

A SEM was performed for flank and crater wear to understand the tool wear mechanism and for each condition. The flank wear observed for set 1 is shown in Figure. 6.5. The dry condition shows wear at the nose of tool, as shown in Figure. 6.5(a). It also shows the wear of cutting edge along with abrasion and adhesion of microparticles of workpiece material at flank face. The nose wear is primarily due to the abrasion of hard particles with the flank face of the tool [180]. In set 1, the feed rate and depth of cut used are higher, reducing the consequence of size effect, which decreases the plowing force in  $\mu$ -turning. On the other hand, a higher feed rate value increases the uncut chip thickness, enhancing the abrasion of workpiece material with the tool. During machining of nickel-base superalloys, stresses induce at the cutting edge are very



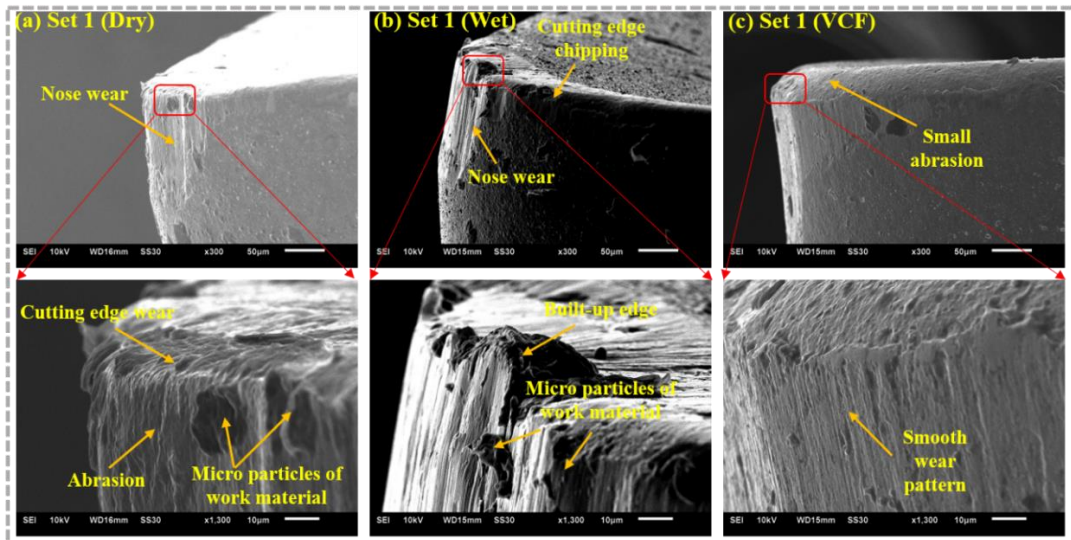


**Figure 6.5** Characteristics of flank wear for set 1 ( $V$ : 10 m/min,  $F$ : 0.03 mm/rev,  $a_p$ : 0.06 mm)

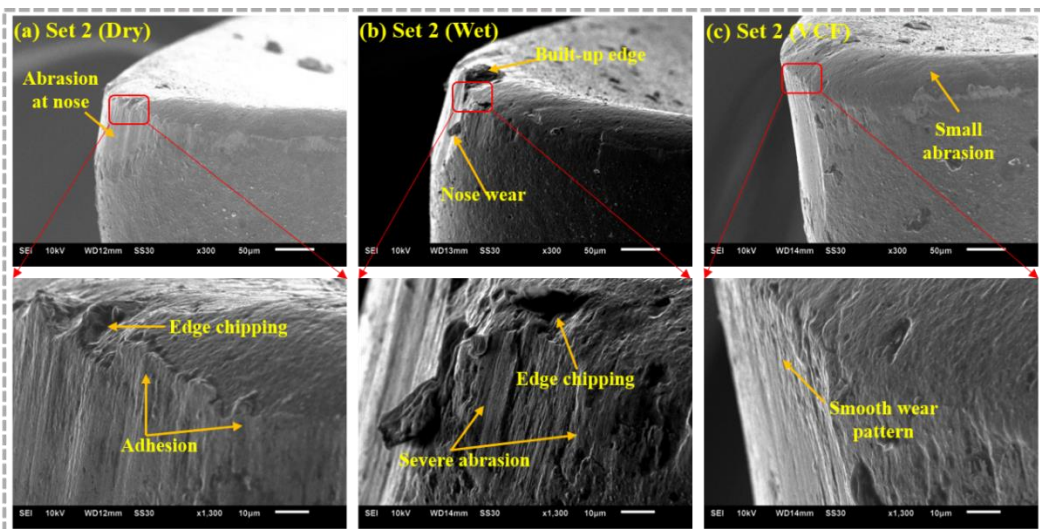


**Figure 6.6** Characteristics of flank wear for set 2 ( $V$ : 25 m/min,  $F$ : 0.02 mm/rev,  $a_p$ : 0.05 mm)

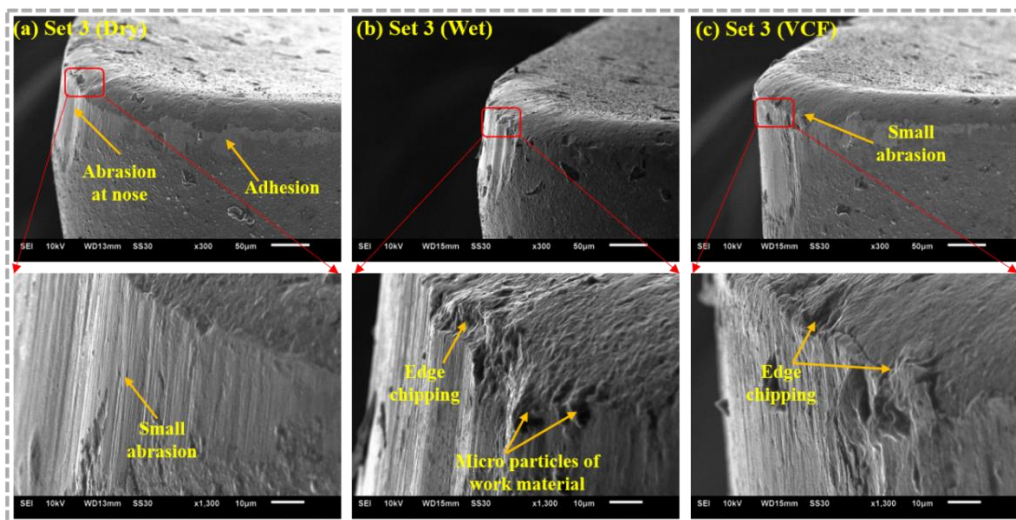


**Figure 6.7** Characteristics of flank wear for set 3 ( $V$ : 40 m/min,  $F$ : 0.01 mm/rev,  $a_p$ : 0.04 mm)

high; increasing the temperature causes the cutting-edge wear. The wet condition shows a built-up edge (BUE), nose wear, cutting edge chipping, and microparticle adhesion at the rake face, as shown in Figure. 6.5(b). The chemical affinity and ductile nature of Nimonic 90 cause the chip to stick to the cutting edge, forming a BUE during machining. When the BUE breaks, it removes a small fragment of the tool material, leading to a fracture of the cutting edge [155]. The edge chipping is attributed to thermal shock generated when the cutting fluid is supplied. The thermal shock reduces the hardness of the tool, enhancing the possibility of edge chipping. The ineffectiveness of coolant forms a BUE in a wet condition which also increases the tendency of edge chipping. VCF condition is not showing significant tool wear on the flank face, as shown in Figure. 6.5(c). A small abrasion at the cutting edge, and a smooth wear pattern on the flank face, are observed. It was observed that VCF prevents BUE formation and accumulation of small particles, reducing abrasive wear on the flank face. This is attributed to a thin layer formed between tool and workpiece, eliminating interaction and lowering friction and wear [238]. Furthermore, a layer formed between chip and tool prevents a BUE formation at cutting edge, and hence flank wear decreases under the VCF.

The mechanism of flank wear observed for set 2 is shown in Figure.6.6. In set 2, a higher cutting speed and a lower feed rate and depth of cut are used compared to set 1. The dry condition shows an abrasion of the tool nose and adhesion of workpiece material on the flank face, as shown in Figure. 6.6(a). It can be seen clearly that the abrasion and edge chipping reduce for set 2, compared to set 1. However, the adhesion of workpiece materials increases for set 2, which is not significant for set 1. The cutting speed used for set 2 is higher than set 1, raising the temperature and pressure, creating a chance to form an adhesive layer between tool and workpiece and chip. As the feed rate decreases, the plowing force dominates the shearing force in  $\mu$ -turning, resulting in the rubbing of the flank face of tool with workpiece, causing the abrasion. A layer formed on the flank face by adhesion protects the abrasion, which is severe at a higher feed rate for set 1. When the adhesive layer is removed, it brings some material and causes the edge chipping, as shown in same conditions. In the wet condition, the BUE, along with severe abrasion on the flank face and cutting-edge chipping, are observed, as shown in Figure. 6.6(b). Bai et al. [239] observed in the micromachining of Titanium 64 that a cutting depth is generally lower than cutting edge radius, forming a negative rake angle, dominating a thrust force that damages the flank face. Ultimately, the adhesion increases, and BUE forms. The BUE is attributed to the adhesion of corrosive particles of Nimonic 90 at the cutting edge of tool, under wet condition. In the subsequent machining, when the BUE breaks, it plucks some tool material, resulting in cutting edge wear. Again, the VCF condition does not show significant tool wear on the flank face, as shown in Figure. 6.6(c). The wear pattern looks very smooth. A small abrasion is observed on the flank face; however, it is not severe. It is thought that the plowing



force and hence friction is reduced by VCF, preventing the rubbing of hard carbide particles between tool and workpiece, reducing abrasion and adhesion wear. Similar observations are made during  $\mu$ -milling of Ti-6Al-4V under MQL condition by Khaliq et al. [240].

The mechanism of the flank wear observed for set 3 is shown in Figure. 6.7. An abrasion and adhesion are observed at a flank face in dry condition, as shown in Figure. 6.7(a). The abrasion marks are more considerable compared to those observed in sets 1 and 2. In set 3, an increment in cutting speed raises the temperature at cutting zone, raises the adhesive wear on the flank face. At the same time, a reduction in feed rate increases the plowing force. Thus, Hard carbide particles of Nimonic 90 are pressurized between the newly generated workpiece surface and tool, removing the material from the flank face by abrasion [240]. The adhesion is typically observed during machining of Nickel base superalloy at medium to high cutting speeds. The adhesion can be overcome by using lubrication and cooling. The use of coolant reduces the adhesion, as shown in Figure. 6.7(b). However, edge chipping is prominent in this condition. A higher cutting speed and low feed rate produce a high temperature near the cutting edge, generating the thermal load under wet conditions, decreasing the strength of the tool and increasing the possibility of plastic deformation [182]. The edge chipping is attributed to breakage of BUE at high cutting speed. The VCF condition also shows edge chipping and a small abrasion on the flank face, as shown in Figure. 6.7(c). However, the wear is not severe as that in wet condition. A long polar fatty acid chain in the Canola oil forms a lubricant film between metallic surfaces, reducing friction and lowering abrasion and adhesion on the flank face. However, a poor heat bearing capacity of VCF, not provide sufficient cooling near the cutting edge at a higher cutting speed, leading to small chipping of cutting edge.

### 6.1.3 Rake face wear

The tool wear mechanism on the rake face has been studied by SEM analysis. The crater wear observed for set 1 is shown in Figure. 6.8. The dry condition shows a predominant abrasion and adhesion of microchips on the rake face, as shown in Figure. 6.8(a). The abrasion is mainly between the tool rake face and the chip. Hard carbide particles of Nimonic 90 sandwiched between tool and chip and remove the material from rake face. Sharp grooves realize the abrasion in the chip flow direction in  $\mu$ -machining. At a higher value of uncut chip thickness, the shearing is mainly happening and chip over the rake face, shearing the material from the rake face. High temperature and pressure near the cutting edge adhere the microchips on the rake face in dry conditions. The wet condition shows adhesion of BUE and chipping of the cutting edge, as shown in Figure. 6.8(b). A crater is also formed under this condition. As explained earlier, a BUE is formed due to pressure and temperature, increasing the thrust force. Furthermore, the BUE increases the plowing effect and surface hardness due to strain hardening, particularly at lower

cutting speed in  $\mu$ -turning [242]. The cutting-edge chipping and crater formation are attributed to the thermal shock when cutting fluid is used. It is seen that oxidation can also occur when air is entrained to the cutting fluid. Oxygen from the air combines with a binder of the WC tool; it removes WC particles rapidly from the rake face [180]. A layer formed by VCF reduces the oxidation by decreasing the chemical reactivity of Nimonic 90 with air, lowering the crater wear, as shown in Figure. 6.8(c). A small abrasion at the tool-chip contact area is observed where an effect of VCF is insufficient. It is also observed that the amount of material adhered to the rake face is lesser than in dry and wet conditions. Similarly, a layer formed between tool and chips reduces the abrasion of tool material, lowering the tool wear.

The crater wears observed for set 2 is shown in Figure.6.9. An adhesion and abrasion are significant in the dry condition, as shown in Figure. 6.9(a). A lesser abrasion is observed in set 2 compared to set 1. The reason could be a reduction in thrust force when a lower feed rate is used in set 2, decreasing the abrasion on the rake face [241]. An adhesion of microchips is due to high pressure and temperature at a higher cutting speed. Compared to the dry condition, the wet condition shows severe cutting-edge chipping and adhesion, as shown in Figure. 6.9(b). Under the cutting fluid, in the absence of the adhesion of BUE, the possibility of abrasion is more than in dry condition. A lower uncut chip thickness increases the effective negative rake angle in  $\mu$ -turning, increasing the thermal load at the cutting-edge, Resulting in cutting-edge chipping. Similar results obtained in  $\mu$ -milling of UNS S32205 duplex stainless steel by Sanots et al. [243] found that The VCF reduces the abrasion near the cutting edge by penetrating between tool and chip. Adhesion of microchips is attributed to a higher temperature near the cutting edge due to an effective negative rake angle. It can be said that VCF can improve the machining performance by reducing the abrasion and adhesion wear from the rake face. It can be said that VCF provides adequate lubrication at a higher cutting speed and lower feed rate, achieving a more stable cutting process.

In set 3, the cutting speed is highest and, feed and depth of cut are the lowest among all the sets. As the cutting speed increases, the temperature at the cutting zone also increases. Moreover, a lower value of uncut chip thickness increases the effective negative rake angle, enhancing the tool wear on the rake face. The crater wears observed for set 3 is shown in Figure.6.10. Severe adhesion and crater formation are observed in set 3, compared to set 1 and 2, in dry condition, as shown in Figure. 6.10(a). When the uncut chip thickness is much lesser than the nose radius of the tool in  $\mu$ -turning, increasing the possibility of crater formation due to adhesion [244].

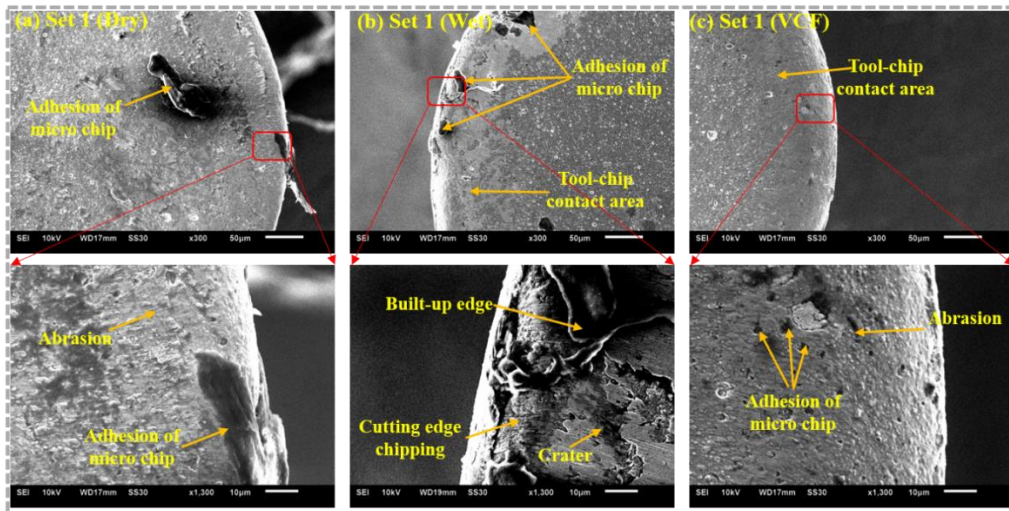


**Figure 6.8** Characteristics of crater wear for set 1 ( $V$ : 10 m/min,  $F$ : 0.03 mm/rev,  $a_p$ : 0.06 mm)

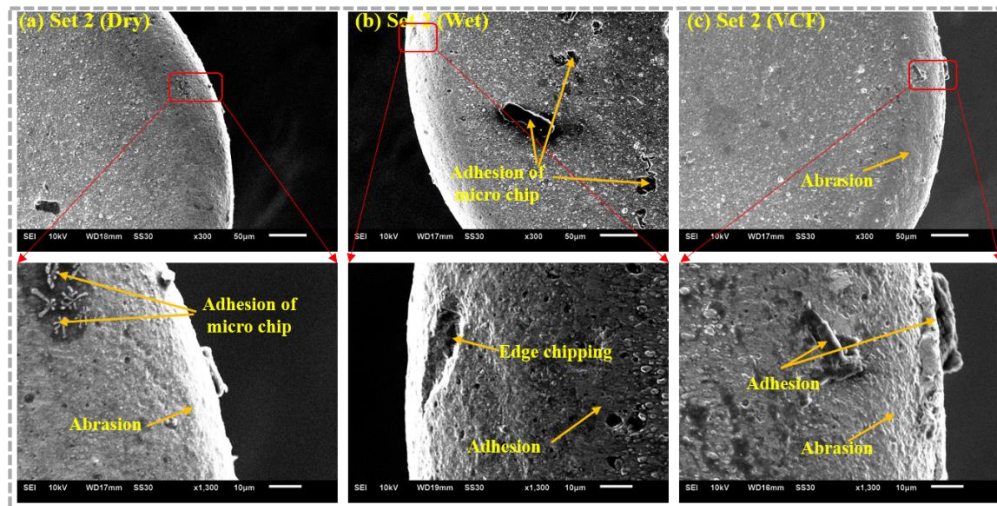


**Figure 6.9** Characteristics of crater wear for set 2 ( $V$ : 25 m/min,  $F$ : 0.02 mm/rev,  $a_p$ : 0.05 mm)

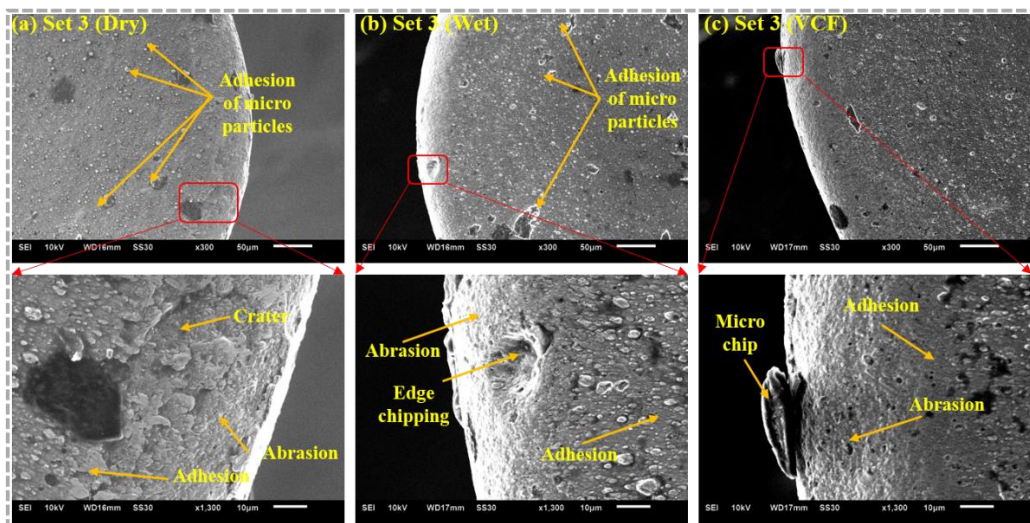


**Figure 6.10** Characteristics of crater wear for set 3 ( $V$ : 40 m/min,  $F$ : 0.01 mm/rev,  $a_p$ : 0.04 mm)



Additionally, Compressive stresses are imposed on the tool at a higher cutting speed, leading to the adhesion of workpiece material with the tool. As the machining progresses, this adhered material breaks, bringing some materials from the rake face, generating the crater. The wet condition shows more prominent wear than the dry condition, as shown in Figure. 6.10(b). Although the coolant is used, adhesion and abrasion are severe. Owing to the high friction and temperature involved during machining of Nimonic-90, some chip particles adhere to rake face even under wet condition. Cyclic removal of an adhesive layer and uneven temperature near the cutting edge in wet condition, leads to edge chipping [245]. The adhesion and abrasion are significantly reduced under VCF condition even at higher cutting speed, as shown in Figure. 6.10(c). A very small amount of abrasion is observed at the tool chip contact zone, under VCF. Compared to dry and wet conditions. The VCF also prevents forming a crater by creating a lubricating layer between tool and chip. Particles of VCF placed between tool and chip limit abrasion and adhesion from the tool's rake face, decreasing the wear from the rake face. Thus, it can be said that the VCF enhances the tribological properties, reducing the tool wear in  $\mu$ -turning.

#### 6.1.4 Chip morphology

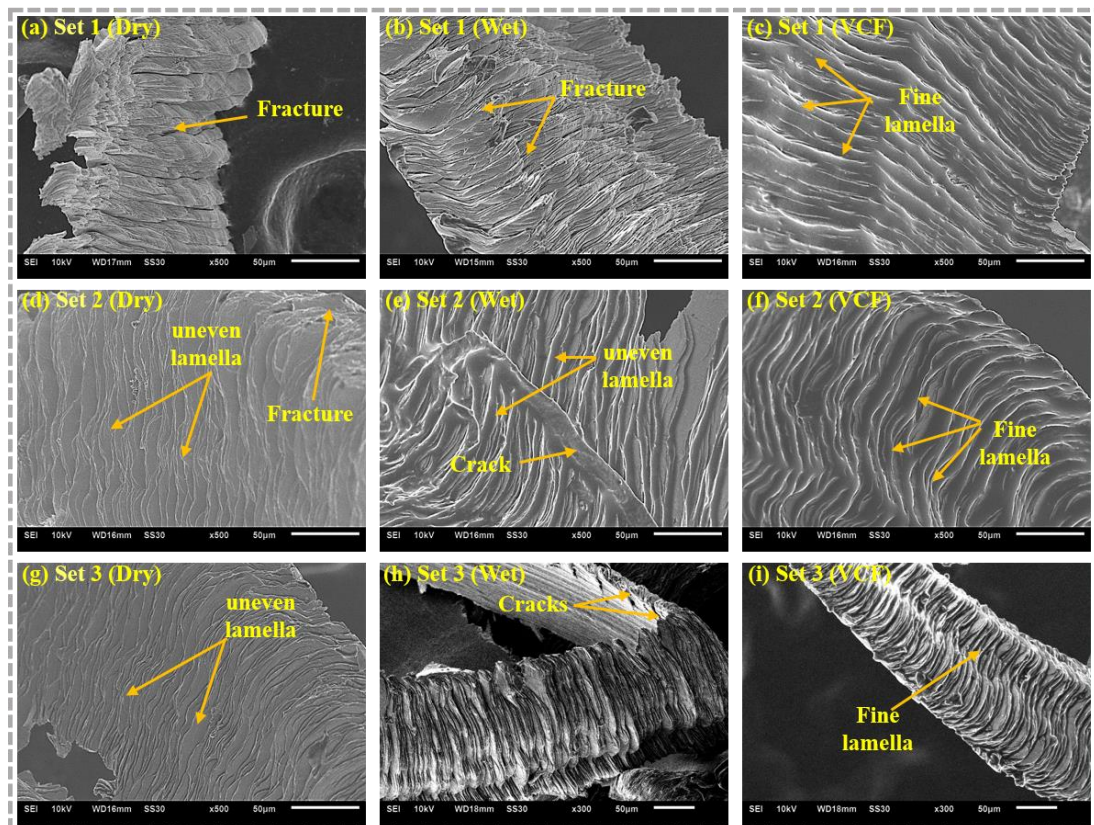


**Figure. 6.11** Chips morphology observed for different cutting conditions

Chip morphology in  $\mu$ -turning depends upon the cutting mechanism. The chip formation mechanism exhibits plowing instead of shearing when the feed rate is much lower. The material

simply crushed or extruded at a cutting of minimal uncut chip thickness. This leads to a formation of powder-type chip formation. On the other side, when the feed rate is higher than the nose radius, the shearing is the dominant mechanism, flowing the chips over the rake face, resulting in a spiral or helical chip formation [244].

Chips produced during experiments are collected and then observed by SEM. A typical chip morphology during  $\mu$ -turning of Nimonic 90 is shown in Figure. 6.11. For set 1, the dry condition shows a fracture on a free surface of the chip, as shown in Figure. 6.11(a). This fracture is due to the severe plastic deformation near the tool nose. Tool wear increases the plastic deformation, leading to fracture on a free surface of the chip [246]. For set 2, at a higher cutting speed, a microcrack initiated near the tool nose does not pass from an entire chip, producing a lamella structure, as shown in Figure. 6.11(d). The plastic deformation becomes more severe at a higher cutting speed and a lower uncut chip thickness, generating a fracture. The lamella structure observed is uneven due to the fracture. This unevenness in lamella structure is also observed for set 3, when the cutting speed further increases, as shown in Figure. 6.11(g). The distance between two lamella decreases as the cutting speed increases. The wet condition reduces the fracture on the free surface of the chip by limiting the severe plastic deformation, as shown in Figure. 6.11(b). At a higher cutting speed, the structure seems like lamella with some cracks is observed, as shown in Figure. 6.11(e). The lamella has a slip line along the shear plane. At a lower depth and higher speed, this lamella comes nearer to each other, as shown in Figure. 6.11(h). In this condition, the crack does not propagate from the chips due to cooling action. It can be noted that wet condition decreases the plastic deformation observed in dry conditions. The VCF produces chips with a fine lamella structure, even at a low cutting speed, as shown in Figure. 6.11(c). Fatty acid and triglyceride in VCF form a lubricating layer on the workpiece surface, reducing the severe plastic deformation, producing chips with fine lamella [247]. At a higher cutting speed and a lower feed rate, the distance between lamella and the width of chips decreases, as shown in Figure. 6.11(f) and Figure. 6.11(i). Furthermore, the VCF improves chip breakability by reducing the strain hardening near the cutting edge, especially at a lower feed rate, improving chip morphology.

### 6.1.5 Conclusions

$\mu$ -turning of Nimonic-90 has been performed to analyze the tungsten carbide tool wear behavior. The experiments are performed under dry, wet, and VCF conditions. 10% emulsion of Canola oil mixed with mineral water are used for VCF condition. Upon the analysis of the tool flank and crater wear, and the chip morphology microscopically, the following can be concluded:

- The VCF shows a significant reduction in the width of flank wear compared to dry and wet conditions. An approximate reduction is 12%-52% in the width of flank wear is observed under VCF compared to dry and wet conditions.
- The main wear mechanisms observed on the flank face are abrasion, adhesion, and edge chipping when dry and wet conditions are used. The adhesion and abrasion are mainly due to the plowing force, particularly at a lower feed rate. The VCF significantly reduces the abrasion and adhesion by forming a lubricating layer on the newly generated workpiece surface.
- The crater wear is mainly due to abrasion and adhesion of built-up edge in all the conditions. In the wet condition, the crater is formed due to oxidation from the rake face. The VCF drastically decreases the oxidation and abrasion from the rake face. Moreover, it also reduces the adhesion of microchips and built-up edge at the rake face.
- The chips produced in dry conditions are fractured and uneven, whereas they show uneven lamella structure in wet conditions. The VCF reduces the plastic deformation in all the cutting conditions, producing the chips with a fine lamella structure.

## **6.2 Experimental analysis for Selective laser melted and Wrought Ti6Al4V in micro-turning**

Additive manufacturing (AM) processes use the materials layer by layer to build complex 3D parts from a predefined model. The AM is quite attractive for intricate design and cost-effective batches applicable in automotive, biomedical, aerospace, etc. The metal parts are mainly printed by laser powder bed fusion using selective laser melting (SLM), selective laser sintering (SLS), and direct metal laser sintering (DMLS) which is a trademark of EOS, Germany. It has been observed that the part produced by AM are not often appropriate for direct application, as they need further processing to overcome certain features such as surface finish, residual stresses, wear, porosity, microhardness, etc. A poor surface property deteriorates mechanical properties, dropping the components' life. AM metal components are being post-processed to enhance their mechanical properties and microstructural features to improve the component life [248]. The post-processing treatments that mitigate the defects are imposed by conventional and non-conventional processes. Although many non-conventional processes can be used for post-processing, conventional processes are more popular as they restore the geometrical accuracy, tolerances, and surface quality. It is observed from the literature that approximately 75% of the machining of additively manufactured parts is performed using traditional machining processes [249]. It has been found that the machining of AM metallic parts is more challenging than the machining of wrought alloys. It is mainly due to the dynamics, such as the interaction between

powder bed and molten pool, powder and laser beam and melting process involved in the AM processes. The dynamics make it difficult to understand the thermophysical and metallurgical phenomena happening in the AM processes [250]. These challenges worsen in micro-machining since the micro-processes are more delicate to the microstructure due to the fluctuation of AM process parameters and cooling rates.

### 6.2.1 Methodology

In the present study, wrought and selective laser melted (SLM) Ti6Al4V are used to perform micro turning experiments. The SLM Ti6Al4V is produced using a system Renishaw AM400 and recommended parameters. The parameters used to produce SLM Ti6Al4V are: Laser power is 175 W, hatch distance is 0.05 mm, scanning speed is 1050 mm/s, and layer thickness is 30  $\mu\text{m}$ . To analyze the microstructure of both the materials, the cross-section of the workpiece is cut through electro-discharge machining. The samples are polished and etched using a Kroll's reagent ( $\text{HF} + \text{HNO}_3 + \text{H}_2\text{O}$ ). The microstructure detected under a scanning electron microscope is revealed in Figure. 6.12. It is observed from Figure. 1 that, the microstructure of Ti6Al4V consists of  $\alpha$  and  $\beta$  phases. The crystal structure of the  $\alpha$  phase is HCP (hexagonal close-packed), whereas the  $\beta$  phase is BCC (body-centered cubic). A fine needle-type microstructure in the SLM

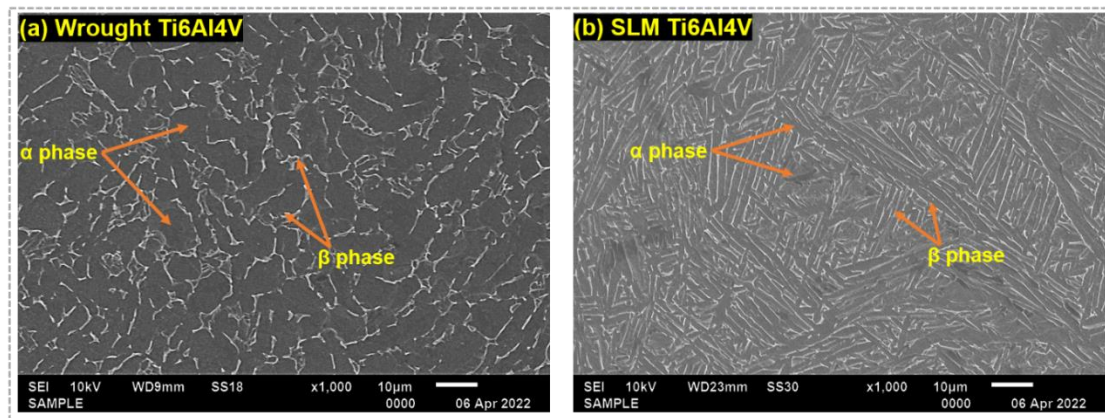


**Figure 6.12** Microstructure of (a) wrought and (b) selective laser melted Ti6Al4V

Ti6Al4V is attributed to the high cooling rate of the SLM process. The elemental composition for wrought and SLM Ti6Al4V are shown in Table 6.3. The microhardness of each material is measured using a universal microhardness tester. Three measurements of hardness are taken for each sample at different positions. The measurement is performed using a load of 1 kgf for a dwelling cycle of 10 s. The hardness of wrought Ti6Al4V is 320 HV and SLM is 365 HV which is approximately 14% higher. The higher hardness of SLM Ti6Al4V is owing to a fine structure of  $\alpha$  phase. The fine structure of the material causes the resistance to plastic deformation, increasing the strength and hardness of SLM Ti6Al4V. According to Keist and Palmer [251], there is a direct relation between microhardness and mechanical properties. They proposed that

the yield and ultimate tensile strength of SLM Ti6Al4V are more than wrought due to the higher hardness of the SLM part.

**Table 6.3.** Elemental structure of Ti6Al4V (wt%)

Element	Ti	Al	V
Wrought	Balance	5.95%	4.33%
SLM	Balance	5.85%	4.2%

The experiments are performed using a multipurpose micromachine tool, as appeared in Figure. 6.2. The machine tool has an accuracy of  $\pm 1\mu\text{m}$  in axial movement with  $0.1\mu\text{m}$  of resolution on a linear optical scale. Tungsten carbide insert, CCMT 060204, having a rake angle of  $0^\circ$  and nose radius of 0.4 mm, is used to cut the materials. The experiments are performed on wrought and selective laser melted Ti6Al4V, with a diameter of 6mm and length of 70mm. The micro turning experiments are performed at cutting speeds of 28 m/min and 56 m/min. The feed rates used are  $20\mu\text{m/rev}$  and  $30\mu\text{m/rev}$ , and the depth of cut used is  $50\mu\text{m}$ . The process parameters are selected based on the previous literatures [4, 16, 18]. Moreover, the feed rates are chosen so that the uncut chip thickness is higher than the critical chip thickness to avoid size effect. Three different sets of experiments are executed under dry conditions. The machining time for set 1, 2 and 3, is 6.73, 3.36 and 4.48 minutes, respectively. Thus, each response is analysed for same machining length and different machining time. Each experiment is performed thrice to check the precision of responses. The details of the experimental condition are given in Table 6.4.

**Table 6.4.** Conditions used for experiments

Parameter	Specification					
Machine tool (make and model)	MIKROTOOLS DT110i, Hybrid micromachine tool,					
Workpiece	Wrought and Selective Laser Melted Ti6Al4V					
	Diameter: 6 mm					
Tool	Tungsten carbide CCMT 060204, Nose radius: 0.4 mm, Rake angle: $0^\circ$					
Cutting condition	Dry					
Width of flank wear	Toolmaker Microscope- Radical RTM 900					
Surface roughness	Contact type surface roughness tester, Handysurf KA8628JK					
Morphology of Tool wear and Chip, Surface characteristics	Scanning electron microscope, JEOL 6610 LV					
<i>Sets of experiment</i>	<i>Set 1</i>		<i>Set 2</i>		<i>Set 3</i>	
Cutting speed (m/min)	28	28	56	56	28	28



Feed rate ( $\mu\text{m}/\text{rev}$ )	20	20	20	20	30	30
Materials	Wrought	SLM	Wrought	SLM	Wrought	SLM
Depth of cut	50 $\mu\text{m}$					
Cutting length	200 mm					

The responses, such as tool wear, surface characteristics and chip morphology, are studied for both the materials at each set. The worn tools are etched and characterized after each experiment. According to Khaliq et al. [240], the maximum flank wear should not exceed 22  $\mu\text{m}$ . This value can be subjective for the machining length. The machining length is considered 200 mm for effective comparison in the present study. A width of flank wear is observed using an optical microscope, and the average is considered for analysis. Tool wear morphology is analyzed using a scanning electron microscope. Furthermore, the surface roughness is measured using Contact type surface roughness tester. Surface topography is inspected using a scanning electron microscope (SEM). The chips produced are collected and examined using optical and SEM for each process parameter and workpiece materials. All the experimental details are given in Table 6.4.

### 6.2.2 Tool wear

In micromachining, an uncut chip thickness is relatively lesser than in macro machining processes. Therefore, the side edge of the tool in micromachining does not participate much in the cutting operation and hence, does not produce stable wear. As the cutting edge is comparable with uncut chip thickness, the plowing force on the thrust direction is prominent, enhancing the tool wear. The tool wear deteriorates the surface quality of a newly generated machined surface. This section analyzes the tool wear, surface characteristics, and chip morphology in micro turning of wrought and SLM Ti6Al4V under dry conditions.

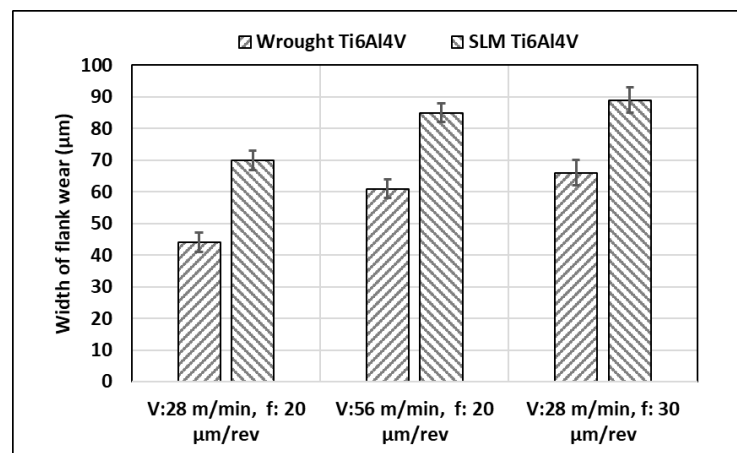


**Figure 6.13** Average flank wear width in wrought and SLM Ti6Al4V in different sets of process parameters

The flank wear is evaluated at three different positions using a toolmaker microscope. The average width of flank wear measured for both the materials and at each set of parameters is given in Figure. 6.13. For all the parameters, the SLM Ti6Al4V produces a higher flank wear width than wrought Ti6Al4V. As mentioned earlier that the hardness of the SLM Ti6Al4V is higher compared to wrought Ti6Al4V. Moreover, it is also observed that the SLM Ti6Al4V has a higher yield and ultimate tensile strength [252], affecting the tool-workpiece interaction and plastic deformation in the machining process. Thus, the SLM alloy accelerates the tool wear compared to wrought Ti6Al4V. A similar observation regarding higher flank wear for SLM Ti6Al4V is made by Sartory et al. [253]. According to Khanna et al. [254], the higher hardness of SLM Ti6Al4V creates the resistance to form a chip, and hence more specific energy is required for plastic deformation. This phenomenon plays a significant role in micro machining, as the specific cutting energy to remove the materials is higher. Thus, the flank face of the tool wears out rapidly during micro turning of SLM Ti6Al4V compared to Wrought Ti6Al4V. The SLM Ti6Al4V shows approximately 35%, 26% and 25% higher flank wear width for set 1, set 2 and set 3, respectively, compared to wrought Ti6Al4V. Furthermore, for the same feed, as the cutting speed increases, the width of flank wear increases for both the alloys. At a higher cutting speed, the heat produced at tool-workpiece contact zone is raised, increasing the width of flank wear. Moreover, the micromachining of Ti6Al4V, at a relatively higher cutting speed and under dry conditions, leads to generating more heat due to the poor heat conductivity of Ti6Al4V. Therefore, the rubbing action between tool and workpiece produces severe flank wear at high cutting speed, increasing the width of flank wear for both the alloys. Similarly, as the feed increases from 20  $\mu\text{m}/\text{rev}$  to 30  $\mu\text{m}/\text{rev}$ , flank wear width increases. At a higher feed, the amount of the material removed by the tool is increased, generating more heat at the machining zone. Moreover, the frictional heat produced at the tool-work contact area enhances the rubbing and increases the flank wear.

A morphology of tool wear at 28 m/min and 20  $\mu\text{m}/\text{rev}$ , and for both the materials, using SEM is shown in Figure. 6.14. For the wrought Ti6Al4V, a severe adhesion of built-up edge (BUE) is noticed at the cutting edge, as appeared in Figure. 6.14(a). The high reactivity and low thermal conductivity of Ti6Al4V are mainly responsible for BUE formation, primarily in dry condition. The formation of BUE in macro-scale machining has been well investigated by researchers [255]. The BUE formation in micromachining is comparable with uncut chip thickness since the feed is taken in the micro range. Thus, the BUE decreases the cutting-edge sharpness and creates a situation that endorses an adhesion of workpiece material to the cutting edge. Figure. 6.14(b) clearly shows an adhesion on the flank face and tool nose. The material side flow increases owing to the adhesion at the cutting edge, reducing the surface quality. According to Vipindas and Mathew [244], the temperature and pressure at tool and workpiece

and tool and chip are quite higher even in micromachining under dry condition, leading to adhere the workpiece material on the tool. Alternatively, when the uncut chip thickness is lesser than the critical value, the plowing action promotes the rubbing between workpiece and tool, increasing the formation of an adhesive layer. When the adhesive material is broken in progressive cutting, it brings a small tool segment with it, causing the flaking or chipping of the cutting edge. The abrasion of the cutting edge is occurred mainly due to the rubbing between hard particles present in Ti6Al4V and the cutting-edge during machining. It generally happens at the flank and rake faces. An EDS image shown in Figure.6.14(c) clearly shows that W and C are the main element, indicating abrasion on the rake face. However, an adhesion of material that happened on the flank face acts as a protection against abrasion. The plowing at low feed is also responsible for the abrasion of the cutting edge. The results are in agreement with the results obtained for micro-milling of Ti6Al4V using coated and uncoated carbide tools by Roushan et al. [256].

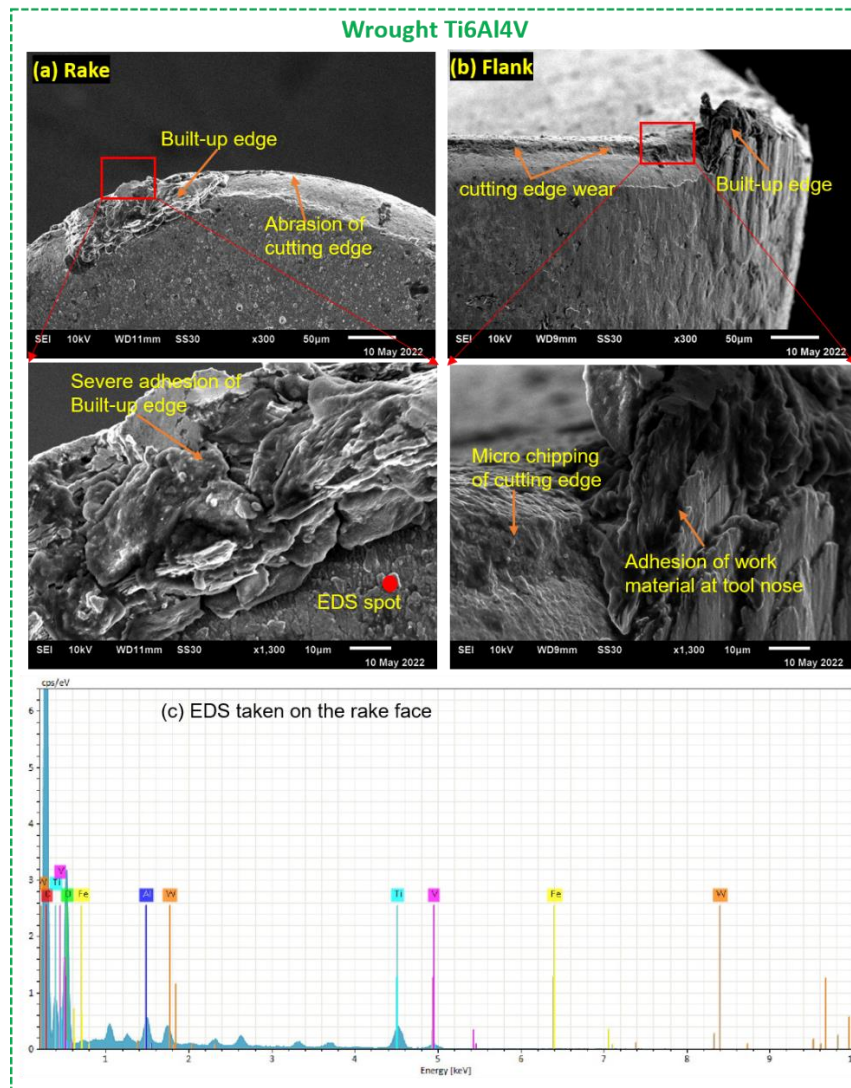


**Figure 6.14** Morphology of tool wear for wrought Ti6Al4V at  $V$ : 28 m/min and  $f$ : 20  $\mu\text{m}/\text{rev}$

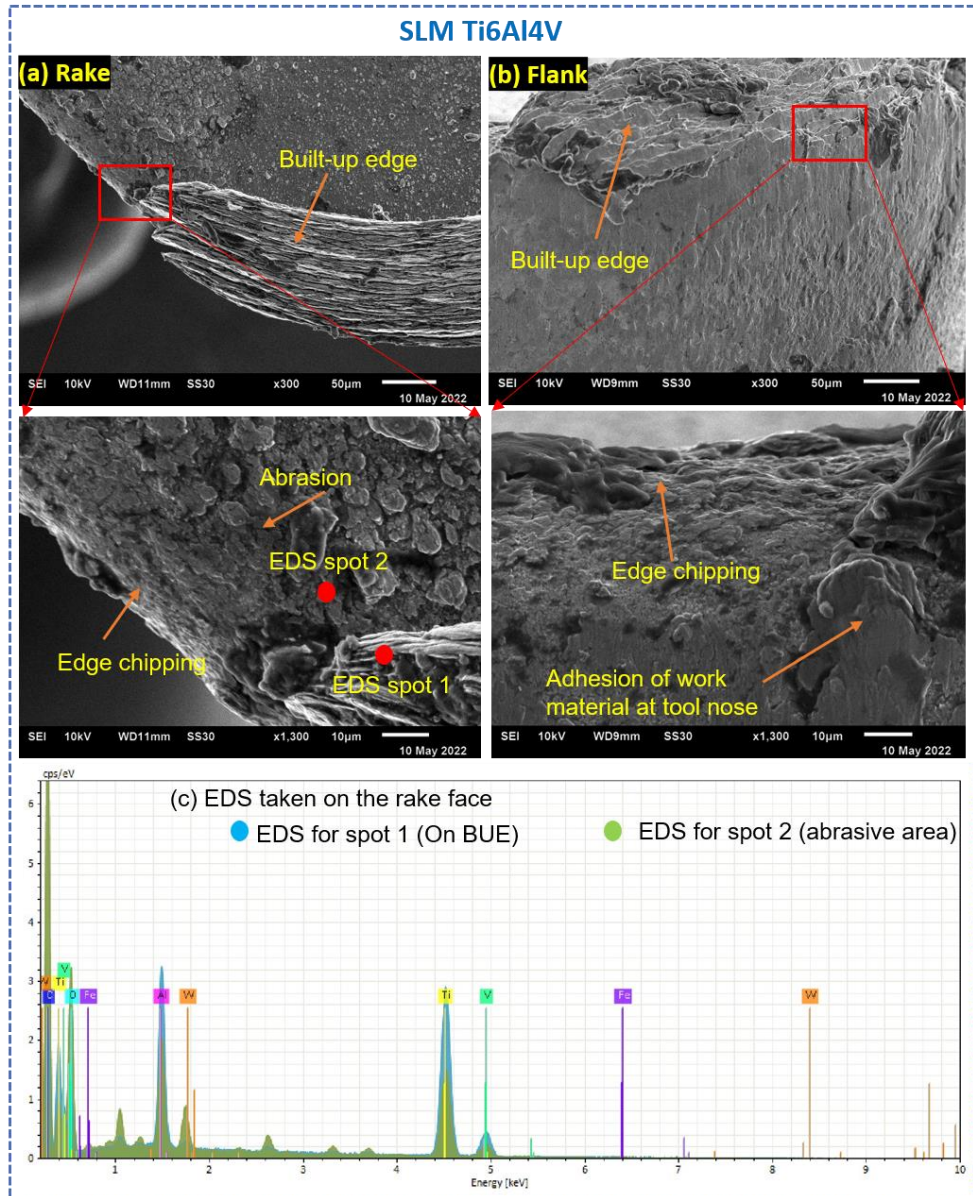


**Figure 6.15** Morphology of tool wear for SLM Ti6Al4V at  $V$ : 28 m/min and  $f$ : 20  $\mu\text{m}/\text{rev}$

The morphology of tool wear for SLM Ti6Al4V shows that the BUE is larger than wrought Ti6Al4V, as shown in Figure. 6.15(a). Moreover, the abrasion, cutting-edge chipping and adhesion on the flank face seem larger compared to that in wrought Ti6Al4V. It is in accordance with the observations made during the turning of wrought and additively manufactured Ti6Al4V by Sartori et al. [253]. As discussed earlier, the BUE formation is commonly observed during the machining of Ti6Al4V. Ahmadi et al. [257] have found during micro milling of heat-treated Ti6Al4V that the material consisting of finer grains resulted in a higher cutting force and a larger BUE formation on the cutting tool. Here, the higher hardness of SLM Ti6Al4V is responsible for a larger BUE formation. A chemical affinity of Ti6Al4V forms a bond between tool and workpiece, causing the adhesion. It is also experienced by the EDS image in Figure. 6.15(b). A higher surface temperature generates due to lower heat conductivity,



enhancing the diffusive action between workpiece and tool materials, and producing more adhesion. An instability of BUE breaks a small lump of material from the cutting edge, resulting in chipping. Alternatively, the high hardness of SLM Ti6Al4V produces a large plowing force on the cutting edge, enhancing the possibility of edge chipping. An increment in cutting edge radius as a result of edge chipping increases the plowing phenomenon. As a result, a high plowing force increases the rubbing between workpiece and tool, accelerating the tool wear. Similarly, a rubbing action between chip and tool removes the material by abrasion. The higher hardness of SLM Ti6Al4V also promotes abrasive wear when chips slide from the rake face. Whereas, at the flank face, a strongly formed adhesive layer prevents direct contact between workpiece and tool, lowering the abrasion on the flank face.

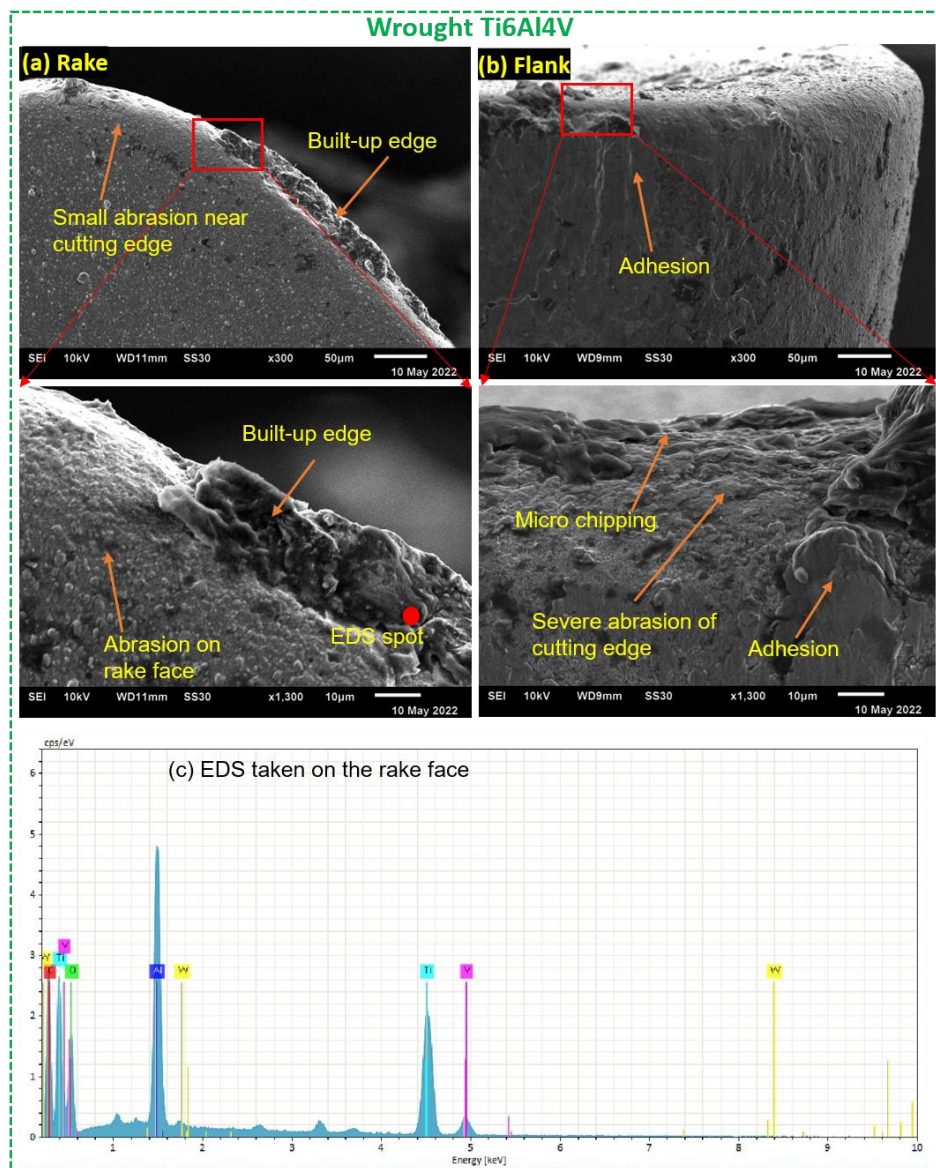


**Figure 6.16** Morphology of tool wear for wrought Ti6Al4V at  $V$ : 56 m/min and  $f$ : 20  $\mu\text{m}/\text{rev}$

Morphology of tool wear at 56 m/min and 20  $\mu\text{m}/\text{rev}$  for wrought and SLM Ti6Al4V is observed in Figure. 6.16 and Figure. 6.17, respectively. The size of BUE is reduced as the cutting speed increases from 28 to 56 m/min for both the alloys. However, a small BUE, abrasion of cutting edge, adhesion of workpiece materials, and edge chipping is noted for both the materials. At a higher speed, the materials get softened, reducing the binding force and lowering the size of BUE. A similar phenomenon happened for SLM Ti6Al4V, as shown in Figure. 6.17(a). A very small BUE attached to the cutting edge is observed. It is noted from the EDS images that the composition of Ti, Al and V are higher in the BUE of SLM Ti6Al4V compared to wrought Ti6Al4V, as appeared in Figure. 6.16(c) and Figure. 6.17(c). It might be due to higher chemical affinity of SLM Ti6Al4V compared to wrought Ti6Al4V. The presence of BUE prevents the contact between tool and chip, reducing the abrasion on the rake face for both the alloys. However, the abrasion looks severe at the cutting edge; removing chip

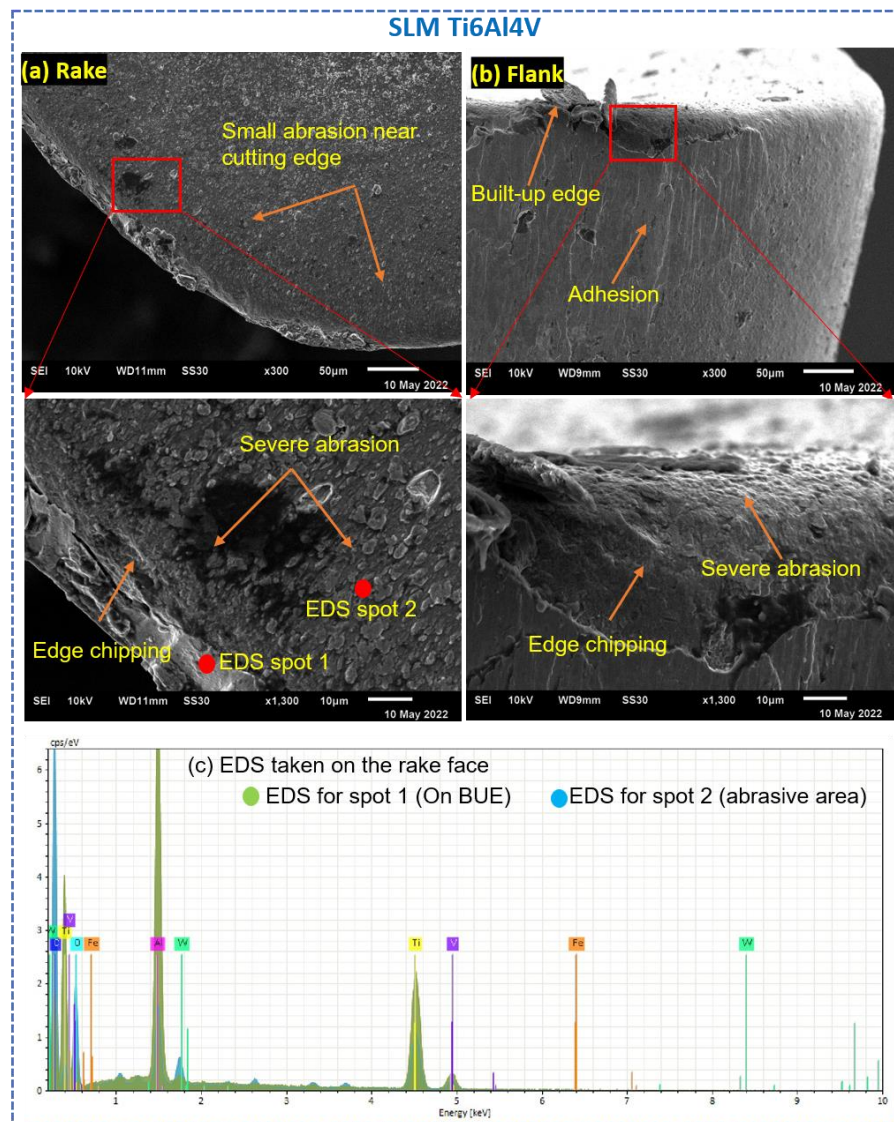


**Figure 6.17** Morphology of tool wear for SLM Ti6Al4V at  $V$ : 56 m/min and  $f$ : 20  $\mu\text{m}/\text{rev}$

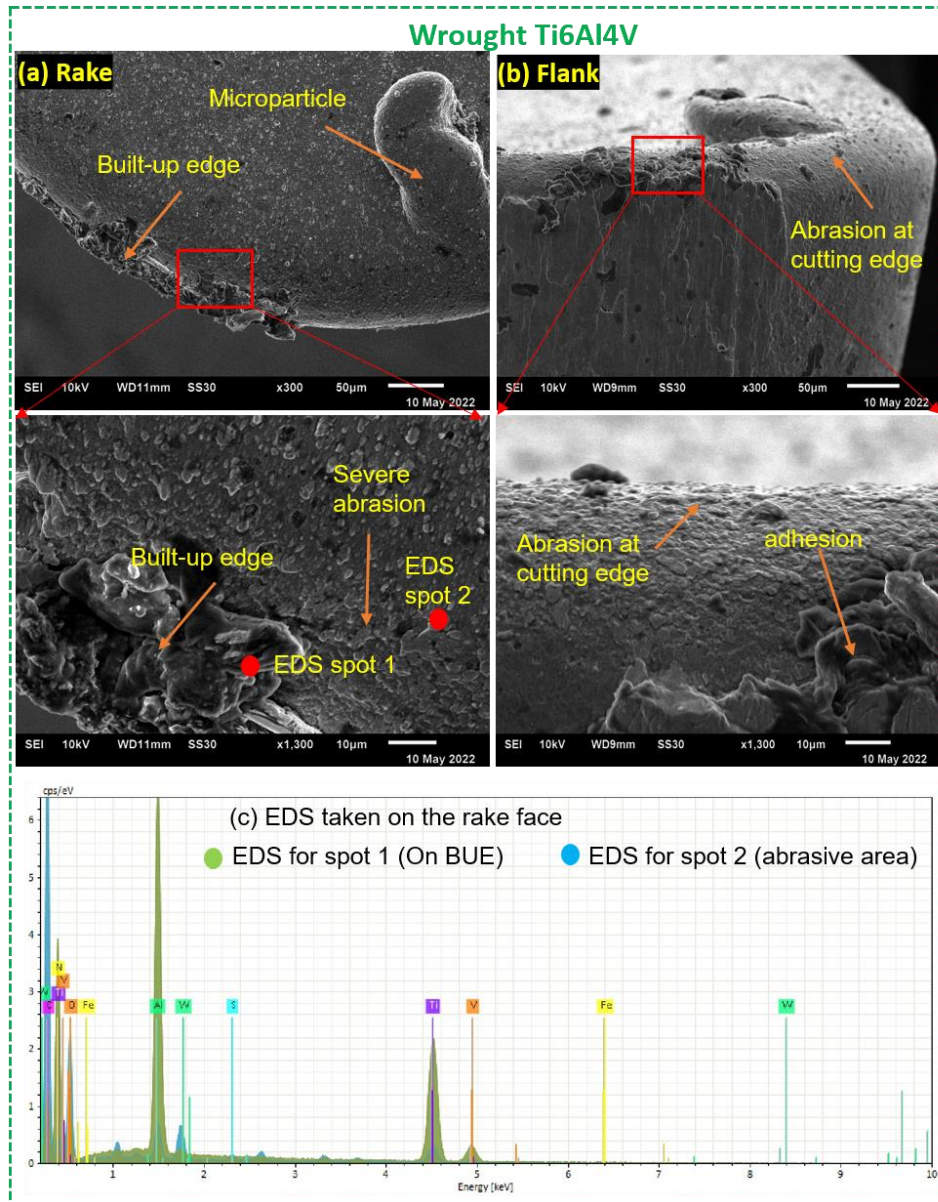


**Figure 6.18** Morphology wear for wrought Ti6Al4V at  $V$ : 28 m/min and  $f$ : 30  $\mu\text{m}/\text{rev}$

particles at a high cutting speed leads to the disarticulation of hard carbide particles from the cutting edge. These hard carbide particles between sliding chip and tool form an abrasion of the cutting edge. In addition to that, the plowing force at the flank face increases the rubbing action between the tool and machined surface at a higher cutting speed, enhancing the abrasive wear. The abrasion is more severe on the cutting edge for SLM Ti6Al4V, as given in Figure. 6.17(b). Consequently, in the same condition, the adhesion is higher on the flank face for both the materials. It is also found that the elemental diffusion takes place from a workpiece to the flank face mainly in the dry condition and at a higher cutting speed, emerging the severe adhesion [258]. Continuous removal of BUE and adhesion results in a microchipping of the cutting edge. A microchipping in wrought and SLM Ti6Al4V is clearly visible in Figure. 6.16(b) and Figure. 6.17(b), respectively. Furthermore, at a higher cutting speed, the SLM Ti6Al4V shears out easily



due to finer grain, whereas larger grain of wrought Ti6Al4V shears partially. The strength of SLM Ti6Al4V reduces under the localized heat generation at the cutting edge, diffusing with the tool, resulting in chipping the cutting edge [259]. Additionally, the additively manufactured alloys contain porosity in most cases, where the deformation-induced cutting mechanism happens mainly in micromachining. Therefore, when the cutting edge of the tool interacts with the workpiece, it intends to act as a pore closer, producing superficial strain hardening of the machined surface. Thus, tool wear accelerates on the flank face in the case of SLM Ti6Al4V. On the other hand, in case of the wrought Ti6Al4V, relatively less hardness and strength reduce the resistance of deformation, lowering the tool wear rate than SLM Ti6Al4V.

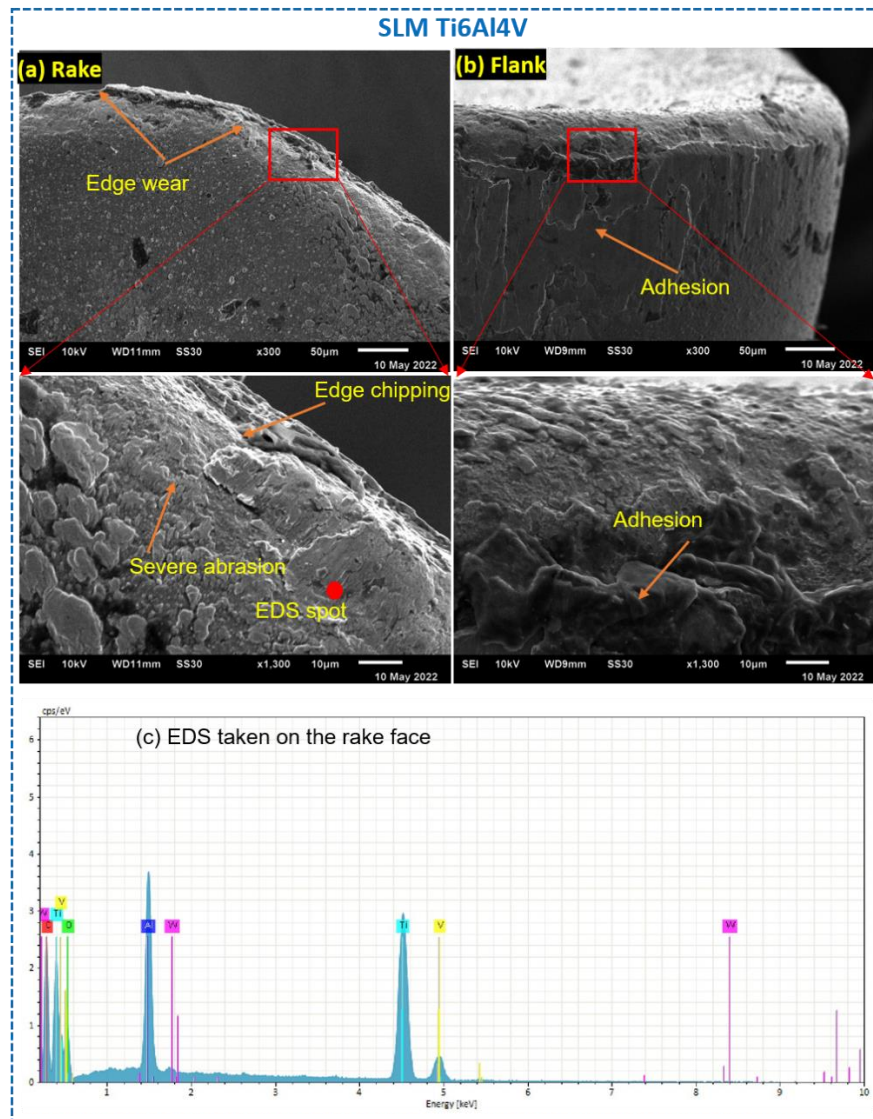


**Figure 6.19** Morphology of wear for SLM Ti6Al4V at  $V$ : 28 m/min and  $f$ : 30  $\mu\text{m}/\text{rev}$

The morphology of crater and flank wear at 28 m/min and 30  $\mu\text{m}/\text{rev}$  for wrought and SLM Ti6Al4V is exposed in Figure. 6.18 and Figure. 6.19, respectively. As the feed rate increases from 20  $\mu\text{m}/\text{rev}$  to 30  $\mu\text{m}/\text{rev}$  for the same cutting speed (28 m/min), the size of BUE



decreases for both the materials. For the wrought Ti6Al4V, a small microparticle on the rake face and a small BUE on the cutting edge appears, as shown in Figure. 6.18(a). Similar can be visualized in EDS image Figure. 6.18(c). As the feed rate increases, an uncut chip thickness, and thus, a material to be removed by tool, increases. At a larger uncut chip thickness, the shearing mechanism dominates the plowing mechanism, allowing the chips to be passed over the rake face, reducing the size of BUE. However, at a higher uncut chip thickness, the chip imposes higher friction and temperature during machining of Ti6Al4V, accelerating the abrasive wear from the rake face. The temperature reaches up to 400-500<sup>0</sup> C during micromachining of Ti6Al4V, which is accountable for abrasion on the rake face [260]. Similar results of tool wear are obtained for micro-milling of Ti6Al4V by Vipindas and Mathew [244]. In case of the SLM Ti6Al4V, the abrasion of the cutting edge and rake face looks severe, as shown in Figure. 6.19(a). The higher strength and hardness of the SLM Ti6Al4V are mainly responsible for the severe abrasion of the cutting edge. Relatively hard chips flow over the cutting edge and rake face, producing a high temperature and friction, generating abrasive wear. The edge radius of the tool increases once the tool edge is worn out due to the abrasion. Therefore, effective stresses imposed on the cutting tool raise, leading to chipping or flaking of the cutting edge, as given in an enlarged view of Figure. 6.19(a). A severe adhesion on the flank face is appeared for wrought and SLM Ti6Al4V in Figure. 6.18(b) and Figure. 6.19(b), respectively. A larger uncut chip thickness and chemical affinity of Ti6Al4V are responsible for adhesion on the flank face. Moreover, during micromachining, when the cutting edge becomes larger due to abrasion, the plowing mechanism causes excessive rubbing between the tool and the newly generated machined surface. As a result, an adhesive layer is produced on the flank face. An adhesive element is clearly visible in the Figure. 6.19(c). A repetitive formation and removal of the adhesive chips from the cutting edge cause the edge chipping. Attanasio et al. [261] have found, during micro-milling of Ti6Al4V of different microstructures, that the materials having smaller grain size and higher hardness produce higher adhesive wear. In this regard, the SLM Ti6Al4V consists of higher hardness, producing more adhesion on the flank face. Furthermore, as discussed earlier, the deformation-induced mechanism that takes place for SLM Ti6Al4V at a larger uncut chip thickness increases the plastic deformation, resulting in severe adhesion on the flank face.

### 6.2.3 Surface characteristics

Surface characteristics of the machined surface are an essential parameter in precision machining processes. The influence of machining parameters on the surface characteristic is quite significant in micro-scale cutting. In this regard, average surface roughness in terms of arithmetic mean height ( $R_a$ ) and surface topography are considered for examination for both the alloys. The surface roughness is examined using a contact-type surface roughness tester. The  $R_a$

measured for wrought and SLM Ti6Al4V for all the parameters is given in Figure. 6.20. It is noted that the  $R_a$  is higher for SLM Ti6Al4V compared to wrought Ti6Al4V. At a 28 m/min and 20  $\mu\text{m}/\text{rev}$ , the SLM Ti6Al4V shows approximately 52% higher  $R_a$  compared to wrought Ti6Al4V. The BUE formation that takes place on the cutting edge deteriorates the surface quality. The BUE scratches the machined surface and produces poor surface quality. However, a larger BUE formed during micro turning of SLM Ti6Al4V significantly deteriorates the surface roughness, producing a larger  $R_a$  compared to wrought Ti6Al4V. It can be noted that higher tool wear for SLM Ti6Al4V worsens surface quality. Moreover, the chipping of the cutting edge generates more heat due to the rubbing between the workpiece and flank face, increasing the  $R_a$  for SLM Ti6Al4V. For a constant feed, as the cutting speed increases, the  $R_a$  increases for both the materials. The SLM Ti6Al4V produces approximately 16% higher  $R_a$  than wrought Ti6Al4V. A higher surface roughness at a higher speed is attributed to higher frictional heat generation during a rubbing action between the tool flank and the newly generated machined surface. It can also be said that at a higher speed, when the cutting edge wears out due to abrasion and chipping, the plowing becomes dominating over shearing. As a result, the chips form elastically under plowing and produce a rough surface, increasing the  $R_a$  for both the alloys. Oliaei and Karpas [255] have found in micro-cutting of Ti6Al4V that the surface quality depreciates considerably at higher cutting speeds because of the scratching effect of BUE. They have noted that there is an intricate relationship between surface roughness, feed, BUE, and cutting speed. As the feed rate or uncut chip thickness increases from 20  $\mu\text{m}/\text{rev}$  to 30  $\mu\text{m}/\text{rev}$  for a constant cutting speed (28 m/min), the  $R_a$  increases for both the materials. The SLM Ti6Al4V produces approximately 40% higher  $R_a$  than wrought Ti6Al4V. At a higher uncut chip thickness, the shearing mechanism dominates the plowing mechanism, improving the surface quality. However, as the machining progresses, the chipping and abrasion of the cutting edge and adhesion on the flank face increases, enlarging the cutting edge of the tool. Thus, the shearing mechanism slowly terminates with the plowing mechanism, worsening the surface quality. The results are in agreement with the observations made in micro-milling of Ti6Al4V by Vipindas and Mathew [244]. A higher  $R_a$  for SLM Ti6Al4V is attributed to a higher deformation-induced cutting at a larger uncut chip thickness, increasing the strain hardening of machined surface, producing more surface roughness.

The surface topography and damage observed for wrought and SLM Ti6Al4V at different cutting speed and feed rate using a scanning electron microscope is revealed in Figure. 6.21. At 28 m/min and 20  $\mu\text{m}/\text{rev}$ , feed marks and microchips adhered to the machined surface are visible for both the materials. In addition to that, the material side flow is noted for SLM Ti6Al4V. The feed marks are generated due to a scratching effect of BUE formed on the cutting edge. The feed marks look more intense in the case of SLM Ti6Al4V. The rubbing between the

machined surface and flank is responsible for the adhesion of microchips with the surface. As the machining progresses, the worn tool imposes higher stress on the machined surface under high temperature, resulting in extrusion of the material from the surface, showing a material side flow as in Figure. 6.21(d). As the cutting speed increases, the feed marks seem reduced for both

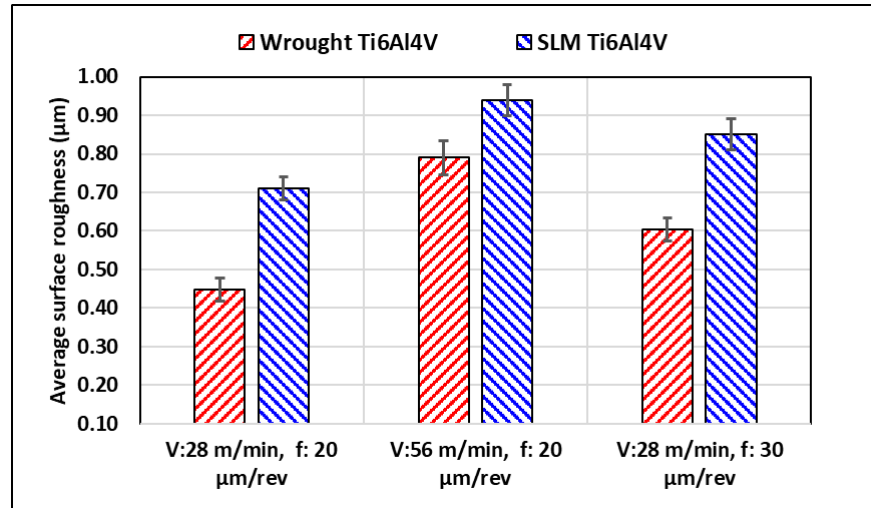


**Figure 6.20** Average surface roughness measured in wrought and SLM Ti6Al4V under different cutting speeds and feed rates

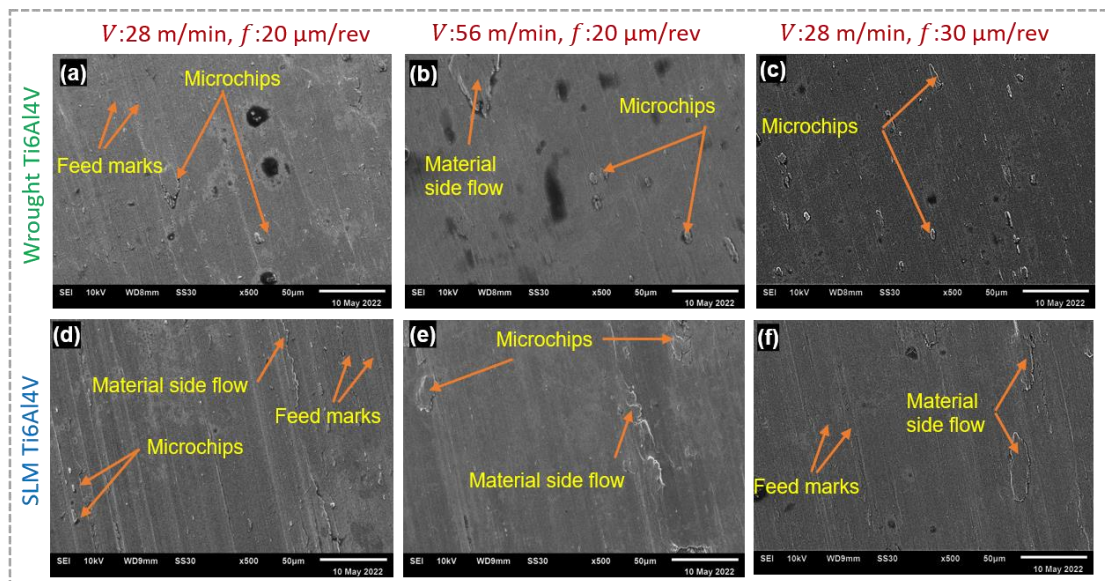


**Figure.6.21** Surface topography observed in wrought and SLM Ti6Al4V under different cutting speeds and feed rates

the materials, as appeared in Figure. 6.21(b) and Figure. 6.21(e). However, the adhesion of microchips and material side flow increases for both the materials. It is mainly due to larger tool wear at a higher speed, increasing the frictional heat and stresses on the machined surface. As a result, the microchip adhesion takes place. Moreover, the chipping of the cutting-edge leads to an increase in the plowing of materials, which leads to more material being extruded from the

machined surface, increasing the material side flow. Bordin et al. [262] have found during the turning of additively manufactured Ti6Al4V that a material side flow is primarily attributed to plastic deformation of surface material imposed by worn tool motion at a higher cutting speed. As the feed rate increases from 20  $\mu\text{m}/\text{rev}$  to 30  $\mu\text{m}/\text{rev}$ , the adhesion of microchips increases for wrought Ti6Al4V, as shown in Figure. 6.21(c). For the SLM Ti6Al4V, material side flow and feed marks appear, as shown in Figure. 6.21(f). At a higher uncut chip thickness, a higher temperature is concentrated between tool and flank face, making the material softer, tending the chips to be welded with the workpiece. A reduction in feed marks for SLM Ti6Al4V at a higher feed rate is due to a reduction in BUE, reducing a scratching effect and lowering the feed marks. Moreover, at a higher uncut chip thickness, the shearing mechanism dominates the plowing, reducing the materials side flow. Similar responses have been noted during the micro milling of Inconel 718 by Uzun et al. [237].

#### 6.2.4 Chip morphology

Chip geometry and morphology in micromachining is depended upon a mechanism involved in the cutting process. When the uncut chip thickness is lower than critical chip thickness, the plowing dominates the shearing and vice versa. The chips simply flow over the rake face during the shearing mechanism, generating a spiral or helical geometry. Moreover, the chips formed during micromachining also depend upon process parameters such as cutting speed, tool geometry, and workpiece materials.

In the present study, the chips formed during micro turning of wrought and SLM Ti6Al4V are collected and observed using optical and scanning electron microscope. Typical chip geometry and morphology are shown in Figure. 6.21. At 28 m/min and 20  $\mu\text{m}/\text{rev}$ , chips produced for wrought Ti6Al4V are continuous, whereas for SLM Ti6Al4V, the chips are discontinuous, as presented in Figure. 6.21(a) and Figure. 6.21(c), respectively. Typically, the Ti6Al4V generates segmented chips almost in all the conditions. Serrated morphology appears on the back surface of the chips for both the materials, as revealed in Figure. 6.21(b) and Figure. 6.21(d). The chip contains a lamella structure due to the ductile nature of wrought Ti6Al4V. Alternatively, due to the higher hardness of the SLM Ti6Al4V, the segments look detached from each other. The ridges are formed on the chips because of higher plastic deformation and intense cutting force. As the cutting speed increases, the chips produced are continuous for wrought Ti6Al4V, as shown in Figure. 6.21(e). However, more plastic deformation is observed at a higher cutting speed, as appeared in Figure. 6.21(f). It is explicated with the fact that at a higher speed, more heat generated makes the chips soften, producing more plastic deformation. Even under more plastic deformation, the shear band front does not pass-through entire chips, producing continuous chips. The SLM Ti6Al4V produces short and discontinuous chips, as given in Figure.



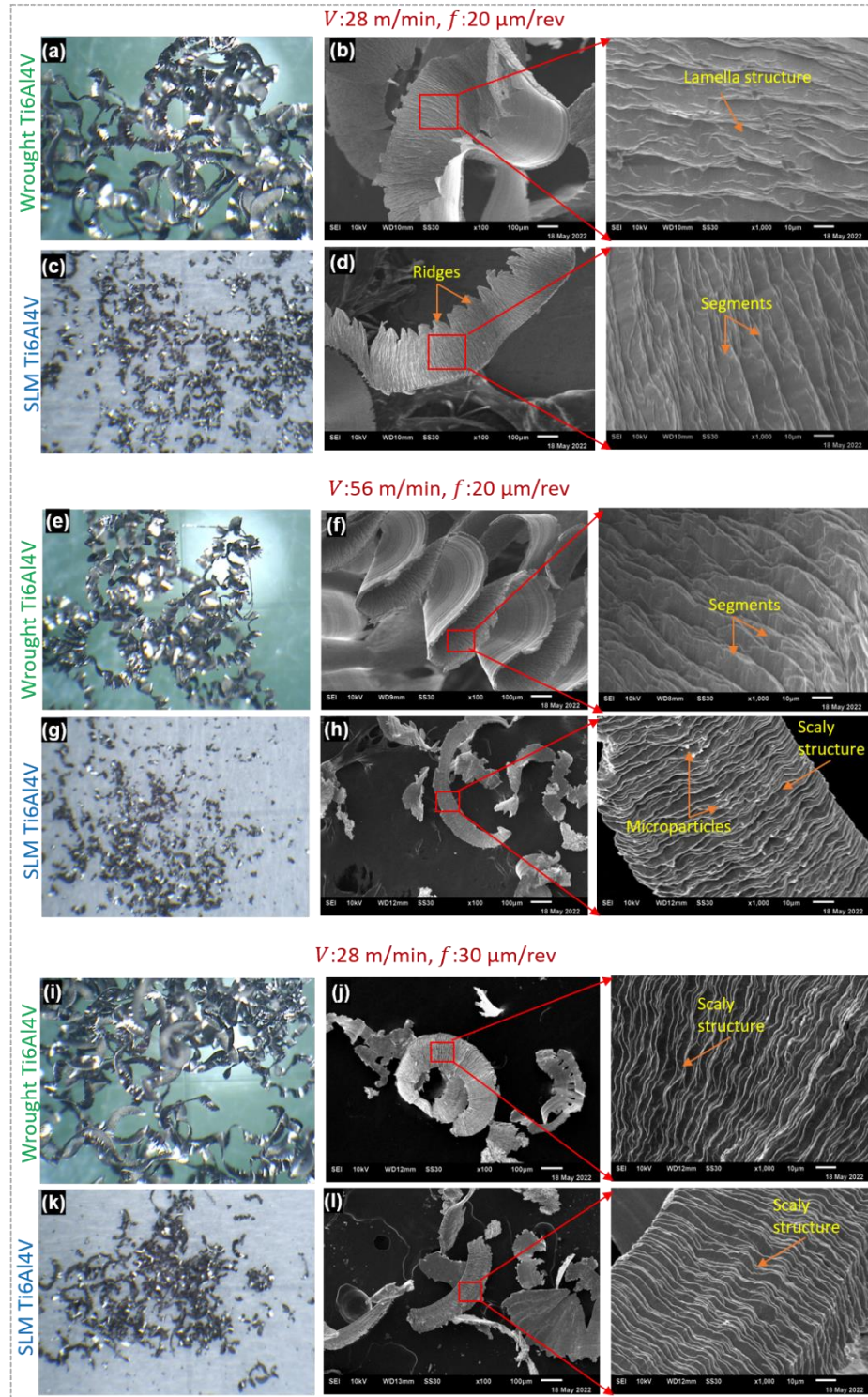


**Figure. 6.22** Chip geometry and morphology observed in wrought and SLM Ti6Al4V under different cutting speed and feed rate

6.21(g). The higher hardness of SLM Ti6Al4V tends to decrease the workpiece plasticity and, ultimately, lateral plastic flow, producing discontinuous chips. However, under the dry conditions, the chips produced with the worn tool increase the plastic deformation. Therefore, more heat is produced at the interface, welding microparticles with the chips, as shown in Figure.

6.21(h). As the feed rate increases from 20  $\mu\text{m}/\text{rev}$  to 30  $\mu\text{m}/\text{rev}$ , the chips produced are continuous for wrought Ti6Al4V and discontinuous for SLM Ti6Al4V, as given in Figure. 6.21(i) and Figure. 6.21(k), respectively. However, the chips look thicker since uncut chip thickness increases. Microscopically, both the materials produce the chips with scaly structures. Due to a more ductility and lower hardness of wrought Ti6Al4V, a large plastic strain is involved in the chips, sliding the segments with each other for both the materials. As a result, chips are generated with a scaly structure [263].

#### 6.2.4 Conclusions

This study gives a comparative assessment of tool wear, surface characteristics and chip morphology in micro turning of wrought and selective laser melted Ti6Al4V. Tool wear, surface topography and roughness, and chip morphology are studied. The following can be concluded from the study.

- The SLM Ti6Al4V produced higher tool wear and poor surface quality compared to wrought Ti6Al4V, for given process parameters. Quantitatively, the SLM Ti6Al4V produced 25-35% higher tool wear and 16-52% higher surface roughness than wrought Ti6Al4V for the given process parameters.
- The surface roughness and tool wear found increased with increasing cutting speed and feed. A higher tool wear deteriorates the surface topography quality at a higher value of speed and feed for both the materials.
- The main tool wear mechanisms at the rake face were observed as built-up edge formation, abrasion, and edge chipping, whereas it was adhesion at the flank face for all the cutting parameters and materials. Lamella microstructure is responsible for a higher abrasion and edge chipping for the SLM Ti6Al4V, whereas, equiaxed microstructure of the is responsible for higher adhesion and lesser abrasion for the wrought Ti6Al4V.
- The surface defects observed were feed marks and adhesion of microchips for both the materials. In addition to that, the surface produced for SLM Ti6Al4V showed a severe material side flow attributed to its higher hardness and plastic deformation for all the parameters.
- The chips produced were continuous for wrought Ti6Al4V, whereas they were discontinuous for SLM Ti6Al4V for all the process parameters. Moreover, the chips showed a plastic deformation at a higher feed rate for both the materials. At a higher cutting speed, the chips were of scaly structure for both the materials. A higher hardness and strength of SLM Ti6Al4V produced sawtooth chips at all the cutting speeds and feed rates.

This research work contains the development of ultrasonic assisted turning setup, analytical and finite element modelling of the UAT process, and experimental investigation on the combined effect of ultrasonic vibration and sustainable cutting fluids i.e., LCO<sub>2</sub> and MQL taking Inconel 718 and Ti6Al4V as workpiece materials. The outcomes such as tool flank and crater wear, surface characteristics and integrity, power and specific cutting energy consumption and chip morphology are examined. Moreover, the study has been extended to analyse the micro-scale cutting performance of wrought and SLM Ti6Al4V. The overall conclusion made are as follows:

- The analytical model developed to predict output responses showed a very good agreement at a lower value of cutting speed and feed rate. As the cutting speed and feed rate increased, the error also increased. It might be due to parameters such as material anisotropy, ultrasonic softening effect, and constant values of material properties. The error could be minimized by incorporating those parameters.
- The FEM and experimental results were in close agreement with an approximate error of 2-25%. The main tool wear mechanisms detected were edge chipping, abrasion, adhesion of BUE, and fracture of the tool nose. The HUAT reduced the tool-chip contact length by 5-21%, cutting force by 5-25% and feed force by 14-36%, compared to CT and UAT.
- In the machining of Ti6Al4V, the UAT shows an approximate reduction of 35%, 54% and 70% in average width of flank wear under wet, MQL and LCO<sub>2</sub>, compared to dry condition.
- An average reduction in average surface roughness for the CT under LCO<sub>2</sub> is 30%, 25% and 12% compared to dry, wet and MQL conditions. Similarly, for the UAT under LCO<sub>2</sub>, it is 43%, 24% and 22% compared to dry, wet and MQL conditions.
- In the machining of Inconel 718, the CT under LCO<sub>2</sub> reduces an average width of flank wear by 60 %, 28 % and 32 %, and the UAT under LCO<sub>2</sub> reduces by 53 %, 39 %, and 32 %, compared to dry, wet, and MQL.
- The intermittent cutting nature of the UAT produces a lower surface roughness compared to the CT, mainly under dry, MQL and LCO<sub>2</sub>. An average reduction in average surface roughness for the CT under LCO<sub>2</sub> is 31 %, 5 % and 9 % compared to other

strategies. Similarly, for the UAT under LCO<sub>2</sub>, it is 31 %, 18 % and 5 % compared to other strategies.

- Comparing micro machinability of wrought and SLM Ti6Al4V, A higher hardness and instability of the  $\beta$  phase at a higher temperature in the LPBF Ti6Al4V are mainly responsible for enhanced tool wear. On the other hand, equiaxed grains and balanced yield strength and hardness of wrought Ti6Al4V are primarily responsible for reduced tool wear. The SLM Ti6Al4V produced higher tool wear and poor surface quality compared to wrought Ti6Al4V, for given process parameters. Quantitatively, the SLM Ti6Al4V produced 25-35% higher tool wear and 16-52% higher surface roughness than wrought Ti6Al4V for the given process parameters.
- The surface roughness and tool wear found increased with increasing cutting speed and feed. A higher tool wear deteriorates the surface topography quality at a higher value of speed and feed for both the materials.

## 7.1 Future scope

The present work incorporates a development of UAT setup for conducting experiments. Moreover, the analytical and FE models have been developed to predict the various machining responses considering the effect of ultrasonic vibrations. In this regard, the following could be suggested to extend of the current work.,

- The feed back system can be incorporated with the existing UAT setup for analysing the nature of frequency and amplitude during machining process.
- The analytical model can further be improved, incorporating the ultrasonic softening effect and anisotropy of workpiece material.
- The FE model can further be improved using different friction and tool wear models.



## References

1. <https://www.prnewswire.com/>
2. Nau B, Roderburg A, Klocke F. Ramp-up of hybrid manufacturing technologies. *CIRP J Manuf Sci Technol.*, 2011;4 (3):313-316.
3. Sun S, Brandt M, Dargusch MS. Thermally enhanced machining of hard-to-machine materials—A review. *Int J Mach Tools Manuf.*, 2010;50:663–680.
4. Choi YH, Lee CM. A study on the machining characteristics of AISI 1045 steel and Inconel 718 with circular cone shape in induction assisted machining. *J Manuf Process.*, 2018;34:463-476.
5. Moon SH, Lee CM. A study on the machining characteristics using plasma assisted machining of AISI 1045 steel and Inconel 718. *Int J Mech Sci.*, 2018;142–143:595–602.
6. Parida AK, Maity K. Study of machinability in heat-assisted machining of nickel-base alloy. *Measurement.*, 2021;170:108682.
7. Antonio J, Egea S, Hernán A, Rojas G, Carlos A, Montana M, Echeverri VK. Effect of electroplastic cutting on the manufacturing process and surface properties. *J Mater Process Technol.*, 2015;222:327–334.
8. Germain G, DalSanto P, Lebrun JL. Comprehension of chip formation in laser assisted machining. *Int J Mach Tools Manuf.*, 2011;51:230–238.
9. Shaw MC. *Metal Cutting Principles*, Oxford University Press, Oxford, 1986.
10. Lawal SA, Choudhury IA, Nukman Y. Application of vegetable oil-based metalworking fluids in machining ferrous metals: A review. *Int J Mach Tools Manuf.*, 2012;52:1-12.
11. Shokrani A, Dhokia V, Newman ST. Environmentally conscious machining of difficult-to-machine materials with regard to cutting fluids. *Int J Mach Tools Manuf.*, 2012;57:83–101
12. Chetan, Ghosh S, Rao PV. Application of sustainable techniques in metal cutting for enhanced machinability: a review. *J Clean Prod.*, 2015;100:17-34.
13. Sharma AK, Tiwari AK, Dixit AR. Effect of minimum quantity lubrication (MQL) in machining processes using conventional and nanofluid based cutting fluids: A comprehensive review. *J Clean Prod.*, 2016;127:1-18.
14. Khanna N, Agrawal C, Pimenov DY, Singla AK, Machado AR, Silva LRRd, Gupta MK, Sarikaya M, Krolczyk GM. Review on design and development of cryogenic machining setups for heat resistant alloys and composites. *J Manuf Process.*, 2021;68:398-422.
15. Thoe TB, Aspinwall DK, Wise MLH. Review on ultrasonic machining. *Int J Mach Tool Manuf.*, 1998;38:239–255.
16. Khanna N, Airao J, Gupta MK, Song Q, Liu Z, Mia M, Maruda R, Krolczyk G. Optimization of power consumption as-associated with surface roughness in ultrasonic assisted turning of Nimonic-90 using hybrid particle swarm-simplex method. *Materials.*, 2019;12:3418
17. Airao J, Khanna N, Roy A, Hegab H. Comprehensive experimental analysis and sustainability assessment of machining Nimonic 90 using ultrasonic assisted turning facility. *Int J Adv Manuf Technol.*, 2020;109:1447-1462.
18. Yang Z, Zhu L, Zhang G, Ni C, Lin B. Review of ultrasonic vibration-assisted machining in advanced materials. *Int J Mach Tool Manuf.*, 2020;156:103594.
19. Skelton RC. Turning with an oscillating tool, *Int. J. Mach. Tool Des. Res.*, 1968;8:239–259.
20. Brehl DE., Dow T.A. Review of vibration-assisted machining. *Prec. Eng.*, 2008;32:153–172.
21. Adnan AS, Subbiah S. Experimental investigation of transverse vibration-assisted orthogonal cutting of AL-2024. *Int J Mach Tool Manuf.*, 2010;50:294–302.
22. Muhammad R, Hussain MS, Maurotto A, Siemers C, Roy A, Silberschmidt VV. Analysis of a free machining  $\alpha+\beta$  titanium alloy using conventional and ultrasonically assisted turning. *J Mater Process Technol.*, 2014;214:906– 915.

23. Amini S, Lotfi M, Paktinat H, Kazemiyoun M. Characterization of vibratory turning in cutting zone using a pneumatic quick-stop device. *Eng Sci Technol, Int J.*, 2017;20:403–410.
24. Xu Y, Wan Z, Zou P, Zhang Q. Experimental study on chip shape in ultrasonic vibration-assisted turning of 304 austenitic stainless-steel. *Adv Mech Eng.*, 2019;11(8):1–17.
25. Bai W, Bisht A, Roy A, Suwas S, Sun R, Silberschmidt VV. Improvements of machinability of aerospace-grade Inconel alloys with ultrasonically assisted hybrid machining. *Int J Adv Manuf Technol.*, 2019;101:1143–1156.
26. Pei L, Wu H. effect of ultrasonic vibration on ultraprecision diamond turning of Ti6Al4V. *Int J Adv Manuf Technol.*, 2019;103:433-440.
27. Peng Z, Zhang X, Zhang D. Improvement of Ti-6Al-4V surface integrity through the use of high-speed ultrasonic vibration cutting. *Tribo Int.*, 2021;160:107025.
28. Peng Z, Zhang X, Zhang D. Effect of radial high-speed ultrasonic vibration cutting on machining performance during finish turning of hardened steel. *Ultrasonics*, 2021;111:106340.
29. Zhang L, Hashimoto T, Yan J. Machinability exploration for high-entropy alloy FeCrCoMnNi by ultrasonic vibration-assisted diamond turning. *CIRP Ann. Manuf Technol.*, 2021;70:37-40.
30. Muhammad R. A Fuzzy Logic Model for the Analysis of Ultrasonic Vibration Assisted Turning and Conventional Turning of Ti-Based Alloy. *Materials*. 2021;14(21):6572.
31. Liu X, Zhang J, Li L. Surface Integrity and Friction Performance of Brass H62 Textured by One-Dimensional Ultrasonic Vibration-Assisted Turning. *Micromachines*. 2021;12(11):1398.
32. Bertolini R, Ghiotti A, Brushi S. Wear behaviour of Ti6Al4V surfaces functionalized through ultrasonic vibration turning. *J Mater Eng Perf.*, 2021;30(10):7597-7608.
33. Kim J, Zani L, Kadir A, Ribeiro ML, Roy A, Baxevanakis KP, Jones LCR, Silberschmidt VV. Ultrasonically assisted turning of micro-SiCp/Al 2124 composites. *Proc Struc Integ.*, 2022;37:282-291.
34. Liu J, Jiang X, Han X, Gao Z, Zhang D. Effects of rotary ultrasonic elliptical machining for side milling on the surface integrity of Ti-6Al-4V. *Int J Adv Manuf Technol.*, 2019;101:1451-1465
35. Zhang M, Zhang D, Geng D, Shao Z, Liu Y, Jiang X. Effects of tool vibration on surface integrity in rotary ultrasonic elliptical end milling of Ti6Al4V. *J Alloy Comp.*, 2020;821:153266.
36. Liu Q, Xu J, Yu H. Experimental study of tool wear and its effects on cutting process of ultrasonic-assisted milling of Ti6Al4V. *Int J Adv Manuf Technol.*, 2020;108:2917-2928.
37. Chen P, Tong J, Zhao J, Zhang Z, Zhao B. A study of the surface microstructure and tool wear of titanium alloys after ultrasonic longitudinal-torsional milling. *J Manuf Process.*, 2020;53:1-11.
38. Xie W, Wang X, Liu E, Wang J, Tang X, Li G, Zhang J, Yang L, Chai Y, Zhao B. Research on cutting force and surface integrity of TC18 titanium alloy by longitudinal ultrasonic vibration assisted milling. *Int J Adv Manuf Technol.*, 2021; <https://doi.org/10.1007/s00170-021-08532-y>.
39. Su Y, Li L. Surface integrity of ultrasonic-assisted dry milling of SLM Ti6Al4V using polycrystalline diamond tool. *Int J Adv Manuf Technol.*, 2021; <https://doi.org/10.1007/s00170-022-08669-4>.
40. Chen J, Ming W, An Q, Chen M. Mechanism and feasibility of ultrasonic-assisted milling to improve the machined surface quality of 2D Cf/SiC composites. *Cera Int.*, 2020;46:15122-15136.
41. Wei L, Wang D. Comparative study on drilling effect between conventional drilling and ultrasonic-assisted drilling of Ti-6Al-4V/Al2024-T351 laminated material. *Int J Adv Manuf Technol.*, 2019;103:141-152.
42. Moghaddas MA, Yi AY, Graff KF. Temperature measurement in the ultrasonic-assisted drilling process. *Int J Adv Manuf Technol.*, 2019;103:187-199.

43. Chu NH, Nguyen VD, Ngo QH. Machinability enhancement of ultrasonic-assisted deep drilling of aluminium alloys. *Mach Sci Technol.*, 2020;24(1):112-135.
44. Saffar S, Abdullah A. Experimental investigation on Ultrasonic Assisted Drilling (UAD). *J Braz Soc Mech Sci Eng.*, 2021;43:351.
45. Moghaddas A. Characterization of thrust force, temperature, chip morphology and power in ultrasonic-assisted drilling of aluminium 6061. *Int J Adv Manuf Technol.*, 2022; <https://doi.org/10.1007/s00170-021-07742-8>.
46. Debnath S, Reddy MM, Yi QS. Environmentally friendly cutting fluids and cooling techniques in machining: A Review. *J Clean Prod.*, 2014; DOI: 10.1016/j.jclepro.2014.07.071.
47. Sankaranarayana R, Rajesh JHN, Kumar SJ, Krolczyk GM. A comprehensive review on research developments of vegetable-oil based cutting fluids for sustainable machining challenges. *J Manuf Process.*, 2021;67:286-313.
48. Pervaiz S, Kannan S, Kishawy H. An Extensive Review of The Water Consumption and Cutting Fluid Based Sustainability Concerns in The Metal Cutting Sector. *J Clean Prod.*, 2018, 10.1016/j.jclepro.2018.06.190.
49. Caballero B, Finglas P, Toldra F. *Encyclopaedia of food sciences and nutrition*. second ed. Elsevier; 2003.
50. Katna R, Suhaib M, Agrawal N. Nonedible vegetable oil-based cutting fluids for machining processes – a review. *Mater Manuf Process.*, 2020;35(1):1-32.
51. Lawal SA, Choudhary IA, Nukman Y. Developments in the formulation and application of vegetable oil-based metalworking fluids in turning process. *Int J Adv Manuf Technol.*, 2013;67:1765-1776.
52. Weinert K, Inasaki I, Sutherland JW, Wakabayashi T. Dry Machining and Minimum Quantity Lubrication. *CIRP Ann—Manuf. Technol.*, 2004;53(2):511–537.
53. Attanasio A, Gelfi M, Giardini C, Remino C. Minimal quantity lubrication in turning: Effect on tool wear. *Wear* 2006;260:333–338.
54. Lawal SA, Choudhury IA, Nukman Y. A critical assessment of lubrication techniques in machining processes: a case for minimum quantity lubrication using vegetable oil-based lubricant. *J Clean Prod.*, 2013;41:210e221
55. Chincharikar S, Choudhury SK, Hard turning using HiPIMS-coated carbide tools: Wear behaviour under dry and minimum quantity lubrication (MQL). *Measurement* 2014;55:536–548
56. Sivaiah P, Guru Prasad M, Singh M, Uma B Machinability evaluation during machining of AISI 52100 steel with textured tools under Minimum Quantity Lubrication – A comparative study, *Mater Manuf Process.* 2020;35(15):1761-1768.
57. Liu N, Zou X, Yuan J, Wu S, Chen Y. Performance evaluation of castor oil-ethanol blended coolant under minimum quantity lubrication turning of difficult-to-machine materials. *J Manuf Process.* 2020;58:1–10.
58. Said Z, Gupta M, Hegab H, Arora N, Khan AM, Jamil M. Evangelos Bellos A comprehensive review on minimum quantity lubrication (MQL) in machining processes using nano-cutting fluids. *Int J Adv Manuf Technol.*, 2019;105:2057–2086.
59. Wang X, Li C, Zhang Y, Ding W, Yang M, Gao T, Cao H, Xu X, Wang D, Said Z, Debnath S, Jamil M, Ali HM. Vegetable oil-based nanofluid minimum quantity lubrication turning: Academic review and perspectives. *J Manuf Process.*, 2020;59:76–97.
60. Najiha MS, Rahman MM, Yusoff AR. Flank Wear Characterization in Aluminum Alloy (6061 T6) With Nanofluid Minimum Quantity Lubrication Environment Using an Uncoated Carbide Tool. *ASME J Manuf Sci Eng.*, 2015;137(6):061004.
61. Sharma P, Sidhu BS, Sharma J. Investigation of effects of Nanofluids on turning of AISI D2 Steel using Minimum Quantity Lubrication. *J Clean Prod.*, 2015, doi:10.1016/j.jclepro.2015.07.122.
62. Yıldırım CV, Sarıkaya M, Kıvak T, Şirin Ş. The effect of addition of hBN nanoparticles to nanofluid-MQL on tool wear patterns, tool life, roughness and temperature in turning of Ni-based Inconel 625. *Trib Int.*, 2019;134:443–456.

63. Gaurav G, Sharma A, Dangayach GS, Meena ML, Assessment of jojoba as a pure and nano-fluid base oil in minimum quantity lubrication (MQL) hard-turning of Ti-6Al-4V: A step towards sustainable machining, *J Clean Prod.*, <https://doi.org/10.1016/j.jclepro.2020.122553>.
64. Pal A, Chatha SS, Sidhu HS. Experimental investigation on the performance of MQL drilling of AISI 321 stainless steel using nano-graphene enhanced vegetable-oil-based cutting fluid. *Trib Int.*, 2020;151:106508
65. Sirin S, Sarikaya M, Yildirim ÇV, Kıvak T. Machinability performance of nickel alloy X-750 with SiAlON ceramic cutting tool under dry, MQL and hBN mixed nanofluid-MQL. *Trib Int.*, 2021;153:106673.
66. Xu X, Huang S, Wang M, Yao W. A study on process parameters in endmilling of AISI-304 stainless steel under electrostatic minimum quantity lubrication conditions. *Int J Adv Manuf Technol.*, 2017;90:979–989
67. Huang S, Lv T, Xu X, Ma Y, Wang M. Experimental evaluation on the effect of electrostatic minimum quantity lubrication (EMQL) in end milling of stainless steels. *Mach Sci Technol.*, 2018;22(2):271–286.
68. Lv T, Huang S, Liu E, Ma Y, Xu X. Tribological and machining characteristics of an electrostatic minimum quantity lubrication (EMQL) technology using graphene nano-lubricants as cutting fluids. *J Manuf Process.*, 2018;34:225–237.
69. Shah P, Gadkari A, Sharma A, Shokrani A, Khanna N. Comparison of machining performance under MQL and ultra-high voltage EMQL conditions based on tribological properties. *Trib Int.*, 2021;153:106595
70. Lv T, Xu X, Yu A, Hu X. Oil mist concentration and machining characteristics of SiO<sub>2</sub> water-based nano-lubricants in electrostatic minimum quantity lubrication-EMQL milling. *J Mater Process Tech.*, 2021;290:116964.
71. Hong SY, Zhao Z. Thermal aspects, material considerations and cooling strategies in cryogenic machining. *Clean Prod Process.*, 1999;1:107–116.
72. Khanna N, Agrawal C, Pimenov DY, Singla AK, Machdo AR, da Silva LRR, Gupta MK, Sarikaya M, Krolczyk GM. Review on design and development of cryogenic machining setup for heat resistant alloys and composites. *J Manuf Process.*, 2021;68:398–422.
73. Yildiz Y, Nalbant M. A review of cryogenic cooling in machining processes. *Int J Mach Tools Manuf.*, 2008;48:947–964.
74. Deshpande Y V, Andhare AB, Padole PM. How cryogenic techniques help in machining of nickel alloys? A review. *Mach Sci Technol.*, 2018;22(4):543–584.
75. Courbon C, Pusavec F, Dumont F, Rech J, Kopac J. Tribological behaviour of Ti6Al4V and Inconel718 under dry and cryogenic conditions—Application to the context of machining with carbide tools. *Tribo Int.*, 2013;66:72–82.
76. Krishnamurthy G, Bhowmick S, Altenhof W, Alpas AT. Increasing efficiency of Ti-alloy machining by cryogenic cooling and using ethanol in MRF. *CIRP J Manuf Sci Technol.*, 2017;18:159–172
77. Kaynak Y, Gharibi A. Cryogenic Machining of Titanium Ti-5553 Alloy. *ASME J Manuf Sci Eng.*, 2019;141:041012.
78. Dhananchezian M. Study the machinability characteristics of Nicked based Hastelloy C-276 under cryogenic cooling. *Measurement* 2019;136:694–702.
79. Jadhav PS, Mohanty CP, Hotta TK, Gupta M. An optimal approach for improving the machinability of Nimonic C-263 superalloy during cryogenic assisted turning. *J Manuf Process.*, 2020;58:693–705.
80. Amigo FJ, Urbikain G, Pereira O, Fernandez-Lucio P, Fernandez-Valdivielso A, Lopez de Lacalle LN. Combination of high feed turning with cryogenic cooling on Haynes 263 and Inconel 718 superalloys. *J Manuf Process.*, 2020;58:208–222.
81. Khanna N, Agrawal C, Dogra M, Pruncu CI. Evaluation of tool wear, energy consumption, and surface roughness during turning of inconel 718 using sustainable machining technique. *J Mater Res Technol.*, 2020;9(3):5794–5804.

82. Halim NHA, Haron CHC, Ghani JA, Azhar MF. Tool wear and chip morphology in high-speed milling of hardened Inconel 718 under dry and cryogenic CO<sub>2</sub> conditions. *Wear* 2019;426–427:1683–1690.
83. Wang F, Wang Y. Investigate on effect of cryogenic cooling on oxidation wear of WC-Co carbide tool milling titanium alloy. *Mach Sci Technol.*, 2019;23(6):906-924.
84. Wang Y, Han L, Liu K, Gan Y, Dai M, Liu H. Optimization of Jet Parameters for Minimizing Surface Roughness in Cryogenic Milling of Ti-6Al-4V. *ASME J Manuf Sci Eng* May 2021;143(5):051011.
85. Jamil M, He N, Zhao W, Li L, Gupta MK, Sarikaya M, Khan AM, Singh R. Heat Transfer Efficiency of Cryogenic-LN<sub>2</sub> and CO<sub>2</sub>-snow and their application in the Turning of Ti-6AL-4V. *Int J Heat Mass Trans.*, 2021;166:120716.
86. Shah P, Bhat P, Khanna N. Life cycle assessment of drilling Inconel 718 using cryogenic cutting fluids while considering sustainability parameters. *Sus Energy Technol Assess.*, 2021;431:100950.
87. Shah P, Khanna N, Chetan. Comprehensive machining analysis to establish cryogenic LN<sub>2</sub> and LCO<sub>2</sub> as sustainable cooling and lubrication techniques. *Tribo Int.*, 2020;148:106314.
88. Attanasio A, Ceretti E, Outeiro J, Poulachon G. Numerical simulation of tool wear in drilling Inconel 718 under flood and cryogenic cooling conditions. *Wear* 2020;458-459:203403.
89. Arrazola PJ, Ozel T, Umbrello D, Davis M, Jawahir IS. Recent advances in modelling of metal machining processes. *CIRP Ann- Manuf Technol.*, 2013;62:695-718.
90. Dixit PM, Dixit US, Finite Element Modeling of Orthogonal Machining Process. In: *Modeling of Metal Forming and Machining Processes. Engineering Materials and Processes.* Springer, London. [https://doi.org/10.1007/978-1-84800-189-3\\_7](https://doi.org/10.1007/978-1-84800-189-3_7).
91. Melkote S, Liang S, Ozel Tawahir IS, Stephenson DA. A review of advances in modelling of conventional machining processes: From merchant to the present. *ASME J Manuf Sci Eng.*, 2022;144:110801.
92. Bai W, Sun R, Roy A, silberschmidt VV. Improved analytical prediction of chip formation in orthogonal cutting of titanium alloy Ti6Al4V. *Int J Mech Sci.*, 2017;133:357-367.
93. Zhang X, Sui H, Zhang D, Jiang X. An analytical transient cutting force model of high-speed ultrasonic vibration cutting. *Int J Adv Manuf Technol.*, 2018;95:3929-3941.
94. Huang W, Yu D, Zhang X, Zhang M, Chen D. Ductile-regime machining model for ultrasonic elliptical vibration cutting of brittle materials. *J Manuf Process.*, 2018;36:68-76.
95. Shan C, Zhang X, Shen B, Zhang D. An improved analytical model of cutting temperature in orthogonal cutting of Ti6Al4V. *Chin J Aero.*, 2019;32(3):759-769.
96. Bai W, Roy A, Guo L, Xu J, Silberschmidt VV. Analytical prediction of shear angle and frictional behaviour in vibration-assisted cutting. *J Manuf Process.*, 2021;62:37-46.
97. Arefin S, Zhang X, Kumar AS, Neo DWK, Wang Y. Study of chip formation mechanism in one-dimensional vibration-assisted machining. *J Mater Process technol.*, 2021;291:117022.
98. Verma GC, Pandey PM. Machining forces in ultrasonic-vibration assisted end milling. *Ultrasonics*, 2018. <https://doi.org/10.1016/j.ultras.2018.07.004>.
99. Verma GC, Pandey PM, Dixit US. Modeling of static machining force in axial ultrasonic-vibration assisted milling considering acoustic softening. *Int J Mech Sci.*, 2018;136:1-16.
100. Yan L, Zhang Q, Yu J. Analytical model for oil penetration and experimental study on vibration assisted machining with minimum quantity lubrication. *Int J Mech Sci.*, 2018, <https://doi.org/10.1016/j.ijmecsci.2018.09.016>.
101. Feng Y, Hsu F, Lu Y, Lin Y, Lin C, Lin C, Lu Y, Liang SY. Temperature prediction of ultrasonic vibration-assisted milling. *Ultrasonics*, 2020;108:106212.

102. Ying N, Feng J, Bo Z, Guofu G, Jing-jing N. Theoretical investigation of machining-induced residual stresses in longitudinal torsional ultrasonic-assisted milling. *Int J Adv Manuf Technol.*, 2020;108:3689-3705.
103. Gao G, Xia Z, Su T, Xiang D, Zhao B. Cutting force model of longitudinal-torsional ultrasonic-assisted milling Ti-6Al-4V based on tool flank wear. *J Mater Process Technol.*, 2021;291:117042.
104. Zai P, Tong J, Liu Z, Zhang Z, Song C, Zhao B. Analytical model of exit burr height and experimental investigation on ultrasonic-assisted high-speed drilling micro-holes. *J Manuf Process.*, 2021;68:807-817.
105. Zhu X, Wang W, Jiang R, Xiong Y, Liu X. Modeling of burr height in ultrasonic-assisted drilling of DD6 superalloy. *Int J Adv Manuf Technol.*, 2022, <https://doi.org/10.1007/s00170-021-08524-y>.
106. Cao S, Li HN, Huang W, Zhou Q, Lei T, Wu C. A delamination prediction model in ultrasonic vibration assisted drilling of CFRP composites. *J Mater Process Technol.*, 2022;302:117480.
107. Huang W, Zhang W, Wu C, Cao S, Zhou Q. Tool wear prediction in ultrasonic vibration-assisted drilling of CFRP: A hybrid data-driven physics model-based framework. *Tribol Int.*, 2022, 107755.
108. Lotfi M, Akbari J. Finite element simulation of ultrasonic-assisted machining: a review. *Int J Adv Manuf Technol.*, 2021, <https://doi.org/10.1007/s00170-021-07205-0>.
109. Lotfi M, Amini S. FE simulation of linear and elliptical ultrasonic vibrations in turning of Inconel 718. *Proc IMech E: J Process mech Eng.*, 2017;1-11.
110. Lotfi M, Amini S, Aghaei M. 3D FEM simulation of tool wear in ultrasonic assisted rotary turning. *Ultrasonics*, 2018;88:106-114.
111. Gholamzadeh B, Soleimanimehr H. Finite element modeling of ultrasonic-assisted turning: cutting force and heat generation. *Mach Sci Technol.*, 2019;23(6):869-885.
112. Shuang F, Ma W. Numerical investigation of orthogonal cutting process with tool vibration of Ti6Al4V alloy. *Proc CIRP*, 2019;82:267-272.
113. Khajehzadeh M, Boostanipour O, Razfar MR. Finite element simulation and experimental investigation of residual stresses in ultrasonic assisted turning. *Ultrasonics*, 2020;108:106208.
114. Lotfi M, Amini S, Akbari J. Surface integrity and microstructure changes in 3D elliptical ultrasonic assisted turning of Ti-6Al-4V: FEM and experimental examination. *Tribol Int.*, 2020;151:106492.
115. Kurniawan R, Kumaran ST, Ko TJ. Finite Element Analysis in Ultrasonic Elliptical Vibration Cutting (UEVC) During Micro-Grooving in AISI 1045. *Int J Prec Eng Manuf.*, 2021;22:1497-1515.
116. Elhami S, Razfar MR, Farahnakian M. Analytical, numerical and experimental study of cutting force during thermally enhanced ultrasonic assisted milling of hardened AISI 4140. *Int J Mech Sci.*, 2015;103:158-171.
117. Chen W, Huo D, Hale J, Ding H. Kinematics and tool-workpiece separation analysis of vibration assisted milling. *Int J Mech Sci.*, 2018;136:169-178.
118. Xiang D, Shi Z, Feng H, Wu B, Zhang Z, Chen Y, Niu X, Zhao B. Finite element analysis of ultrasonic assisted milling of SiCp/Al composites. *Int J Adv Manuf Technol.*, 2019;105:3477-3488.
119. Chen W, Zheng L, Teng X, Yang K, Huo D. Finite element simulation and experimental investigation on cutting mechanism in vibration-assisted micro-milling. *Int J Adv Manuf Technol.*, 2019;105:4539-4549.
120. Ying N, Feng J, Bo Z. A novel 3D finite element simulation method for longitudinal-torsional ultrasonic-assisted milling. *Int J Adv Manuf Technol.*, 2020;106:385-400.
121. Lotfi M, Amini S. Experimental and numerical study of ultrasonically-assisted drilling. *Ultrasonics*, 2017;75:185-193.
122. Paktinat H, Amini S. Ultrasonic assistance in drilling: FEM analysis and experimental approaches. *Int J Adv Manuf Technol.*, 2017;92:2653-2665.

123. Paktinat H, Amini S. Experiments and Finite Element Simulation of Ultrasonic Assisted Drilling. *ASME J Manuf Sci Eng.*, 2018;144:101002.
124. Wang P, Wang D. Experiments and Finite Element Simulation of Ultrasonic Assisted Drilling. *Proc IMech Part C: J Mech Eng Sci.*, 2019;1-13.
125. Wang P, Wang D. Evaluation of different tool geometries in the finite element simulation of ultrasonic-assisted drilling of Ti6Al4V. *J Braz Soc Mech Sci Eng.*, 2020;42:181.
126. Razavi H, Mirbagheri M. Design and fabrication of a novel vibrational system for ultrasonic assisted oblique turning process. *J Mech Sci Technol.*, 2016;30:827-835.
127. Fahy F, Gardonio P, Sound and structural vibration- radiation, transmission and response Elsevier, 2007, ISBN 13: 978-0-12-373633-8.
128. Uoussef H, El-Hofy H, Machining technology- Machine tools and operations, Taylor and Francis Group, CRC press 2008.
129. Xiao M, Karube S, Soutome T, Sato K. Analysis of chatter suppression in vibration cutting. *Int J Mach Tools Manuf.*, 2002;42:1677–1685.
130. Gulia P, Gupta A, Mathematics Applied to Engineering, Elsevier, 2017. <http://dx.doi.org/10.1016/B978-0-12-810998-4.00003-X>.
131. Webster AG, Acoustical impedance, and the theory of horns and of the phonograph. Physics, 1919.
132. Leyens C, Peters M. Titanium and Titanium alloys: Fundamentals and applications. Wiley-VCH, Weinheim. 2003.
133. Reed RC. The superalloys: Fundamentals and applications. Cambridge university press. Cambridge, 2006.
134. Sarikaya M, Gupta MK, Tomaz I, Danish M, Mia M, Rubaiee S, Jamil M, Pimenov DY, Khanna N. Cooling techniques to improve the machinability and sustainability of light-weight alloys: A state-of-the-art review. *J Manuf process.*, 2021;62:179-201.
135. Pimenov DY, Mia M, Gupta MK, Machado AR, Pintaude G, Unune DR, Khanna N, Khan AM, Tomaz I, Wojciechowski S, Kuntoglu M. Resource saving by optimization and machining environments for sustainable manufacturing: A review and future prospects. *Renew Sustain Energy Rev.*, 2022;166:112660.
136. Wickramasinghe KC, Sasahara H, Rahim EA, Perera GIP. Green Metalworking Fluids for sustainable machining applications: A review. *J Clean Prod.*, 2020;257:120552.
137. Ghazani, SM, Marangoni AG. Healthy Fats and Oils. *Encyc Food Grains*, 2016;257–267. doi:10.1016/b978-0-12-394437-5.00100-5.
138. Kaynak Y, Lu T, Jawahir IS. Cryogenic machining-induced surface integrity: a review and comparison with dry, MQL, and flood-cooled machining. *Mach Sci Technol.*, 2014;18:149–98.
139. Melkote S, Liang S, Ozel T, Jawahir IS, Stephenson DA, Wang B. A review of advances in modelling of conventional machining processes: From merchant to the present. *ASME J Manuf Sci Eng.*, 2022;144(1) 110801.
140. Merchant ME, Basic mechanics of the metal cutting process. *ASME J Appl Mech.*, 1944;11(3):A168-A175.
141. Oxley PLB, Welsh MJM. An explanation of the apparent bridgman effect in Merchant's orthogonal cutting results. *ASME J Eng Ind.*, 1967;89(3):549-555.
142. Lee EH, Shaffer BW. The theory of plasticity applied to a problem of machining. *ASME J Appl Mech.*, 1951;18(4):405-413.
143. Palmer WB, Oxley PLB. Mechanics of orthogonal machining. *Proc Inst Mech Eng.*, 1959;173(1):623-654.
144. Fang N, Jawahir IS. An analytical predictive model and experimental validation for machining with grooved tools incorporating the effects of strains, strain rates and temperatures. *CIRP Ann.*, 2002;51(1):83-86.
145. Manyindo BM, Oxley PLB. Experimental investigation of a slip-line field model for a worn cutting tool. *Proc Inst Mech Eng Part C.*, 2014;228(8):1398-1404.
146. Uysal A, Jawahir IS. A slip-line model for serrated chip formation in machining of stainless steel and validation. *Int J Adv Manuf Technol.*, 2019;101:2449-2464.



147. Nath C, Rahman M. Effect of Machining Parameters in Ultrasonic Vibration Cutting, *Int J Mach Tools Manuf.*, 2008;48:965–974.
148. Merchant ME, Mechanics of the Metal Cutting Process. I. Orthogonal Cutting and a Type 2 Chip, *J App Phys.*, 1945;16(267).
149. Merchant ME, Mechanics of the Metal Cutting Process. II. Plasticity Conditions in Orthogonal Cutting, *J App Phys.*, 1945;16(318).
150. Oxley PLB. Mechanics of Machining: An Analytical Approach to Assessing Machinability, Ellis Horwood, Chichester, 1989.
151. Shaw MC. Metal Cutting Principles, Oxford university press, 2005.
152. Kalpakjian S, Schmid SR, Sekar KSV, Manufacturing Engineering and Technology, Pearson, 2004.
153. Toropov A, Ko, SL. Prediction of Shear Angle for Continuous Orthogonal Cutting Using Thermo-Mechanical Constants of Work Material and Cutting Conditions, *J Mater Process Technol.*, 2007;182:167–173.
154. Hill R. The Mathematical Theory of Plasticity, Oxford-Clarendon press, 1956.
155. Trent EM, Wright PK. Metal Cutting, Butterworth-Heinemann Elsevier, 2000.
156. Oxley PLB, Hastings WF. Predicting the Strain Rate in the Zone of Intense Shear in Which the Chip is Formed in Machining from the Dynamic Flow Stress Properties of the Work Material and the Cutting Conditions, *Proc. R. Soc. Lond. A*, 1977;356:395–410.
157. Boothroyd G. Temperatures in Orthogonal Metal Cutting, *Proceed. Inst. Mech. Eng.* 1933;177(1):789–810.
158. Johnson GR, Cook WH. A Constitutive Model and Data for Metals Subjected to Large Strains, High Strain Rates and High Temperatures, in: *Proceed 7th Int. Symp. Ballistics*, 1983;541–547.
159. Wright PK, Horne JG, Tabor D. Boundary Conditions at The Chip-Tool Interface in Machining: Comparisons Between Seizure and Sliding Friction, *Wear*, 1979;54:371–90.
160. Zorev N. Inter-Relationship Between Shear Processes Occurring Along Tool Face and Shear Plane in Metal Cutting, *Int Res Prod Eng.*, 1963;49:143–152.
161. Roth RN, Oxley PLB. Slip-Line Field Analysis for Orthogonal Machining Based Upon Experimental Flow Fields, *J Mech Eng Sci.*, 1972;14:85–97.
162. Fatima A, Mativenga PT. A review of tool-chip contact length models in machining and future direction for improvement, *Proceed Inst. Mech. Eng. Part B: J.Eng. Manuf.*, 2013;227- 345.
163. Pittalà GM, Monno M. Flow stress determination in orthogonal cutting process combining the primary and the secondary shear zones, *Int J Mater Form.*, 2010;3(1)483–486.
164. Guo YB. Mechanical Behaviour Characterization of the Secondary Shear Zone in Metal Cutting, In: *Trans. NAMRI/SME* 2002;30:423–430.
165. Moufki A, Molinari A, Dudzinski D. Modelling of Orthogonal Cutting with A Temperature Dependent Friction Law, *J Mech Phys Solids.*, 1998;46:2103–2138.
166. Childs T, Maekawa K, Obikawa T, Yamane Y. Metal Machining, Oxford: Butterworth-Heinemann, 2000.
167. Ozlu E, Molinari A, Budak E. Two-Zone Analytical Contact Model Applied to Orthogonal Cutting, *Mach Sci Technol.*, 2010;14(3):323–343.
168. Chagas GMP, Machado IF. Numerical Model of machining considering the effect of MnS inclusions in an Austenitic Stainless Steel, *Proc. CIRP*, 2015;31:533–538.
169. Verma GC, Pandey PM, Dixit US. Modelling of Static Machining Force in Axial Ultrasonic-Vibration Assisted Milling Considering Acoustic Softening, *Int J Mech Sci.*, 2018;136:1–16.
170. Markopoulos AP. Finite Element Method in Machining Processes, Springer, 2013.
171. Xi Y, Bermingham M, Wang G, Dargusch M. Finite Element Modeling of Cutting Force and Chip Formation During Thermally Assisted Machining of Ti6Al4V Alloy. *ASME J Manuf Sci Eng.*, 2013;135(6): 061014.
172. Cockroft MG, Latham DJ Ductility and workability of metals. *J Inst Met.*, 1968;96:33–



- 39.
173. Umbrello D. Finite element simulation of conventional and high-speed machining of Ti6Al4V alloy. *J Mater Process Technol.*, 2008;196:79-87.
174. Chetan, Ghosh S, Rao PV. Specific cutting energy modeling for turning nickel-based Nimonic 90 alloy under MQL condition, *Int J Mech Sci.*, 2018;146–147:25-38.
175. Lotfi M, Saeid A, Mohsen A. Tool wear modelling in rotary turning modified by ultrasonic vibration, *Simul Model Prac The.*, 2018;87:226-238.
176. Yen YC, Jain A, Altan T. A finite element analysis of orthogonal machining using different tool edge geometries. *J Mater Process Technol.*, 2004;146(1):72–81
177. Ozel T. The influence of friction models on finite element simulations of machining. *Int J Mach Tools Manuf.*, 2006;46:518-530.
178. Usui E, Shirakhashi T, Kitagawa T. Part: 3 analytical predictions of three-dimensional cutting process. *Trans ASME: J Eng Ind.*, 1978;1: 33–38.
179. Airao J, Nirala CK, Lacalle LNdl, Khanna N. Tool Wear Analysis during Ultrasonic Assisted Turning of Nimonic-90 under Dry and Wet Conditions, *Metals* 2021;11(8):1253.
180. Stephenson DA, Agapiou JS. *Metal Cutting Theory and Practice*, CRC Press, 1997.
181. Choi YH, Lee CM. A study on the machining characteristics of AISI 1045 steel and Inconel 718 with circular cone shape in induction assisted machining. *J Manuf Process.*, 2018;34:464-476.
182. Ezugwu EO, Wang ZM, Machado AR. The machinability of Nickel-based alloys: A review. *J Mater Process Technol.*, 1999;86:1-16.
183. Ozler L, Inan A, Ozel C. Theoretical and experimental determination of tool life in hot machining of austenitic manganese steel. *Int J Mach Tools Manuf.*, 2001;41:163-172.
184. Zhu D, Zhang X, Ding H. Tool wear characteristics in machining of Nickel-based superalloys, *Int J Mach Tools Manuf.*, 2013;64:60-77.
185. Devillez A, Schneider F, Dominiak S, Dudzinski D, Larrouquere D. Cutting forces and wear in dry machining of Inconel 718 with coated carbide tools. *Wear* 2007;262:931-942.
186. Ambhore N, Kamble D, Agrawal D. Experimental Investigation of Induced Tool Vibration in Turning of Hardened AISI52100 Steel. *J Vib Eng Technol.*, 2022, <https://doi.org/10.1007/s42417-022-00473-4>
187. Chetan, Behra BC, Ghosh S, Rao PV. Wear behaviour of PVD TiN coated carbide inserts during machining of Nimonic 90 and Ti6Al4V superalloys under dry and MQL conditions. *Cera Int.*, 2016;42:14873-14885.
188. Bermingham MJ, Oalanisamy S, Dargusch MS. Understanding the tool wear mechanism during thermally assisted machining Ti-6Al-4V. *Int J Mach Tools Manuf.*, 2012;62:76-87.
189. Thakur DG, Ramamoorthy B, Vijayaraghavan L. Study on the Machinability Characteristics of Superalloy Inconel 718 During High-Speed Turning *Mater Des*, 2009;30:1718-1725.
190. Singh A, Ghose S, Aravindan S. State of art for sustainable machining of nickel-based super alloy using coated and uncoated tools and machining of high strength materials using surface modified cutting tools. *Tribo Int.* 2022;170:107517.
191. Nath C, Rahman M, Andrew SSK. A study on ultrasonic vibration cutting of low alloy steel. *J. Mater Process Technol.* 2007;192-193:159-165
192. Singh A, Ghosh S, Aravindan S. Flank wear and rake wear studies for arc enhanced HiPIMS coated AlTiN tools during high speed machining of Nickel-based super alloy. *Surf Coat Technol.* 2020;381:125190.
193. Chaabani S, Arrazola PJ, Ayed Y, Madariaga A, Tidu A, Germain G. Comparison between cryogenic coolants effect on tool wear and surface integrity in finishing turning of Inconel 718. *L Mater Process Technol.* 2020;285:116780.
194. Cantero JL, Diaz-Alvarez J, Miguelez MH, Marin NC. Analysis of tool wear pattern in finishing turning of Inconel 718. *Wear* 2013;297:885-894.
195. Yan L, Zhang Q, Yu J. Effects of continuous minimum quantity lubrication with

- ultrasonic vibration in turning of titanium alloy. *Int J Adv Manuf technol.* 2018;98:827-837.
196. Khanna N, Shah P, Chetan, Comparative analysis of dry, flood, MQL and cryogenic CO<sub>2</sub> techniques during the machining of 15-5-PH SS alloy. *Tribo Int* 2020;146:106196.
  197. Hong SY, Ding Y, Jeong W, cheo I. Friction and cutting forces in cryogenic machining of Ti-6Al-4V. *Int J Mach Tools Manuf* 2001;41:2271-2285.
  198. Patil NG, Asem A, Pawade RS, Thakur DG, Brahmanekar PK. Comparative study of high speed machining of Inconel 718 in dry condition and by using compressed cold carbon dioxide gas as coolant *Proc CIRP*, 2014;24:86-91.
  199. Ezugwu EO, Olajire KA, Jawaid A. Wear performance of multiplayer coated carbide tools. *Mach Sci Technol*, 2001;5(1):115-119.
  200. Ezugwu EO, Bonney J, Yamane Y. An overview of the machinability of aeroengine alloy. *J Mater Process Technol*, 2003;134:233-253.
  201. Alagan NT, Hoier P, Zeman P, Klement U, Beno T, Wretland A. Effects of high-pressure cooling in the flank and rake faces of WC tool on the tool wear mechanism and process conditions in turning of alloy 718. *Wear* 2019;434-435:102922.
  202. Halim NHA, Haron CHC, Ghani JA. PVD multi-coated carbide milling inserts performance: Comparison between cryogenic and dry cutting conditions. *J Manuf Process.* 2022;73:895-902.
  203. Khanna N, Agrawal C, Gupta MK, Song Q, Singla AK. Sustainability and machinability improvement of Nimonic-90 using indigenously developed hybrid machining technology. *J Clean Prod.* 2020;263:121402.
  204. Koyilada B, Gangopadhyay S, Thakur A. Comparative evaluation of machinability characteristics of Nimonic C-263 using CVD and PVD coated tools. *Measurement* 2016;85:152-163.
  205. Grzesik W, Nieslony P, Habrat W, Sieniawski J, Laskowski P. Investigation of tool wear in the turning of Inconel 718 superalloy in terms of process performance and productivity enhancement. *Tribo Int* 2018;118:337-346.
  206. Groover M. *Fundamentals of Modern Manufacturing: Materials, Processes, and Systems*, 7th edition. John Wiley & Sons, 2020.
  207. Ji M, Xu J, Chen M, Mansori ME. Effects of different cooling methods on the specific energy consumption when drilling CFRP/Ti6Al4V stacks. *Proc Manuf.* 2020;43:95-102.
  208. Garcia LCF, Rojas HAG, Egea AJS. Estimation of specific cutting energy in an S235 alloy for multi-directional ultrasonic vibration-assisted machining using the finite element method. *Materials.* 2020;13:567.
  209. Komanduri R, Schroeder TA. On shear instability in Machining a Nickel-iron base superalloy. *J Eng Ind.* 1986;108.
  210. Yildirim CV, Kivak T, Sarikaya M, Sirin S. Evaluation of tool wear, surface roughness/topography and chip morphology when machining of Ni-based alloy 625 under MQL, cryogenic cooling and cryoMQL. *J Mater Res Technol.* 2020;9(2):2079-2092.
  211. Khanna N, Shah P, Lacalle LNLd, Rodriguez A, Pereira O. In pursuit of sustainable cutting fluid strategy for machining Ti-6Al-4V using life cycle analysis. *Sustain Mater Technol.* 2021;21:e00301.
  212. Biksa A, Yamamoto K, Dosbaeva G, Veldhuis SC, Fox-Rabinovich GS, Elfizy A, Wagg T, Shuster LS. Wear behavior of adaptive nano-multi layered AlTiN/MexN PVD coatings during machining of aerospace alloys. *Tribo Int.* 2010;43:1491-1499.
  213. Çalışkan H, Küçükköse M. The effect of aCN/TiAlN coating on tool wear, cutting force, surface finish and chip morphology in face milling of Ti6Al4V superalloy. *Int J Ref Mater Hard Met* 2015;50:304-312
  214. Kramer BM. On tool materials for high speed machining. *J Eng Ind.* 1987;109:87-91.
  215. Pusavec F, Deshpande A, Yang S, M'Saoubi R, Kopac J, Dillon Jr OW, et al. Sustainable machining of high temperature Nickel alloy – inconel 718: part 1 – predictive performance models. *J Clean Prod* 2014;81:255–69.
  216. Jayal AD, Balaji AK. Effects of cutting fluid application on tool wear in machining:

- Interactions with tool-coatings and tool surface features. *Wear* 2009;267:1723-1730.
217. Sadik MI, Isakon S. The role of PVD coating and coolant nature in wear development and tool performance in cryogenic and wet milling of Ti-6Al-4V. *Wear* 2017;386-387:204-210.
  218. Wang CY, Xie YX, Qin Z, Lin HS, Yuan YH, Wang QM. Wear and breakage of TiAlN- and TiSiN-coated carbide tools during high-speed milling of hardened steel. *Wear* 2015;336-337:29-42.
  219. Stolf P, Paiva JM, Ahmed YS, Endrino JL, Goel S, Veldhuis SC. The role of high-pressure coolant in the wear characteristics of WC-Co tools during the cutting of Ti-6Al-4V. *Wear* 2019;440-441:203090.
  220. Ni C, Zhu L, Yang Z. Comparative investigation of tool wear mechanism and corresponding machined surface characterization in feed-direction ultrasonic vibration assisted milling of Ti-6Al-4V from dynamic view. *Wear* 2019;436-437:203006.
  221. Gajarani KK. Assessment of cryo-MQL environment for machining of Ti-6Al-4V. *J Manuf Process*. 2020;60:494-502.
  222. Pawlus P, Reizer R, Wiczorowski M. Analysis of surface texture of plateau-honed cylinder liner – A review. *Prec Eng*. 2021;72:807-822.
  223. Zhang D, Shao Z, Geng D, Jiang X, Liu Y, Zhou Z, Li S. Feasibility study of wave-motion milling of carbon fiber reinforced plastic holes. *Int J Extrem Manuf*. 2021;3:01401.
  224. Kaynak Y, Karaca HE, Noebe RD, Jawahir IS. Tool-wear analysis in cryogenic machining of NiTi shape memory alloys: A comparison of tool-wear performance with dry and MQL machining. *Wear* 2013;306:51-63.
  225. Geng D, Liu Y, Shao Z, Zhang M, Jiang, X, Zhang D. Delamination formation and suppression during rotary ultrasonic elliptical machining of CFRP. *Comp Part B*. 2020;183:107698.
  226. Agrawal C, Wadhwa J, Pitroda A, Pruncu CI, Sarikaya M, Khanna N. Comprehensive analysis of tool wear, tool life, surface roughness, costing and carbon emissions in turning Ti-6Al-4V titanium alloy: Cryogenic versus wet machining. *Tribo Int*. 2021;153:106597.
  227. Maruda R, Krolczyk G, Wojciechowski S, Powalka B, Klos S, Szczotkarz N, Matuszak M, Khanna N. Evaluation of turning with different cooling-lubricating techniques in terms of surface integrity and tribological properties. *Tribo Int*. 2020;148:106334.
  228. Chen G, zou Y, Qin X, Liu J, Feng Q, Ren C. Geometrical texture and surface integrity in helical milling and ultrasonic vibration helical milling of Ti-6Al-4V alloy. *J Mater Process Technol*. 2020;278:116494.
  229. Rotella G, Dillon Jr OW, Umbrello D, settineri L, Jawahir IS. The effects of cooling conditions on surface integrity in machining of Ti6Al4V alloy. *Int J Adv Manuf Technol*. 2014;71:47-55.
  230. Willert M, Zielinski T, Rickens K, Riemer O, Karpuschewski B. Impact of ultrasonic assisted cutting of steel on surface integrity. *Proc CIRP*. 2020;87:222-227.
  231. Rahim EA, Sasahara H. An analysis of surface integrity when drilling Inconel 718 using palm oil and synthetic ester under MQL condition. *Mach Sci Technol*. 2011;11(9):76-90.
  232. Astakhov VP. *Tribology in metal cutting*. 2006, Elsevier, Oxford, UK.
  233. Jain VK, Balasubramaniam R, Mote RG, Das M, Sharma A, Kumar A, Garg V, Kamaliya B. Micromachining: An overview (Part 1), *J MicroManuf*. 2020;1-17.
  234. Anand RS, Patra K. Modeling and simulation of mechanical micro-machining-A review. *Mach Sci Technol*., 2014;18(3):323-347.
  235. Boswell B, Islam MN, Davies IJ. A review of micro-mechanical cutting. *Int J Adv Manuf Technol*., 2018;94:789-806.
  236. Chae J, Park SS, Freiheit T. Investigation of micro-cutting operations. *Int J Mach Tools Manuf*., 2006;46:313-332.
  237. Ucun İ, Aslantas K, Bedir F. An experimental investigation of the effect of coating material on tool wear in micro milling of Inconel 718 super alloy, *Wear*, 2013;300(1-

- 2):8-19.
238. Lawal SA. A review of application of vegetable oil-based cutting fluids in machining non-ferrous metals, *Indian J Sci Technol.*, 2013;6:3951e3956.
  239. Bai J, Bai Q, Tong Z. Experimental and multiscale numerical investigation of wear mechanism and cutting performance of polycrystalline diamond tools in micro-end milling of titanium alloy Ti-6Al-4V, *Int J Refract Metals Hard Mater.*, 2018;74:40–51.
  240. Khalid W, Zhang C, Jamil M, Khan AM. Tool wear, surface quality, and residual stresses analysis of micro-machined additive manufactured Ti-6Al-4V under dry and MQL conditions, *Tribo Int.*, 2020;151:106408.
  241. Akhtar W, Sun J, Sun P, Chen W, Saleem Z. Tool wear mechanisms in the machining of Nickel based superalloys: A review. *Front Mech Eng.*, 2014;9:106–119.
  242. Huang P, Li H, Zhu WL, Wang H, Zhang G, Wu X, To S, Zhu Z. Effects of eco-friendly cooling strategy on machining performance in micro-scale diamond turning of Ti-6Al-4V, *J Clean Prod.*, 2020;243:118526.
  243. Santos AGD, Silva MBD, Jackson MJ. Tungsten carbide micro-tool wear when micro milling UNS S32205 duplex stainless steel, *Wear*, 2018;414-415:109-117.
  244. Vipindas K, Mathew J. Wear behavior of TiAlN coated WC tool during micro end milling of Ti-6Al-4V and an alysis of surface roughness, *Wear*, 2019;424-425:165-182.
  245. Elkaseer A, Dimov SS, Popov KB, Minev RM. Tool Wear in Micro-Endmilling: Material Microstructure Effects, Modeling, and Experimental Validation, *ASME J Micro Nano-Manuf.*, 2014;2(4):044502.
  246. Wang Y, Zou B, Wang J, Wu Y, Huang C. Effect of the progressive tool wear on surface topography and chip formation in micro-milling of Ti-6Al-4V using Ti(C7N3)-based cermet micro-mill, *Tribo Int.*, 2020;141:105900.
  247. Korkmaz ME, Gupta MK, Boy M, Yaşar N, Krolczyk GM, Günay M. Influence of duplex jets MQL and nano-MQL cooling system on machining performance of Nimonic 80A, *J Manuf Process.*, 2021;69:112- 124.
  248. Khan HM, Karabulut Y, Kitay O, Kaynak Y, Jawahir IS. Influence of the post-processing operations on surface integrity of metal components produced by laser powder bed fusion additive manufacturing: A review, *Mach Sci Technol.*, 2021;25 (1):118-176.
  249. Peng X, Kong L, Fuh JYH, Wang H. A review of post-processing Technologies in additive manufacturing, *Manuf Mater Process.*, 2021;5:38.
  250. Gomes MC, Santos AGD, Oliveira D, Figueiredo GV, Ribeiro KSB, Rios GABDL, Silva MB, Coelho RT, Hung WNP. Micromachining of additively manufactured metals: A review. *Int J Adv Manuf Technol.*, 2022;118:2059-2078.
  251. Keist JS, Palmer TA. Development of strength-hardness relationships in additively manufactured titanium alloys. *Mater Sci Eng A*, 2017;693:214–24.
  252. Li G, Chandra S, Rashid RAR, Palanisamy S, Ding S. Machinability of additively manufactured titanium alloys: A comprehensive review. *J Manuf Process* 2022;75:72-99.
  253. Sartori S, Moro L, Ghiotti A, Bruschi S. On the tool wear mechanism in dry and cryogenic turning additive manufactured titanium alloys. *Trib Int* 2017;105:264-273.
  254. Khanna N, Zadafiya K, Patel T, Kaynak Y, Rashid RAR, Vafadar A. Review on machining of additively manufactured nickel and titanium alloys. *J Mater Res Technol* 2021;15:3192-3221.
  255. Oliaei SNB, Karpat Y. Investigating the influence of built-up edge on forces and surface roughness in micro scale orthogonal machining of titanium alloy Ti6Al4V. *J Mater Process Technol.* 2016;235:28-40.

256. Roushan A, Rao US, Patra K, Sahoo P. Performance evaluation of tool coatings and nanofluid MQL on the micro-machinability of Ti-6Al-4V. *J Manuf Process.* 2022;73:595-610.
257. Ahmadi M, Karpat Y, Acar O, Kalay YE. Microstructure effects on process outputs in micro scale milling of heat treated Ti6Al4V titanium alloys. *J Mater Process Technol.* 2018;252:333-347.
258. Hao Z, Gao D, Fan Y, Han R. New observations on tool wear mechanism in dry machining Inconel 718. *Int J Mach Tools Manuf.* 2011;51:973-
259. Sharma S, Meena A. Microstructure attributes and tool wear mechanisms during high-speed machining of Ti-6Al-4V. *J Manuf Process.* 2020;50:345-365.
260. Ozel T, Thepsonthi T, Ulutan D, Kaftanoglu B. Experiments and finite element simulations on micro-milling of Ti-6Al-4V alloy with uncoated and cBN coated micro-tools. *CIRP Ann. Manuf. Technol.* 2011;60:85-88.
261. Attanasio A, Gelfi M, Pola A, Ceretti E, Giardini C. Influence of material microstructures n micromilling of Ti6Al4V alloy. *Materials*, 2013;6:4268-4283.
262. Bordin A, Sartori S, Bruschi S, Ghiotti A. Experimental investigation on the feasibility of dry and cryogenic machining as sustainable strategies when turning Ti6Al4V produced by Additive Manufacturing. *J Clean Prod* 2017;142:4142–51.
263. Shunmugavel M, Goldberg M, Polishetty A, Nomani J, Sun S, Littlefair G. Chip formation characteristics of selective laser melted Ti-6Al-4V. *Aus J Mech Eng.* 2016;17(2):109-126.